

Robert Bosch GmbH

Corporate Sector Research and Advanced Engineering
Advanced Technologies for Chemical and Biological Systems

in Zusammenarbeit mit

Medizinische Universitätsklinik und Poliklinik Tübingen

Abteilung Innere Medizin I

(Schwerpunkt: Gastroenterologie, Gastrointestinale Onkologie,
Hepatologie, Infektiologie und Geriatrie)

**Enrichment and molecular analysis of circulating tumor
cells in a microfluidic environment**

**Inaugural-Dissertation
zur Erlangung des Doktorgrades
der Humanwissenschaften**

**der Medizinischen Fakultät
der Eberhard-Karls-Universität
zu Tübingen**

vorgelegt von

Lux, Astrid, geb. Roth

2024

Dekan: Professor Dr. B. Pichler

1. Berichterstatter: Professor Dr. N. P. Malek

2. Berichterstatter: Professorin Dr. K. Schenke-Layland

3. Berichterstatter: Professor Dr. P. Michl

Tag der Disputation: 16.04.2024

MEINER OMA

„Das habe ich noch nie vorher versucht, also bin ich völlig sicher, dass ich es schaffe.“

- Astrid Lindgren

List of contents

List of contents	IV
List of tables	IX
List of figures	X
List of abbreviations	XII
1. INTRODUCTION.....	1
1.1. Lab-on-chip systems.....	1
1.1.1. Advantages and challenges of LoC systems.....	2
1.1.2. Vivalytic LoC system	2
1.2. Cancer detection and monitoring methods	5
1.2.1. Liquid Biopsy – analysis of blood samples for therapy monitoring.....	7
1.2.2. Metastasis and circulating tumor cells (CTCs).....	9
1.2.2.1. Characteristics of CTCs used for their detection in liquid biopsies	11
1.2.3. LoC systems for CTC analysis and integration of CTC analysis into Vivalytic	16
1.2.3.1. Requirements for integration of CTC analysis into the Vivalytic LoC system	17
1.3. Aim of the study	18
2. MATERIAL AND METHODS	20
2.1. Material.....	20
2.1.1. Chemicals.....	20
2.1.2. Solutions and Buffers.....	21
2.1.3. Cell culture.....	21
2.1.4. Cell lines	22
2.1.5. Kits.....	22

2.1.6.	Antibodies and cell staining solutions	23
2.1.7.	Nucleic acids, Oligonucleotides.....	24
2.1.8.	Standards.....	25
2.1.9.	Data bases and software.....	25
2.2.	Cell biological methods.....	27
2.2.1.	Blood samples.....	27
2.2.2.	Cell culture.....	28
2.2.2.1.	Cell counting and viability determination by trypan blue exclusion.....	28
2.2.2.2.	Cell viability assay.....	29
2.2.2.3.	Immunocytochemistry with and without fixation.....	29
2.2.3.	CTC detection according to maintrac®	30
2.2.3.1.	maintrac® trial with SIMFO and UKT – experimental set-up.....	31
2.2.4.	Decision matrix for CTC isolation evaluated regarding LoC integrability	32
2.2.5.	Blood sample pre-processing.....	33
2.2.5.1.	Density gradient centrifugation	33
2.2.5.2.	Erythrocyte aggregation.....	33
2.2.5.3.	Selective erythrocyte lysis	34
2.2.5.4.	SEM-analysis of blood cells and ESEM analysis of cancer cells.....	34
2.2.5.5.	Determination of the erythrocyte lysis buffer efficiency.....	34
2.2.6.	Generation and evaluation of model samples for target cell isolation.....	35
2.3.	Microfluidic methods for LoC integration of CTC detection	36
2.3.1.	Cell isolation by filtration – off-chip methods.....	36
2.3.1.1.	Rapid prototyping of a filtration functional model.....	36
2.3.1.2.	Verification of the TEM-grid properties.....	37
2.3.1.3.	TEM-grid cell filtration procedure off-chip.....	37

2.3.1.4. Methods for determination of the cell capture rate	40
2.3.2. Integration of CTC-detection into the LoC system	40
2.3.2.1. Integration of TEM-grid cell filter into the LoC cartridge	41
2.3.2.2. Microfluidic cell processing on-chip – influence on the cells	41
2.3.2.3. Optical cell detection in the LoC system	42
2.4. Molecular biological methods	44
2.4.1. Nucleic acid extraction	44
2.4.1.1. RNA extraction	44
2.4.1.2. Quantification nucleic acids and quality control	45
2.4.2. Primer and probe design	45
2.4.3. Expression analysis	45
2.4.3.1. Relative quantification of transcripts	46
2.4.3.2. Absolute quantification of transcripts	47
2.4.3.3. Multiplex one-step-RT-qPCR	49
2.4.3.4. Liquid RT-qPCR vs. lyophilized RT-qPCR	50
2.4.3.5. Stability testing of air-dried primer and probe mixes	52
2.4.3.6. Nested-PCR	52
2.5. Statistical analysis	53
3. RESULTS	54
3.1. CTC detection in patient samples according to the maintrac® method	54
3.2. Establishment of LoC compatible unit operations for CTC detection	58
3.2.1. Establishment and adaptation of CTC detection for integration onto the LoC-system ..	58
3.2.2. Selection of a method for erythrocyte depletion in blood samples	62
3.2.2.1. Minimization of erythrocyte lysis buffer volume	65

3.2.2.2.	SEM-analysis of blood cells after erythrocyte lysis	66
3.2.2.3.	Influence of the ELB on cell viability	67
3.2.3.	Evaluation of RBC depletion and CTC isolation methods in regard of LoC integration	68
3.2.4.	Evaluation of filtration-based methods for CTC isolation.....	69
3.2.4.1.	Evaluation of filtration for CTC isolation using the current Vivalytic cartridge.....	69
3.2.4.2.	Filtration functional model for CTC-isolation and detection using TEM-grids	70
3.2.4.3.	Real-time detection for quantification of CTCs and evaluation of cell detection	81
3.2.4.4.	Leukocyte depletion for background reduction and increased sample purity	85
3.2.4.5.	ESEM analysis of the cells captured on the filter	87
3.3.	Integration of the CTC detection method into the LoC.....	89
3.3.1.	Influence of the forces inside the microfluidic system on the cells.....	90
3.3.2.	Cell capture by filtration in the microfluidic system (on-chip)	97
3.3.3.	Optical cell detection using the Vivalytic analyzer	100
3.4.	Molecular characterization of the cells captured on the filter	103
3.4.1.	Correlation of EpCAM staining to EpCAM and mesenchymal marker expression.....	105
3.4.2.	Evaluation of direct cell lysis and usage of cell lysates as template in RT-qPCR.....	107
3.4.3.	Maximal tolerance of leukocyte background in cell lysates.....	110
3.4.4.	Cell lysis on the filter.....	111
3.4.4.1.	Increase of sensitivity by nested RT-qPCR	113
3.4.5.	Establishment of RT-qPCR protocols for LoC integration	114
3.4.5.1.	Establishment of duplex and multiplex RT-qPCR protocols.....	114
3.4.5.2.	Evaluation of long-term stability of RT-qPCR components	117
4.	DISCUSSION	121
4.1.	Reproducibility of the maintrac® method and correlation to the disease progression	121

4.2.	Establishment of protocols for LoC integration of CTC detection	125
4.2.1.	Evaluation of erythrocyte depletion methods in regard of LoC integration	128
4.2.2.	CTC isolation evaluated in regard of the integrability to the LoC system	129
4.2.2.1.	Cell detection and tracking in real-time increased quantification efficiency	133
4.2.3.	Integration of CTC isolation and detection into the Vivalytic LoC platform.....	134
4.2.3.1.	Optical cell detection using Vivalytic.....	137
4.3.	Complementary information obtained from molecular analysis of captured CTCs.....	137
4.3.1.	Compatibility of the filtration-based CTC capture with downstream analysis	139
5.	CONCLUSION AND OUTLOOK.....	144
5.1.	Summary.....	148
5.2.	Zusammenfassung	150
	REFERENCES	CLII
	APPENDIX	CLXVII
	LIST OF PUBLICATIONS, INVENTIONS, AND CONFERENCE CONTRIBUTIONS	CLXXIV
	ERKLÄRUNG ZUM EIGENANTEIL DER DISSERTATIONSSCHRIFT.....	CLXXVI
	DANKSAGUNG	CLXXVIII

List of tables

Table 1: List of chemicals used and information on purity, concentration, and supplier.....	22
Table 2: List of buffers and their composition.....	23
Table 3: Cell lysis buffers for generation of cell lysates as templates for RT-qPCR.....	23
Table 4: List of cell culture media and reagents.....	24
Table 5: List of cell lines, their provider, and the applied media for cultivation.....	24
Table 6: List of commercially available kits for nucleic acid extraction and analysis methods.....	24
Table 7: List of antibodies and staining reagents used for cell detection.....	25
Table 8: List of oligonucleotides.....	26
Table 9: List of commercially available standards applied for analysis methods.....	27
Table 10: List of databases and analysis software.....	27
Table 11: List of patient pseudonyms and sample time points.....	34
Table 12: Different lysis buffer volumes evaluated to determine the minimal volume required.....	37
Table 13: Syringe pump settings for the off-chip filtration experiments.....	41
Table 14: Fluorescent dyes used for CTC detection.....	45
Table 15: Composition of RT-qPCR mastermix using Luna® Universal Probe One-Step RT-qPCR..	48
Table 16: Program for the RT-qPCR using Luna® Universal Probe One-Step RT-qPCR Kit.....	48
Table 17: Reaction setup using SuperScript™ III First-Strand Synthesis SuperMix Kit.....	49
Table 18: Temperature setup for SuperScript™ III First-Strand Synthesis SuperMix Kit.....	50
Table 19: Reaction setup for two-step RT-PCR using Q5 High-Fidelity 2X Master.....	50
Table 20: Temperature setup for Q5 High-Fidelity 2X Master Mix.....	50
Table 21: Composition of the primer and probe mixes with different primer concentrations.....	52
Table 22: Composition of RT-qPCR multiplex mastermix using Luna® Universal Probe One-Step RT-qPCR.....	52
Table 23: Pipetting scheme for CIRRUS™ Strips RNA and SCRIPT RT-qPCR ProbesMaster mix...	53
Table 24: PCR program for the CIRRUS™ strips RNA reactions.....	53
Table 25: PCR program for the SCRIPT RT-qPCR ProbesMaster Lyophilisate reactions.....	54
Table 26: Fluorescent dye combination for CTC detection and characterization.....	63
Table 27: Comparison of the recovery rate of stained BT-474 cells spiked into whole blood using three erythrocyte depletion methods.....	66
Table 28: Cells stained with different fluorescent dyes detected using the Vivalytic analyzer and VPhotoStar control software.....	104

List of figures

Figure 1: Vivalytic analyzer (A) and Vivalytic cartridge (B).	3
Figure 2: Schematic overview of the Vivalytic cartridge is composed of several layers.	4
Figure 3: Scheme of the setup and working principle of the pneumatically actuated microvalve.	4
Figure 4: Possibilities to separate the different fractions of whole blood.	8
Figure 5: The process of metastasis.	9
Figure 6: Scheme of gene expression during the EMT and MET process.	11
Figure 7: Overview of different CTC isolation and characterization methods.	12
Figure 8: Possible LoC workflow for automation of CTC analysis.	19
Figure 9: User interface of the Fluculator software.	26
Figure 10: User interface of the VPhotoStar software for cartridge processing and imaging.	27
Figure 11: Schematic overview of the maintrac® method.	31
Figure 12: Design and fabrication steps of the cell capture device.	37
Figure 13: Filtration functional model for cell capture.	38
Figure 14: Microfluidic paths visualized using the Fluculator software.	42
Figure 15: Optical cell detection using the Vivalytic analyzer.	43
Figure 16: Example images of cells detected in patient samples.	55
Figure 17: Patient samples obtained from the UKT analyzed by the maintrac® method.	57
Figure 18: EpCAM-FITC and PI staining of cell lines.	59
Figure 19: Adapted staining protocol.	60
Figure 20: HCT116 cells stained with CFSE, EpCAM-APC and PI.	61
Figure 21: Leukocytes stained with CD45-PE.	62
Figure 22: Microscopy of the cells extracted from buffy coat after density gradient centrifugation.	62
Figure 23: Blood sample observed by light microscopy during selective erythrocyte lysis.	63
Figure 24: Erythrocyte depletion by aggregation.	64
Figure 25: Determination of the minimum required erythrocyte lysis buffer.	66
Figure 26: Blood sample spiked with BT-474 cells analyzed by SEM.	67
Figure 27: Cell viability after erythrocyte lysis.	68
Figure 28: A: Experimental set-up and B: results of cell filtration using the filter B and D.	70
Figure 29: TEM-grid imaged by SEM for pore size measurement.	71
Figure 30: Filtration functional model.	72
Figure 31: Cell recovery by the system with and without passivation of the channels and tubes.	73
Figure 32: Images of the (A) one-armed and (B) two-armed single unit operation model.	74
Figure 33: Comparison of cell retention rates achieved by the two different filter slide designs.	75
Figure 34: Comparison of the capture rate for BT-474, K562 and HCT116.	76
Figure 35: Capture rates of HCT116 cells without blood and spiked into whole blood.	77
Figure 36: Different cell numbers spiked into 200 μ L blood.	78
Figure 37: CTC capture rates after TEM-grid filtration of patient blood samples.	79
Figure 38: Influence of flow rate and flow profile on cell filtration.	80
Figure 39: Comparison of endpoint and real-time cell counting on the filter.	82
Figure 40: Schematic overview of the object detection pipeline applied for cell tracking in videos.	83
Figure 41: Automated cell counting in images and videos.	84
Figure 42: Leukocyte depletion by filtration of blood using the TEM-grid.	86
Figure 43: Leukocyte depletion determined by RT-qPCR with the target GAPDH.	87
Figure 44: ESEM analysis of HCT116 cells filtered using the two-armed filtration functional model.	88
Figure 45: ESEM analysis of blood spiked with HCT116 captured on the TEM-grid.	89
Figure 46: Viability of HCT116 cells after 15 min, 30 min and 60 min incubation at 40°C.	90

Figure 47: Fluidic paths for transport of cells on the cartridge and evaluation of cell viability.	91
Figure 48: CFSE stained HCT116 cells in the microfluidic channels of a Vivalytic cartridge.	92
Figure 49: Quantification of cells after microfluidic transport.	93
Figure 50: Cell viability after on-chip processing using different paths, cycle numbers and pump rates....	94
Figure 51: Determination of cell viability after transport of cells through the filter.....	96
Figure 52: Vivalytic cartridge with enlarged TPU membrane and TEM-grid integrated into the filter chamber for a proof-of-principle experiment of cell filtration.....	98
Figure 53: CFSE stained HCT116 cells filtered on-chip.	98
Figure 54: Cell capture on the TEM-grid integrated into the Vivalytic cartridge.....	99
Figure 55: Number of cells captured on the TEM-grid integrated into the Vivalytic cartridge.....	100
Figure 56: 3D printed cartridge used as a cell counting slide holder for optical analysis of stained cells in the Vivalytic analyzer.....	101
Figure 57: HCT116 cells stained with CFSE and captured on a TEM-grid.....	103
Figure 58: Determination of the RNA integrity after extraction from whole blood.	104
Figure 59: CTC count course and gene expression results of patient BO-645.	106
Figure 60: CTC count course and gene expression results of patient BO-408.	107
Figure 61: Possibilities for the generation of cell lysates for usage as templates in RT-qPCR.	109
Figure 62: Ct values of the RT-qPCR with lysates of 10^4 HCT116 cells mixed with different leukocyte dilutions obtained from a blood sample of 1 mL after erythrocyte lysis.....	110
Figure 63: (A) EpCAM, (B) Twist and (C) Snail copy number determined in HCT116 lysates by RT-qPCR.	112
Figure 64: Comparison of conventional and nested RT-qPCR using cell lysates of 10^4 , 10^3 , 10^2 and 10^1 HCT116 cells as templates.....	114
Figure 65: Multiplex RT-qPCR with different primer and target concentration combinations.	116
Figure 66: (A): Exemplary EpCAM standard curves.....	118
Figure 67: Results of multiplex RT-qPCR with air-dried primers and probes.....	119

List of abbreviations

Abbreviation	Definition
μTAS	micro total analysis systems
APC	Allophycocyanin
BSA	Bovine serum albumine
CFSE	Carboxyfluorescein succimidyl ester
CMOS	complementary metal-oxide-semiconductor
CT	Computer tomography
CTC(s)	Circulating tumor cell(s)
DNA	Desoxyribonucleic acid
DxC	Data exchange control
DxU	Data exchange unit
EDTA	Ethylenediaminetetraacetic acid
ELB	Erythrocyte lysis buffer
EMT	Epithelial mesenchymal transition
EpCAM	Epithelial cell adhesion molecule
ESEM	Environmental scanning electron microscopy
FSS	Fluid shear stress
GAPDH	Glyceraldehyde-3-phosphate dehydrogenase
LED	Light emitting diode
LoC	Lab-on-chip
MET	Mesenchymal epithelial transition
MNBCs	Mononuclear blood cells
MRI	Magnetic resonance imaging
MRSA	methicillin-resistant Staphylococcus aureus
PBS	Phosphate buffered saline
PE	Phycoerythrin
PET	Positron emission tomography
PI	Propidium iodide
PoC	Point-of-care
RBC	Red blood cell
RNA	Ribonucleic acid
RT-qPCR	Reverse transcription quantitative polymerase chain reaction
SEM	Scanning electron microscopy
SIMFO	Spezielle Immunologie und Forschung GmbH
TEM	Transmission electron microscopy
TPU	Thermoplastic polyurethan
UKT	Universitätsklinikum Tübingen

1. Introduction

Medical samples such as swabs, urine, sputum, or blood are commonly collected in clinical practice but analyzed in external, centralized biomedical laboratories. Therefore, several days can pass before test results are available which might result in a delay of critical therapy decisions. In various cases i.e., sepsis diagnosis or viral infections like COVID-19, a fast sample analysis and treatment decision is of great interest to prevent serious health consequences or spreading of the disease. Thus, in recent years, point-of-care (PoC) testing, beyond pregnancy tests and blood glucose measurements, has gained interest.

Regarding cancer therapy monitoring, recognizing the development of treatment resistance is important for therapy adaptation and might influence the overall success of the therapy. However, given the invasive, costly, and time-consuming nature of many cancer monitoring methods, patients often do not take advantage of the analyses or might not have access due to geographical and ecological barriers (1). Primary tumors constantly release cells into the bloodstream and thus, the risk for metastasis might increase continuously. The presence of these circulating tumor cells which are present in the bloodstream correlates with prognosis and measuring their number might provide valuable information regarding progression, tumor growth dynamics and therapy success (2). Therefore, continuous and minimally invasive monitoring at the point-of-care might provide a possibility to react to changes in therapy response much earlier than changes are recognized by imaging techniques or only after symptoms get worse. Moreover, point-of-care test systems for cancer might enable access to early diagnosis, therapy monitoring and management in low resource areas (3).

1.1. Lab-on-chip systems

Classical medical diagnostic assays encompass numerous manual handling steps from sample taking to the final diagnosis. Trained and experienced staff, elaborate and costly equipment are required to conduct the analyses. Depending on the sample type, the analyses often need to be performed in specialized laboratories. Therefore, test results for subsequent evaluation and therapy decision will often be obtained only after several days. A possibility of increasing interest to simplify and automatize molecular diagnostic assays is provided by the integration of test assays into microfluidic systems, also called micro total analysis systems (μ TAS) or lab-on-chip (LoC) that combine the functionalities of a whole laboratory in a miniaturized, microfluidic circuit (4). In such way LoC systems enable the transition to molecular diagnostics in a sample-to-result manner at the PoC.

1.1.1. Advantages and challenges of LoC systems

Advantages of LoC test systems compared to the classical sample analysis procedures are the reduced hands-on time, the elimination of manual preparation steps and sample transport to external laboratories altogether leading to a cost and time reduction (5) (6). Furthermore, the systems are easy to operate, and the automation increases the reproducibility of results and decreases the risk of contamination. Samples are processed in a sample-to-result manner, meaning that a sample is placed in a device that operates all the necessary steps automatically and displays the result in the end. Thus, no experienced staff is required for sample preparation or bioanalytical evaluation (7). In this way manual, operator-related variations and errors are prevented. Examinations and sample analyses can be performed quickly and regularly. This is essential for the development of approaches in personalized medicine or in case of critical infections or diseases that require immediate action. The result is available at the point-of-care (PoC). Thus, the treatment strategy in acute diseases can be adapted earlier and targeted. In addition, PoC technologies might help to overcome geographical, cultural, and economic barriers (8).

Challenges, on the other hand, that appear with integration of sample preparation and analysis into LoC systems are the incompatibility of the chip materials with certain chemicals and the limited volume capacity due to miniaturization. This makes robust and sensitive assays crucial that can cope with minimal sample input. The reference assay must be very well known to adapt the single unit operation steps for LoC integration by measures like sample and reagent volume reduction, replacement of certain assay compounds, reduction of time for the single processing steps and evaluation of compatibility of all the components to microfluidics concerning viscosity, shear forces and air bubble formation during transport. Thereby, assays integrated to LoC systems should achieve the same result in quality and quantity as the conventional manual (off-chip) assay. Furthermore, many LoC systems do not generate a quantitative result but offer either a positive or negative result only. Obtaining quantitative answers is challenging, as the readout often requires complex and expensive electronics and electrical systems and sensors (9).

1.1.2. Vivalytic LoC system

The Bosch Healthcare Solutions GmbH has developed an automated microfluidic platform for molecular diagnostics such as the rapid PCR testing of SARS-CoV-2, respiratory infections, sexually transmitted infections, or methicillin-resistant *Staphylococcus aureus* (MRSA)

detection (10). The processing steps for sample preparation such as cell lysis, nucleic acid extraction, amplification, and bioanalytical detection are carried out automatically in one universal analyzer, the data exchange unit (DxU; Figure 1A) that operates the required steps on a microfluidic, assay-specific disposable cartridge, the data exchange control (DxC; see Figure 1B).

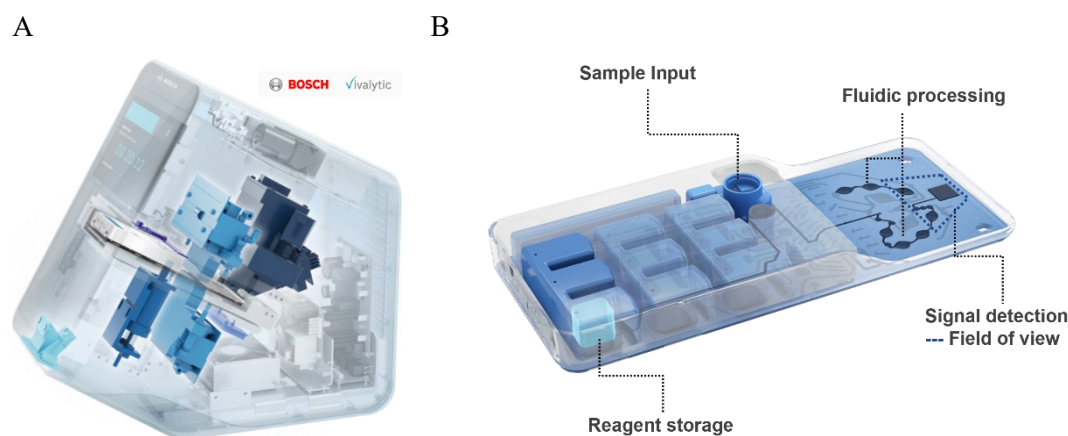


Figure 1: Vivalytic analyzer (A) and Vivalytic cartridge (B).

The analyzer (A) is the data exchange unit and enables automated processing of biological assays on the data exchange control, a disposable cartridge (B), which contains all the required assay-specific reagents and biological content. The sample can be transferred into the cartridge, irreversibly closed and after insertion into the analyzer, the fluidic and thermal protocol is run automatically. Afterwards, the test result is presented on the display of the analyzer.

The analyzer is a stand-alone device containing a sample and cartridge barcode scanner needed for the assay specific settings and test documentation, a sonotrode for cell disruption, pneumatics and thermal elements required for actuation and processing of the sample on the cartridge, an optical system for the readout and a display as user interface. The cartridge is composed of polymer layers that are connected via a laser welding process: a fluidic layer and a pneumatic layer separated by a thermoplastic polyurethane (TPU)-membrane, and a sealing layer. Each cartridge is closed with a lid included in the cover with the label for each specific assay. Beneath the cover, reagent chambers are included with pre-stored assay-specific reagent bars that are sealed and only opened upon cartridge processing in the analyzer. Below the reagent storage, a sample with a volume between 50 μL and 2 mL can be filled into the sample chamber. On the lower part of the cartridge, the fluidic network is placed composed of microchannels, membrane-based pump chambers, reaction chambers and microvalves. These serve as micropumps that are opened and closed by the pressure-driven flexible TPU-membrane and realize the fluid transport through the network as shown schematically in Figure 3 (11).

A

B

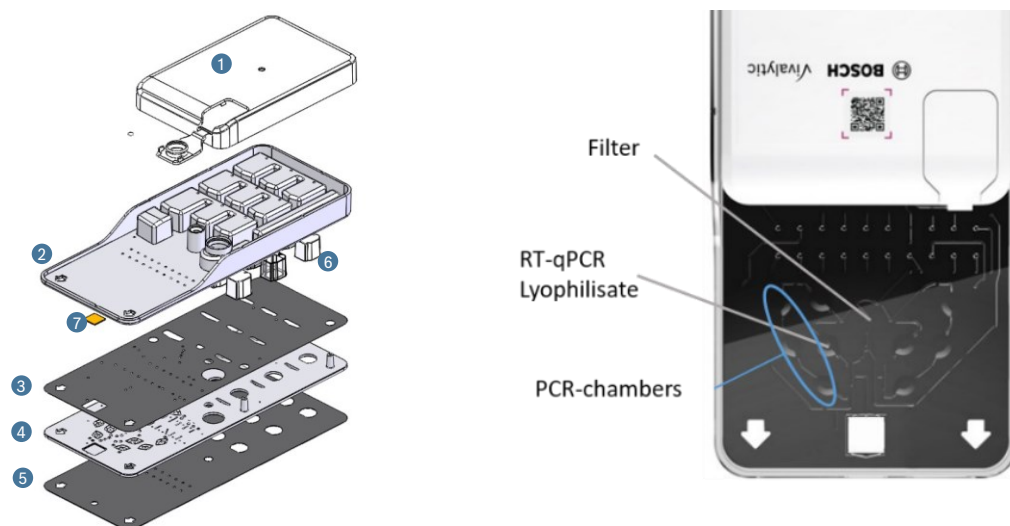


Figure 2: Schematic overview of the Vivalytic cartridge is composed of several layers. (A): (1) a cover with an assay specific label, (2) a fluidic layer made of injection molded PC, (3) a TPU membrane, (4) the pneumatic layer and (5) a PC seal film. Below the cover reagent bars (6) are placed for prestorage of buffers and reagent required for the assay. Within the fluidic network (B) of the cartridge, three PCR chambers are on the left and right side, possibly storing a PCR lyophilisate for low-multiplex PCR. Alternatively, a silicon or ceramic array (7) can be placed in the array chamber for high-multiplex reactions in microcavities.

The micropumps process the fluids by application of two different pressure levels: overpressure ($P_c > P_h$) pushes the TPU onto the pneumatic layer and liquid in the chamber is displaced from the chamber or valve. In turn, by applying vacuum the TPU is pulled towards the fluidic layer and the liquid can flow into the chamber or valves. By alternating vacuum and overpressure, the liquid can be transported through the complete microfluidic network using different paths that can be defined depending on the sequential actuation of valves and chambers. This results in a pulsatile flow whose flow rate is influenced by the pump frequency (duration of actuation steps).

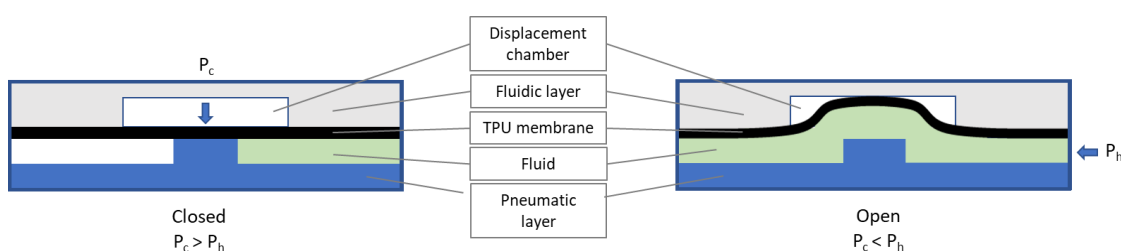


Figure 3: Scheme of the setup and working principle of the pneumatically actuated microvalve. The functional unit is made of a three-layer stack consisting of an upper fluidic layer and a lower pneumatic layer made of polycarbonate separated by a thermoplastic polyurethane membrane. Scheme modified according to (11).

The three PCR chambers on each side of the microfluidic network can be heated and cooled, and the PCR is performed by cyclic transport of the fluid into the chambers of different temperatures for denaturation, annealing and extension. The lowermost chambers and the rectangular array chamber are within the optical system's field of view and used for fluorescence

signal detection. Possible read outs are microarrays, qualitative or quantitative PCR and melting curve analyses.

Therefore, the Vivalytic analyzer is equipped with an optical system for excitation and detection of fluorescence probes and dyes. The excitation is achieved by a white light emitting diode (LED) and detection is realized by a complementary metal-oxide-semiconductor (CMOS) sensor. Four different filters are included in the analyzer enabling the detection of 4 fluorescent labels or probes: FAM (Abs/Em: 495 nm/517 nm, CAL Fluor Orange (Abs/Em max: 538 nm/559 nm), CAL Fluor Red (Abs/Em max: 569 nm/591 nm) and Quasar (Abs/Em max: 647 nm/670 nm). The field of view is limited to the lower part of the cartridge encompassing the lowermost PCR chambers and the array chamber. The resolution of the optical system is approx. 56 μm . This is suitable for the detection of the mean fluorescence signal in the PCR chamber or microwells in a microarray, where the complete area is used for read-out.

Due to the platform character of the Vivalytic system, the test portfolio can be continuously extended by additional assays that are integrated onto the same device after assay-specific adaptations within the cartridges such as the prestored reagents and volumes and the biological content like a lyophilized PCR reaction mix bead. For integration of existing or novel biological assays into the LoC system, the required processing steps of the reference assay need to be identified and understood. Afterwards these steps are miniaturized if necessary and implemented to the microfluidic system as single unit operations to optimize the individual steps. At last, all single unit operations are combined into an automated protocol. In such way, the molecular diagnostic assay portfolio could also be extended by oncology applications for cancer therapy monitoring as presented in this study.

1.2. Cancer detection and monitoring methods

Cancer is estimated to be the second leading cause of death globally by the World Health Organization with breast and lung cancer being the most prevalent and colorectal cancer being the third most prevalent malignant tumor worldwide (12) (13). In most cases, not the primary tumor itself but metastases that develop in later stages of the disease are the most common cause for cancer-related deaths (14). Metastases can occur even several years after therapy or removal of the primary tumor (15). Although the metastatic process is not fully elucidated, it is known that primary tumors release cells into the blood and lymph system that can exit at a distant site in the body and cause metastasis. Under therapy, tumor cells tend to develop treatment resistance leading to a decreased or failed response to therapy (16). Therefore, there is a global

unmet need for rapid and cost-effective prognostic and diagnostic methods that enable to detect spreading cancer before the formation of metastases. However, due to individual manifestation and high variability and heterogeneity of metastases there is no universal treatment concept for all patients. Ideally, optimal personalized therapy should be determined for each patient (17). Therefore, methods and suitable biomarkers for therapy monitoring that enable adaptation of treatment accordingly are extensively studied (3).

Classically, solid tumors are detected by image-based methods such as computer tomography (CT), magnetic resonance imaging (MRI) or positron emission tomography (PET). These methods are rapid, easy to use and display the tumor visually, but are limited to detection of tumors above 1 cm in diameter (18). Thus, they are unable to detect minimal residual disease or recurrence of a tumor or metastases after surgical removal at an early state. Also, imaging methods are limited to specific sites of the body and are exposing patients to additional ionizing radiation and should therefore not be repeated in short intervals (19). When a solid tumor was recognized and localized by imaging, a biopsy is performed, and the tissue sample is examined by a pathologist. This enables histological and molecular analyses for the characterization of tumor tissues and requires only short operation time. On the other hand, a classical biopsy is limited to the sampled site. Hence, it is unable to represent the entire tumor mass present in the body and does not cover the inter- and intra-tumor heterogeneity. In addition to some tumors not being accessible for a biopsy, the sampling method is invasive and serial biopsy is often not practicable or can be accompanied with discomfort for the patient.

Nevertheless, the therapeutic strategy is often defined based on the characteristics of the primary tumor that are frequently removed by surgery or destroyed by radiation. However, tumor development and metastatic spread might not be based on the same genetic features and metastases require systemic treatment such as (targeted) chemotherapy or immune therapy (20). For those reasons, in recent years the analysis of blood samples for cancer detection or disease monitoring was intensively studied. Thereby, blood is analyzed for suspicious cells (circulating tumor cells; CTCs) or other biomarkers (e.g., circulating tumor DNA; ctDNA) indicating tumor activity in the body. These liquid biopsies represent a minimally invasive method for cancer detection or treatment monitoring. Especially after surgical removal of the tumor and in the adjuvant setting, periodical monitoring using liquid biopsies could be beneficial to detect regression in early phases or spare the patients side effects of ineffective or unnecessary therapies. Moreover, the molecular profile and potential therapy induced changes can mirror therapy response as well as emerging therapy resistances or progression.

1.2.1. Liquid Biopsy – analysis of blood samples for therapy monitoring

Blood of the human body is composed of liquid and solid components. The liquid part of the blood, plasma, contains water, salts, proteins, and nucleic acids. The solid part contains different numbers of erythrocytes (red blood cells; RBCs), leukocytes (white blood cells; WBC) and thrombocytes (platelets). The platelets are present in numbers of 150-400/nL and are the smallest components of the solid matter with 2-4 μm in diameter. The most abundant cell type in the blood are the RBCs with 4.1 to 5.1/pL and have a size of approximately 8 μm in diameter. Erythrocytes have no nucleus and are therefore very flexible and able to pass the smallest capillaries in the body. The nucleated cell fraction of the blood is represented by the leukocytes (4 to 11/nL) with sizes ranging from 8 to 25 μm in diameter. There are different types of leukocytes: granulocytes (neutrophils, eosinophils, and basophils), monocytes, and lymphocytes (T cells and B cells).

Depending on the analysis, separation of the different blood components can be necessary. The different centrifugation-based methods are shown in Figure 4. The most common method to separate the liquid part of the blood from the solid components is centrifugation. Thereby, the cells sediment to the bottom of the sample tube and the plasma can be collected. Depending on the centrifugal force applied, plasma can still contain the platelets or be completely free of solid material only containing nucleic acids, salts, and proteins. By centrifugation, the erythrocytes and leukocytes end up in one fraction. For separation of RBC and WBC from each other, one option is a density gradient centrifugation. Thereby, the blood sample is layered on top of a reagent containing a neutral, highly branched, high-mass, hydrophilic polysaccharide such as Ficoll™. This reagent takes advantage of the density differences between mononuclear cells and other blood components. After centrifugation, the cells are distributed in the sample tube in layers based on the differences in density: the erythrocytes are aggregated and sediment through the reagent to the bottom of the tube, followed by the Ficoll™ reagent, on top of which the WBCs (or peripheral blood mononucleated cells; PBMCs) are concentrated into the so-called buffy coat. On top of the buffy coat, the plasma can be collected (21). Another method for PBMC isolation is the selective lysis of erythrocytes by ammonium chloride buffer (22) (23). Thereby, PBMCs remain intact whereas the RBCs are lysed due to the $\text{Cl}^-/\text{HCO}_3^-$ -transporter on their membrane and the enzyme carbonic anhydrase, present in RBC. Ammonia (NH_3), formed by dissociation from NH_4^+ in the lysis buffer, enters the RBC by diffusion. Inside the RBC, the NH_3 is bound to H^+ derived from H_2CO_3 , formed by the carbonic anhydrase from H_2O and CO_2 . The remaining HCO_3^- inside the cell is exchanged for Cl^- from the medium

surrounding the RBC by the $\text{Cl}^-/\text{HCO}_3^-$ -transporter. This results in accumulation of NH_4^+ and Cl^- in the RBC and finally osmotic swelling and lysis of the RBC (24). During centrifugation, the intact PBMC can be pelleted while the lysed RBC remain in the supernatant. In all described cases, potentially present CTCs would be recovered in the PBMC fraction.

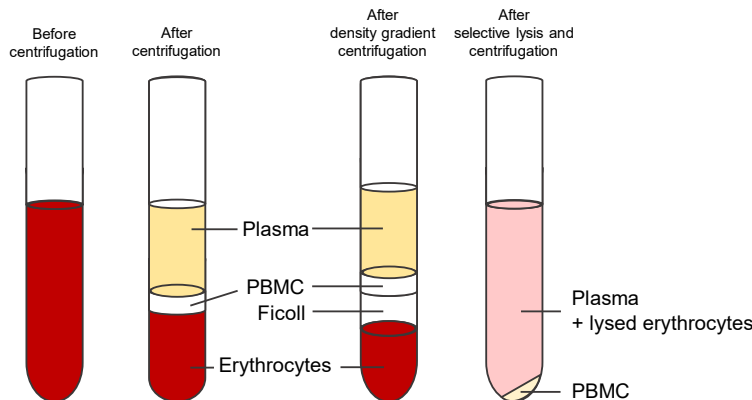


Figure 4: Possibilities to separate the different fractions of whole blood.

Simple centrifugation leads to sedimentation of RBC and PBMC into the same fraction, whereby most of the PBMC are on top of the RBC and are visible as white layer. After density gradient centrifugation with Ficoll, the PBMC are collected in one fraction between the Ficoll and the plasma and are separated from the RBC that sediment below the Ficoll. Thereby RBC and PBMC can be collected separately and intact. After selective lysis of the erythrocytes and centrifugation, the RBC are lysed and locates in the supernatant and the PBMC sediment to the bottom and form a pellet that can be collected after removal of the supernatant.

None of the above-mentioned methods (schematically shown in Figure 4) ensure separation of the different cell fractions with 100 % purity. For example, after density gradient centrifugation, PBMCs (and if present CTCs) can be recovered from the buffy coat. But due to density variations it is possible that some PBMCs or CTCs sediment below the Ficoll™ phase or remain above the Ficoll™ phase and are not recovered with the buffy coat. In case of selective erythrocyte lysis, some erythrocyte might sediment to the PBMC pellet due to incomplete lysis. Some PBMCs, in turn, might remain in the supernatant or might be negatively impacted by prolonged incubation time with the lysis buffer. However, in comparison cell recovery is higher using the selective lysis method than density gradient centrifugation (25) (26). In addition, selective lysis renders RBCs transparent as their inside hemoglobin is exchanged for the surrounding medium. After centrifugation, the red color in the suspension and the lysed RBCs are removed by discarding the supernatant facilitating optical analysis of the remaining intact cells.

After both density gradient centrifugation and selective lysis with subsequent centrifugation, CTCs and PBMCs are recovered in the same fraction. One option to differentiate the cell types e.g., WBCs from CTCs, in a mixed cell suspension is microscopic analysis. The different blood

cell types can be differentiated by their size but also by specific antigens that can be stained using fluorophore-labeled antibodies. Leukocytes can be detected by staining leukocyte specific cluster of differentiation (CD) antigens, such as CD-45 (27) (28). Epithelial CTCs on the other hand do not express CD-45 but do express the epithelial cell adhesion molecule (EpCAM) or certain cytokeratins (CK) (29).

1.2.2. Metastasis and circulating tumor cells (CTCs)

Circulating tumor cells were first reported in 1869 after tumor cells with similarities to the cells from the primary tumor were found in the blood of a man who died of metastatic cancer (30). CTCs are regarded as the major cause for metastasis and their presence in blood has been found to correlate with treatment response and prognosis (17). An increase of CTCs correlates with a bad prognosis or resistance to therapy (31). Therefore, detection and quantification of CTCs could help to predict the risk of metastatic relapse thereby monitoring treatment efficacy (32). As shown in Figure 5, CTCs can detach from the primary tumor, enter the vasculature, and circulate in the blood stream or lymph system. In such a way they can reach distant organs or tissue and form metastases at various sites in the body after extravasation. The first step for the metastasis formation after intravasation is a reprogramming of the cell specific characteristics through epithelial-mesenchymal transition (EMT) including tight junction dissolution, disruption of apical–basal polarity, and cytoskeletal rearrangement (33). Originally, EMT was discovered as part of embryogenesis. It plays a significant role in development, wound healing but also malignant progression through which cancer cells acquire properties associated with more aggressive phenotypes.

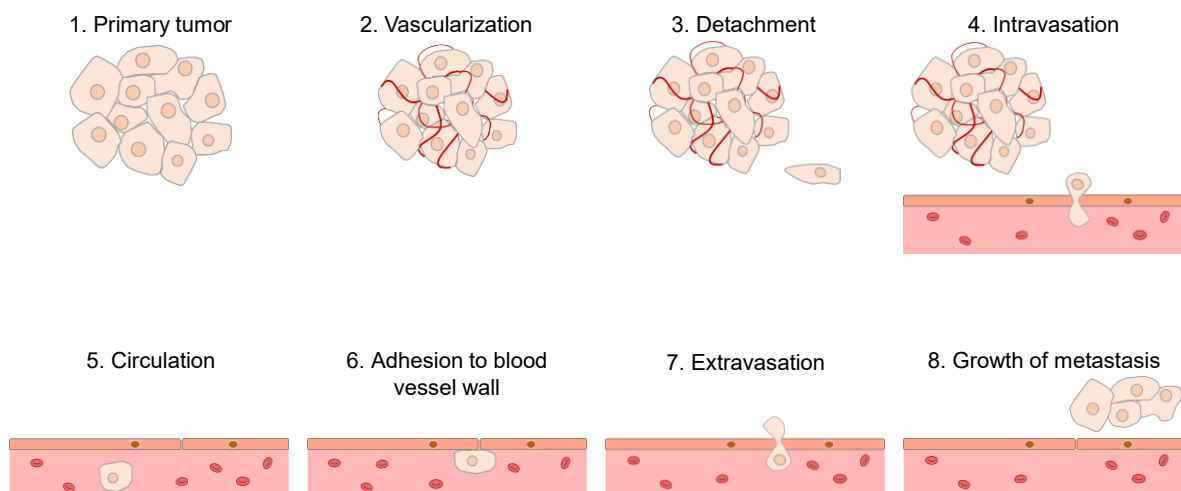


Figure 5: The process of metastasis.

Thereby, cells from a primary (1), vascularized tumor (2) detach (3) and intravasate nearby blood vessels (4). The cell can circulate in the vascular system (5) and eventually adhere to blood vessel walls (6). From there they extravasate (7) and migrate into the surrounding tissue, where they can form a metastasis (8). Scheme adapted from (34).

The acquired mesenchymal characteristics confer the cells the ability to leave the primary tumor site, invade and migrate in the bloodstream either as single cells or cell clusters. Most of these cells are destroyed by the immune system, succumb to shear forces, or become apoptotic (with a half-life of < 30 min for single cells and < 10 min for clusters) (35). In addition, the missing cell-cell contact to the stromal tissue of the primary tumor induces anoikis, a subset of apoptosis that is induced as a response to detachment of the cells from their original matrix (36) (37) (38). Only approximately 0.1 % of the CTCs in the bloodstream can survive in the vasculature and invade the surrounding tissue (39) (40) (41). There the process is reversed, and cells undergo mesenchymal to epithelial transition (MET; schematically shown in Figure 6) leading to the formation of metastases in distant organs.

The factors involved in induction of carcinogenic EMT and repressing epithelial proteins such as the tumor suppressor E-cadherin include members of the Snail and Twist transcription-factor families. They promote cancer cells motility and invasive properties, and EMT-induction correlates with a gain of some malignant properties. A large fraction of human cancers overexpresses Twist1 and/or Twist2 that have been shown to favor the metastatic dissemination of cancer cells through their ability to induce and regulate EMT (42) (43). Activation of *SNAIL* or *SNAIL2* has been associated with inhibition of apoptosis and increased invasiveness and therefore with elevated risk of metastasis and a poor prognosis in different tumor progression models (44) (45). During EMT, the expression of epithelial markers like EpCAM, cytokeratin, and E-Cadherin is downregulated (relevant markers are exemplarily shown in Figure 6). There are numerous data suggesting that individual markers of EMT (e.g., loss of EpCAM or E-cadherin expression and overexpression of Twist, Snail, or vimentin) might act as predictors for therapeutic and survival outcomes of patients with cancer. Recently, it has been stated that the EMT is a process of transitional stages between the epithelial and mesenchymal phenotypes. Thus, tumor cells that express a mix of epithelial and mesenchymal phenotypes can be present in liquid biopsies. These are described to be even more effective in circulation, colonization at the secondary site, and the development of metastasis (46). Therefore, expression analysis of EMT-related markers in liquid biopsies in addition to CTC enumeration, is regarded as additional promising prognostic indicator.

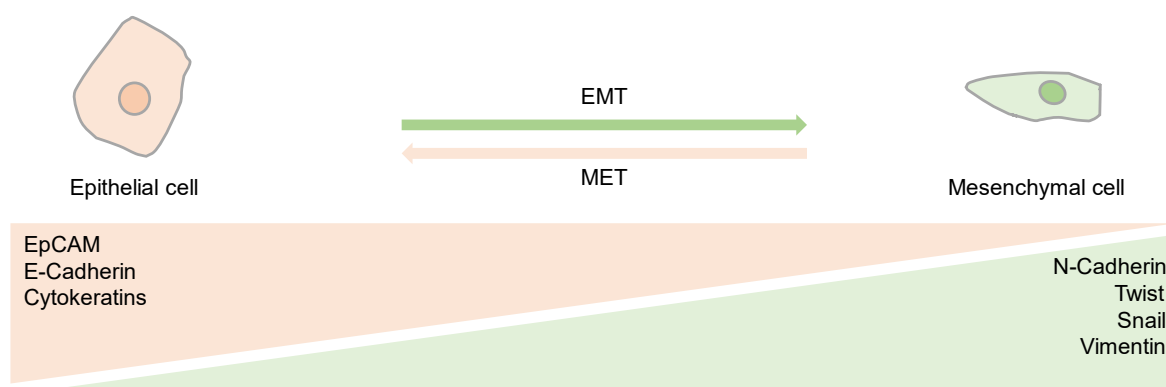


Figure 6: Scheme of gene expression during the EMT and MET process.

It is involved in intravasation and extravasation of tumor cells during metastasis formation. Epithelial genes are downregulated during EMT whereas mesenchymal genes are upregulated and vice versa.

The physical and biological characteristics enabling the CTCs to survive after their release from the primary tumor are not fully elucidated. Recent studies stated that various blood and immune cells or multiple CTCs are involved in survival of the CTCs in the bloodstream and the formation of metastases (47) (48) (49) (50). Therefore, the detection and characterization of both epithelial and mesenchymal CTCs can be relevant for prognostic predictions and clinical management during therapy and represent an additional diagnostic marker (51) (52) to detect metastases in early stages and for efficiency control during and after a therapy to adapt or recommence therapy in case of a recurrence.

1.2.2.1. Characteristics of CTCs used for their detection in liquid biopsies

CTCs are highly amenable to PoC detection due to their presence in blood. This enables minimally invasive sample taking that can be repeated in short time intervals for treatment or relapse monitoring. The unique potential of CTCs as a clinically useful biomarker in a liquid biopsy relies in the possibility to gain insight on the burden of disease via cell enumeration and on the overall molecular state and risk of progression or therapy failure by downstream analysis of phenotype, gene expression, mutational status of the detected cells (53). Cells that are isolated viable can even be further cultivated *in vitro* and subjected to drug sensitivity testing (54). Nevertheless, there is no applied standardized concept for therapy monitoring for cancer patients based on CTCs so far. The major challenge of CTC detection is posed by their rarity among the millions of surrounding WBCs and RBCs per mL blood but also their inter- and intra-patient heterogeneity on phenotypic and molecular level. The exact number in patient samples is not known and definition and therefore application of a positive control is difficult and represents an additional challenge during assay development. Numbers of 1-1000 CTCs per mL of blood are reported in the literature, a number which is strongly depended on the

applied method. Generally accepted controls are blood samples from healthy donors with no detectable CTCs as negative control and with high recovery of cell line cells spiked into healthy blood as positive control (55). To successfully investigate CTCs, they must be detected with high sensitivity, reproducibility and, depending on the desired analysis, with sufficient purity. Over the past years, several CTC isolation and detection methods have been investigated. These isolation methods (as schematically shown in Figure 7) are based on either biological or physical differences between CTCs and the healthy blood cells.

Biological methods encompass immunocapture and immunodetection techniques. Cells can be isolated by capturing on functionalized surfaces or using functionalized magnetic beads. Thereby, CTCs are either positively enriched by direct capture of the target cells or negatively enriched by capture of non-target cells for depletion. Physical isolation methods take advantage of the differences in size and mechanical compressibility of the CTCs and healthy blood cells. After capture, the enriched cells are usually analyzed by immunostaining of characteristic antigens which enables the distinction of CTCs from normal blood cells. However, there is no standardized and definite staining strategy that encompasses all subpopulations of CTCs.

As most cancers originate from epithelial tissues, epithelial CTCs express different adhesion and structure proteins, e.g., cytokeratins such as CK8, CK18 and CK19 that are intracellular structure proteins and the surface protein EpCAM (CD326). These tumor-associated antigens can be used for immunocapture and can be optically detected after labeling with specific conjugated antibodies. An accepted definition for CTCs is positive staining for EpCAM and/or cytokeratins 8, 18 and 19 as epithelial tumor antigens and DAPI or Hoechst33342 for nucleus detection. Some methods extended these criteria for negative CD45 staining to exclude leukocytes.

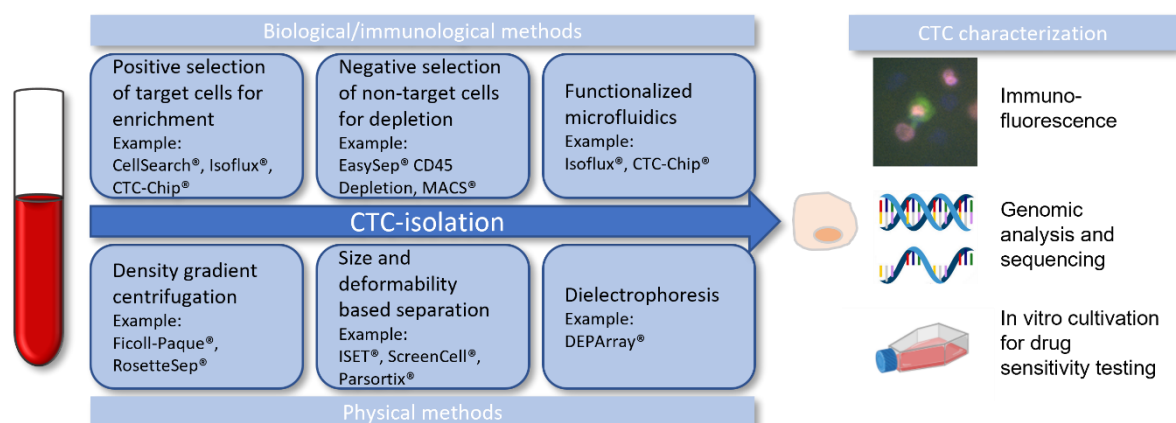


Figure 7: Overview of different CTC isolation and characterization methods.

Most methods for separation of CTCs from normal blood cells take advantages of differences between the cells in terms of biological or physical properties such as surface proteins, size, or electric charge.

For many years, the most widely used technology for prognostic purposes in clinical studies and the only FDA approved CTC enumeration method was the CellSearch[®] method (Menarini Silicon Biosystems, Florence, Italy). For this technique blood is collected in CellSave[®] tubes containing a fixation agent. Epithelial CTCs are isolated from the sample using magnetic beads functionalized with EpCAM specific antibodies. The leukocytes are depleted as they are not bound by magnetic beads. After immunomagnetic capture, the enriched cells are permeabilized and stained with a CK-8, 18, 19, CD-45-antibody cocktail and nuclear stain DAPI. Through simultaneous isolation with EpCAM and staining with CK antibodies, CTCs can be identified based on their expressed proteins and due to CD-45 staining discrimination of CTCs and leukocytes is ensured. Several studies using the CellSearch[®] have stated that the detection of more than 3 to 5 CTC present in the patients' blood sample correlated with decreased progression-free survival in case of metastatic breast, colorectal, or prostate cancer (56) (57). For instance, in the case of breast cancer one study showed that women with <5 CTC/7.5 mL of blood before therapy had a statistically significantly longer overall survival (OS) of 18 months and progression free survival (PFS) of 7 months compared to women with >5 CTC/7.5 mL of blood (OS of 10 months; PFS of 2.7 months) (58). However, the total number of CTCs detected by the CellSearch[®] method within 7.5 mL is very low regarding the high blood sample volume that is required. This leads to the assumption that EpCAM^{low} and EpCAM- CTCs might be lost during sample preparation, so their number is underestimated. Moreover, interpretation of therapy success from a cell count course described for the CellSearch[®] method might be difficult if for example 3 CTCs are found in the baseline sample before therapy, 4 CTCs in the following sample and 2 CTCs are found in the next samples after two cycles of therapy.

Besides the CellSearch[®] system, many other EpCAM-based methods have been developed for CTC enrichment, capture, and enumeration. The GILUPI CellCollector[®] is composed of a functionalized nanowire that is introduced into the vein for 30 minutes for in vivo capture of EpCAM⁺ CTCs (59). However, the isolation efficiency is rather low due to the high blood flow rate and comparable low surface of the wire compared to the vein diameter. Consequently, many CTCs can pass the wire without being captured. Moreover, optical detection and recovery of the cells from the wire can be difficult.

All enrichment methods based on immunoaffinity capture of EpCAM expressing CTCs have in common that they do not detect certain subpopulations. In the case of CTCs that underwent

EMT, the expression of the epithelial (surface) proteins is downregulated and therefore certain subpopulations of CTCs can be lost if positive selection is conducted based on EpCAM only. Selection based on biological characteristics ensures a high selectivity and specificity. Nonetheless, immuno-based isolation is prone to cell loss due to inhomogeneous antigen expression or insufficient access of the antibodies on the cell surface. The clustering of CTCs with other blood cells and components (as described in chapter 1.2.2) could influence the accessibility for EpCAM specific antibodies (60) (61) (62). Thus, some epitopes might be masked due to the clustering of CTCs with other blood cells. Additionally, surface proteins can be expressed only locally in form of ‘caps’ and cannot be recognized by the respective antibody (60).

To increase the sensitivity and detect EMT cells, different cancer-specific antigens (epithelial and mesenchymal) can be targeted along with the surface protein EpCAM. Immunodetection of cytokeratins as additional epithelial marker or vimentin as mesenchymal marker might increase the probability to detect a wider range of CTCs. However, this would require fixation and permeabilization of the cells as these are intracellular proteins leading to some critical disadvantages. Fixation causes cross-linking of the proteins, and this may alter the epitopes making it difficult for the antibody to recognize the antigen. Furthermore, fixation renders cells nonviable such that they are not usable for potential functional analyses such as cultivation.

An example for a method that forgoes enrichment and cell fixation prior to immunofluorescent staining is the maintrac[®] method (SIMFO, Bayreuth, Germany). In brief, this method starts with 1 mL blood that is processed 24-72 h after sample taking. It was reported that the storage of the blood samples for at least 24 h helps in demasking of EpCAM on the cell surface that is probably caused by clustering of CTCs with platelets or leukocytes (60) and the leukocytes and CTCs are selectively stained after selective lysis of the RBCs. The advantage of this method consists of the few sample processing steps and the omission of CTC enrichment (63). The leukocytes and CTCs are processed together in one suspension by staining with conjugated EpCAM-antibodies. This results in reduced cell loss and higher sensitivity (threshold 10 CTCs in 1 mL blood) regarding the detection of EpCAM positive cells. Moreover, the staining technique does not require cell fixation and thus also provides information on the viability of the cells identified as epithelial CTCs and the possibility to cultivate CTCs with stem-cell like properties (64). The main advantage of this method is the small blood sample volume required and the high CTC number reported despite limitation to EpCAM immunodetection. However, as all nucleated cells are transferred to a microtiter plate for immunofluorescence detection, the

staining strategy could probably be extended to further tumor specific markers to detect different CTC subpopulations.

To overcome the disadvantages of biological isolation methods, label-free and antigen independent approaches can be applied. These include methods that separate CTCs and other blood cells mainly based on their differences in size, stiffness, and increased nucleus to cytoplasm ratio (65). In particular, the physical methods stand out for the high throughput, but are less specific and do aim at high yield rather than high purity. The main reason for that is the overlap in characteristics of leukocytes and CTC leading to leukocytes being enriched or captured along with CTCs. Isolation of CTCs based on their antigen-independent, physical differences to leukocytes, has been applied by different filtration-based approaches. An example is the commercialized system called isolation by size of epithelial tumor cells (ISET®, Rarecells, Paris, France). It is an antibody-independent whole blood filtration approach for CTCs that captures CTCs from 10 mL (threshold 1 CTC in 10 mL blood) of whole blood based on their larger size. It enables quantification and immunomorphological and molecular characterization (66). Another example is ScreenCell® also enabling filtration-based isolation of either live or fixed cells by filtration of blood samples of 3 mL (67). The drawbacks of the filtration-based technologies are membrane clogging and decrease in purity due to co-capture of leukocytes in case of small pores or loss of small and deformable CTCs in case of too large pore sizes. To overcome clogging and pressure increase, the area of the filtration unit needs to be increased. This in turn makes optical detection of the whole area in real-time during the capture process challenging and strongly dependent on an optical system with large field of view, which in turn often possesses lower resolution. Therefore, staining, and optical detection are often carried out at the end of the capture process by optically scanning the surface in the respectable channels. This way, small or deformable cells that can pass the capture unit are not detected and the actual number of CTCs present might be underestimated. The clear benefits are ease of use, short processing times, high efficiency, fast detection, and label-independency. Thus, also cells that underwent EMT and cells with low or no EpCAM expression are captured. The biology of EpCAM and its role are not completely understood but different studies hypothesize that expression of this epithelial cell-surface protein is crucial for metastasis-competent CTCs. Therefore, it may not be lost completely during the epithelial-to-mesenchymal transition (29) (68). The development and validation of a method is often performed with model cell lines with known characteristics. For these model samples, EpCAM seems to be a suitable marker. However, to cover the complete heterogeneity of CTCs it would

be beneficial to develop an isolation method based on both biological and physical characteristics and combine the detection of different markers for higher efficiency and improved characterization. A method established with one or a few specific markers should be easily expandable to multi-marker detection without interfering with cell capture.

1.2.3. LoC systems for CTC analysis and integration of CTC analysis into Vivalytic

To increase reproducibility of sample preparation and enable CTC analysis at the point-of-care, several technologies have been established for automated or semi-automated CTC analysis in recent years (69) (70). They provide the possibility to unite biological and physical methods for CTC monitoring and thereby achieve a combination of isolation of (viable) CTCs and further morphological or molecular characterization of these cells of interest in one device. LoC systems enable microfluidic processing of samples for separation of different cell fractions and isolation of target cells from blood. These can be based on immunoaffinity (71), centrifugo-magnetophoretic (72) or dielectrophoretic methods (73), filtration (74) (75), or a combination thereof (76). The major challenge is the throughput and the optimization of the detection despite the limitation in applicable sample volumes in microfluidic systems.

The IsoFlux[®] system (Fluxion Biosciences Inc, Oakland, USA) combines capture of EpCAM-positive cells via antibody-coated magnetic beads with microfluidic processing (77). Another system described in the literature is a micro vortex-generating herringbone-chip that captures EpCAM-positive cells within a microfluidic device containing antibody-functionalized micro posts (78). A similar system is the CTC-chip[®] that is composed of a silicon chip in the size of a standard microscope slide containing an array with numerous micro posts with specific geometric pattern that are functionalized with antibodies to EpCAM. CTCs are captured directly onto the sides of the posts. The captured cells can then be confirmed as CTCs through staining which differentiates nonspecifically bound leukocytes from epithelial CTCs (52).

In May 2022, a second CTC analysis method, the Parsortix[®] system (Angle plc, UK) was authorized by the FDA for the capture and harvest of CTCs from metastatic breast cancer patient blood. The method enables isolation of CTCs for subsequent downstream analysis. In a microscopic slide format device, non-target cells from whole blood can pass a constricting stair-like structure and are depleted by the virtue of their differences in size and deformability whereas target cells are captured and can be released in reverse direction (79).

1.2.3.1. Requirements for integration of CTC analysis into the Vivalytic LoC system

Among the methods described in chapter 1.2.2.1, mechanical filtration has the benefit of being relatively robust to flow rate variations, making it a suitable method for integration into pneumatically driven, membrane-based LoCs like the Vivalytic system described in chapter 1.1.2. The Vivalytic system was developed and established for PCR-based molecular diagnostic assays. The microfluidic network was intended for the transport of liquid samples, for nucleic acid extraction and amplification. Cells and cellular material are so far only processed after cell lysis for RNA and DNA extraction. Therefore, the system was not validated for processing of cell suspensions in such way that cells remain intact and viable. An important aspect to be considered during microfluidic transport of cells is the fluid shear stress inside the channels and valves. Moreover, the influence of a pulsatile flow profile on cell capture needs to be evaluated and the flow path and profile should be optimized to minimize cell loss within the channels and during capture. In case of a filtration based-method, immunocytochemistry is essential for phenotypic characterization and discrimination of large blood cells like megakaryocytes, large monocytes, epithelial cells from the puncture site, and mesenchymal cells enriched in parallel. This requires an optical system capable of fluorescence imaging. The optical system of the Vivalytic analyzer was intended for detection of fluorescence increase in PCR chambers rather than detection of single fluorescent particles such as cells with sizes between 10 and 30 μm . The resolution therefore might be more challenging for measuring the fluorescent signal from an area like the PCR chamber or a microcavity. The major difference between the detection of fluorescence in a qPCR assay and the detection of immunofluorescent cells is the required magnification factor and optical resolution. Moreover, for the optical fluorescence detection of cells as comparable to a microscopic detection, the cells must be captured in one optical focus plane. This could be realized by capturing the cells on a microporous structure. Above all, the major challenge that is posed by the limited sample volume capacity of LoC systems is the scarcity of CTCs in blood and thus, the need for identification of a highly sensitive method with minimal cells loss.

1.3. Aim of the study

In the initial diagnosis, tumors might resemble one another. Characterization using imaging techniques and molecular proceedings reveal that tumors differ in their molecular composition. Therefore, next generation sequencing (NGS) of tumor material on DNA and RNA levels is becoming increasingly important as it can reveal genetic alterations within a tumor. In consequence, secreted proteins are analyzed for over- or underexpression. This might enable oncologic patients to receive targeted and personalized therapies according to the molecular profile of the tumor. Oncologists in turn are confronted with novel therapeutic substances and heterogeneous therapeutic strategies. One of the major challenges is assessing therapy responses and conventional radiologic imaging procedures. Therefore, approaches for a close and accurate monitoring of each patient are urgently needed. Besides the sole detection of CTCs in the peripheral blood as a prognostic marker, a reliable method for the isolation and further characterization of CTCs, e.g., by single cell sequencing could substantially improve therapy monitoring and reveal emerging therapy resistances.

Therefore, the **overall aim** of this dissertation was the evaluation of existing CTC analysis methods and the assessment of the feasibility of subsequent establishment of a LoC-compatible technique for the isolation, enumeration, and characterization of the detected CTCs. Besides quantification, the possibility to recover the captured cells or extract nucleic acids was assessed as starting point for expression analysis or preparation of nucleic acid samples for sequencing. The focus was set on the identification of a technique that can cope with boundary conditions given by the Vivalytic LoC system such as a pulsatile flow, limited sample input volume and fluorescence-based read-out.

As a **first step**, a method for CTC detection method that holds promise to minimize cell loss was reproduced and evaluated using samples of gastrointestinal tumor patients. Patient and model samples were analyzed in two laboratories using maintrac[®] as benchmark method and the results were retrospectively correlated to the clinical observations of the respective patients. Thereby, the overall aim was to assess and evaluate the feasibility of CTC isolation and detection for usage as tracking marker for cancer treatment monitoring and detection of therapy resistances.

In the **second step**, the method was adapted with the aim of automated processing by the Vivalytic LoC system. The integration was executed sequentially by breaking down the overall workflow into single unit operations that were adapted based on the specifications of the Vivalytic system. This included adaptations of the sample and reagent volumes, incubation

times, staining protocol, and read-out. As there are no established assays for the Vivalytic system processing viable cells so far, in the **third part** of the study unit operations that are required for transport of cell suspensions were evaluated. First experiments with cells in the microfluidic network of the cartridge were executed to determine the influence of microfluidic system parameters on cell capture, viability, and cell recovery.

Besides CTC isolation and enumeration, the **fourth part** of the dissertation included phenotypic and molecular characterization of the captured cells. Thereby, the extraction of nucleic acids from the captured cells was implemented. The extracted RNA was used for gene expression analysis on mesenchymal markers to evaluate both the possibility to detect viable epithelial cells and estimate the extent of EMT cells.

The LoC integrated workflow including whole blood processing, depletion of erythrocytes and partly leukocytes, the capture of CTCs and the expression analysis after nucleic acid extraction is schematically shown in Figure 8.

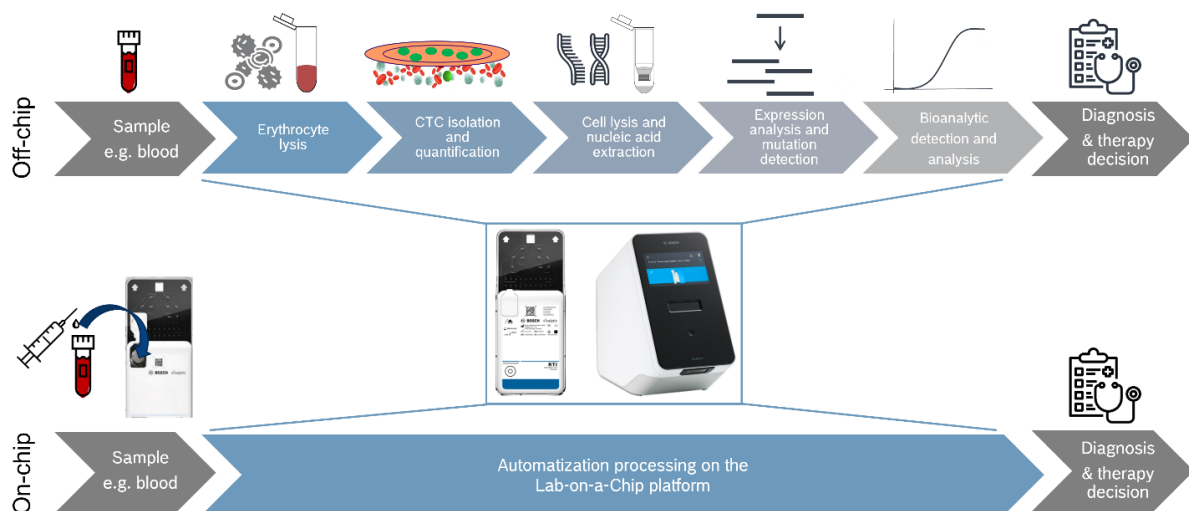


Figure 8: Possible LoC workflow for automation of CTC analysis. The overview on top shows the manual steps (off-chip) that are necessary steps for analysis of liquid biopsy. The Lab-on-Chip (on-chip) platform enables automatization of all the steps in between sample input and diagnosis and therapy decision.

2. Material and Methods

2.1. Material

2.1.1. Chemicals

Table 1: List of chemicals used and information on purity, concentration, and supplier.

Chemical	Purity and Concentrations	Manufacturer
Agarose standard		Carl Roth, Karlsruhe, Germany
Ammonium chloride	99.5 %	Carl Roth, Karlsruhe, Germany
Bacillol AF		Paul Hartmann, Heidenheim, Germany
Bovine serum albumin	> 96.0 %	Sigma Aldrich, Steinheim, Germany
DMSO	99.5 %	AppliChem GmbH, Darmstadt, Germany
DNA ExcitusPlus™		PanReac AppliChem, Darmstadt, Germany
Ethanol for mol. biology	> 99.8 %	Merck, Darmstadt, Germany
EDTA		VWR, USA
Formaldehyde	37.5 %	Sigma Aldrich, Steinheim, Germany
Potassium hydrogen carbonate	> 99.5 %	AppliChem GmbH, Darmstadt, Germany
Molecular grade water,	RNase, DNase, protease free	G-Biosciences, St. Louis, USA
Chemical	Purity and Concentrations	Manufacturer
Phosphate buffered saline		Gibco, Thermo Fisher Scientific, Waltham, USA
RNase Zap		Sigma Aldrich, Steinheim, Germany
β-Mercaptoethanol	> 99 %	Sigma Aldrich, Steinheim, Germany
Triton-X-100	10 % in H ₂ O	Sigma Aldrich, Steinheim, Germany
Tween®20	10 %	Sigma Aldrich, Steinheim, Germany
Tween®80	58 %	Sigma Aldrich, Steinheim, Germany

2.1.2. Solutions and Buffers

Table 2: List of buffers and their composition.

Buffer name	Function	Component	Concentration
Alkaline lysis buffer	Purification of filtration functional models	NaOH	200 mM
		SDS	2.5 % (w/v)
Erythrocyte lysis buffer	Selective lysis of red blood cells	NH ₄ CL	155 mM
		KHCO ₃	10 mM
		EDTA	1 mM
		pH 7.2	
Passivation buffer	Blocking of unspecific protein binding and adsorption	PBS	1 X
		BSA	1 % (w/v)
		EDTA	1 mM

Table 3: Cell lysis buffers for generation of cell lysates as templates for RT-qPCR.

Buffer name	Function	Component	Concentration
LB01	Nonionic detergent	Tween20	2 % (v/v)
		Chaotropic salt	Guanidinium chloride
LB02	Nonionic detergent	Tween80,	0.1 % (v/v)
		Buffer component	
LB03.1	Nonionic detergent	Preservative	1.0 % (v/v)
LB03.2	Nonionic detergent	Tween20	2.0 % (v/v)
LB03.3	Nonionic detergent	Tween20	2.0 % (v/v)
		Buffer-component	Tris-HCl
LB03.4	Nonionic detergent	Tween20	2 % (v/v)
		Protein	BSA
LB04	Nonionic surfactant	TritonX-100	0.25 % (v/v)
		Protein	BSA
LB05	Nonionic detergent	NP-40/Igepal360	0.3 % (v/v)
		Protein	BSA
LB06	Protein	BSA	1 % (w/v)
LB07	Protein denaturant	Guanidine thiocyanate	50 mM

2.1.3. Cell culture

Table 4: List of cell culture media and reagents.

Substance	Supplier
Heat Inactivated FBS, gibco®	Life Technologies; Thermo Fisher
DMEM; GlutaMAX, gibco®	Thermo Fisher
PBS, gibco®	Thermo Fisher
Trypan Blue Stain (0,4 %), gibco®	Life Technologies; Thermo Fisher
Trypsin-EDTA solution, 1X (0,25%/0,02%), in PBS	Biochrom Merck Milipore

2.1.4. Cell lines

Table 5: List of cell lines, their provider, and the applied media for cultivation.

Cell line	Provider	Cultivation medium
BT-474	German Cancer Research Center	DMEM 10 % (v/v) FBS 5 % (v/v) Penicillin/Streptomycin
BT-20	German Cancer Research Center	DMEM 10 % (v/v) FBS 5 % (v/v) Penicillin/Streptomycin
HCT116	German Collection of Microorganisms and Cell Cultures GmbH	DMEM 10 % (v/v) FBS 5 % (v/v) Penicillin/Streptomycin
K562	German Collection of Microorganisms and Cell Cultures GmbH	RPMI 10 % (v/v) FBS 5 % (v/v) Penicillin/Streptomycin
NCI-H1975	Cooperation partner	RPMI 10 % (v/v) FBS 5 % (v/v) Penicillin/Streptomycin

2.1.5. Kits

Table 6: List of commercially available kits for nucleic acid extraction and analysis methods.

Kits	Application	Manufacturer
CIRRUS™ Strips RNA	Lyophilized PCR master mix	Fluorogenics, Wiltshire, UK
QiAmp DNA Blood Midi Kit	DNA extraction from blood samples	Qiagen, Hilden, Germany
DNase	Digestion of gDNA during RNA extraction	Macherey Nagel,
KRAS, BRAF, PIK3CA Array	Mutation detection	Randox

Luna® Universal Probe One-Step RT-qPCR Kit	RT-qPCR	New England Biolabs,
Qiamp RNA Blood RNA 6000 Nano Kit	RNA extraction Determination of RNA purity and integrity	Qiagen, Hilden, Germany Agilent, Santa Clara, USA
Rneasy PureLink™ Quick Gel Extraction Kit	RNA extraction Extraction of DNA from bands in agarose gels	Qiagen, Hilden, Germany Thermo Fisher Scientific, Waltham, USA
SCRIPT RT-qPCR ProbesMaster Lyophilisate	Lyophilized PCR master mix	Jena Bioscience, Jena, Germany

2.1.6. Antibodies and cell staining solutions

Table 7: List of antibodies and staining reagents used for cell detection.

Substance	Isotype	Full name	Manufacturer
CD45 (PE)	Recombinant human IgG1	CD45, Clone: REA747, human	Miltenyi-Biotec, Bergisch Gladbach, Germany
Carboxyfluorescein succinimidyl ester (CFSE)	n.a.	CellTrace™ CFSE Cell Proliferation Kit	Thermo Fisher Scientific, Waltham, USA
CellTracker™ Deep Red (CTDR)	n.a.		Thermo Fisher Scientific, Waltham, USA
Cytokeratin (APC)	Recombinant human IgG1	Cytokeratin Antibody, anti-human, APC, REAfinity™	Miltenyi-Biotec, Bergisch Gladbach, Germany
EpCAM (Alexa Fluor 488)	Mouse / IgG2a, kappa	CD326 (EpCAM) Monoclonal Antibody (MH99), Alexa Fluor 488, eBioscience™	Thermo Fisher Scientific, Waltham, USA
EpCAM (APC)	Recombinant human IgG0	CD326 (EpCAM)-FITC, human	Miltenyi-Biotec, Bergisch Gladbach, Germany
EpCAM (FITC)	Recombinant human IgG0	CD326 (EpCAM)-FITC, human	Miltenyi-Biotec, Bergisch Gladbach, Germany
EpCAM (unlabeled)	Recombinant human IgG1		OriGene

Hoechst 33342	n.a.	n.a.	Thermo Fisher Scientific, Waltham, USA
Isotype control (FITC)	Recombinant mouse IgG1	n.a.	Miltenyi-Biotec, Bergisch Gladbach, Germany
Propidium iodide	n.a.	n.a.	Sigma Aldrich, St. Louis, USA
SYTO9	n.a.	n.a.	Thermo Fisher Scientific, Waltham, USA
Vimentin (APC)	Recombinant human IgG1		Miltenyi-Biotec, Bergisch Gladbach, Germany

2.1.7. Nucleic acids, Oligonucleotides

Table 8: List of oligonucleotides.

Name	Sequence 5' – 3'	Product size [bp]
EpCAM forward		163
EpCAM reverse	Proprietary primer sequence of 20-30 bases	
EpCAM probe (Cy3/BHQ-2 or FAM/BHQ-1)		
EpCAM standard forward	Proprietary primer sequence of 20-30 bases	851
EpCAM standard reverse		
GAPDH forward		
GAPDH reverse	Proprietary primer sequence of 20-30 bases	138
GAPDH probe (FAM/BHQ-1)		
Snail forward		
Snail reverse	Proprietary primer sequence of 20-30 bases	151
Snail probe (HEX/ or Cy3/BHQ-2)		
Snail standard forward	Proprietary primer sequence of 20-30 bases	661
Snail standard reverse		
Twist forward		
Twist reverse	Proprietary primer sequence of 20-30 bases	147
Twist probe (HEX/)		
Twist standard forward	Proprietary primer sequence of 20-30 bases	800
Twist standard reverse		

2.1.8. Standards

Table 9: List of commercially available standards applied for analysis methods.

Name	Application	Manufacturer
DNA ladder	Agarose gel electrophoresis	Lonza, Basel, Switzerland
Human blood, peripheral leukocytes total RNA	Background RNA for RT-qPCR with model samples	Takara Bio, Kusatsu, Japan
Human genomics DNA; human peripheral leukocytes total DNA	Background DNA for mutation detection with model samples	Roche, Basel, Switzerland

2.1.9. Data bases and software

Table 10: List of databases and analysis software.

Name	Resource
CellSens Dimension	Olympus, Shinjuku, Japan
Fluculator	Robert Bosch GmbH, Stuttgart, Germany
Fusion Solo X	Vilber Lourmat, Eberhardzell, Germany
ImageJ	National Institutes of Health (NIH), Bethesda, USA
MATLAB	MathWorks, Natick, USA
PrimerBLAST	National Center for Biotechnology Information (NCBI), Bethesda, USA
SPSS	IBM, Armonk, USA
UniProt	EMBL-EBI, SIB, PIR
VPhotoStar	Robert Bosch GmbH, Stuttgart, Germany

An image of the Fluculator user interface is shown in Figure 9.

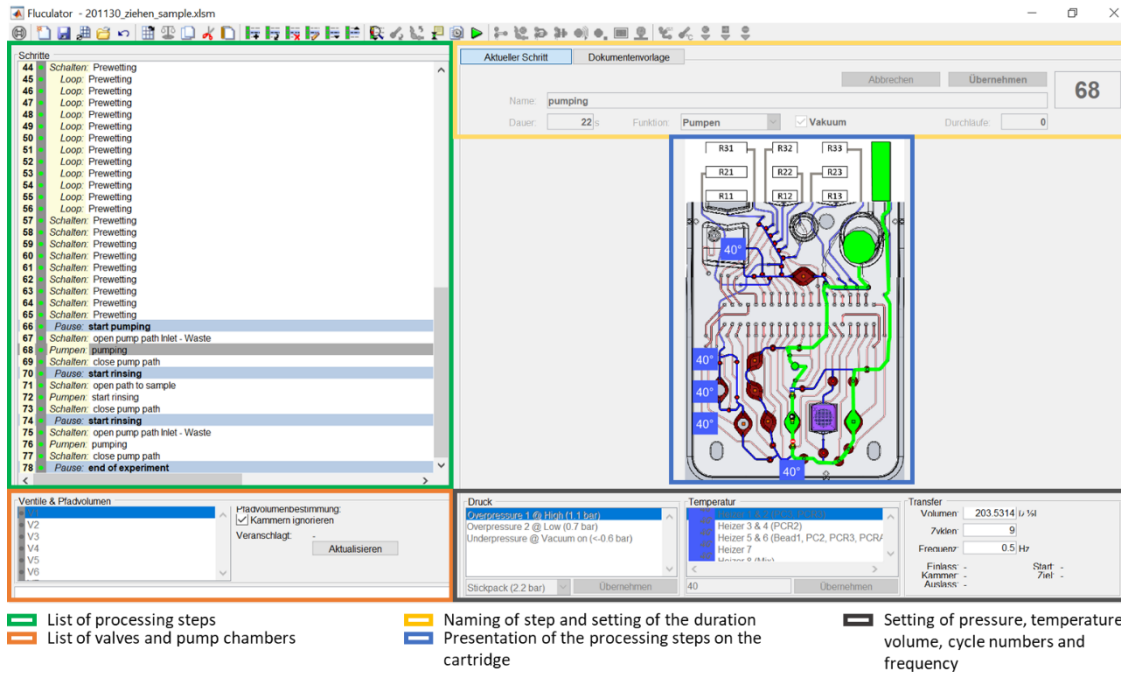
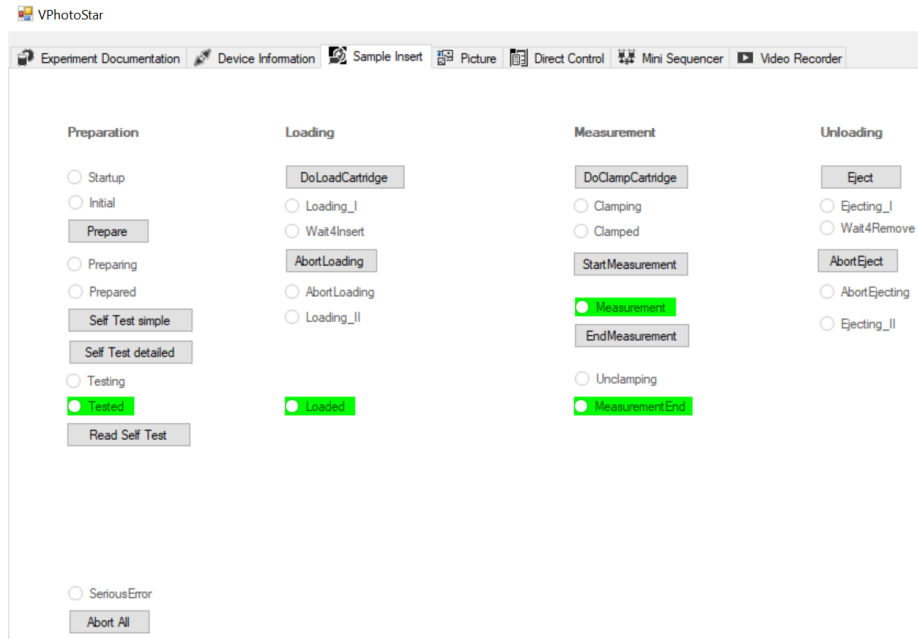


Figure 9: User interface of the Fluculator software.

The Fluculator software is used for programming and processing fluidic protocols on the Vivalytic cartridge. Shown in green is the list of processing steps of an exemplary protocol. By choosing a step in this list, the settings of the chambers and valves on the cartridge are marked in green (shown in the box marked in blue). Each step can be named, and the duration can be set in the area marked by the yellow box. In the area of the orange box, the valves and pump chambers are listed. In the grey box, the pressure, temperature, frequency, volumes, and cycles can be set.

A



B

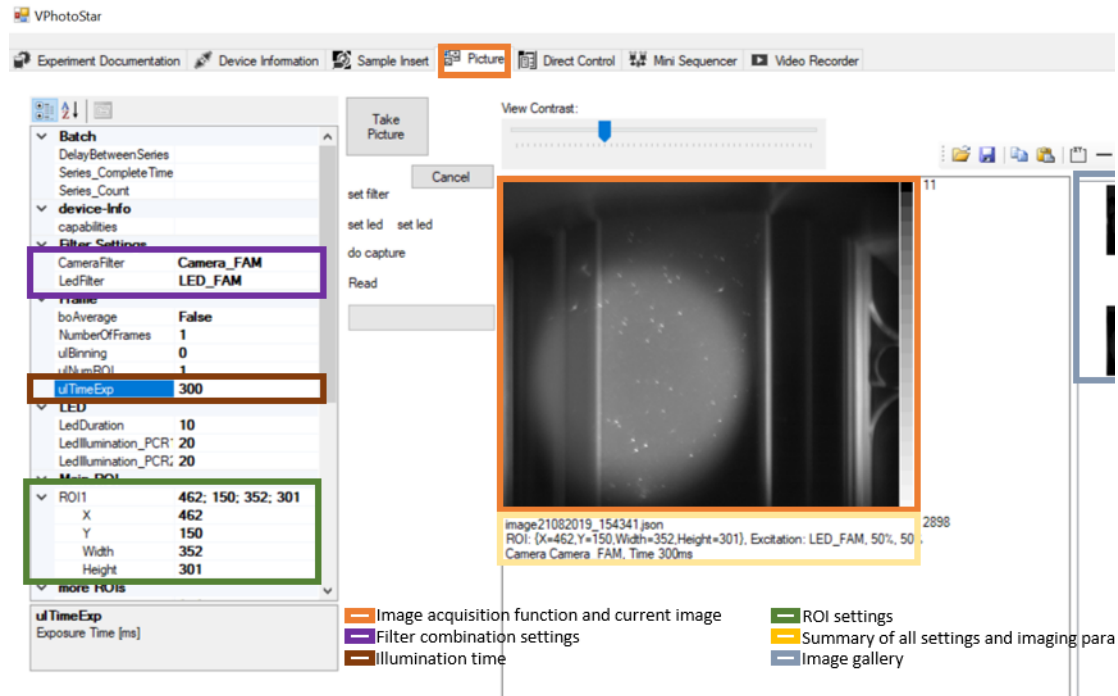


Figure 10: User interface of the VPhotoStar software for cartridge processing and imaging.

(A) Interface for device preparation and cartridge insertion. After the analyzer was prepared and a functionality test was performed, the sample could be loaded and clamped for the start of an experiment. (B) Interface for image acquisition. The respective filter sets were set, the illumination time adapted, and the ROI set for imaging of a desired region on the cartridge.

2.2. Cell biological methods

2.2.1. Blood samples

Blood samples were obtained from volunteers who have signed written informed consent. The blood samples were used to generate blood cell background for spike-in experiments. Thus, known markers from spiked cells were analyzed and no information on the health status of the donors was obtained from the experiments. Blood samples were collected into 3.4 mL or 7.5 mL EDTA tubes (Sarstedt, Nümbrecht, Germany) and stored for a maximum of 3 days at 4 °C or room temperature. Patient blood samples were obtained from patients suffering from gastrointestinal cancer who were treated at the university hospital Tübingen. The patients had signed written informed consent and the experiments were approved by the ethics committee of the university hospital under the ethics statement project number 480/2019BO2. Patient blood samples were

collected into 7.5 mL EDTA tubes, shipped to Bosch and SIMFO and stored in maintrac® boxes at room temperature for a maximum of 72 hours.

2.2.2. Cell culture

Different cell lines were used as model cells. Human breast cancer cell lines BT-474 and BT-20 were obtained from the DKFZ (Deutsches Krebsforschungszentrum), human colon cancer cell line HCT116 and hematopoietic cell line K-562 were obtained from the Leibniz Institute DSMZ and human lung cancer cell line NCI-H1974 was kindly provided by a cooperation partner. For long-term storage, cells were preserved in the liquid nitrogen vapor phase in a cryotank at -135 °C. For cultivation, cells were thawed quickly (< 1 min) at 37 °C in a water bath and transferred into a 15 mL tube containing 5 mL of the respective medium prewarmed to 37 °C. The cryo vial was rinsed with 4 mL of medium. The cell suspension was centrifuged at 150 x g for 3 min and the supernatant was discarded. The pellet was resuspended in 10 mL of prewarmed medium, and the complete cell suspension was transferred into a cell culture flask. The 15 mL tube was rinsed with an additional 5 mL of medium and transferred to the cell culture flask. Cell lines BT-474, BT-20 and HCT116 were routinely cultured in DMEM medium and cell lines K-562 and NCI-H1975 in RPMI medium supplemented with 10 % (w/v) fetal serum albumin and 1 % (v/v) Pen/Strep under standard conditions (37°C, 5 % CO₂, 100 % humidity). Cells were harvested by trypsinization with 0.25 % (w/v) trypsin and 0.02 % (w/v) EDTA in PBS for 3 min to 5 min at room temperature. Cell passages from 4 to 30 were used for experiments. For freezing, cells were harvested by trypsinization, washed with fresh medium, and counted using a hemocytometer or automated cell counter R1 (Olympus, Shinjuku, Japan). The cell number was adjusted to 1 x 10⁶ to 3 x 10⁶ cells per mL and 950 µL of the suspension were mixed with 50 µL DMSO. Before freezing, a sample for mycoplasma PCR (polymerase chain reaction) was taken. The cryo tubes were placed in a CoolCell® cell freezer in the -80 °C freezer. After 7 days the tubes were transferred into the liquid nitrogen tank.

2.2.2.1. Cell counting and viability determination by trypan blue exclusion

A cell suspension was mixed with the equal volume (1:1) of a 0.4 % (v/v) trypan blue solution. The stained cell suspension was transferred into a Neubauer counting chamber or an Olympus cell counting slide. Trypan blue can pass the membranes of dead cells, which resulted in a blue staining

of dead cells. Viable cells appeared white in transmitted light microscopy. The number of blue and white cells was determined and the cell number per mL of cell suspension was calculated by equation 1 for the Neubauer chamber or automatically by the Olympus cell counter. The cell counter determined the average cell diameter, additionally.

$$\text{Cells/mL} = \frac{\text{Number of cells counted}}{\text{Number of squares counted}} \times df \times 10^4 \quad \text{Equation 1}$$

2.2.2.2. Cell viability assay

Cell viability was either assessed by trypan blue exclusion assay as described in chapter 2.2.2.1 or by CellTiter-Glo® Luminescent Viability Assay (Promega G7570, Madison, USA). The latter is an assay for determination of the number of viable cells based on quantitation of the ATP present. The assay was performed as described in the manufacturer's technical bulletin (80). In short, 100 µL of the CTG reagent were added to 100 µL cell suspension and mixed on an orbital shaker for 2 min. The mix was incubated for 10 min at room temperature in the dark, followed by luminescence measurement using the SpectraMax M (Molecular Devices, San Jose, USA) and the preinstalled assay settings. In addition to the samples, blank wells were prepared for each assay with PBS or medium without cells, a cell dilution series, and an ATP dilution series. The relative luminescence units (RLU) were plotted against the cell number or ATP concentration for the generation of standard curves.

2.2.2.3. Immunocytochemistry with and without fixation

Cells were stained with 5 µM CellTrace™ CFSE or CellTracker™ Deep Red for viable cell detection, with 1 µM propidium iodide for dead cell detection and with 2 µM Hoechst33342 for nuclei staining. Cell-membrane bound EpCAM was stained with antibodies conjugated to either FITC (fluorescein isothiocyanate) or APC (allophycocyanin). Leukocytes were stained with antibodies against CD-45 conjugated to PE (phycoerythrin; all antibodies: Miltenyi Biotec, Bergisch Gladbach, Germany). Cell surface markers were stained without prior fixation. Therefore, a cell suspension of 100 µL to 200 µL was stained with 2 µL of the desired antibody with a concentration of 20 µg/mL and incubated for 20 min at 4 °C in the dark.

For staining of intracellular antigens like cytokeratin, cells were fixed prior to staining. For this purpose, the cell pellet was resuspended in 1 mL ethanol (C₂H₅OH) with 2 % (v/v) formaldehyde (CH₂O) and incubated for 10 min at room temperature (RT). After centrifugation at 150 x g for 3 min, the supernatant was discarded, and the cells were resuspended in 1 mL 0.25% (v/v) triton X-100. After 10 min, centrifugation was repeated, cells were resuspended in PBS and stained with anti-Cytokeratin-APC or anti-vimentin-APC (Miltenyi Biotec, Bergisch Gladbach, Germany) as described for the unfixed cells. The stained cells were observed by transmitted light and fluorescence microscopy in the respective channel and manually adjusted illumination time using the inverted microscope IX83 (Olympus, Shinjuku Japan).

2.2.3. CTC detection according to maintrac®

The maintrac® method developed by SIMFO (Bayreuth, Germany) was used for detection circulating epithelial tumor cells (CETCs) present in a blood sample based on the EpCAM-antigen. Briefly, 1 mL blood stored at RT for at least 24 h and 72 h at most was mixed with 14 mL of erythrocyte lysis buffer and incubated for 15 min. After centrifugation at 700 x g for 7 min, the supernatant was discarded, and the pellet was resuspended in 500 µL PBS + 1 % (w/v) BSA + 1 mM EDTA. Afterwards, 25 µL of the cell suspension were transferred into a sample tube and 4 µL of EpCAM-FITC antibody (Miltenyi Biotec, Bergisch Gladbach, Germany) were added and incubated for 20 min at 4 °C in the dark. Then, the suspension was filled up to 250 µL with PBS + 1 % (w/v) BSA + 1 mM EDTA and 100 µL thereof were transferred into a microtiter plate in duplicate. Added were 5 µL of propidium iodide (Thermo Fisher Scientific) to each well and the suspension was layered with 100 µL PBS + 1 % (w/v) BSA + 1 mM EDTA. After sedimentation of 1 h, the wells were analyzed by fluorescence microscopy using the inverted microscope IX83 (Olympus, Shinjuku Japan). EpCAM-positive and PI-negative cells with a visually intact nucleus, detected in transmitted light, were considered for CETC quantification.

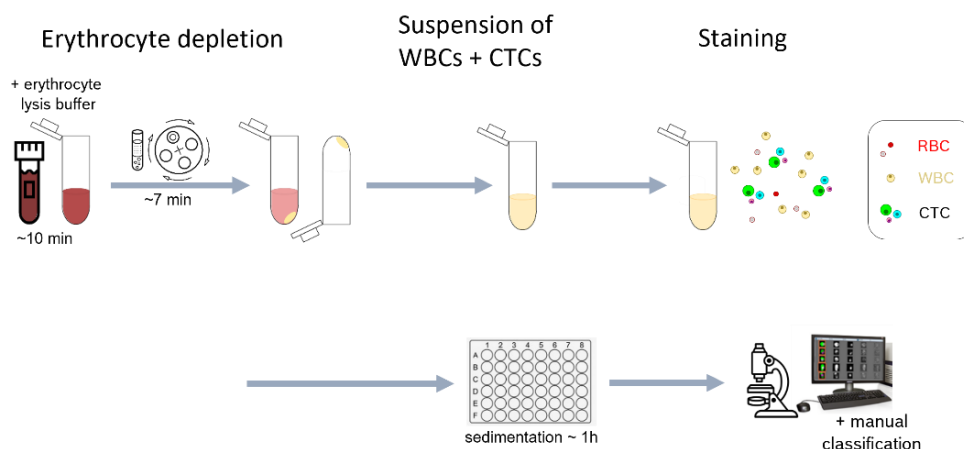


Figure 11: Schematic overview of the maintrac® method.

Starting with 1 mL blood that was prestored for 24 h at RT, the erythrocytes are selectively lysed and depleted by centrifugation. Afterwards, the pellet of WBC and CTCs are stained with conjugated EpCAM-antibodies and PI for detection and quantification of EpCAM-positive, viable and nucleus containing cells.

2.2.3.1. maintrac® trial with SIMFO and UKT – experimental set-up

For evaluation of the reproducibility and comparability of the maintrac® method, the possibility to adapt and integrate the method into a microfluidic sample preparation system and the correlation of the maintrac® results to the clinical observations, a methodological feasibility study was conducted together with SIMFO and the university clinic Tübingen (UKT). The Maintrac® method used in the study is protected by a patent held by Katharina Pachmann (81). The trial was conducted under the ethics statement project number 480/2019BO2 with the title ‘Therapy monitoring by circulating tumor cells (CTC) for patients with advanced gastrointestinal tumors (GI-CTC monitoring)’ as an observational, prospective, single center study including 30 patients with gastrointestinal tumors and treatment recommendation with molecular targeted agents. Therapy monitoring was performed using the maintrac® method and results were correlated with clinical, radiological and laboratory chemistry findings during therapy at the UKT.

Blood samples were collected prior to therapy (baseline) and at predefined points in time during the treatment period. The aim of the trial was to assess the main research questions: whether it is possible to detect CETCs by the maintrac® method in the patient cohort with advanced GI tumors, to isolate CETCs for further characterization (feasibility of isolation) and whether changes in the CETC counts correlate with disease response under the new targeted or immune therapeutic approach at any point in time.

Patients were separated into three groups:

- 1) Upper gastrointestinal tract (esophageal cancer and gastric adenocarcinoma)
- 2) Hepato-/pancreatobiliary type (HCC, CCA and pancreatic adenocarcinoma)
- 3) Colorectal cancer

Table 11: List of patient pseudonyms and sample time points. The last sample obtained is marked, bold and highlighted in grey. Sampling ended in case of death or because therapy ended.

Pseudonym	BO-749	BO-184	BO-572	BO-408	BO-645	BO-720
Sample 1	19.05.20*	02.07.20	09.07.20	21.08.20	10.02.21	17.03.21
Sample 2	09.06.20		06.08.20	18.09.20	10.03.21	
Sample 3	08.07.20		10.09.20	16.10.20	31.03.21	
Sample 4	23.07.20		08.10.20	31.10.20	21.04.21	
Sample 5	05.08.20		19.11.20		04.06.21	
Sample 6			17.12.20			
Sample 7			** (n.a.)			
Sample 8			21.01.21			
Sample 9			04.03.21			
Sample 10			15.04.21			
Sample 11			02.07.21			
Sample 12			30.07.21			
Sample 13			27.08.21			
			05.11.21			

*Analysis after 8 days due to problems during delivery; **Blood was coagulated at arrival; n.a.: not analyzed

2.2.4. Decision matrix for CTC isolation evaluated regarding LoC integrability

To determine a CTC isolation method that is suitable for integration into the Vivalytic LoC system, a decision matrix according to Pugh (82) was created including all important criteria for efficient isolation and considering the boundary conditions given by the current Vivalytic system. Several different CTC isolation techniques described in literature were ranked. The concept selection was shown as a chart including criteria after which it should be chosen, weighting of the criteria, and different benchmark concepts.

The following steps were conducted:

- 1) Collection of evaluation criteria
- 2) Weighting according to importance of the solution
- 3) Decision on a benchmark method
- 4) Set-up of alternative concepts
- 5) Rating of the alternatives in comparison to the benchmark
- 6) Analysis of the rating and elaboration of a hydride concept from the best concepts

2.2.5. Blood sample pre-processing

One major challenge in either method used for isolation of CTCs from blood is the large number of erythrocytes accounting for the viscosity and optical properties due to the hemoglobin present. Thus, one crucial step in blood sample pre-processing was the depletion of erythrocytes.

2.2.5.1. Density gradient centrifugation

The blood sample was mixed 1:1 with PBS and overlaid on the Histopaque® in a conical centrifugation tube. The tube was centrifuged at 400 x g for 30-40 min at RT with brakes off. Using a sterile Pasteur pipette, the upper two thirds of the supernatant were removed. The buffy coat (containing the mononuclear cells and the CTCs) was carefully aspirated and transferred into another conical tube. For subsequent washing of the isolated cells, 10 mL of PBS were added, and the tube was again centrifuged at 400 x g for 10 min. The washing step was performed twice.

2.2.5.2. Erythrocyte aggregation

Erythrocyte depletion by aggregation was achieved with the commercially available HetaSep™ (Stemcell Technologies Inc., Vancouver, Canada) and either by centrifugation or sedimentation. Therefore, five parts of blood were mixed well with one part of the HetaSep™ solution and incubated at 37 °C for 30 min. This step could have been shortened by centrifugation at 90 x g. However, as centrifugation was not possible on the Vivalytic LoC system, the sedimentation-based method was evaluated only.

2.2.5.3. Selective erythrocyte lysis

One volume of whole blood was mixed with 10 to 15 volumes of erythrocyte lysis buffer. After 10 min of incubation, the suspension was centrifuged at 400 x g to 700 x g for 7 min to 10 min. Afterwards, the supernatant was discarded, and the leukocyte (and CTC) pellet was used for experiments or washed two times with ELB and once with PBS for RNA or DNA extraction.

2.2.5.4. SEM-analysis of blood cells and ESEM analysis of cancer cells

Scanning electron microscopy (SEM) analysis was planned and performed in cooperation with Samir Kadic (PhD in CR/ATM3, Robert Bosch GmbH) as preliminary research for both dissertations.

For SEM-sample preparation, either 100 μ L of whole blood or blood containing lysed erythrocytes were spiked with tumor cells and mixed with 1 mL of a 2.5 % (v/v) glutaraldehyde solution and incubated for 1 h. Afterwards, the suspension was centrifuged at 200 x g for 2 min, the supernatant was removed, and the fixed cells were washed with 1 mL ddH₂O. For dehydration of the sample, an ethanol series followed by addition of 30 %, 50 %, 70 %, 80 %, 90 %, 100 % (v/v) ethanol with 10 min incubation and centrifugation between each step. The fixed and dehydrated sample was transferred onto a cellulose acetate filter and air dried before sputtering and analysis.

As an additional possibility, cells were analyzed without fixation and dehydration using an environmental scanning electron microscope (ESEM) to analyze native, humid cells. Analyses were performed in the chemical analytics department CR/ANA1 or CR/ANA2 of Bosch corporate research.

2.2.5.5. Determination of the erythrocyte lysis buffer efficiency

Different blood to RBC lysis buffer ratios were analyzed as shown in Table 12. The lysis efficiency was assessed by optical evaluation of the transparency of the suspension and the color/purity of the leukocyte pellet.

Table 12: Different lysis buffer volumes evaluated to determine the minimal volume required for efficient erythrocyte lysis.

Blood volume [μL]	RBC lysis buffer volume [μL]	Dilution
100	1400	1:15
100	900	1:10
200	800	1:5
200	600	1:4
200	400	1:3

2.2.6. Generation and evaluation of model samples for target cell isolation

To evaluate and validate CTC isolation and detection methods, model samples were generated by using defined cell line samples or spiking whole blood samples with cell lines. Three cell lines, NCI-H975, BT-474 and HCT-116 cells, were stained with 0.02 μg of anti-EpCAM-FITC (stock concentration 20 $\mu\text{g}/\text{mL}$) or with 5 μM carboxyfluorescein succinimidyl ester (CFSE) and analyzed by fluorescence microscopy as described in section 2.2.2.3.

Cells were diluted to the desired cell concentration, and the required number of aliquots were transferred into sample tubes and a 96-well microtiter plate in triplicates for counting. After sedimentation of the cells, the wells were scanned by the fluorescence microscope (Olympus, Shinjuku, Japan) in the “Instant Multiple Image Alignment” mode at 40-fold magnification. The stitched image was automatically assembled by the software and the cell number was determined using the ‘count and measure tool’ of the cellSens Dimension software of the microscope. Therefore, background subtraction was applied, and threshold object detection was set to a minimum intensity of 300 before segmentation. The object filter was set at a diameter of 5 to 35 μm , at a shape factor higher than 0.3 and a roundness of at least 0.2. Manual corrections were made when cell clusters were recognized. The determined number of cells was then either used for experiments with cell lines only or spiked into a blood sample for generation of a model liquid biopsy sample.

2.3. Microfluidic methods for LoC integration of CTC detection

2.3.1. Cell isolation by filtration – off-chip methods

For integration of cell isolation and detection into a microfluidic system, a filtration-based method was chosen. To evaluate the efficiency of the filtration method and characterize and verify the chosen assay, a single unit operation model was produced to simplify the implementation of the experiments. Afterwards, the functional structures and parameters were transferred to the existing Vivalytic LoC platform using adapted cartridges with specific modifications.

2.3.1.1. Rapid prototyping of a filtration functional model

Microfluidic structures were designed using computer aided design (CAD) by Hannah Bott (CR/ATM3, Robert Bosch GmbH). They were micromachined into injection-molded polycarbonate (PC) slides with the dimensions 75.5 mm x 25.5 mm x 3 mm by ultrashort pulse laser ablation (Nd:YAG USP-UV-laser, GL.compact, GFH GmbH, Germany). For the microfluidic unit operation model for cell capture, a cavity for integration of a filtration component was incorporated into the microfluidic structure. After laser micromachining, the polymer parts were smoothed by vapor-chemical treatment (as described in (83)). Thereby, optical transparency of the channels was achieved. As porous structure for cell filtration, a transmission electron microscopy (TEM) grid (G2799C, Plano GmbH) was used. It was mounted manually with adhesive bonding (2-component epoxide glue Plus *endfest* 300, UHU GmbH) applied using a microdispenser (Microdispenser Ultimus 1, Nordson Deutschland GmbH). After a curing time of 24 h the channels were sealed with adhesive film (MicroAmp™ Optical Adhesive Film, Thermo Fisher) and tubing adapters were mounted at the inlet and outlet of the channels via adhesive bonding (2-component epoxide glue Plus *schnellfest*, UHU GmbH) and cured for 12 h. For operation, the filtration functional model was connected to a syringe pump (Low Pressure Syringe Pump neMESYS, Cetoni GmbH) using silicone tubes. The fabrication workflow is shown schematically in Figure 12.

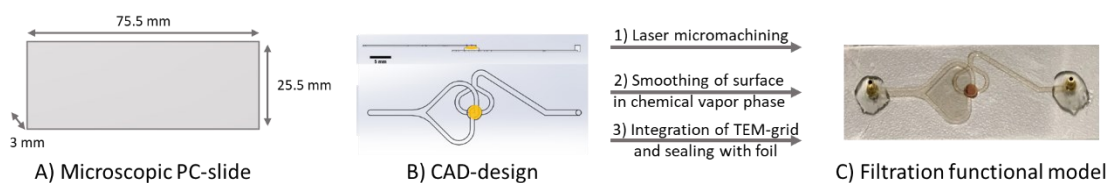


Figure 12: Design and fabrication steps of the cell capture device.

(A) Dimensions of a microscopic PC-slide. (B) CAD design of a microscopic PC slide and fabrication steps for PC slide to obtain cell capture device. The CAD design was 1) micromachined into a PC slide through laser ablation. After 2) vapor-chemical surface polishing and smoothing, 3) the filtration component was integrated using an adhesive. After sealing of the microfluidic structures through sealing foil and adaptation of tube adapters, the slide was ready to use. (C) Fabricated PC slide as filtration functional model with integrated TEM-grid as filtration component.

2.3.1.2. Verification of the TEM-grid properties

According to the manufacturer, the TEM-grids (Plano GmbH, Wetzlar, Germany) with 2000 mesh had a pore size of 6.5 μm . For verification, the TEM-grid was analyzed by scanning electron microscopy (TM300 Tabletop Microscope, HITACHI, Japan). Images were taken at two different positions and 5 pores and pore-to-pore distances were measured in each image using ImageJ (National Institutes of Health, Bethesda, Maryland, USA).

2.3.1.3. TEM-grid cell filtration procedure off-chip

For evaluation of the cell isolation efficiency of the filtration functional model and determination of the ideal parameters, a model sample composed of cell lines spiked into a blood sample as described in chapter 2.2.6 was drawn over the filter with the help of a syringe pump. Different parameters were varied and optimized as shown in Table 13. Before filtration, the set-up was passivated by rinsing with PBS + BSA (1 % w/v) and incubation for at least 30 min and images of the filter in the required fluorescent channels (EGFP, DAPI, DsRED) were acquired to subtract this background after filtration. The sample was transferred into a pipet tip that served as funnel and was connected to the filtration model by silicon tubes. The sample was drawn over the filter, followed by a washing step with one volume of 1 \times PBS. Cell capture was observed by fluorescence microscopy either in real-time, video recording, serial imaging or end-point imaging after the filtration process as described in chapter 2.3.1.3. In addition to determination of the cell capture on the filter, cell recovery with and without passivation of the system was analyzed to determine the system-related cell loss in experiments without integrated TEM-grid filter.

One-armed structure vs. two-armed filtration functional model

Two different designs of the filtration functional model were investigated regarding an even perfusion of the filter and the capture rate. The first design had one inlet channel and one outlet channel, the second design had two inlet channels and two outlet channels. The samples were drawn over the filter at a flow rate of $2 \mu\text{L/s}$ and the cell capture rate was determined by fluorescence microscopy at the end of the filtration process.

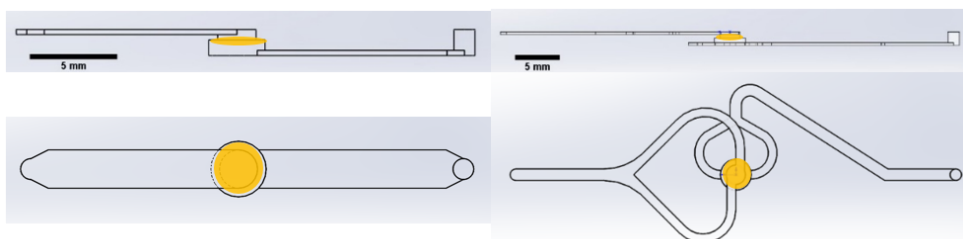


Figure 13: Filtration functional model for cell capture. One-armed and two-armed design of the filtration functional model for integration of a TEM-grid into a microfluidic network.

Cell types

Three different cell lines were evaluated regarding their capture rate on the TEM-grid filter. BT-474 cells were used for the evaluation of the two filtration functional models. Afterwards, BT-474, HCT116 and K562 capture was analyzed using the two-armed structure. Pre-determined (see chapter 2.2.6) numbers (approx. 300 cells) of cells were filtered separately at a flow rate of $2 \mu\text{L/s}$, the capture rate was determined and compared by fluorescence microscopy (chapter 2.3.1.3).

Blood sample volumes

The effect of the leukocytes and lysed erythrocytes on the retention of tumor cells was evaluated by using different blood sample volumes. $40 \mu\text{L}$, $100 \mu\text{L}$, $200 \mu\text{L}$ and $1000 \mu\text{L}$ of blood were spiked with a pre-determined (see chapter 2.2.6) amounts of stained cell line cells. The blood sample was mixed at a ratio of 1:5 with erythrocyte lysis buffer before filtration at $2 \mu\text{L/s}$. The capture rate of the spiked and stained cells was determined by fluorescence microscopy as described in chapter 2.3.1 after filtration of the different volumes.

Spike cell numbers

Cell suspensions with different pre-determined cell numbers (10 cells, 50 cells, 100 cells, 300 cells, 600 cells, 1000 cells, 5000 cells) were prepared according to the method described in chapter 2.2.6 for filtration to investigate the limit of the cells that can be effectively captured from a blood sample and detected by fluorescence microscopy.

Flow rates and flow profiles

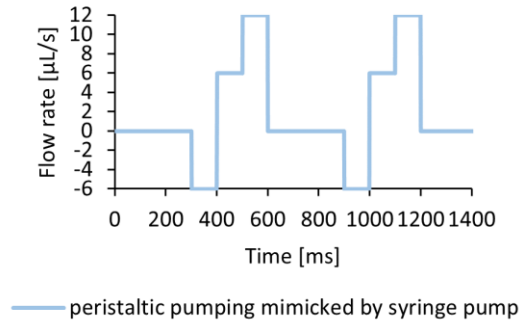
The syringe pump was programmed to generate flow rates of 1 $\mu\text{L/s}$, 2 $\mu\text{L/s}$, 5 $\mu\text{L/s}$ and 100 $\mu\text{L/s}$ either with a continuous, laminar or a pulsatile flow profile. The pulsatile profile was chosen to mimic the flow in the pressure-driven LoC system. The mimicked actuation mechanisms include pumping via a pump chamber with a volume of 25 μL and peristaltic pumping via the pressure-driven valves of the LoC system with a volume of 1 μL . The exact parameters set for the syringe pump and the flow profiles are shown in Table 13.

Table 13: Syringe pump settings for the off-chip filtration experiments.

Flow profile	Syringe pump flow rate settings	Syringe pump time settings	Resulting flow profile
Laminar	– 2 $\mu\text{L/s}$	Continuous	
	– 5 $\mu\text{L/s}$	Continuous	
	– 100 $\mu\text{L/s}$	Continuous	
Pulsatile pumping	– 100 $\mu\text{L/s}$	300 ms	
	0 $\mu\text{L/s}$	1700 ms	

— Pump chamber mimicked by syringe pump

Peristaltic pumping	0 $\mu\text{L/s}$	300 ms
	6 $\mu\text{L/s}$	100 ms
	- 6 $\mu\text{L/s}$	100 ms
	- 12 $\mu\text{L/s}$	100 ms



2.3.1.4. Methods for determination of the cell capture rate

The cell retention rate was determined by fluorescence microscopy after spiking the sample with a pre-determined number of stained cells and counting of the number of cells captured on the filter after the filtration process and the number of cells in the waste fraction, additionally. Afterwards, the number of captured cells was divided by the number of spiked cells and multiplied by 100 to obtain the capture rate in percentage.

$$Capture\ rate\ [\%] = \frac{number\ of\ captured\ cells}{number\ of\ spiked\ cells} \times 100 \quad \text{Equation 2}$$

Two evaluation methods were compared: the captured rate was either determined based on an endpoint image, or in real-time based on a video or image series. Endpoint counting of the cells was either performed using the cellSens Dimension Count and Measure Solution as described in chapter 2.2.6, or manually using ImageJ. For real-time counting, a MATLAB based, and a Python based method were developed. All evaluation methods were compared using the same images and videos.

2.3.2. Integration of CTC-detection into the LoC system

For the experiments described in this thesis, the analyzer prototypes (referred to as processing station on the following for differentiation from the Vivalytic analyzer) were used to process cartridges. For evaluation of the optical detection system, the Vivalytic analyzers were used. Fluidic protocols were established using the MATLAB based software ‘Fluculator’ (Robert Bosch GmbH).

2.3.2.1. Integration of TEM-grid cell filter into the LoC cartridge

The filter chamber of the Vivalytic cartridges for silica filters have a diameter of 3.2 mm. The TEM-grid with a diameter of 3 mm was fitted into this filter chamber. To introduce the TEM-grid into the cartridge, a modification of the TPU membrane was necessary at the filter position. By CO₂ laser cutting, the TPU membrane was enlarged to the appropriate diameter at the filter's position. Before complete assembly of the cartridge, the TEM-grid was mounted between the layers manually using adhesive bonding. However, the microfluidic channel geometry was not changed and thus differed from the off-chip functional model used for assay characterization. Nevertheless, the selected cartridge position provided no access for optical evaluation of the filtration process of whole cells. Thus, direct optical detection of the filter is not possible for which reason the cartridge was withdrawn from the processing station and observed under the conventional microscope. As a result, the on-chip experiments were performed as a proof-of-principle for the current Vivalytic cartridge with modifications regarding the filtration unit and only end-point determination of the cell capture rate was possible.

2.3.2.2. Microfluidic cell processing on-chip – influence on the cells

The viability of cells was assessed using two different assays: trypan blue exclusion and CellTiter-Glo® viability assay as described in chapter 2.2.2.2.

Influence of the temperature on cell viability

The Vivalytic system operates at a minimum temperature of 40 °C. The maximum time range cells survive at this elevated temperature was assessed using HCT116 cell suspension and a leukocyte suspension. The cells were transferred into sample tubes and incubated for 15 min, 30 min, and 45 min at 40 °C and viability was determined for each time point in comparison to a control incubated at room temperature.

Influence of the microfluidic transport on cell viability and cell capture rate

Different microfluidic programs were evaluated to determine the influence on the cell viability and the capture rates achieved.

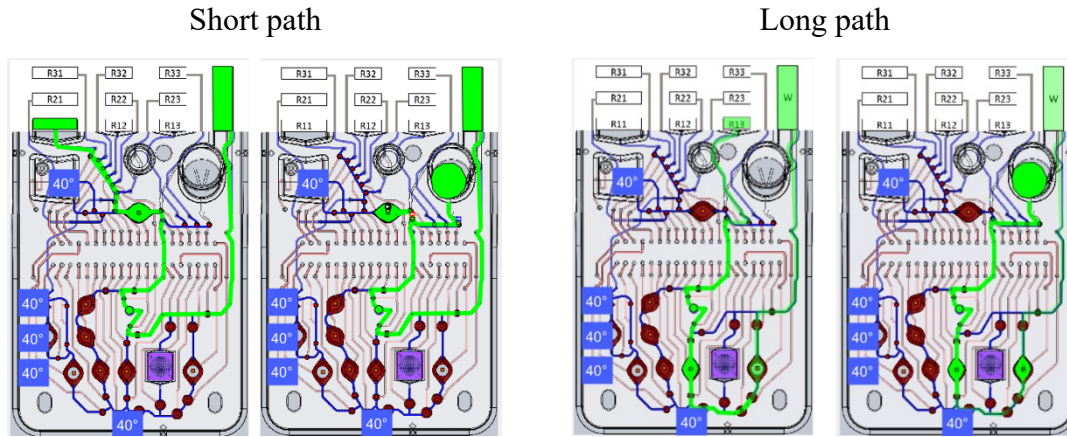


Figure 14: Microfluidic paths visualized using the Fluculator software.

- 1) Short path using pump chambers
- 2) Long path using pump chamber
- 3) Long path using peristaltic pumping using valves only
- 4) Long path using suction pumping with the pump chamber beneath the filter

The same microfluidic programs were used to determine the cell capture rate on the TEM-grid integrated into the Vivalytic cartridge. Cell suspensions were transferred into the sample chamber or a reagent chamber by pipetting and the cartridge was inserted into the processing station. After cells were transported over the filter using the different microfluidic programs, the cartridge was retrieved from the processing station and the stained cells were analyzed by fluorescence microscopy. Furthermore, the remaining cells in the channels before and after the filter were counted to determine the number of cells that have passed the filter and the number of cells that did not reach the filter.

2.3.2.3. Optical cell detection in the LoC system

A 3D-printed sample holder in the shape of a Vivalytic cartridge (shown in Figure 15) was used for simple optical cell detection in the Vivalytic analyzer. Model cells were stained with CFSE, PI, SYTO9, CellTracker™ Deep Red (CTDR), anti-EpCAM-FITC, anti-EPCAM-AlexaFluor488 and anti-EpCAM-APC according to chapter 2.2.2.3. Stained cells were transferred to a cell counting slide (shown in Figure 15A) or a TEM-grid mounted on a microscope slide (shown in Figure 15) and imaged with the Vivalytic analyzer and the software VPhotoStar with varying illumination

duration. For comparison, the cells were additionally analyzed by fluorescence microscopy, so that the limit of resolution of the Vivalytic system could be determined.

All fluorescent dyes required for efficient CTC detection and several fluorescent dye combinations were evaluated and are listed in Table 14.

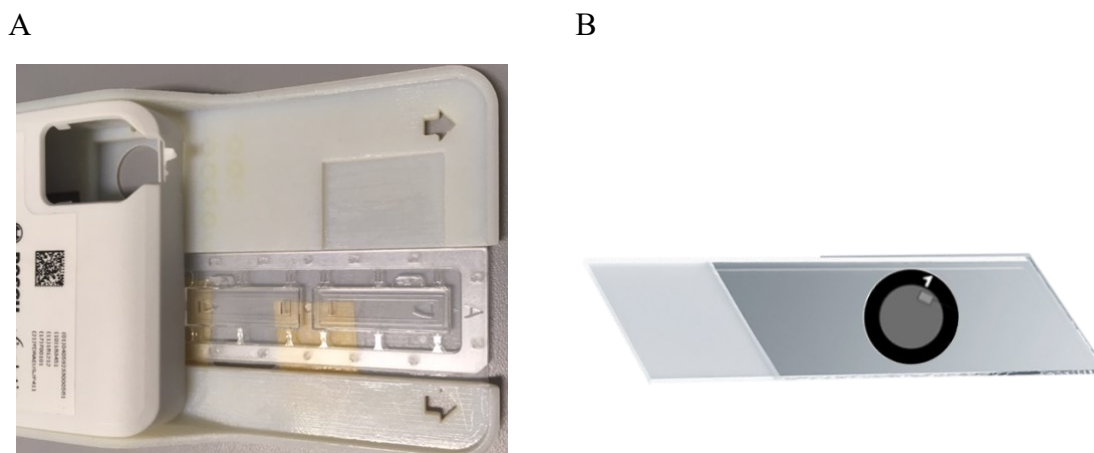


Figure 15: Optical cell detection using the Vivalytic analyzer.

A: cell counting slide mounted on a 3D printed sample holder with the shape of a Vivalytic cartridge. It was used for simple optical analyses in the Vivalytic analyzer. B: Scheme of microscopic slide with mounted TEM-grid for evaluation of stained cells on the grid.

Table 14: Fluorescent dyes used for CTC detection by fluorescence microscopy and with the Vivalytic system, the respective excitation and emission wavelength and detection channels.

Fluorescent dye or conjugate	Excitation/Emission [nm]	Filter channel microscope	Filter channel Vivalytic analyser
Hoechst33342	361/497	DAPI	N.a.
CFSE	494/521	EGFP	FAM
FITC	490/525	EGFP	FAM
PI	535/617	DsRed/Cy3	CalFluorOrange/ CalFluorRed
APC	594/633	Cy5	CalFluorOrange/ CalFluorRed

N.a. = not applicable

2.4. Molecular biological methods

The determination of the CTC count in a blood sample can give information of the therapy success (84). To further increase the information obtained from one liquid biopsy, molecular biological methods were used to characterize the isolated CTCs.

2.4.1. Nucleic acid extraction

For molecular analysis, RNA and DNA were extracted from either model samples or patient samples. Model samples were either cell lines only, or cell lines spiked into blood. The patient samples were obtained pseudonymized from the UKT.

2.4.1.1. RNA extraction

RNA from blood and cancer cell lines was extracted using the QIAamp Blood Mini Kit (Qiagen, Hilden, Germany) according to the manufacturer's protocol. For RNA extraction from blood, 1 mL whole blood was mixed with 5 mL buffer ELB and incubated on ice for 15 min. After centrifugation at 400 x g for 10 min, the supernatant was discarded and the remaining leukocyte pellet was washed two times with 2 mL buffer ELB, repeating the centrifugation step. The washed leukocyte pellet, or alternatively a pellet of cell line cells, was mixed with 600 μ L buffer RLT. The suspension was mixed by pipetting and transferred into a QIAshredder column and centrifuged at 8000 x g for 30 s at RT. The flowthrough was mixed with 600 μ L 70 % (v/v) ethanol and transferred to a QIASpin-column in two aliquots of 600 μ L followed by centrifugation at 8000 x g for 30 s after each aliquot. The spin column was washed with 350 μ L buffer RW1 and centrifuged at 8000 x g for 30 s. 75 μ L of rDNase (Macherey Nagel, Düren, Germany) were added and incubated for 15 min at RT. After that, 300 μ L of buffer RW1 were added followed by centrifugation at 8000 x g for 30 s. A volume of 500 μ L buffer RPE was added and centrifuged at 8000 x g for 30 s and the step was repeated with centrifugation at 8000 x g for 3 min. Afterwards the spin column was centrifuged on an empty collection tube at 20,000 x g for 1 min. For elution, the spin column was placed on a PCR-clean sample tube and 30-50 μ L nuclease free H₂O were added and the spin column was centrifuged at 8000 x g for 30 s. The extracted RNA was stored at -80 °C.

2.4.1.2. Quantification nucleic acids and quality control

RNA and DNA concentration as well as purity were assessed using the NanoDrop2000 (Thermo Fisher Scientific, Waltham, USA). The NanoDrop2000 device was blanked using H₂O before measurement of the samples. 1 μ L of each sample was pipetted onto the measurement pedestal, the sampling arm was lowered, and the spectral measurement was initiated. The concentration in ng/ μ L, the absorbance at 230 nm, 260 nm, and 280 nm, as well as the 260/230 and the 260/280 ratio were determined (LOD = 2 ng/ μ L).

Additionally, the RNA quality was evaluated using the Agilent 2100 Bioanalyzer by determination of the RNA integrity number (RIN). Therefore, an RNA 6000 Nano Kit (Agilent, Santa Clara, Germany) was used and performed according to the manufacturer's protocol. A RIN above 5 was regarded as sufficient.

DNA fragments and PCR products were analyzed by agarose gel electrophoresis for analysis of their purity. Therefore, 1-2 % agarose gels were prepared by solving agarose in 1 \times TAE buffer by heating. The melted agarose was poured into a gel casting tray and a 10 well comb was inserted. After approximately 30 min, the comb was removed, the agarose gel was overlaid with 1 \times TAE buffer and samples were loaded after mixing with 6 \times loading dye (Lonza, Basel, Switzerland) in a ratio of 1:6. Besides the samples, a DNA ladder (Thermo Fisher Scientific, Waltham, USA) was loaded onto the gel for comparison of the DNA fragment sizes. The gel was run at 110 V for 1 h and analyzed using UV-light.

2.4.2. Primer and probe design

Primers were designed using Primer BLAST (NCBI) in such way that all primers consisted of 18-29 nucleotides, a GC-content of approximately 40-60 % and the melting temperatures were between 50 $^{\circ}$ C and 60 $^{\circ}$ C. Furthermore, whenever possible, primers were designed to bind at exon-exon-boundaries to prevent binding to genomic DNA.

2.4.3. Expression analysis

If not otherwise stated, expression analysis was performed by RT-qPCR using the Luna[®] Universal Probe One-Step RT-qPCR Kit Protocol (New England Biolabs) using the composition and protocol shown in Table 15 and Table 16. Thereby, in the same tube, RNA was first transcribed into cDNA

and afterwards, the respective target was amplified. Amplification was detected due to the added hydrolysis probe. Solely for generation of standards for absolute quantification, a two-step RT-PCR was applied as described in 2.4.3.2.

Table 15: Composition of RT-qPCR singleplex mastermix using the Luna® Universal Probe One-Step RT-qPCR.

Components per reaction	Volume per reaction [μL]	Final concentration
Luna Universal One-Step Reaction Mix (2X)	10	1 \times
Luna WarmStart® RT Enzyme Mix (20X)	1	1 \times
Forward primer (10 μM)	0.8	0.4 μM
Reverse primer (10 μM)	0.8	0.4 μM
Probe (10 μM)	0.4	0.2 μM
Template RNA	variable	$\leq 1 \mu\text{g}$ (total RNA)
Nuclease free water	to 20	

The RT-qPCR program was set according to Table 16.

Table 16: Program for the RT-qPCR using Luna® Universal Probe One-Step RT-qPCR Kit

Cycle step	Temperature [$^{\circ}\text{C}$]	Time [min:s]	Cycles
Reverse transcription	55	10:00	1
Initial Denaturation	95	01:00	1
Denaturation	95	00:10	40
Annealing	60	00:30	
Extension	72	01:00	

2.4.3.1. Relative quantification of transcripts

For the $\Delta\Delta\text{Ct}$ -method, the housekeeping gene GAPDH was used in each RT-qPCR reaction to normalize the amplification data of the genes of interest. All samples were compared either to a reference blood leukocyte sample or patient samples were compared to the baseline sample before treatment. The Ct-values of each target were subtracted by the Ct value of GAPDH for the

respective sample resulting in the ΔCt value. The ΔCt value of the control sample was subtracted from the ΔCt value of all other samples, resulting in the $\Delta\Delta\text{Ct}$ value. The change in expression fold was calculated by $2^{(-\Delta\Delta\text{Ct})}$.

$$\Delta\text{Ct} = \text{Ct}_{\text{target}} - \text{Ct}_{\text{housekeeping}} \quad \text{Equation 3}$$

$$\Delta\Delta\text{Ct} = \text{Ct}_{\text{test samples}} - \text{Ct}_{\text{control samples}} \quad \text{Equation 4}$$

$$\text{Relative fold expression} = 2^{-\Delta\Delta\text{Ct}} \quad \text{Equation 5}$$

2.4.3.2. Absolute quantification of transcripts

For absolute quantification of transcripts of interest, standards of approximately 800 bp to 1000 bp of all analyzed targets were generated to enable the analysis of dilution series with known copy numbers for standard curves. Therefore, additional primers for PCR products of at least 800 bp were designed. The standards were generated by two-step RT-PCR using the SuperScript™ III First-Strand Synthesis SuperMix Kit (Thermo Fisher Scientific, Waltham, USA) for cDNA synthesis using HCT116 cell RNA. The pipetting schemes and PCR programs are listed in Table 17 and 18.

Table 17: Reaction setup using SuperScript™ III First-Strand Synthesis SuperMix Kit by Invitrogen (Thermo Fisher Scientific, Waltham, USA) for generation of cDNA.

Component	Volume [μL]
RT Reaction Mix (2X)	10
RT Enzyme Mix	2
RNA	1
Nuclease free water	7

Table 18: Temperature setup for SuperScript™ III First-Strand Synthesis SuperMix (Thermo Fisher Scientific, Waltham, USA) for first strand cDNA synthesis using the Mastercycler® Gradient cycler (Eppendorf, Hamburg, Germany).

Cycle step	Temperature [°C]	Time [hh:mm:ss]	Cycle
Primer Annealing	25	00:10:00	1
cDNA synthesis	50	00:30:00	1
Heat inactivation	85	00:05:00	1

After reverse transcription, the cDNA was used as template for specific PCR for amplification of the EpCAM, Snail and Twist standards using the Q5 High-Fidelity 2X Master Mix (New England Biolabs, Ipswich, USA) as listed in Table 19 and Table 20.

Table 19: Reaction setup for two-step RT-PCR using Q5 High-Fidelity 2X Master Mix (New England Biolabs, Ipswich, USA).

Component	Volume [μL]	Final Concentration
Q5 High-Fidelity 2X Master Mix	12.5	1X
Forward standard primer (10 μM)	1.25	400 nM
Reverse standard primer (10 μM)	1.25	400 nM
DNA template	2	250 mM
	8	-
Nuclease-free water		

Table 20: Temperature setup for Q5 High-Fidelity 2X Master Mix (New England Biolabs, Ipswich, USA) PCR using the Mastercycler® Gradient cycler (Eppendorf, Hamburg, Germany).

Cycle step	Temperature [°C]	Time [hh:mm:ss]	Cycles
Initial Denaturation	98	00:00:30	1
Denaturation	98	00:00:10	40
	50-72	00:00:30	
	72	00:00:30	
Final extension	72	00:02:00	1

After PCR with the standard primers, the products were analyzed on an agarose gel and the respective bands were cut out and purified using the PureLink™ Quick Gel Extraction Kit (Thermo

Fisher Scientific; Waltham, USA) as described in the manual. The purified PCR-products were sequenced by GATC Biotech (Ebersberg, Germany) and stored at -20 °C. From the nucleic acid concentration measured using the NanoDrop, the exact copy number was calculated using Equation 6.

$$\text{Number of copies} = \frac{\text{Amount [ng]} \times 6.022 \times 10^{23}}{\text{Length [bp]} \times 1 \times 10^9 \times 660} \quad \text{Equation 6}$$

Using a dilution series of the standards or total RNA, the theoretical PCR efficiency could be calculated by Equation 7. The copy number of selected targets could be determined from PCR with dilution series of the standards (10^1 to 10^6 copies) using Equation 8 and Equation 9.

$$\text{Theoretical PCR efficiency} = 10^{-1/\text{slope}} \quad \text{Equation 7}$$

$$y = mx + b \quad \text{Equation 8}$$

$$x = \frac{y - b}{m} \quad \text{Equation 9}$$

With y = Ct value, m = slope, x = copy number,
b = y-intercept

2.4.3.3. Multiplex one-step-RT-qPCR

To simplify the assay, a multiplex approach of expression analysis was established. Therefore, a mix of primers and probe was prepared for each target as listed in Table 21. Different primer concentrations of 150 nM, 400 nM or 900 nM for each target were evaluated to compensate for low and high expression levels (85). For establishment, singleplex reactions for each target were prepared in addition as control (as described in Table 15) and to directly compare the Ct values and relative fluorescence of the singleplex and multiplex approaches (composition as shown in Table 22).

Table 21: Composition of the primer and probe mixes with different primer concentrations
Concentration

Expression level	Assay mix final	Primer 1	Primer 2	Probe
High	20X	3 μ M	3 μ M	5 μ M
Medium	20X	8 μ M	8 μ M	5 μ M
Low	20X	18 μ M	18 μ M	5 μ M

Table 22: Composition of the RT-qPCR multiplex mastermix using Luna® Universal Probe One-Step RT-qPCR Kit
Components per reaction Volume per reaction [μ L] Final concentration

Luna Universal One-Step Reaction Mix (2X)	10	1 \times
Luna WarmStart® RT Enzyme Mix (20X)	1 per target	1 \times
Primer and probe mix (20X)	1	150 nM, 400 nM, 900 nM
Template RNA	Variable	\leq 1 μ g (total RNA)
Nuclease free water	to 20 μ L	

2.4.3.4. Liquid RT-qPCR vs. lyophilized RT-qPCR

In order to prestore master mixes and other PCR components on the cartridge and preserve their functionality, the components need to be dried or lyophilized. For evaluation of a suitable lyophilized master mix, two different one-step RT-qPCR beads were tested: CIRRUSTRM Strips RNA (Fluorogenics) and the SCRIPT RT-qPCR ProbesMaster Lyophilisate (JENA Bioscience). The reaction mixes for the RT-qPCR beads were set up as listed in Table 23.

Table 23: Pipetting scheme for the CIRRUS™ Strips RNA and SCRIPT RT-qPCR ProbesMaster Lyophilisate master mix.

Component	Volume [μL]	Final concentration [μM]
CIRRUS Strips RNA or SCRIPT RT-qPCR ProbesMaster Lyophilisate	1 Bead	-
Forward primer	1.0	0.5 μM
Reverse Primer	1.0	0.5 μM
Probe	0.5	0.25 μM
Template	Varying	Varying
Nuclease free water	Up to 20	Varying

The required volume of master mix was prepared in one tube without added template and transferred into a sample tube containing one bead per reaction. Depending on the experiment, 1 to 5 μL of target containing cell lysate, corresponding to 5 to 25 % of the reaction volume, were added to determine the maximum volume of lysate that is PCR compatible and not inhibiting. The applied PCR programs are shown in Table 24.

Table 24: PCR program for the CIRRUS™ strips RNA reactions.

Phase	Temperature [$^{\circ}\text{C}$]	Duration [hh:mm:ss]	
Reverse transcription	55	00:02:00	
RT inactivation and Initial Denaturation	95	00:01:00	
Denaturation	95	00:00:10	40 cycles
Annealing	60	00:00:30	
Elongation	60	00:00:30	

Table 25: PCR program for the SCRIPT RT-qPCR ProbesMaster Lyophilisate reactions.

Phase	Temperature [°C]	Duration [hh:mm:ss]	
Reverse transcription	55	00:10:00	
RT inactivation and Initial Denaturation	95	00:05:00	
Denaturation	95	00:00:15	40 cycles
Annealing	60	00:00:30	
Elongation	60	00:00:30	

2.4.3.5. Stability testing of air-dried primer and probe mixes

Primers were air-dried with and without the addition of the additives trehalose (33.3 mM end concentration) or xanthan (1.6 mM end concentration) (86). The primer and probes were added in the same concentrations as given in Table 15. The additives were solved in molecular grade H₂O to obtain stock solutions of 100 mM trehalose and 5 mM xanthan of which 1 μ L was used for the primer and probe mix for drying. After drying of the primer and probe mixes, their functionality was assessed by multiplex RT-qPCR as described in 2.4.3.3 after storage of 3 h, 24 h, 21 d and 42 d at RT and after storage at 55 °C for accelerated aging analysis that can be calculated according to Equation 10 to Equation 12.

$$\text{Accelerated aging factor AAF} = Q_{10}^{\left(\frac{T-T_{\text{room}}}{10}\right)} = 7.82 \quad \text{Equation 10}$$

$$\text{Accelerated aging [d]} = t \times \text{AAF} \quad \text{Equation 11}$$

$$\text{Expected storage stability [d]} = \text{accelerated aging} + \text{storage time} \quad \text{Equation 12}$$

2.4.3.6. Nested-PCR

For targeted pre-amplification of a defined region of interest, an additional primer pair was designed that binds outside the inner primer pair used for RT-qPCR. Then, the nested PCR approach consisted of two PCR runs. The first PCR was performed as RT-qPCR with 15 PCR cycles according to Table 16, followed by an additional qPCR run for quantification of the inner target. Linearity of the nested RT-qPCR was assessed, and the Ct-values of the samples amplified

by nested RT-qPCR in comparison to conventional RT-qPCR as well as the minimal copy number or cell suspension dilution detected were compared.

2.5. Statistical analysis

Data are presented as means \pm standard deviation of the mean. Statistical analysis was performed using SPSS statistics software version 25 (IBM, Armonk, NY, USA). Shapiro-Wilk's test and Levene's test ($p < 0.05$) were applied to evaluate normal distribution and homogeneity of variances. Differences between groups were determined using t-test or one way ANOVA for normally distributed data sets with homogeneous groups variances, Welch's test with the Dunnett-T3 posthoc test for normally distributed data sets with heterogeneous group variances, or Kruskal-Wallis's test for data sets that are not normally distributed. $p < 0.05$ was considered to indicate significant difference. Significant differences were displayed by different letters above the bars.

3. Results

In the following chapter, the results on the clinical trial using patient samples for CTC analysis and the results on the established of a LoC compatible cell staining are presented. The aim was to reproduce a benchmark methods and to make the necessary adjustments to Vivalytic integration. Moreover, first proof-of-concept experiments on protocols for downstream molecular analysis of the isolated CTCs are shown.

3.1. CTC detection in patient samples according to the maintrac® method

For enrichment-free detection of epithelial tumor cells from blood samples the maintrac® method (SIMFO, Bayreuth), as described in chapter 2.2.3, was applied as reference method. The reproducibility of the method and the possibility for integration of a similar method into a LoC platform were evaluated using patient samples obtained from the UKT for proof-of-principle studies. Patients suffering from gastrointestinal tumors were included into the study and donated blood before treatment and every 3 to 4 weeks during therapy. The number of CTCs present in the blood samples was determined and correlated to the clinical presentation of the patient. Therefore, samples of the patients were analyzed at BOSCH and SIMFO in parallel to evaluate interlaboratory reproducibility and identify differences or challenges. Example images of the cells detected in the patient samples are shown in Figure 16.

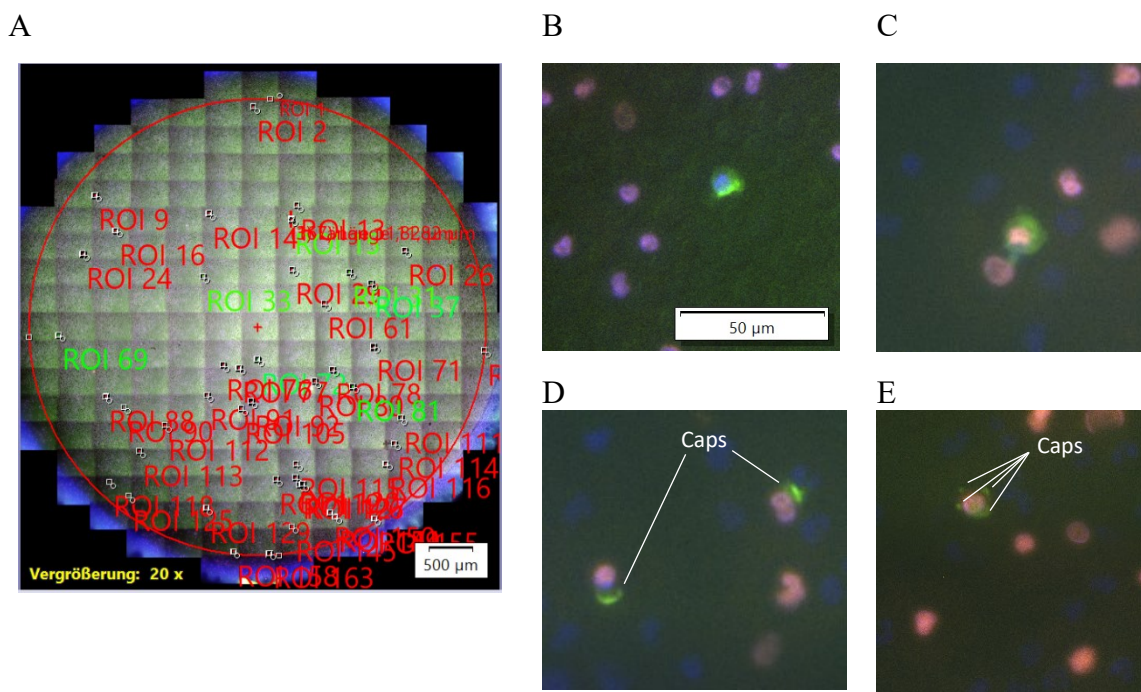
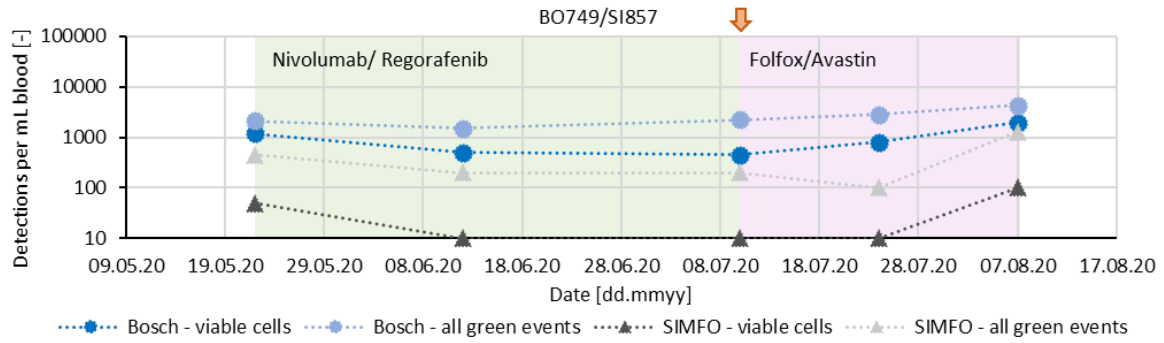


Figure 16: Example images of cells detected in patient samples.

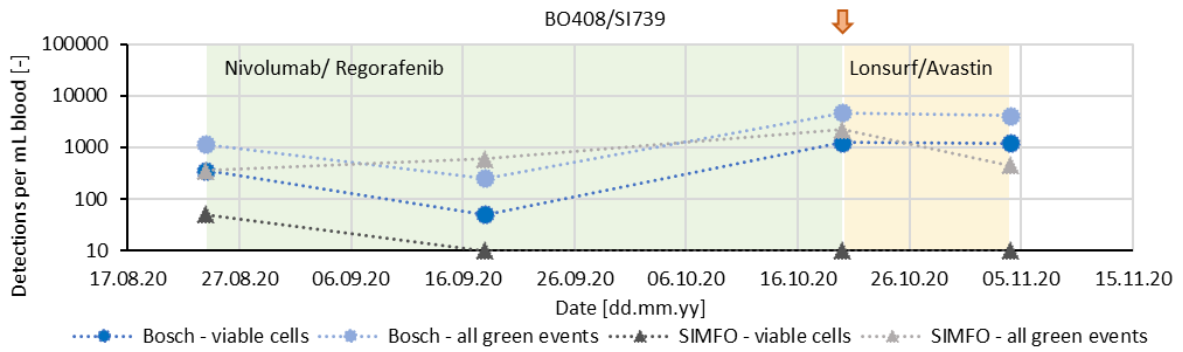
The cells were stained with Hoechst33342 for nucleus detection (blue), EpCAM-FITC for EpCAM detection (green), and PI for detection of dead cells (red). A: result of the image acquisition using the well navigator of the cellSens Dimension software of the Olympus IX83 fluorescence microscope (Olympus, Shinjuku, Japan) at 200-fold magnification. Images are acquired sequentially in each channel and the single images are stitched (with 10 % overlap) to one overview image by the software. B to E: example images of EpCAM-positive cells with uniform EpCAM expression (B viable and C non-viable), single EpCAM-‘caps’ (D), and several EpCAM-‘caps’ (E).

CTCs with uniform EpCAM staining on the surface were observed by microscopic analysis, as well as CTCs with punctual EpCAM staining, where only a part of the membrane was stained (so called “EpCAM caps”). Figure 16B and C show CTCs with uniformly stained membranes, whereas Figure 16D shows cells with one EpCAM cap and Figure 16E shows a CTC with several EpCAM caps on one cell. This means that the EpCAM expression was not evenly distributed over the whole cell membrane but rather condensed and limited to certain areas on the membrane. EpCAM positive cells were counted independent of the homogeneity of EpCAM staining on the surface. However, these observations raised the questions whether the differences in EpCAM localization on the cell surface have a clinical relevance, and whether uniformly stained cells differ from cells with EpCAM caps in terms of invasiveness.

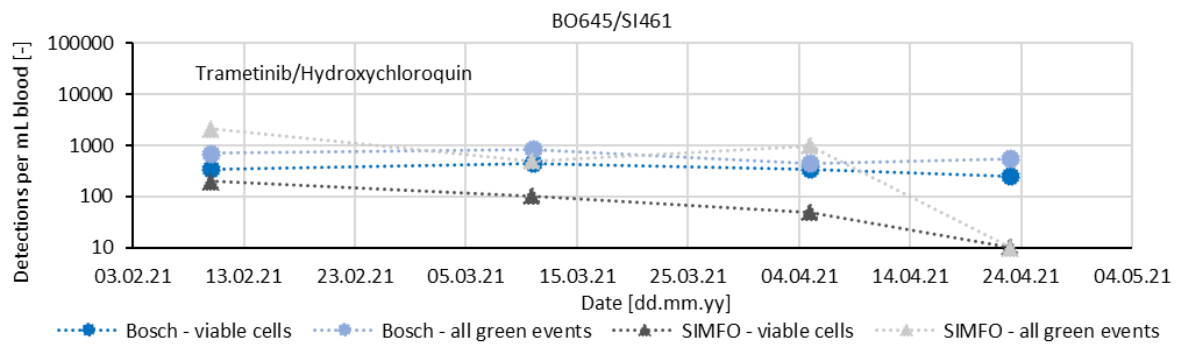
A



B



C



D

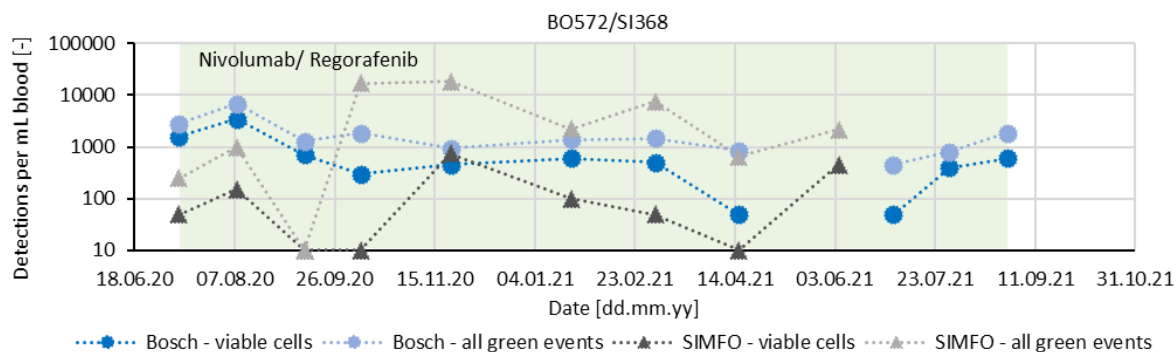


Figure 17: Patient samples obtained from the UKT analyzed by the maintrac® method.

Blood samples of four pseudonymized patients (A-D) were subjected to CTC detection using the maintrac® method. Analysis was conducted at BOSCH and SIMFO in parallel. The number of EpCAM-positive events is shown as 'all green events' and the number of EpCAM-positive, viable and nucleus containing cells is given as 'viable cells'. The colors in the background mark the administered drug and the orange arrow marks a progression detected by CT scan.

The CTC count course of patient BO-749 as determined in this study at Bosch showed a baseline CTC count of 1200 CTC/mL blood at baseline that decreased to 450-500 CTCs/mL blood at the second and third sampling point. The count increased to 800 and 1950 CTC/mL again at the fourth and fifth sampling point. Thus, the CTC count in the last samples was even higher than the baseline. The CTC course determined by SIMFO started at 50 CTC/mL blood at baseline and decreased below the LOD at the second, third and fourth sampling point. At the fifth sampling point, the count increased to 100 CTC/mL blood. The courses of the counts were similar, but the absolute counts differed due to differences in image evaluation. However, both detected an increase after the initial decrease that correlated with a progression observed by CT scan indicating the prognostic value of the CTC count for detection of a therapy resistance or failure.

For Patient BO-408, a baseline CTC count of 350 CTC/mL blood was determined by BOSCH. The count decreased after therapy started but increased again at the third and fourth sampling point. In contrast, SIMFO observed a decrease from 50 CTC/ml to below LOD at the following time points. The fourth sample was not analyzed by SIMFO, or data was not transmitted. The increase observed by the BOSCH analysis correlated with a progression observed in the CT scan.

The CTC count of patient BO-645 as determined by BOSCH showed a baseline of 350 and increased to 450 (1.2-fold increase) at the second time point. After the second time point a constant decrease to 350 CTC/mL (0.7-fold) and 250 CTC/mL (0.7-fold) was observed. SIMFO determined a baseline count of 200 CTC/mL. For the following samples, a constant 0.5-fold decrease to

100 CTC/mL, 50 CTC/mL, and 10 CTC/mL was observed. Again, not the absolute values but the CTC count courses of Bosch and SIMFO were comparable.

The CTC count of patient BO-572 showed a heterogeneous CTC count course over the 12 sampling time points. This observation was consistent with the results of SIMFO and with the observations made in the clinical setting via investigation of tumor markers CEA and CA 19-9. This can be an indicator for a response to therapy that was not only observable by tumor marker analysis but also by CTC quantification.

In the case of patients BO-184 and BO-720, only the baseline samples were analyzed. Patient BO-184 had a baseline CTC count of 400 CTC/mL and for patient BO-720 a baseline count of 150 CTC/mL was determined.

The absolute CTC count differed from the absolute CTC count reported by SIMFO. However, the CTC count course over time was comparable in most of the samples.

For simplification of the CTC count course evaluation, the CTC counts were normalized to range between zero and one using the lowest and highest count observed, respectively.

3.2. Establishment of LoC compatible unit operations for CTC detection

For integration of a CTC enrichment and characterization method, including whole blood preparation, isolation of the target cells, immunocytochemistry, counting of the cells, cell lysis and nucleic acid analysis, the sample processing steps were adapted to the technical parameters and boundary conditions of the LoC system. These included the processing of a whole blood sample without external preprocessing such as centrifugation and with limited volume capacity. Furthermore, the optical analysis of the CTCs in the Vivalytic system was limited to fluorescence detection and reduced resolution.

3.2.1. Establishment and adaptation of CTC detection for integration onto the LoC-system

According to the maintrac® protocol (chapter 2.2.3), a cell suspension containing leukocytes and circulating epithelial tumor cells (CETCs) was obtained after red blood cell lysis, centrifugation, and resuspension. These were stained with anti-EpCAM-FITC for identification of CETCs and PI for exclusion of dead cells. Furthermore, cells were analyzed using transmitted light imaging for identification of nuclei containing cells. First, the maintrac® method was reproduced using whole blood spiked with different cell lines, either NCI-H1975, BT-474 or HCT116 to identify a suitable

cell line with homogeneous EpCAM expression on the surface of all cells for generation of reproducible model samples. As exemplarily shown in Figure 18A, only approximately 50-60 % of the NCI-H1975 cells were EpCAM-positive, whereas the BT-474 cells (Figure 18B) and HCT116 cells (Figure 18C) showed uniform EpCAM distribution on the cell surface as well as a uniform EpCAM protein expression throughout 100 % of the cells. Therefore, the BT-474 and the HCT116 were used for positive controls in spike-in experiments.

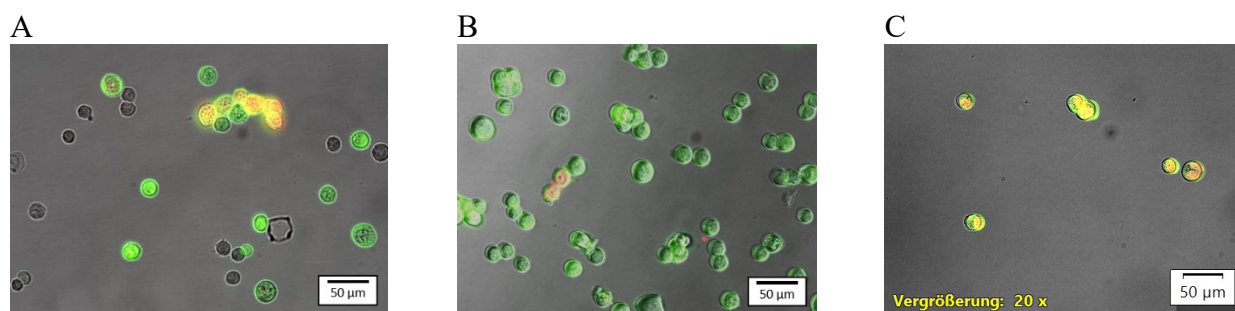


Figure 18: EpCAM-FITC and PI staining of cell lines.

(A) NCI-H1975 cells; (B) BT-474 cells and (C) HCT116 cells. Imaging was performed using the inverted fluorescence microscope IX83 at 200-fold magnification separately using transmitted light with 3 ms illumination, the EGFP channel (Ex/Em 470/525) and the DsRed channel (Ex/Em 545/620) with 50 ms illumination and the acquired images were merged afterwards.

For integration into the LoC system, all required cell characteristics had to be detected using fluorescence staining as there was no possibility for transmitted light imaging in the system. Therefore, the staining protocol was adapted for Vivalytic compatible detection. The cells were stained with anti-EpCAM-FITC or anti-EpCAM-APC for antigen detection, with CFSE and PI for live/dead distinction and additionally with Hoechst33342 for nucleus detection using fluorescence microscopy. As shown in Figure 19, the staining protocol was confirmed suitable using BT-474 and HCT116 cells. Especially the possibility to detect all nuclei using Hoechst33342 instead of transmitted light was shown.

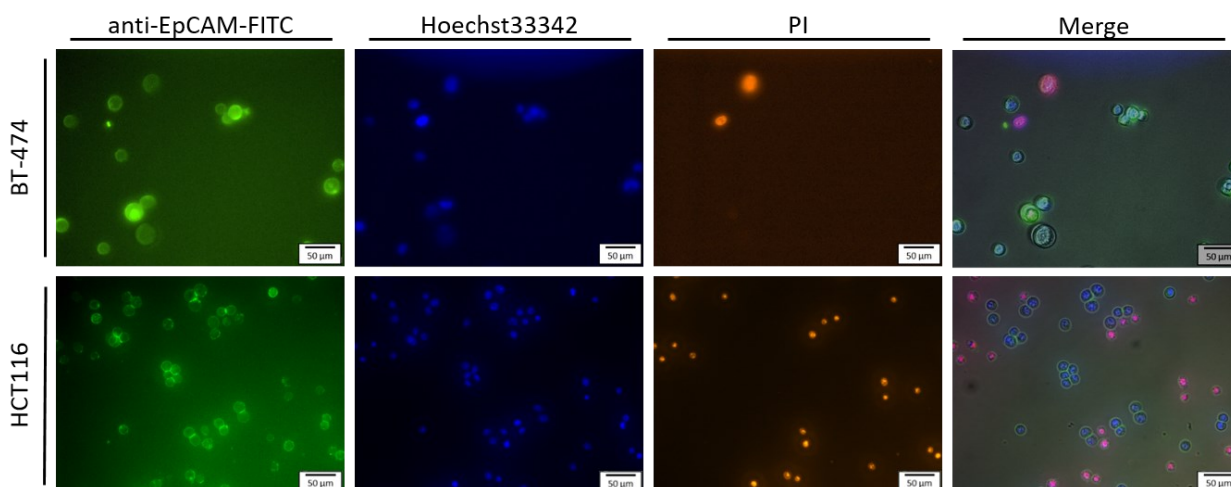


Figure 19: Adapted staining protocol.

BT-474 and HCT116 cells stained with anti-EpCAM-FITC (Ex/Em 490/525, 50 ms illumination), Hoechst33342 (Ex/Em 350/461, 15 ms illumination) and PI (Ex/Em 535/617, 50 ms illumination). Imaging was performed using the inverted fluorescence microscope IX83 at 200-fold magnification separately using transmitted light with 3 ms illumination. The acquired images were merged afterwards.

Both cell lines were suitable for application as EpCAM-positive model cells for spike-in experiments. The BT-474 cells represented large cells and the HCT116 smaller cells, covering the heterogeneity of real CTCs as isolated from patient samples. During routine cultivation and passaging of the cells, their average diameter was determined by the Cell Counter R1 (Olympus, Shinjuku, Japan). The mean diameter of the BT-474 and HCT116 cells was $17.4 \mu\text{m} \pm 1.5 \mu\text{m}$ and $12.6 \mu\text{m} \pm 1.6 \mu\text{m}$.

For integration of cell detection (detection of EpCAM-positive, PI-negative, nucleus containing cells) into the current Vivalytic system, further fluorescent dye combinations were evaluated using cell lines. As there was no possibility to integrate transmitted light analysis into the Vivalytic system the aim was to provide the possibility of cell differentiation and characterization of the given prerequisites solely by fluorescence detection without transmitted light and without loss of information. The different combinations evaluated are listed in Table 26.

Table 26: Fluorescent dye combination for CTC detection and characterization.

Cell characteristic	EpCAM antibody (labeled)	Viable	Dead	Nucleus
Combination 1 According to maintrac®	FITC	No dye (PI-negative)	PI	No dye (Bright field)
Combination 2	FITC	CTDR (optional)	PI	Hoechst
Combination 3	APC	CFSE (optional)	PI	Hoechst
Combination 4	APC	CTDR (optional)	PI	Syto9

Including Hoechst33342 into the staining protocol provided the possibility for nucleus detection without transmitted light imaging. Although the current Vivalytic system does not provide UV-light excitation required for Hoechst33342 detection, the integration of a UV-light source would be easier than the integration of transmitted light imaging. Therefore, Hoechst was regarded as one suitable possibility for nucleus detection. Alternatively, another nucleus dye such as SYTO9 could be used if the EpCAM antibody labelled with FITC was replaced by another label, e.g., APC.

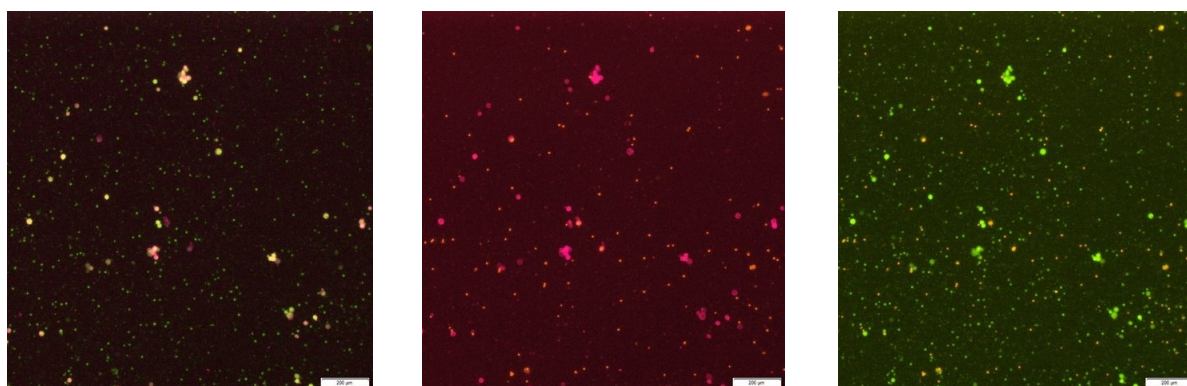


Figure 20: HCT116 cells stained with CFSE for viable cell detection, EpCAM-APC for detection of EpCAM-positive cells and PI for dead cell exclusion.

The dye combination represented an alternative staining strategy in which the green EGFP channel was not used for EpCAM detection but was available for another cell dye such as CFSE or SYTO9. 40-fold magnification. The white bars represent 200 μ m.

In addition, leukocytes could be stained for identification using anti-CD45-PE which stained the cell membrane and provided a way of differentiating leukocytes from spiked or real cancer cells. An image of the CD45-PE-stained leukocytes is shown in Figure 21.

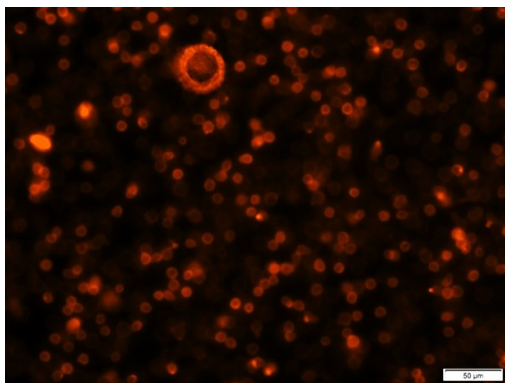


Figure 21: Leukocytes stained with CD45-PE. 200-fold magnification. The white bars represent 50 μm .

3.2.2. Selection of a method for erythrocyte depletion in blood samples

Three common methods for erythrocyte depletion were evaluated with the aim of identifying a method that is suitable for separation of nucleated blood cells from erythrocytes without losing CTCs: density gradient centrifugation, selective erythrocyte lysis and erythrocyte aggregation (described in chapter 2.2.5.2). The recovery rate of spiked cell lines was determined for all three methods.

After density gradient centrifugation, a buffy coat was visible between the upper phase, the blood plasma, and the erythrocyte pellet. The buffy coat containing the nucleated cells was transferred into a microtiter plate for microscopic analysis (Figure 22).

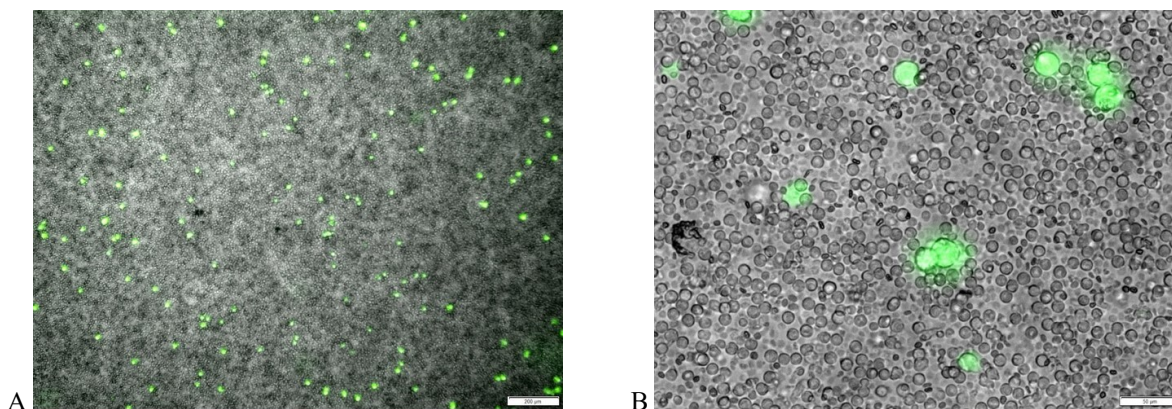


Figure 22: Microscopy of the cells extracted from buffy coat after density gradient centrifugation. The BT-474 cells were stained with CFSE before spiking into to whole blood prior to centrifugation. The images were acquired at (A) 40-fold magnification (bar = 200 μm) and (B) 200-fold magnification (bar=50 μm) in transmitted light (2 ms) and the EGFP channel (50 ms) separately and merged by the software.

As shown in Figure 23, before selective erythrocyte lysis only erythrocytes were visible by transmitted light microscopy of a blood sample. After lysis, the other blood cells like leukocytes

and, if present CTCs, became visible and the erythrocytes became transparent. The contrast decreased mainly because of the simultaneous release of hemoglobin and uptake of the surrounding medium of the erythrocytes. Before lysis, the blood and lysis buffer suspension appeared red and turbid by optical inspection, whereas after lysis, the solution was red and transparent. After centrifugation, most of the lysed erythrocytes were contained in the supernatant and were discarded. The pellet containing most of the leukocytes and spiked cells was resuspended and transferred into a microtiter plate for microscopic analysis. As $97\% \pm 2\%$ of the spiked cells were recovered in the pelleted fraction, it was assumed that the loss of target cells into the supernatant could be neglected in the case of the cell lines.

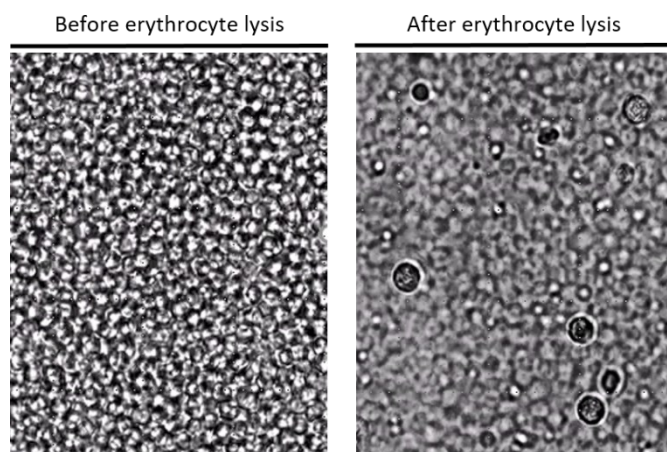


Figure 23: Blood sample observed by light microscopy during selective erythrocyte lysis. The left image was taken before lysis and the right image was taken after 10 min incubation with erythrocyte lysis buffer. After lysis, the contrast of the erythrocytes decreased, and the leukocytes were visible.

Erythrocyte depletion by aggregation consists of increasing their density relative to the other blood cells leading to accelerated sedimentation without centrifugation. After treatment with the HetaSep™ solution (chapter 2.2.5.2), the supernatant was transferred into a microtiter plate for fluorescence microscopy evaluation (shown in Figure 24A-C). The erythrocyte fraction was selectively lysed, and the remaining cell pellet was also analyzed microscopically (shown in Figure 24D). Although, the erythrocytes formed rouleaux and thus sedimented to the bottom of the tube, residual erythrocyte aggregates were found in the supernatant, where only leukocytes were expected. Staining of the leukocytes with anti-CD45-PE revealed that the supernatant contained all three cell types, leukocytes, the spiked BT-474 cells and erythrocytes. However, the erythrocytes were depleted in number and most of the erythrocytes sedimented to the bottom. As shown in

Figure 24D, a high number of spiked BT-474 cells was found in the erythrocyte fraction, leading to the assumption that the erythrocyte rouleaux trapped some of the target cells and dragged them to the bottom.

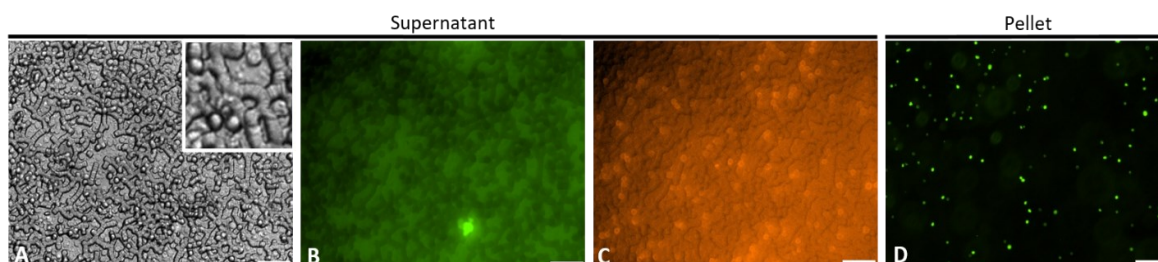


Figure 24: Erythrocyte depletion by aggregation.

The supernatant fraction in which the leukocytes and CTCs were expected, and the pellet in which the aggregated erythrocytes were sedimented were analyzed by microscopy. (A) erythrocyte aggregates found in the supernatant fraction, in the right corner, the image is enlarged for better visualization of the erythrocyte rouleaux; (B) one spiked CFSE stained BT-474 cell recovered in the supernatant; (C) anti-CD45-PE-stained leukocytes recovered in the supernatant; (D) spiked, CFSE stained BT-474 cells found in the erythrocyte fraction as analyzed by fluorescence microscopy after erythrocyte lysis. The white bars in A-C represent 50 μm , the white bar in D represents 200 μm .

The recovery rates of target cells from the spiked blood samples in the leukocyte fraction using the three methods are shown in Table 27.

Table 27: Comparison of the recovery rate of stained BT-474 cells spiked into whole blood using three erythrocyte depletion methods.

Method	Target cell recovery in the leukocyte fraction [%]
Erythrocyte aggregation	76 % \pm 6 %
Erythrocyte lysis	97 % \pm 2 %
Density gradient centrifugation	88 % \pm 3 %

Results are given as mean \pm SD of 2 biological and 3 technical replicates.

Erythrocyte aggregation resulted in a recovery rate of 76 % \pm 6 % and density gradient centrifugation in 88 % \pm 3 %. Selective erythrocyte lysis resulted in the highest recovery rate of 97 % \pm 2 %. Thus, this method was selected for further adaptation for a LoC integration of CTC isolation from blood samples.

3.2.2.1. Minimization of erythrocyte lysis buffer volume

As the LoC cartridge sample chamber encompassed a maximal volume of 1.1 mL, a minimization of the required erythrocyte lysis buffer volume would enable a maximization of the blood sample volume that can be analyzed by the system. A reduction of the blood sample volume, in contrast, would decrease assay sensitivity and reliability. Analysis of high blood sample volumes was preferred due to rarity of the CTCs present. Thus, the reduction of the reagents needed for sample preparation was more favorable. First, the minimum required volume of erythrocyte lysis buffer (ELB) was determined as described in chapter 2.2.5.3. Therefore, blood was mixed with erythrocyte lysis buffer at different ratios. These were evaluated regarding transparency of the suspension before centrifugation and purity of the leukocyte pellet after lysis and centrifugation. According to the maintrac® method, a blood to ELB ratio of 1:15 was required, whereas a published Qiagen protocol recommended a ratio of 1:5 (63) (87). Thus, ratios of 1:15, 1:10, 1:5, 1:4 and 1:3 were investigated. After an incubation time of 10 min, the transparency of the suspension was optically evaluated and is shown in Figure 25. The 1:4 ratio was the minimal ratio resulting in a completely transparent blood ELB suspension. The 1:3 resulted in sedimented, intact (dark red) erythrocytes at the bottom of the sample tube. After centrifugation, the purity of the leukocyte pellet was evaluated and is shown in Figure 25. The preferred ratio of 1:4 could also be confirmed to provide the purest pellet. At a ratio of 1:15, the leukocyte pellet appeared smaller than at other ratios, indicating undesired lysis of the leukocytes.

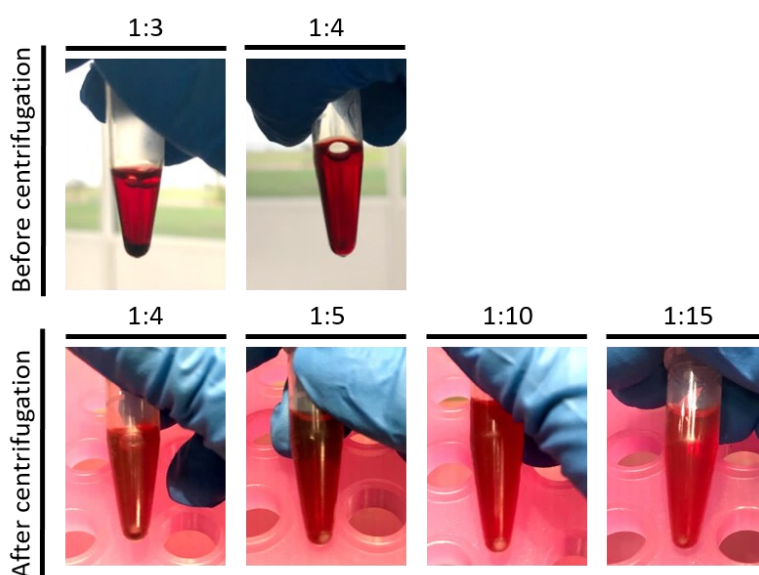


Figure 25: Determination of the minimum required erythrocyte lysis buffer.
Upper row: suspension before centrifugation. Lower row: sample after centrifugation with visible pellet.

All subsequent experiments were performed with a blood to ELB ratio of 1:4. Regarding the maximum sample volume that can be applied to the Vivalytic cartridge this enabled the input of 200 μ L blood. As relatively high numbers of CTCs were detected in the patient sample (described in chapter 3.1), in which only a blood equivalent of 20 μ L were analyzed optically, the volume of 200 μ L was regarded as sufficient even for samples with low CTC numbers.

3.2.2.2. SEM-analysis of blood cells after erythrocyte lysis

For a better understanding of the erythrocyte lysis process and for evaluation of potential benefits for the whole assay, all cells present in a blood sample were analyzed by SEM after selective lysis of the erythrocytes. Therefore, the blood sample was spiked with BT-474 cells, treated with erythrocyte lysis buffer, and washed with 1 x PBS after 10 min incubation. Afterwards, intact erythrocytes of 20 μ L of blood were added as control to enable visual comparison of lysed and unlysed erythrocytes. The sample was prepared for SEM as described in chapter 2.2.5.4. Figure 26A shows an overview of all present cell types: spiked BT-474 cells, leukocytes, unlysed erythrocytes, lysed erythrocytes, and thrombocytes. Figure 26B shows an unlysed erythrocyte in comparison to an intact erythrocyte. The lysed erythrocytes lost their stability due to release of their intracellular protein, the hemoglobin, and membrane collapse during the fixation process. The SEM-analysis proved that erythrocytes lose their integrity due to selective lysis and the density is decreased after hemoglobin release. Therefore, lysed erythrocyte can be separated more easily from the intact nucleated blood cells by gravity or centrifugation. Furthermore, the remaining erythrocyte membranes after lysis were expected to be even more deformable than the intact ones and thus easily pass a porous structure in a filtration process.

A

B

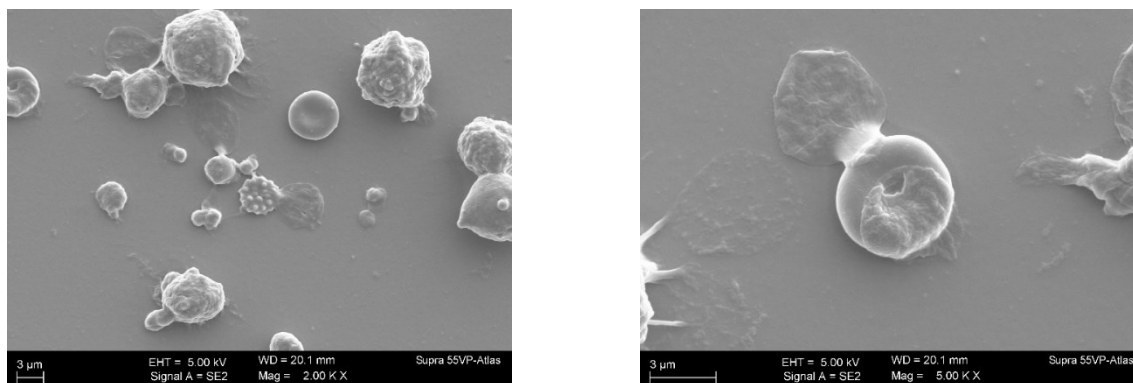


Figure 26: Blood sample spiked with BT-474 cells analyzed by SEM. (A) Overview at 2000-fold magnification; all types of cells are visible: leukocytes, BT-474, lysed and unlysed erythrocytes and thrombocytes. B: Lysed and unlysed erythrocyte at 5000-fold magnification.

3.2.2.3. Influence of the ELB on cell viability

The viability of the cells after incubation in ELB was assessed by *CellTiter-Glo*® assay (chapter 2.2.2.2) to ensure, that only erythrocytes but not leukocytes or CTCs were lysed by the ELB at a ratio of 1:4. The viability of HCT116 cells before addition of ELB and the viability of the leukocytes after 15 min incubation in ELB and centrifugation were considered as 100 % reference. As shown in Figure 27A, HCT116 viability decreased by 7 % after 45 min and did not significantly decrease further after 60 min. After the recommended 15 min incubation, viability did not significantly change. An incubation time of 10-15 min was required for sufficient erythrocyte lysis before centrifugation. The prolonged incubation time was evaluated to ensure that longer processing time needed for leukocyte and CTC isolation from the sample was still possible without adverse effects on the target cells.

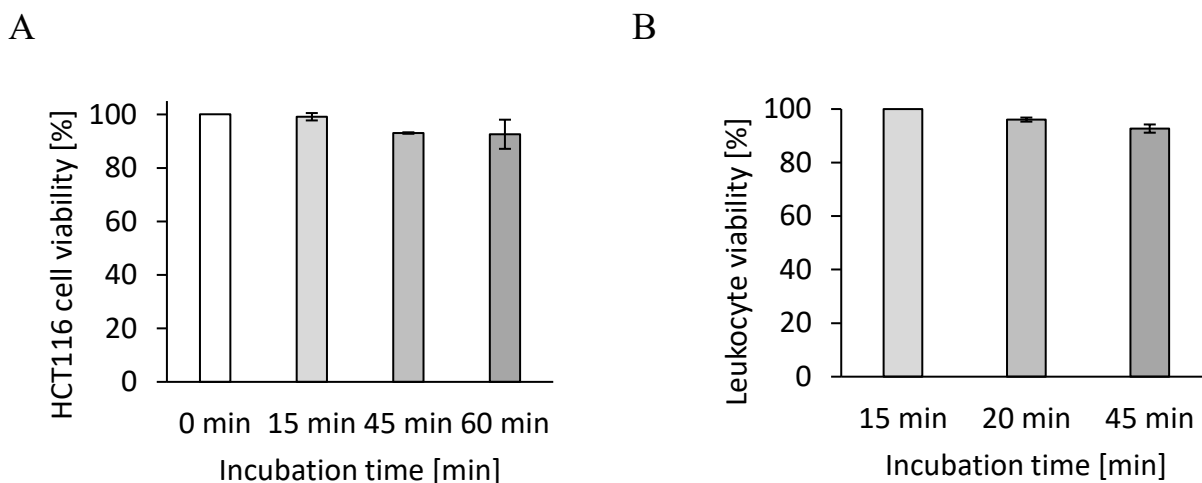


Figure 27: Cell viability after erythrocyte lysis.

Viability of A: HCT116 cells and B: leukocytes after 15 min, 45 min, and 60 min incubation in ELB. The viability of the first measurement was set as 100 %. Results are given as means \pm SD of two biological and three technical replicates.

3.2.3. Evaluation of RBC depletion and CTC isolation methods for LoC integration

One of the major challenges during CTC isolation and detection in front of the high number of healthy blood cells (non-target cells) within the sample. Different CTC isolation and cell separation systems and methods from literature were compared and rated using the concept decision matrix according to Pugh. The most important criteria for the concept selection included boundary conditions given on one the hand by the Vivalytic system and on the other hand by the sample composition and included:

- Complexity of the fluidics: limited continuous flow, requirement of a sheath flow, clogging, dependency of the diameter, dilution of the sample
- Separation efficiency: collection rate, purity, throughput
- Integrability: Component's complexity, external field, space and location, manufacturing technology, independent of a 30° angle, storage conditions
- Benefits from selective RBC lysis

As described in chapter 3.2.2, selective erythrocyte lysis was selected as beneficial method for depletion of erythrocytes. The method included lysis of the erythrocytes in the first step and centrifugation in the second step. As there was no possibility for centrifugation in the LoC system, the most important criterium for the LoC concept selection was to define an alternative for

centrifugation. Taking into consideration all the criteria above, mechanical filtration was considered the most suitable method for Vivalytic integration.

3.2.4. Evaluation of filtration-based methods for CTC isolation

The main advantages of a filtration-based approach were the interdependency of a constant flow rate and the possibility to remove red blood cells and partially leukocytes without centrifugation. The filtration process's aim was to capture CTCs with a high rate and deplete lysed erythrocytes and leukocytes if possible. The focus however was set on a high capture rate of CTCs over high purity. First, the integrated glass fiber filters B and D that were already used for nucleic acid extraction in other diagnostic assays in the Vivalytic cartridge were tested. Additionally, a filtration functional model was established for simple evaluation of the compatibility of the filtration method with on-chip conditions.

3.2.4.1. Evaluation of filtration for CTC isolation using the Vivalytic cartridge

A whole blood sample of 200 μL spiked with 500 stained BT-474 cells was transferred into a self-assembled spin-column containing either the filter B (particle retention rating 1.0 μm , thickness 550 μm) or filter D (particle retention rating 2.7 μm , thickness 640 μm ; Figure 28A). The erythrocytes were previously selectively lysed as described in chapter 2.2.5.3. The spin column containing the spiked blood sample was centrifuged at 3000 x g for 1 min. Afterwards, the filtrate was transferred into a 96-well plate and the cell count in the filtrate was determined by fluorescence microscopy.

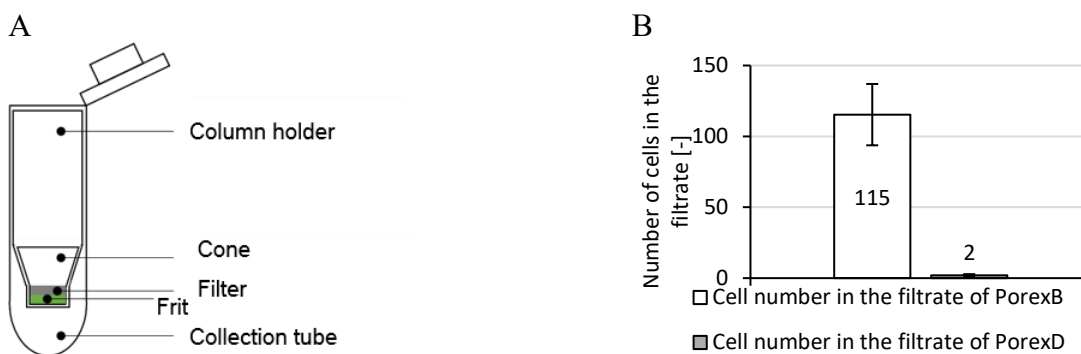


Figure 28: A: Experimental set-up and B: results of cell filtration using the filter B and D integrated into a spin column. The cells recovered in the filtrate were counted by fluorescence microscopy to determine the cell recovery rate and the cell ratio retained by the filter.

As shown in Figure 28B, in the filtrate of the B spin column, 115 ± 20 cells ($23 \% \pm 4 \%$) were counted. As expected, the thicker filter D was able to retain more cells than the B filter. Here, only 2 ± 1 cells ($<1 \%$) were able to pass the filter. However, as both filters retained at least 77 % of the spiked cells, both filters were used for on-chip cell filtration on the Vivalytic cartridge. Hereby, a blood sample of 200 μL spiked with 500 BT-474 cells was transferred into the sample chamber, 800 μL erythrocyte lysis buffer was added and incubated for 10 min at RT. The sample was then pumped over the filter into the waste chamber and the filtrate from the waste chamber was analyzed by microscopy. In the case of the filters being inserted loosely into the filter chamber more than 50 % of the cells were found in the filtrate. Subsequently, the filters were mounted into the filter chamber leakproof by welding with the TPU membrane and the experiment was repeated. In these experiments, the filter was clogged after 200 μL to 700 μL of the sample observed by residual sample (300 μL to 800 μL) in the sample chamber. Only up to around 30 cells were found in the waste chamber after filtration. But, due to clogging of the filters and recovery of the captured cells not being possible, the filter material currently integrated into the current Vivalytic cartridge was considered not suitable for filtration and recovery of cells from a blood sample which is why an alternative filtration system was established for the proof-of-principle of LoC-compatible CTC isolation by filtration.

3.2.4.2. Filtration functional model for CTC-isolation and detection using TEM-grids

Parts of the results presented in this chapter were published in *Biosensors* 2021, 11, 312, 3 September 2021: Real-time detection of circulating tumor cells during capture on a filter element

significantly enhancing detection rate (88). The results were complemented by unpublished data of additional experiments in this thesis.

To ensure reproducibility and enable microfluidic processing in a LoC-like environment, rapid prototyping is a valuable method to produce functional models. A filtration functional model was fabricated using TEM-grids as filters and cell retention was evaluated. The TEM-grids with a diameter of 3 mm were integrated into the fabricated microfluidic slide with either one or two inlets and outlets (chapter 2.3.1.1). The grid was analyzed by scanning electron microscopy (Figure 29) and revealed a pore size of $7.4 \pm 0.1 \mu\text{m}$ and pitch size of $4.5 \pm 0.2 \mu\text{m}$. According to the manufacturer, a pore size of $6.5 \mu\text{m}$ and a pitch size of $5 \mu\text{m}$ was expected.

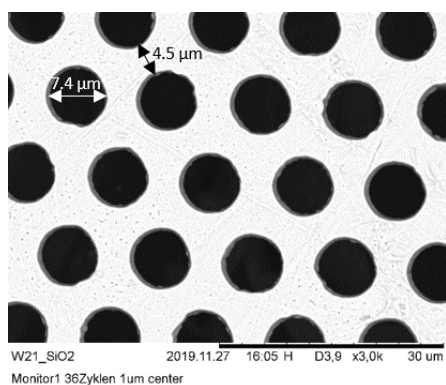


Figure 29: TEM-grid imaged by SEM for pore size measurement.

The white arrow represents the pore diameter of $7.4 \mu\text{m}$, the black arrow shows the pitch size of $4.5 \mu\text{m}$ (88).

Evaluation of the impact of surface passivation for cell capture optimization

For experiments, the slide was connected to a syringe pump on the outlet side and to a funnel on the inlet side using silicon tubes (Figure 30A). The set-up was placed on an upright fluorescence microscope for optical detection of the cells (see Figure 30B).

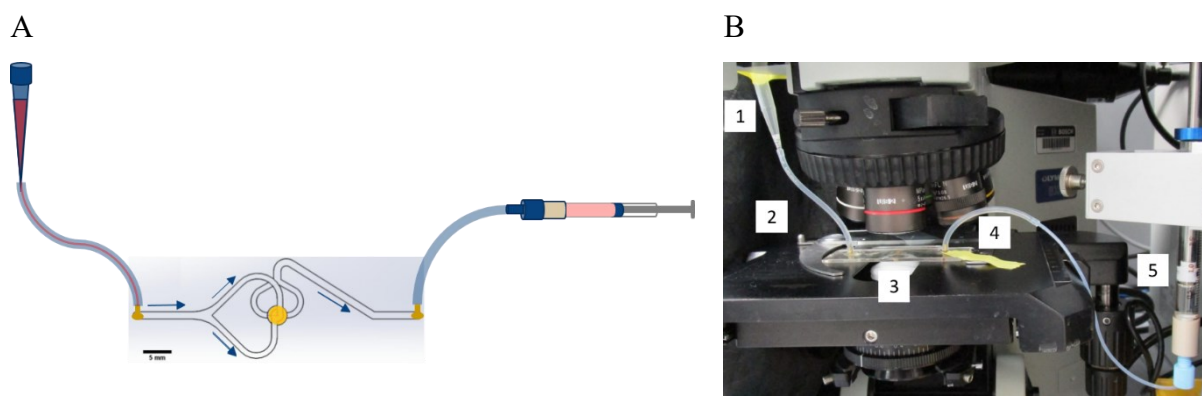


Figure 30: Filtration functional model.

A: Filtration functional model connected to a funnel and a syringe via silicon tubes. The arrows indicate the sample pumping direction. B: Observation by fluorescence microscopy was possible in real-time. 1: Pipette tip used as funnel; 2 and 4: tube connecting the funnel and syringe with the filtration slide; 3: filtration slide as single unit operation model; 5: syringe connected to syringe pump for precise processing of the sample (88).

First, the cell loss by the microfluidic system was analyzed by pumping cells through a slide passivated with 1 x PBS/1 % (w/v) BSA/1 mM EDTA for 30 min without TEM-grid integrated compared to a non-passivated slide. As shown in Figure 31, approximately $18\% \pm 4\%$ of the spiked cells were lost in the system without passivation, due to adherence to the microfluidic channel and tube walls. After passivation, $100\% \pm 9\%$ of the spiked cells could be recovered. One reason for the recovery rate above 100 % could be cell clusters that were not counted correctly during determination of the initial spike cell number. After transport through the system, these cell clusters could have been separated into single cells that were then counted separately and resulted in the cell number being slightly higher than initial.

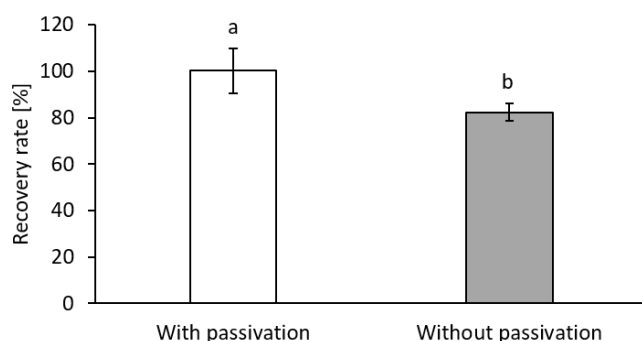


Figure 31: Cell recovery by the system with and without passivation of the channels and tubes with 1x PBS/ 1 % BSA/ 1 mM EDTA. Without passivation, 18 % of the cells were not recovered. With passivation, recovery of 100 % was achieved. Results are given as mean values \pm SD of two biological and technical replicates. Different letters above the bars (a and b) indicate statistical significance, $p < 0.5$ (88).

Consequently, the passivation step with 1 x PBS/1 % (w/v) BSA/1 mM EDTA for 30 min was performed before each experiment to minimize the effect of cell loss by the system.

Capture rate dependent on filtration functional model design

Two different designs of the filtration functional model were used for integration of the TEM-grid and cell capture: a one-armed structure, with one channel leading to the filter and one channel leading to the outlet; and a two-armed structure with two inlet-channels and two outlet channels, twisted by 90°. The two designs are shown in Figure 32A and B.

The cell distribution on the filter was evaluated for the two filter slide designs. As shown in Figure 32C to F, cell capture and distribution on the surface was dependent on the design of the channels. On the filter with one inlet and one outlet channel, the cells were captured mainly on one side of the filter close to the inlet channel, leaving a dead zone on the filter side closer to the outlet channel (Figure 32C and E). The cells were captured on approximately 60 % of the filter area. In contrast, the design with two inlet and two outlet channels favored an even distribution of the cells over the whole filter surface (Figure 32D and F) and only a minimal dead zone was visible in the center of the filter (Figure 32F). These distribution differences were confirmed by simulation. The results of the simulation were published in (88).

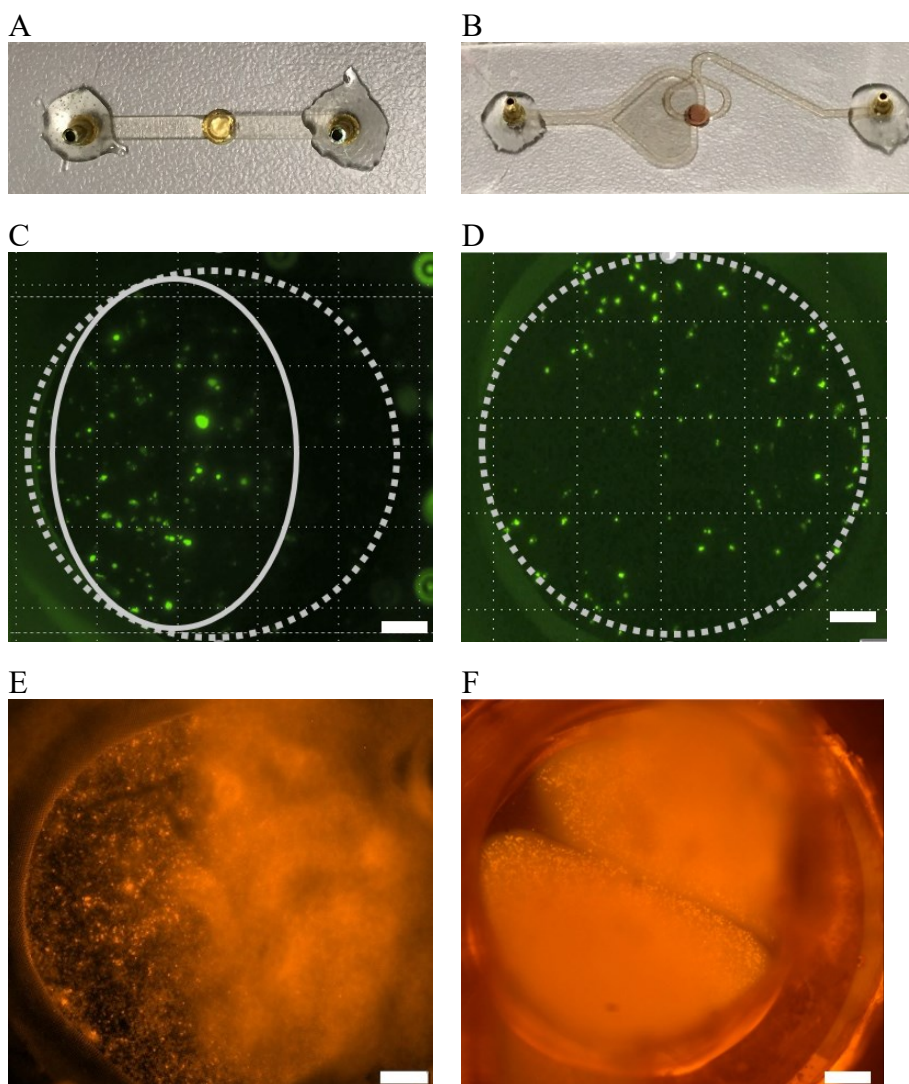


Figure 32: Images of the (A) one-armed and (B) two-armed single unit operation model for integration of a TEM-grid for cell capture.

The designs are shown as a top view photograph after fabrication and mounting of the TEM-grid, the sealing foil, and the tube connectors. C to F: Cells captured on the filter after filtration with filter slides with different channel designs. The one-armed design led to cell capture on 60 % of the filter area only (C and E), whereas the two-armed design (D and F) favored an even cell distribution on the whole filter area. Modified from (88).

The two filter slide designs were also evaluated for cell capture efficiency. Therefore, a known number of stained BT-474 cells were filtrated using the two different slides and the captured cells were counted on the filter by fluorescence microscopy after the filtration process. This revealed a capture rate of 75 % for the one-armed structure and a significantly higher capture rate of 89 % for the two-armed structure (Figure 33).

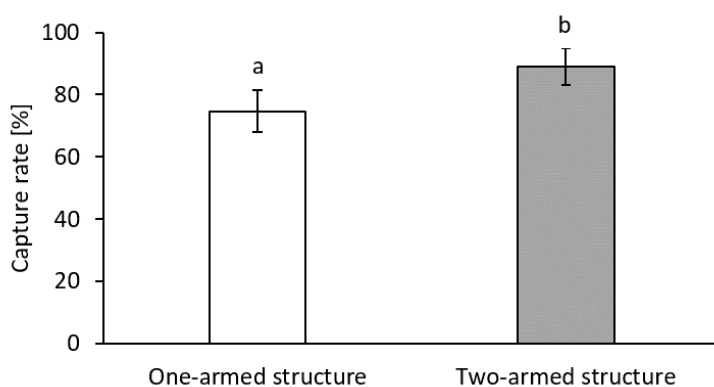


Figure 33: Comparison of cell retention rates achieved by the two different filter slide designs. With the two-armed filter slide design, a higher retention could be achieved. Results are given as mean values \pm SD of two biological and technical replicates. Different letters above the bars (a and b) indicate statistical significance, $p < 0.5$; (88).

The results led to the assumption that an even distribution of the cells on the filter favors both the optical detection and the retention of the cells on the filter and thus, the two-armed filter slide was used for all further experiments.

Cell type dependent capture rate with the passivated two-armed filtration functional model

Known numbers of stained BT-474, HCT116 and K562 cells were filtrated, and the cells captured on the filter were counted by fluorescence microscopy. The results are shown in Figure 34. The highest capture rate of $89 \% \pm 6 \%$ was achieved for the breast cancer cells BT-474. This was the cell line with the largest cell diameter of $17.4 \mu\text{m} \pm 1.5 \mu\text{m}$. As expected, the lowest capture rate of $54 \% \pm 10 \%$ was achieved for the K562 cells. As this cell line originates from the bone marrow and is cultivated in suspension, the cells were assumed to be more deformable than epithelial cells, and thus, pass the filter more easily. Their median diameter was $15.4 \mu\text{m} \pm 0.8 \mu\text{m}$. For the colorectal carcinoma cell line HCT116, a capture rate of $64 \% \pm 5 \%$ was determined. Of the cell lines evaluated, this was the cell line with the lowest diameter of $12.8 \mu\text{m} \pm 1.6 \mu\text{m}$.

However, the capture rate was higher than for the K562 cells, reinforcing the assumption that the K562 cells are retained poorly due to their increased deformability.

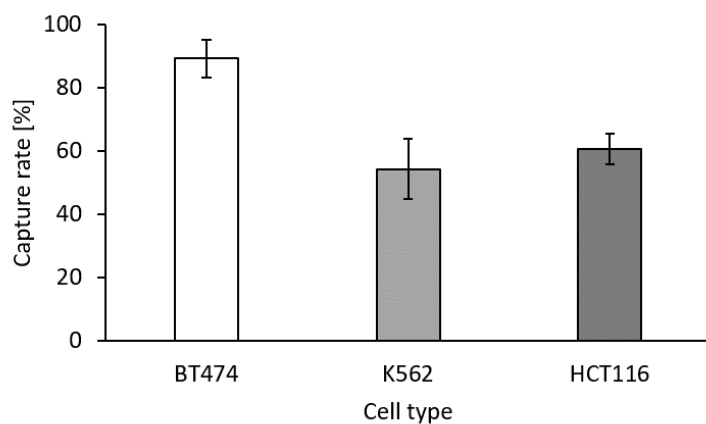


Figure 34: Comparison of the capture rate for BT-474, K562 and HCT116 filtrated using the two-armed filter slide. Results are given as mean values \pm SD of n=5 (88).

To challenge the filtration system with a cell line with small cell diameter that resembles real CTCs the most, the HCT116 cell line was used for all further filtration experiments.

Blood sample volume dependent capture rate using the two-armed filtration functional model

Known numbers of HCT116 cells were spiked into different volumes of blood to evaluate the possibility to isolate the cells from blood by filtration and the influence of the cells contained in blood on the capture rate. HCT116 cells in PBS without blood and spiked into 40 μL and 200 μL of whole blood were filtrated at 2 $\mu\text{L}/\text{s}$. The capture rates are given in Figure 35.

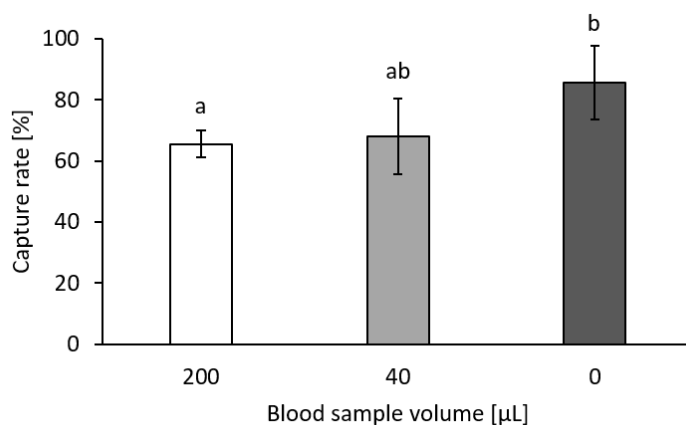


Figure 35: Capture rates of HCT116 cells without blood and spiked into 40 μL and 200 μL of whole blood. Results are given as mean values \pm SD of $n=5$. The different letters above the bars (a and b) indicate statistical significance, $p < 0.5$; (88).

The highest capture rate of 85 % \pm 12 % was achieved for HCT116 cells filtered without the presence of blood. Presumably, the presence of blood cells increased the pressure difference on the filter, leading to cell loss. However, there was no significant difference between the capture rate of 68 % \pm 12 % for a volume of 40 μL blood and a capture rate of 66 % \pm 4 % for 200 μL whole blood. Thus, it was possible to apply the higher blood volume of 200 μL for CTC isolation, generally increasing the probability to effectively isolate these rare cells.

Cell number dependent capture rate using the two-armed filtration functional model

Capture rates for several spike-in concentrations were evaluated ranging from 10 cells to 5000 HCT116 cells per sample of 200 μL blood. As shown in Figure 36, no significant difference was observed regarding the capture rate of different cell spike numbers in a range of realistically expected CTC numbers in patient samples. The cell capture rate determined was 60 % \pm 14 % with

a correlation coefficient of 0.95 leading to the assumption that the CTC count course could be evaluated despite the cell loss as the proportion of cells captured is constant.

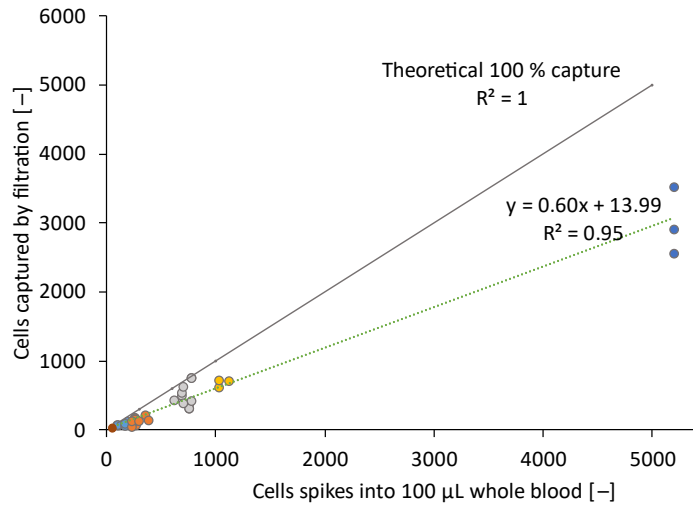


Figure 36: Different cell numbers spiked into 200 µL blood for evaluation of the blood volume dependent capture rate. Results are given as mean values \pm SD of at least $n=3$; (88).

Filtration of patient samples using the two-armed filtration functional model

Exemplary patient samples in which at least 300 CTCs per mL were detected by the maintrac® method as described in chapter 2.2.3 were subjected to filtration using the filtration functional model. Three samples of each patient sample were filtered, and the captured cells were quantified. There were $70\% \pm 10\%$ of the EpCAM-positive cells of BO408-3 captured, $68\% \pm 19\%$ of the cells of BO408-4 and $75\% \pm 5\%$ of the cells of BO572-4 were captured. Thus, on average $70\% \pm 13\%$ of the EpCAM positive cells detected in patient samples by the maintrac® method were captured and detected on the TEM-grid after filtration. These results are shown in Figure 37.

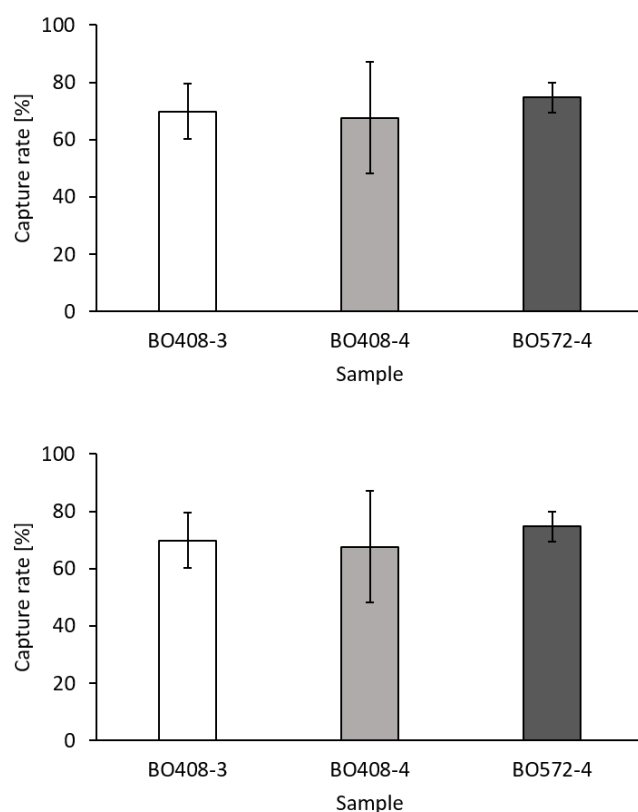


Figure 37: CTC capture rates after TEM-grid filtration of patient blood samples.

The number of cells captured was compared to the number of cells detected by the maintrac® method as reference. Samples were analyzed in triplicates. Results are given as mean values \pm SD of $n=2$.

The capture rates were comparable to the capture rates obtained for samples spiked with HCT116 cells (as shown in Figure 34), where on average $64\% \pm 5\%$ could be captured. It was therefore

assumed that the HCT116 as colorectal cancer cell line represented the size and deformability of real CTCs from colorectal and gastrointestinal tumor patients well. Thus, the HCT116 cell line was regarded as a suitable cell model for further experiments with model samples representing a cell line with similar cell diameter as colorectal patients' CTCs, uniform EpCAM expression and comparable deformability as patients' CTCs.

Flow rate and flow profile dependent capture rate

The influence of different flow rates and profiles on the cell capture efficiency was evaluated to estimate the possibility for on-chip cell capture. First, cell capture at different flow rates was analyzed. Additionally, two different flow profiles available on the Vivalytic cartridge were mimicked with the syringe pump (shown in chapter 2.3.1.3) and cell capture rates were compared to continuous flow: firstly, a flow profile as realized by peristaltic pumping using valves on the cartridge and secondly, a flow profile realized using pump chambers on the cartridge further on called pump chamber pumping.

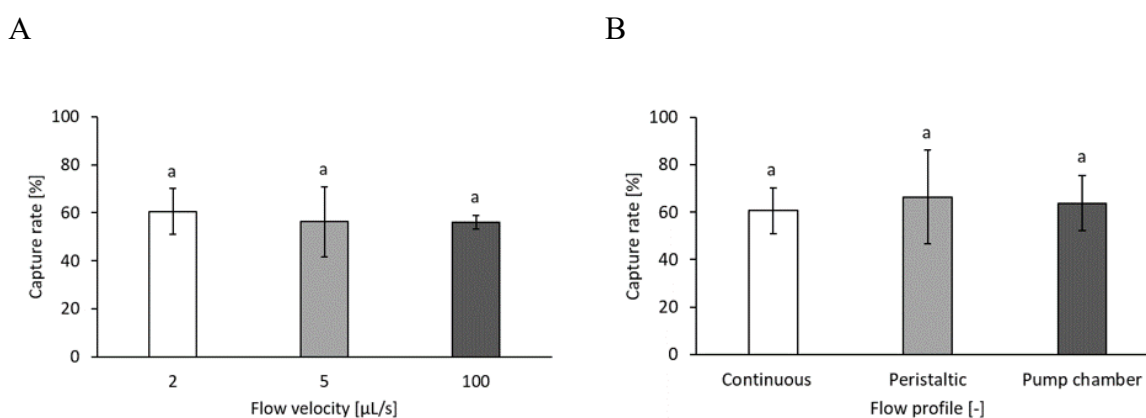


Figure 38: Influence of flow rate and flow profile on cell filtration.

A: Capture rates of HCT116 cells filtered at different flow rates. B: Comparison of the capture rate achieved by continuous flow and by mimicking flow profiles that can be realized on the Vivalytic cartridge. Results are given as mean values \pm SD of $n=9$. The letters above the bars (a) indicate that no statistical significance was determined, $p < 0.5$.

As shown in Figure 38, neither the different flow rates (A) nor the flow profiles (B) had a significant influence on the HCT116 cell capture rate. The mean capture rate was $64 \% \pm 13 \%$ without significant differences between the different flow rates and profiles.

Therefore it was assumed that filtration was independent of a constant flow rate, cell spike number and blood volumes up to 200 μL and was suitable for integration into a membrane-driven microfluidic system with pulsatile or peristaltic flow.

3.2.4.3. Real-time detection for CTC quantification and evaluation of cell detection

During filtration experiments described in chapter 3.2.4.2, it was observed that EpCAM-positive target cells were captured on the filter but passed the structure after some time, possibly due to the constant flow over the filter and increasing pressure difference. Owing to the transparency of the two-armed filtration functional model (Figure 32B), the process could be observed in real-time and videos, or time serial images could be acquired by the microscope software. This enabled quantification of cells captured until the end of the filtration process and cells captured for a short time. Thus, small CTCs that could pass the filter after some time were detected and quantification efficiency was increased. Quantification was performed either based on an endpoint image or based on serial images acquired every minute (shown in Figure 39A) by using the cellSens software with additional manual cell counting named *real-time manual* in Figure 39B. In addition, a MATLAB based cell counting script was used for cell counting in the end-point image and the serial images (Figure 39C). *Manual end-point* counting resulted in a detection rate of $64 \% \pm 3 \%$ whereas by *manual real-time* counting $84 \% \pm 4 \%$ of the spiked cells could be detected. The MATLAB based end-point counting resulted in $57 \% \pm 14 \%$ and real-time counting resulted in a detection rate of $73 \% \pm 8 \%$. Although the MATLAB based tool performed better in separating and recognizing cell clusters, the determined cell capture rate was lower than in the case of manual counting. Just as the microscope evaluation tool of the cellSens software, the MATLAB based counting was based on thresholding methods according to Otsu (89) for cell detection and segmentation. However, only the microscope evaluation tool allowed for manual correction of the cells not recognized due to changing signal to noise ratios during serial imaging. Therefore, the manual counting of cells in serial images was still more efficient. The MATLAB based tool needed further improvement. The challenges of correct cell detection resided in the heterogeneous background noise due to overlapping fluorescent spectra when samples were stained with different specific fluorescent dyes and highly different signal to noise ratios from experiment to experiment. Furthermore, the region of interest changed for each image series or video, cells could appear as clusters or air bubbles could be trapped on the filter.

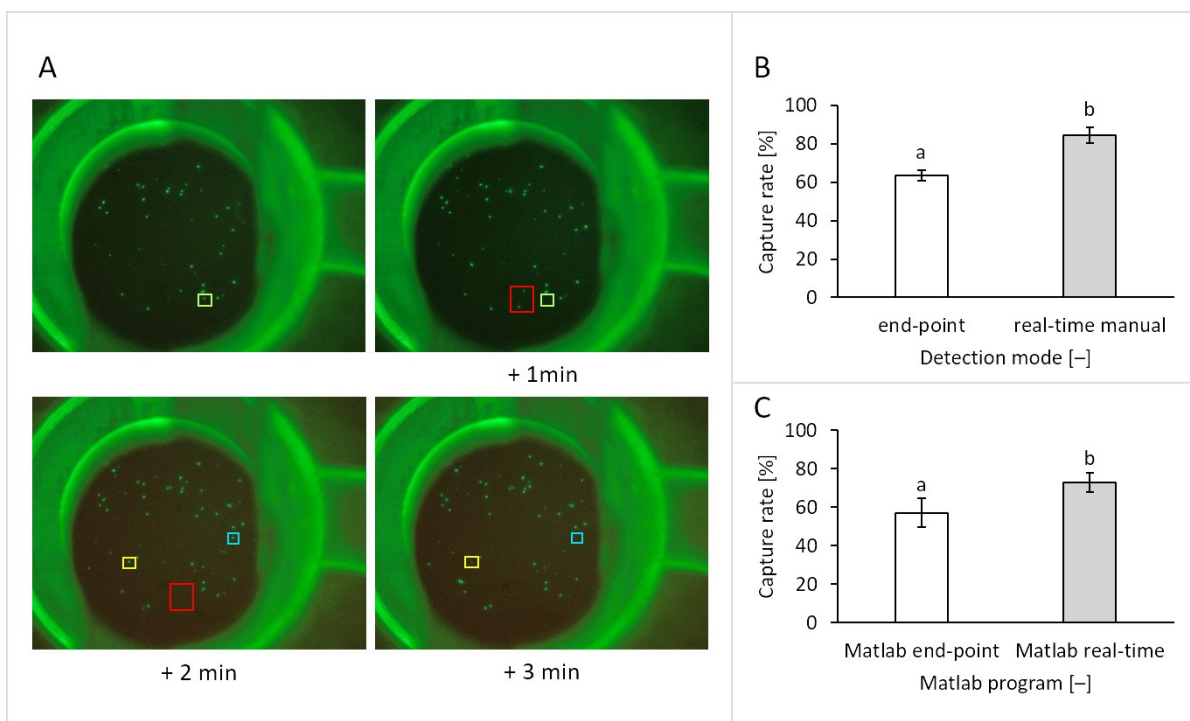


Figure 39: Comparison of endpoint and real-time cell counting on the filter.

A: serial images of HCT116 cells arriving on the filter. The colored squares mark cells that are not detected in the next frame. B: Cells were counted manually using the cellSens software after the filtration process and in serial images acquired every minute during the filtration process. C: Endpoint and real-time counting were performed automatically using a MATLAB based tool applied to the endpoint image and the serial images. Results are given as mean values \pm SD of $n=5$. Different letters above the bars (a) indicate statistical significance with $p < 0.5$; (88).

For complete automation of the cell detection process, machine learning tools were evaluated for real-time counting of the cells captured on the filter. This aimed at enabling integration of automated cell recognition and counting into the Vivalytic system. A Python based convolutional neural network was established and used for the detection and segmentation of cells in fluorescence microscopy images. The first steps were the same as in the standard microscope software: an ROI was identified, and the background was subtracted. Then, specialized algorithms e.g., for detecting star-convex polygons were adapted by using data available from literature for training of the networks. Each cell that appeared in the ROI was tagged and tracked throughout all frames of the video. Thereby, different situations were possible: an ‘enter’ when a cell appeared for the first time, an ‘exit’ when a cell passed through the filter, a ‘miss’ for a cell that was detected in some frames but not in others, and a ‘track’ for a cell that was recognized in all frames. This is schematically depicted in Figure 40.

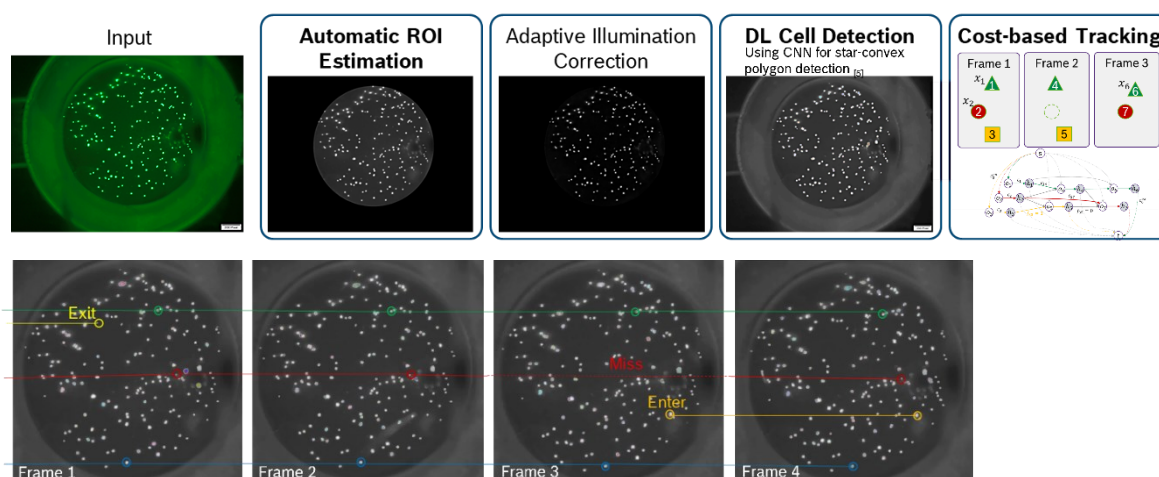


Figure 40: Schematic overview of the object detection pipeline applied for cell tracking in videos of the filtration process. Each cell was tagged upon an ‘enter’ event and tracked until the ‘exit’. Cells that were tracked in several frames but not detected in one frame in between, were labeled as a ‘miss’.

In this study, a method for automatic real-time detection and tracking of CTCs in sequences of fluorescent microscopy images was established. The qualitative performance of the algorithm was demonstrated on several experiments using the filtration functional model for CTC capture. The results are shown in Figure 41. In the videos of the cell filtration process, fluorescent target cells were detected and marked with a certain color (as shown in Figure 41A). The color for each cell was depicted in a diagram shown in Figure 41B and the location on the filter was plotted by their x,y -position. The period in which a cell was kept back on the filter was plotted on the z -axis and depicted as a colored line. The longer the colored line, the longer the period a cell was retained on the filter. For quantitative evaluation of the algorithm, the cell counts as determined by counting of the object in the last frame of a video versus counting the objects in real-time throughout the video were compared. By cell-tracking and real-time counting, between 5 % and 50 % more cells were detected than by counting the cells that were present on the filter in the last frame. On average, in the given example videos, only $70 \% \pm 20 \%$ of the initially spiked cells were detected using the last frame, whereas $92 \% \pm 7 \%$ of the cells were detected by tracking resulting in the detection of significantly more cells observed by real-time detection. The established method increased quantification precision compared to end-point detection of the cells on the filter.

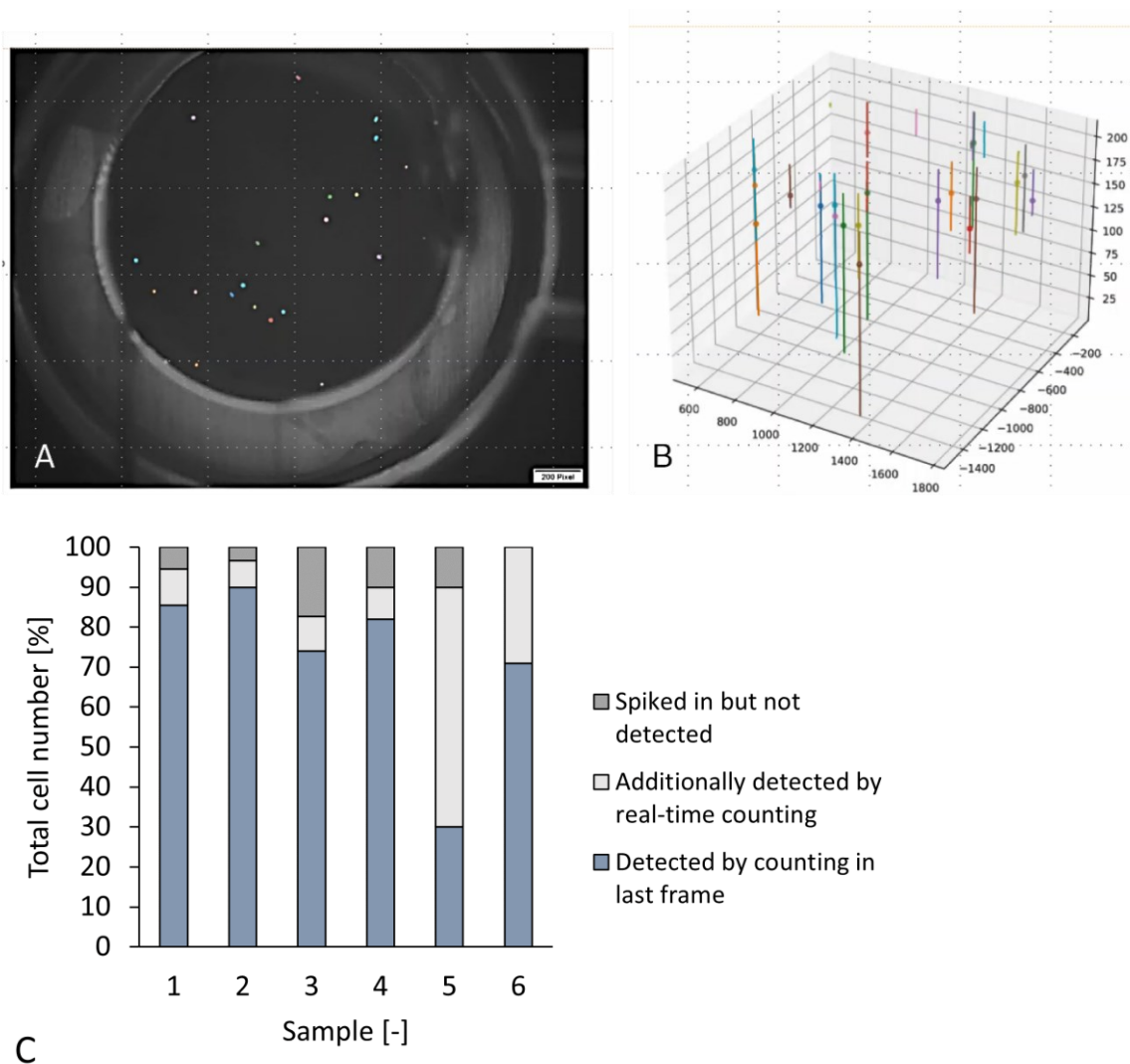


Figure 41: Automated cell counting in images and videos.

(A) Detection of cells captured and passing the filter in a video acquired during the filtration process using the fluorescence microscope. (B) Cell detections plotted by their x-y-positions as detected on the filter represented by the colored dots. The colored lines represent the time-resolved tracking/ number of frames in which a cell is detected (z-axis). (C) Number of target cells present in the blood sample as detected by endpoint vs. real-time detection. The total number of spiked cells was set to 100 %.

Taken together, the filtration set-up presented in this study provides a system for isolation and simultaneous counting of viable CTCs present in blood samples. Keeping in mind that the absolute number of CTCs in the bloodstream is important for therapy monitoring and that the phenotype of the CTCs (size, deformability) might change under therapy, this method improves reproducibility at each time point during serial assessment of the CTC count.

3.2.4.4. Leukocyte depletion for background reduction and increased sample purity

Besides high capture efficiency, sample purity and depletion of non-target cells are often evaluated in CTC isolation methods, because the isolated cells can be used for further analysis on molecular level such as expression analysis or mutation detection. Thereby, high numbers of non-target cells such as leukocytes would decrease sensitivity. It was shown that the described filtration method was suitable for removal of lysed erythrocytes. Additionally, the leukocytes that could pass the filter during filtration were quantified to determine the proportion of leukocytes contaminating the fraction of CTCs captured. These leukocytes might influence further molecular analysis by lowering their sensitivity. Blood samples of 20 μL and 40 μL were first stained with anti-CD45-PE and Hoechst33342 as described in chapter 2.2.2.3 for visualization of the leukocytes and afterwards the erythrocytes were selectively lysed. The samples were filtrated using the two-armed filtration functional model and the leukocytes captured were counted after filtration (as described in chapter 2.3.1.3). The leukocyte count of the samples was estimated from the average leukocyte count of a healthy adult (4,000/ μL to 11,000/ μL) resulting in about 150,000 leukocytes in 20 μL and about 300,000 in 40 μL blood. After filtration of 20 μL samples (n=2), 8,041 and 10,868 leukocytes could be detected on the filter. After filtration of 40 μL blood (n=2), 18,535 and 25,960 leukocytes were captured. This amounted to a depletion rate of 93 % \pm 1.4 %. However, the sum of the leukocyte counted in the filter and in the waste did not add up to the expected leukocyte count that was assumed from the average number of 7500 leukocytes in one microliter of human blood. The number can however vary between 4000 and 11000 and the exact leukocyte count of the anonymized, voluntary donor was not known. Therefore, the value for the depletion rate must be considered as an approximate value. Figure 42 shows leukocytes of 40 μL blood stained with Hoechst33342 as detected on the filter after the filtration process. The leukocytes were captured separately on one pore per leukocyte but there were still empty pores available. During filtration, leukocytes passed the filter, and the filter was at no point during the filtration completely covered by leukocytes.

A

B

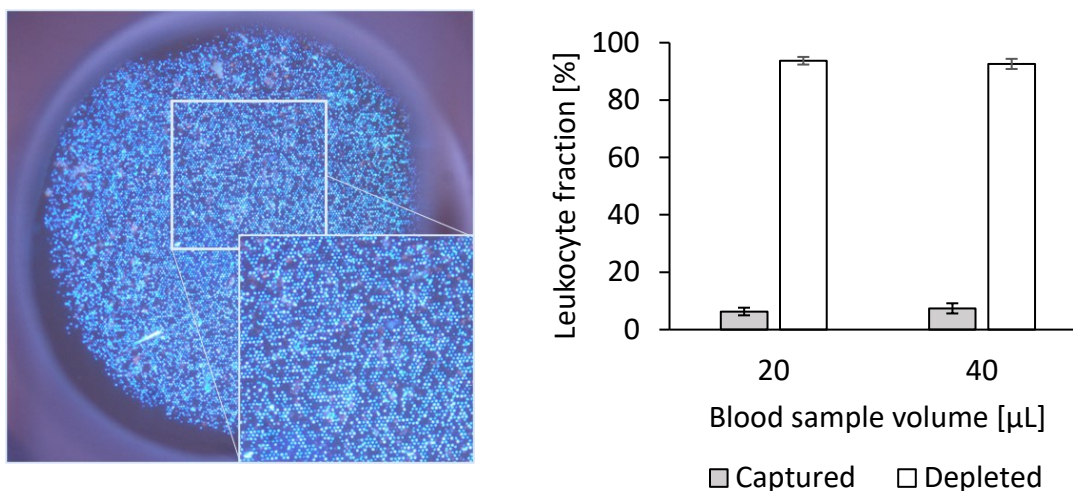


Figure 42: Leukocyte depletion by filtration of blood using the TEM-grid two-armed filtration functional model. Blood samples of 20 µL or 40 µL were treated with ELB and the resulting lysed blood sample was drawn over the filter at a flow rate of 2 µL/s. After two washing steps with 200 µL PBS, the number of leukocytes captured on the filter counted with the cellSens Dimension *Count and Measure* tool. A: leukocytes stained with Hoechst3342 captured on the filter. B: leukocyte capture and depletion rate after filtration of 20 µL and 40 µL blood. Experiments were performed in biological and technical replicates, n=2.

Additionally, the leukocyte depletion rate was determined by RT-qPCR as described in chapter 2.4.3.2. Therefore, the leukocytes captured on the filter, as well as the leukocytes in the waste fraction were lysed separately, and the lysates were used as template for RT-qPCR with GAPDH as target gene. These samples were compared to lysates from leukocytes included in 40 µL of blood. As shown in Figure 43, in the first experiment, a difference of 7 cycles was determined between the control (Ct 25.8) and the filter lysate (Ct 32.9). In the second experiment, 10 cycles were determined between the control (Ct 25.3) and the filter lysate (Ct 35.9). From the difference in the CT values, depletion rates of > 93 % were estimated.

A		B			
Sample	Ct	ΔCt	Δ log level	Depletion [%]	
Control 1	25.8	7 ± 2	2.1	~97 ± 2	
Filter 1	32.9				
Control 2	25.3	10 ± 2	3.2	~98 ± 1	
Filter 2	35.9				

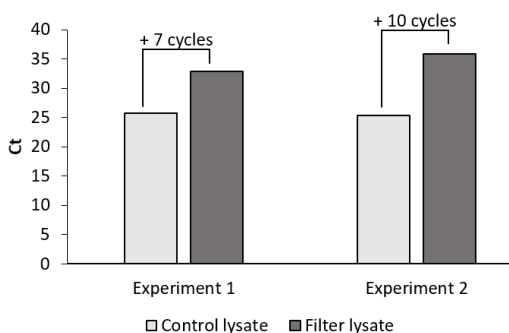


Figure 43: Leukocyte depletion determined by RT-qPCR with the target GAPDH.

Leukocyte lysates of 40 μ L blood were used as control lysates for comparison to the lysates generated from the leukocytes captured on the filter. The reduction in the GAPDH amount was regarded as depletion rate given in %. (A) Ct values of GAPDH detected in the control lysates and the filter lysates with the increase in cycles. (B) Calculation of the depletion rate from the Ct difference of the control lysate and the filter lysate; 3.3 cycles difference represent a change of approximately one log-stage at 100 % of RT-qPCR efficiency.

It was assumed that the filter was not clogged completely at any time of the filtration with the applied blood sample volume, due to microscopic evaluation of the pores on the filter. Furthermore, high depletion of leukocytes resulted in higher purity of the isolated CTC fraction and thus in a probable lower background for molecular analysis.

3.2.4.5. ESEM analysis of the cells captured on the filter

The TEM-grid was analyzed by ESEM after the filtration process of either cell lines HCT116 only or cell line spiked blood samples to better understand the process of cell capture on the filter. First, HCT116 cells in PBS were filtered using the two-armed filtration functional model (as described in chapter 2.3.1.3) and the filter was analyzed by ESEM afterwards without further preparation. Figure 44 shows the cells captured on the filter. The cells were either captured inside of the pores adhered to the surface or were captured on the surface of the pores. It was theorized that smaller and more deformable cells could pass the pore or got stuck inside it, while larger and less deformable cells were captured on the surface.

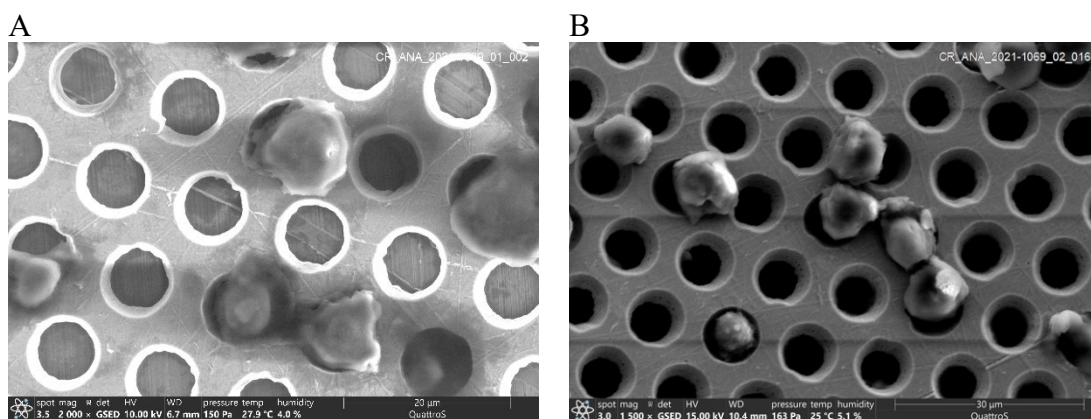


Figure 44: ESEM analysis of HCT116 cells filtered using the two-armed filtration functional model. The filter was analyzed directly after filtration without fixation or drying. Images were acquired at A: 2,000 and B: 1,500-fold magnification.

Filtration of blood samples have shown that more than 93 % of the leukocytes pass the filter (Chapter 3.2.4.4). For better understanding of the target cell and leukocyte capture, a spiked blood sample was filtered using the two armed-filtration functional model and analyzed by ESEM. In this case, the cells captured on the filter were fixed, dehydrated, and dried prior to analysis to maintain the exact localization of the cells after filtration. The fixation solution was pumped through the filter using the syringe pump right after the sample was filtered without additional washing step. Due to this, not only the cells but also the remaining hemoglobin in the system was crosslinked and the filter was clogged instantly. Consequently, the cover foil of the two-armed filtration functional model was removed after the fixation step and the dehydration was performed by incubating the slide in the alcohol series according to chapter 2.2.2.3. As shown in Figure 45, cells were stuck in most of the pores while some cells were located on the surface of the filter or on top of pores.

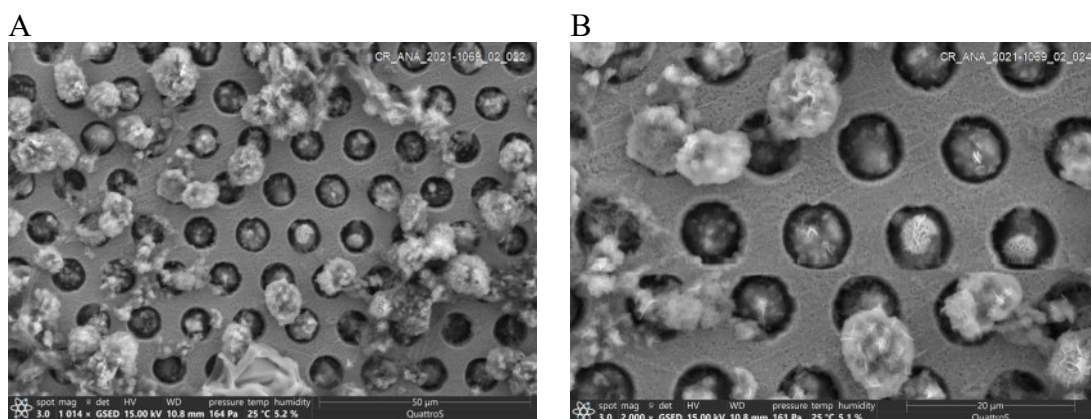


Figure 45: ESEM analysis of blood spiked with HCT116 captured on the TEM-grid. After filtration, the cells were fixed with 2.5 % (v/v) glutaraldehyde and dehydrated in an ethanol series prior to air drying. Images were acquired at 1,014-fold and 2,000-fold magnification.

Possibly, leukocytes that were deformable or small enough to pass the filter during the washing steps in the previous experiments as described in chapter 3.2.4.4 were retained inside the pores due to fixation without a washing step. Larger cells like the HCT116 cells or large leukocytes like monocytes, were captured on the surface of the filter. As shown in chapter 3.2.4.2, similar capture rates were determined for the HCT116 cell line and the patients' CTCs. From these results, it was assumed that the CTCs would be captured on the surface of the filter as seen in Figure 45 for the HCT116 cells.

3.3. Integration of the CTC detection method into the LoC

The microfluidic unit operations and the filter element that were evaluated using the two-armed filtration functional models were integrated into the Vivalytic cartridge for an on-chip proof-of-principle. First, the microfluidic transport of cells in the system was examined in general without isolation or capture of the cells to evaluate the influence of the shear stress on cell viability and channel geometry on cell recovery. In the next step, the filter element was integrated at a location suitable for optical detection using the fluorescence microscope after processing in the analyzer prototype. Hereby, the cell capture rate by the filter on the cartridge was determined. As a last step, the optical detection of the cells in the Vivalytic analyzer was evaluated to define requirements for an improved optical system.

3.3.1. Influence of the forces inside the microfluidic system on the cells

The Vivalytic system was established for and is used for molecular diagnostic assays. Thus, the implemented unit operations were so far optimized for the microfluidic transport of nucleic acids containing liquids rather than for the transport and processing of intact human cells. Therefore, established protocols were evaluated in regard of the processibility of cells and the influence of the forces inside of the microfluidic network on the cells.

Influence of the operating temperature on cell viability

The operation temperature of the Vivalytic analyzer is specified to be at least 40 °C whenever the heaters are turned off. Human body temperature and optimal cell cultivation temperature is 37 °C. The *CellTiter Glo assay* was used to evaluate the HTC116 cell viability at 40 °C and to determine the time span in which the cells survive this elevated temperature. As shown in Figure 46, after 15, 30 and 60 min at 40 °C viability decreased to 91 % ± 5 %, 87 % ± 7 % and 82 % ± 9 % respectively. However, in summary the elevated temperature had no significant influence on the cells.

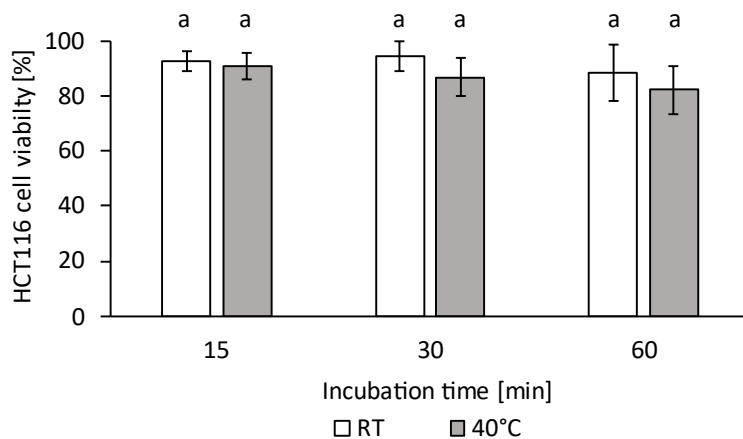


Figure 46: Viability of HCT116 cells after 15 min, 30 min and 60 min incubation at 40°C. Analyses were performed in triplicates; results are given as means ± SD of biological and technical triplicates. The letters above the bars (a) indicate that no statistical significance was determined, $p < 0.5$.

Influence of the material and forces in the microfluidic system on cell viability and recovery

Fluid samples can be transported in the microfluidic system using different pump mechanisms and different paths on the cartridge. Two paths suitable for mixing of the suspension and transport of the cell line samples from the mix through the filter chamber back into the mix chamber were defined to evaluate the influence of the microfluidic transport itself without capture of the cells. The cell suspensions were circulated for 20 or 200 cycles at 1 Hz using the pump chamber P1 for a short path (Figure 47A) or pump chamber P1 and PCRmm2 for a long path (Figure 47B) on the cartridge to determine the influence on the cell viability and number. The protocol for the short path with 200 cycles was evaluated at 0.5 Hz, 1 Hz and 2 Hz.

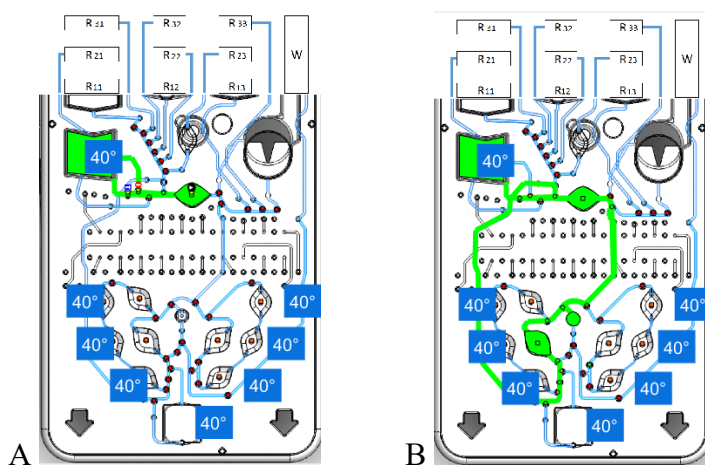


Figure 47: Fluidic paths for transport of cells on the cartridge and evaluation of the influence on cell viability. (A) short path, (B) long path.

To examine where the cells are retained in the system, stained cells were transported through the microfluidic channels using the long path and the cartridge was optically examined by fluorescence microscopy. Figure 48 shows microscopic images of different channels of the cartridge after the cell suspension was transported into the channels without subsequent washing of the channels.

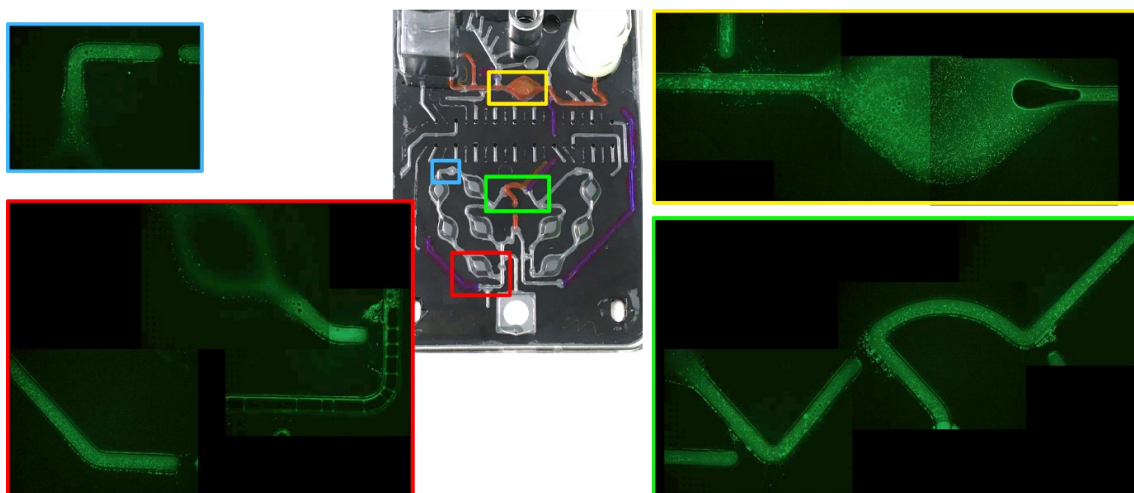


Figure 48: CFSE stained HCT116 cells in the microfluidic channels of a Vivalytic cartridge. The different positions on the cartridge are visualized by the colored squares. Images were acquired at 25-fold magnification.

It was observed that cells got stuck between the polycarbonate and the TPU membrane. This might lead to loss of target cells and was therefore quantified by transport of HCT116 cells using the different protocols described before and quantification of the cells extracted from the waste chamber after processing. A BT-474 suspension with a concentration of $2.3 \times 10^5 \pm 0.5 \times 10^5$ cells was transported on the cartridge. After 20 and 200 cycles in the long path at 1 Hz, only 59 % and 40 % of the BT-474 cells could be recovered. Transport in the short path for 20 cycles and 1 Hz and 200 cycles at 2 Hz resulted in the highest recovery of 91 % and 93 %. After 200 cycles at 1 Hz and 0.5 Hz, 83 % of the BT-474 cells were recovered. In the case of the HCT116 cells, the highest cell recovery of 95 % and 97 % cells was achieved by the long and short path for 20 cycles at 1 Hz. The lowest recovery of 70 % and 77 % was achieved by the long path for 200 cycles at 1 Hz and short path for 200 cycles at 0.5 Hz. Probably because these were the two protocols with the longest residence time of the cells in the channels. At 1 Hz, 78 % and at 2 Hz 81 % of the cells were recovered.

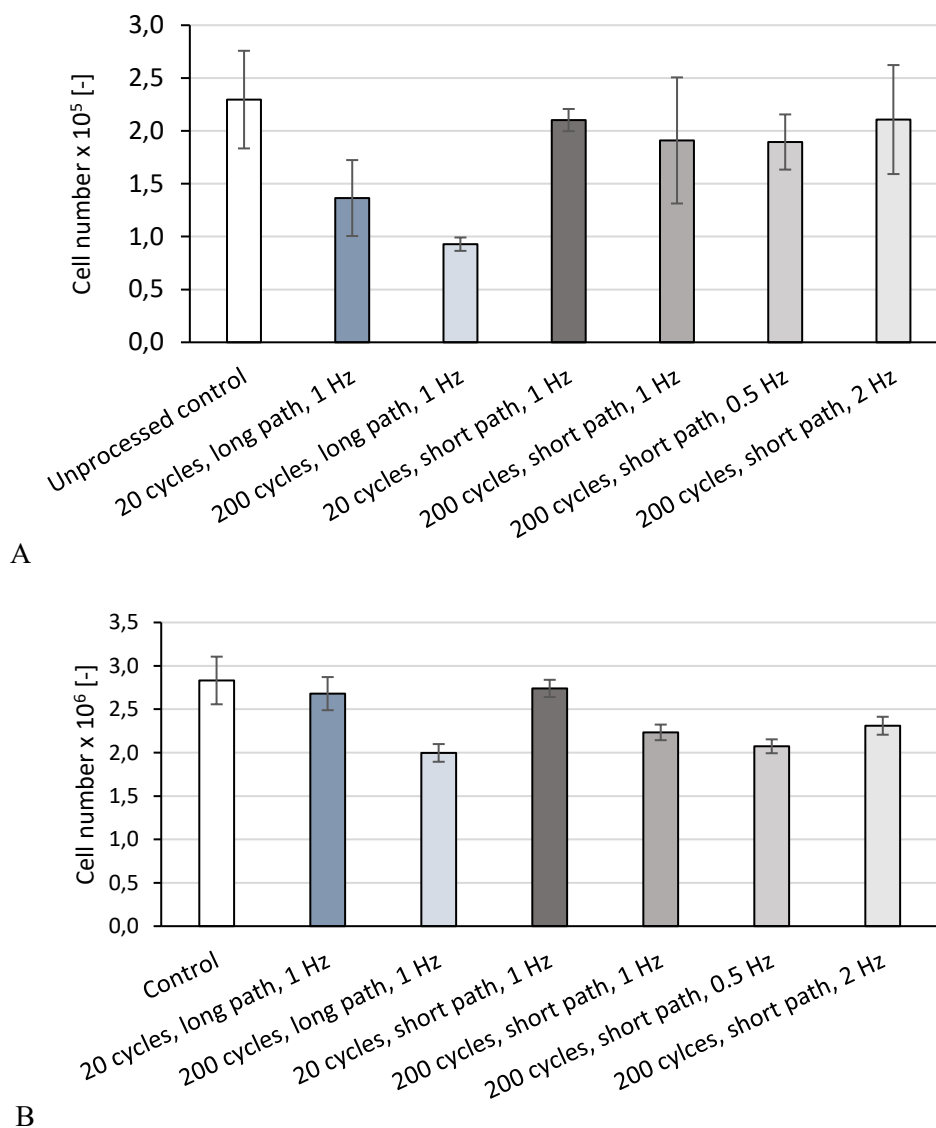


Figure 49: Quantification of cells after microfluidic transport.

A: BT-474 and B: HCT116 extracted from the waste chamber of the cartridge after processing using different microfluidic protocols. The results are given as means \pm SD of biological and technical triplicates.

The viability of the cells was assessed by trypan blue exclusion as described in chapter 2.2.2.2. An unprocessed cell suspension of the same cell line was used as viability control sample. The results are shown in Figure 50. The effect on cell viability was higher in the case of the BT-474 cells than in the case of the HCT116 cells. One reason could be the larger cell diameter of the BT-474 cells. The smaller HCT116 cells might be transported through the channels more easily and shear stress could be smaller. The impact on cell viability was higher when the short path was used, and viability further decreased with increasing cycle number and pump rate. Viability was best

preserved using the protocol for the long path and decreased by 10 % after the 20 cycles protocol and by 19 % after the 200 cycles protocol in case of the BT-474 cells and by 8 % and 17 % in case of the HCT116 cells. BT-474 cell viability was reduced by 21 % after 20 cycles at 1 Hz, by 25 % after 200 cycles at 1 Hz, by 19 % after 200 cycles at 0.5 Hz and by 31 % after 200 cycles at 2 Hz by the short paths, whereas HCT116 cell viability was reduced by 12 %, 24 %, 7,4 % and 28 % by the same protocols.

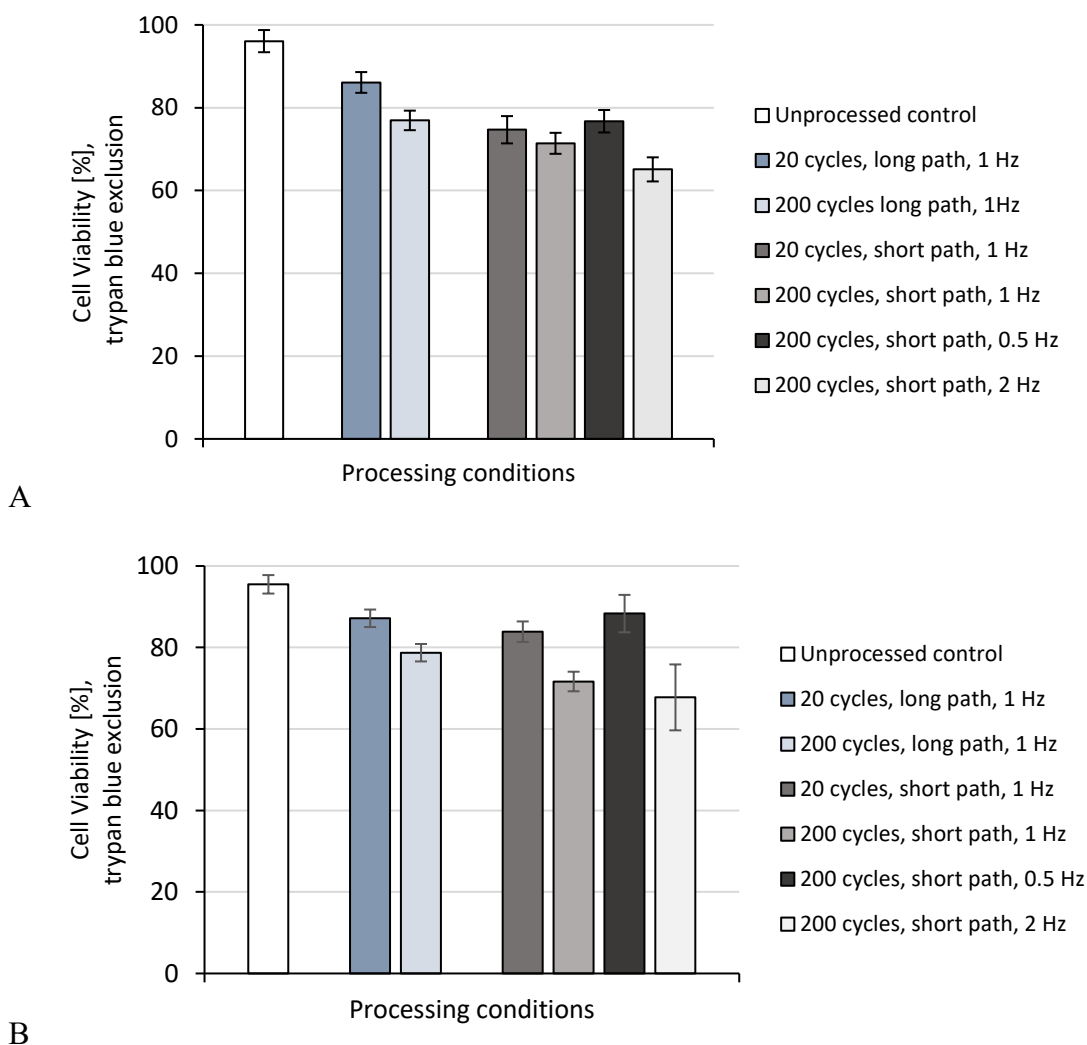


Figure 50: Cell viability after on-chip processing using different paths, cycle numbers and pump rates. A: BT-474 cells, B: HCT116 cells. The results are given as means \pm SD of biological and technical triplicates.

In summary, recovery of both cell types was highest using the short paths. However, cell viability was best preserved using a long path at pump rate of 1 Hz or a short path at reduced pump rate

whereas the impairment on the viability was higher in case of the short paths with 1 Hz or 2 Hz pump rate. As cell viability is an important characteristic determined according to the maintrac® method, the paths that preserve cell viability were preferred to the paths with the highest recovery in terms of cell numbers. The latter might be optimized by passivation of the microfluidic channels or adaptation of the channel geometry to prevent cell loss.

In the next step, different pump mechanisms possible for cell transport over the filter using long paths on the cartridge were compared in regard of their effect on the cell viability: the pump chamber pumping and peristaltic pumping using valves. The paths on the cartridge are shown in Figure 51. The path for the transport using the pump chamber above the filter is shown in Figure 51A and Figure 51B shows the path for the peristaltic transport using valves or the transport by suction using the pump chamber beneath the filter. For determination of the effect on the cell viability, no filter was integrated into the cartridge. The cells were transported into the waste chamber from which an aliquot was analyzed by trypan blue exclusion as described in chapter 2.2.2.2. Figure 51C shows the results of the viability determination.

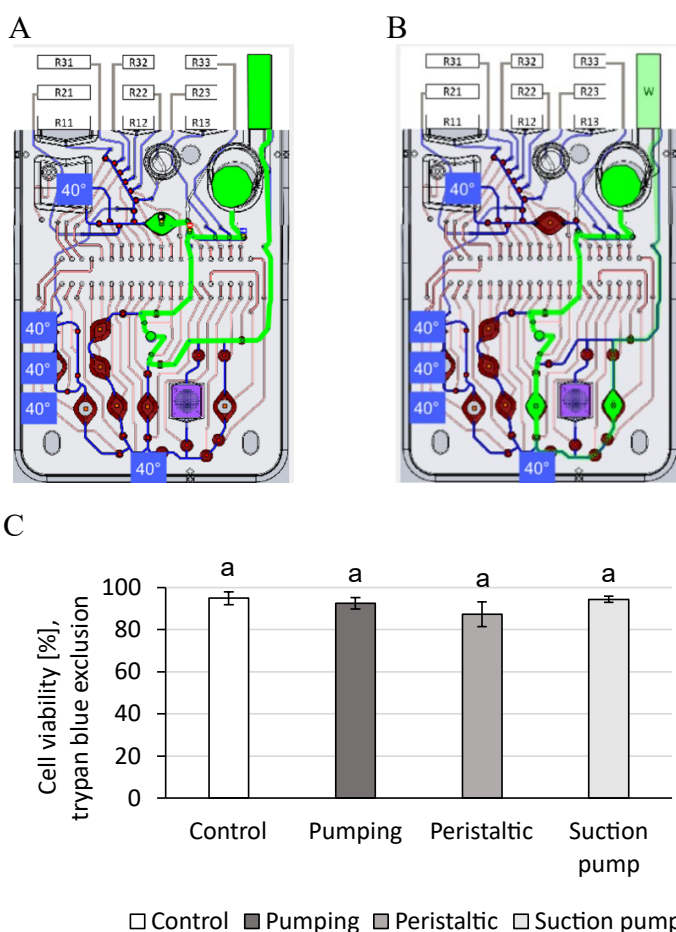


Figure 51: Determination of cell viability after transport of cells through the filter chamber on the cartridge without integrated filter.

(A) shows the path for the transport by pumping using the pump chamber above the filter. (B) shows the paths for transport by peristaltic pumping and suction with the pump chamber beneath the filter. (C) shows the results for the viability determination by trypan blue exclusion. The results are given as means \pm SD of biological and technical triplicates. The letters above the bars (a) indicate that no statistical significance was determined, $p < 0.5$.

Active pumping using the pump chamber above the filter, and passive pumping by suction using the pump chamber beneath the filter had the lowest impact on cell viability. Whereas 95 % \pm 3 % of the cells in the unprocessed control were viable, the cells after transport by pumping and suction showed a viability of 93 % \pm 3 % and 94 % \pm 2 %, which correspond to a reduction by 6 % \pm 7 % and 5 % \pm 8 %. Peristaltic pumping resulted in the highest reduction of cell viability to 87 % \pm 6 %. Also, the standard deviation was the highest for the peristaltic transport using valves. Probably cells were damaged in between the flexible TPU membrane and the fluidic layer by actuation of the TPU at the valves. However, although there is a tendency towards higher cell damage by

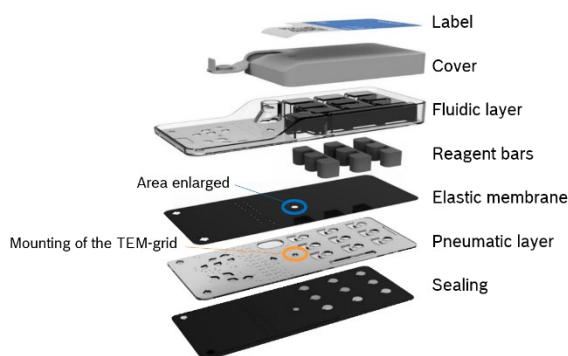
peristaltic pumping, the changes in viability were not significant for all the evaluated fluidic programs.

In summary, transport of the cells in the microfluidic environment was possible. By varying and adapting the pumping techniques, the paths and the flow rate applied the loss of cells and the influence on the cell viability could be reduced. The most favorable was the transport of the cells using the suction pumping via the pump chamber beneath the filter chamber.

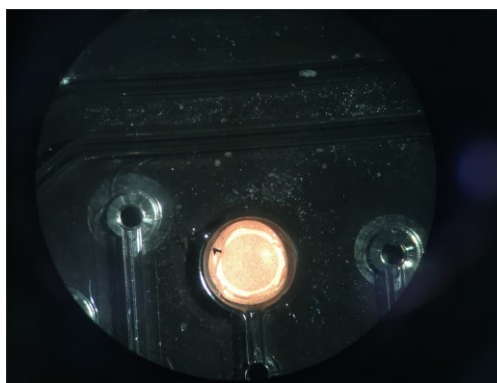
3.3.2. Cell capture by filtration in the microfluidic system (on-chip)

The dimensions of the filter chamber fitted the dimensions of the TEM-grid used in the two-armed filtration functional models and was therefore also used for a proof-of-principle of cell filtration on the current Vivalytic cartridge without the need of major modifications of the design. The TPU was enlarged in the filter area to enable optical observation of the filter. A cartridge with an integrated TEM-grid is shown in Figure 52. In Figure 52A, an explosion image of the cartridge is shown for visualization of the integration location of the TEM-grid. An image of the TEM-grid mounted into the cartridge is shown in Figure 52B and C. In Figure 52D, the integrated TEM-grid is shown as observed by microscopy after complete assembly of the cartridge. Thus, the inlet channel disturbed the clear view on the TEM-grid which was not optimal for optical detection of the cells captured by on-chip filtration. However, this set up was used for a simple proof-of-principle experiment and evaluation of the cartridge compatibility with cell processing.

A



B



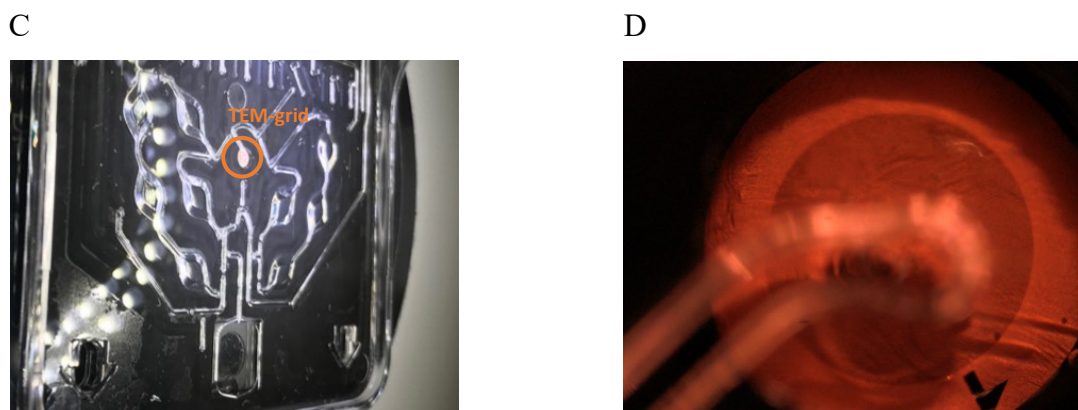


Figure 52: Vivalytic cartridge with enlarged TPU membrane and TEM-grid integrated into the filter chamber for a proof-of-principle experiment of cell filtration.

(A) Exploded view drawing of the Vivalytic cartridge composed of different layers with the enlarged area in the TPU membrane and the location of the TEM-grid, (B) top view of the TEM-grid mounted into the cartridge, (C) image of the fluidic network of the cartridge with integrated TEM-grid, (D) microscopic image of the TEM-grid integrated to the cartridge, 10-fold magnification.

A HCT116 cell suspension was transferred into the cartridge and transported onto the integrated TEM-grid using the Vivalytic analyzer. After filtration, the cartridge was removed and analyzed by fluorescence microscopy. Thereby, the filter was optically evaluated as well as the channels leading to the filter and the channel behind the filter to determine whether cells could pass the filter. As shown in Figure 53, cells were captured on the TEM-grid, and many cells could be detected in the inlet channel (Figure 53A) whereas only a few cells were detected behind the filter (Figure 53C). Consequently, to ensure that all cells are transported onto the filter, one or more washing steps with 1 x PBS/1 % (w/v) BSA/1 mM EDTA were included into the on-chip protocol.

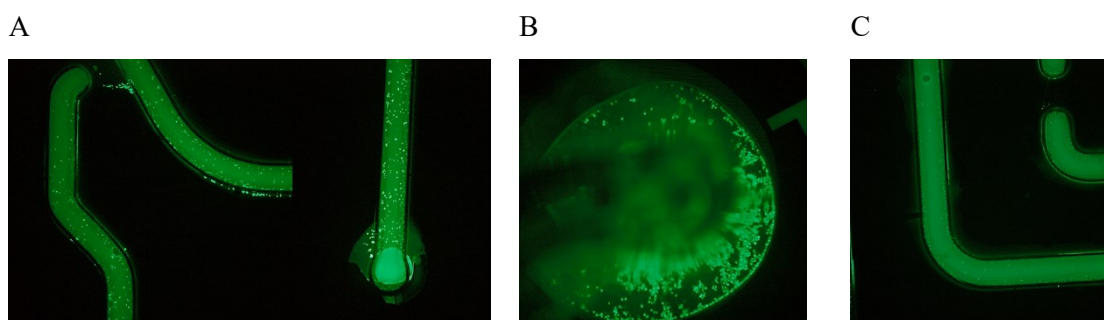


Figure 53: CFSE stained HCT116 cells filtered on-chip.

A: channels in front of the filter, B: Cells captured on the filter, C: channels behind the filter. 2.5-fold magnification, 200 ms illumination.

For quantitative evaluation of the on-chip filtration, HCT116 cell suspensions with defined cell numbers were transferred into the sample chamber of the Vivalytic cartridge and processed using

the Vivalytic analyzer prototype. First, the sample was introduced from the sample chamber and transported onto the filter by peristaltic pumping. After the first cycle of pumping until the sample chamber was emptied, only $18\% \pm 11\%$ of the cells were detected on the filter (Figure 54). The sample chamber design contained a ledge at which cells could get stuck. This could be prevented by back flushing or by active resuspension of the cells via pipetting. Therefore, one volume of PBS was pipetted into the sample chamber and the remaining cells were resuspended prior to a second round of pumping that resulted in detection of $34\% \pm 9\%$ of the cells. The resuspension step was repeated and resulted in a $39\% \pm 11\%$ recovery rate. $43\% \pm 10\%$ of the cells were retained in the sample chamber despite washing. The missing $18\% \pm 20\%$ of the cells could not be detected and passed the filter or were retained inside the channels leading to the filter.

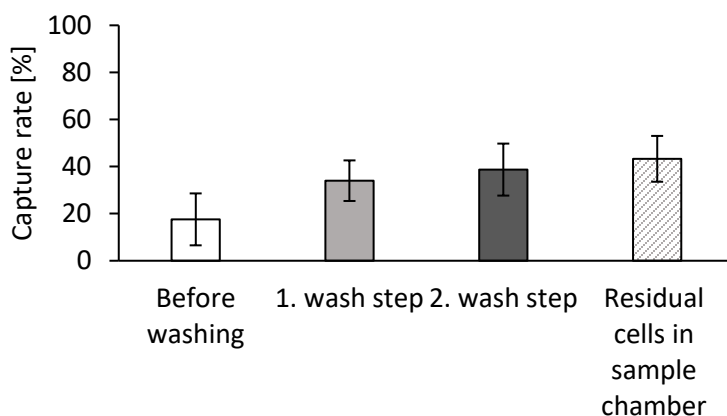


Figure 54: Cell capture on the TEM-grid integrated into the Vivalytic cartridge. After the first cycle of cell transport from the sample chamber onto the filter and after two washing steps as determined by fluorescence microscopy detection and manual counting. Additionally, the number of the residual cells in the sample chamber was determined.

To prevent the loss of cells at the ledge of the sample chamber, the cell suspension was transferred to a reagent chamber (R13) above the sample chamber without ledge, for microfluidic transport onto the filter. Different microfluidic programs, pump mechanisms and paths were compared regarding the cell capture rate on the TEM-grid: Peristaltic pumping, pump chamber pumping, and suction pumping. As shown in

Figure 55, peristaltic pumping and suction pumping resulted in the highest cell capture rates of $55\% \pm 17\%$ and $55\% \pm 7\%$, whereas pumping resulted in a capture rate of $34\% \pm 8\%$. In total, the maximal capture rate achieved after transport of the cell suspension from the reagent chamber

R13 instead of the sample chamber was higher indicating that less cells remained in the chamber R13 than in the sample chamber. This supported the assumption that the ledge in the sample chamber could be a reason for cell loss.

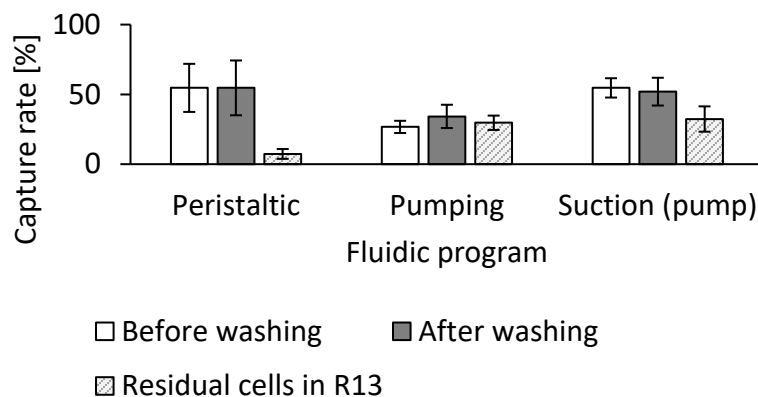


Figure 55: Number of cells captured on the TEM-grid integrated into the Vivalytic cartridge. After one cycle of transport from the reagent chamber onto the filter, one washing step, and residual cells in *the reagent chamber* as determined by fluorescence microscopy detection with manual counting. Results are given as mean values \pm SD of three individual experiments.

In summary, cell capture rates on the Vivalytic cartridge adapted for cell detection were lower and the variations were higher than the capture rates achieved using the two-armed filtration functional model. A major reason could be the limited view onto the filter on the cartridge due to the channel leading to the filter chamber. Approximately one third of the TEM-grid was covered by the channel. Furthermore, the cartridge needed to be removed from the analyzer prototype for optical evaluation using the fluorescence microscope. Due to this, the TPU membrane of the cartridge was relaxed, and all chambers and valves were opened leading to dispersion of the sample into the surrounding channels.

3.3.3. Optical cell detection using the Vivalytic analyzer

Differentiation of CTCs from leukocytes and evaluation of the cells regarding viability, integrity and target antigen expression was evaluated by fluorescence cytochemistry. A cell-detection system requires a light source for excitation, respective filters for the desired fluorescent dyes and a detection system, such as a camera. All these components were already integrated into the Vivalytic analyzer. However, the system was established for fluorescence readout of qPCR assays via intensity measurement using a whole chamber on the cartridge. In this study, the possibility to

detect stained cells in the existing system was evaluated and characterized using model samples. Therefore, cells were transferred into a cell counting slide (Olympus, Shinjuku, Japan) that was placed on a 3D printed slide holder with the shape of a Vivalytic cartridge. This enabled placing the cell counting slide in the field of view of the Vivalytic analyzer (see Figure 56).

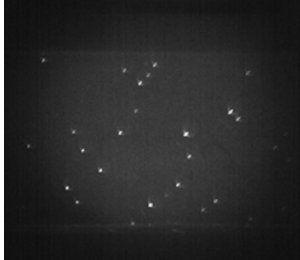
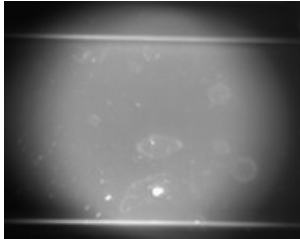
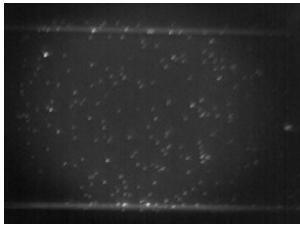
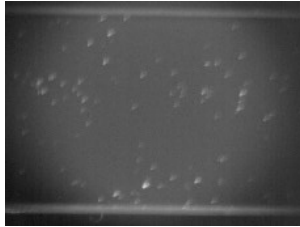


Figure 56: 3D printed cartridge used as a cell counting slide holder for optical analysis of stained cells in the Vivalytic analyzer.

Different fluorescent dyes enabling the detection of CTCs within a blood sample were evaluated regarding their detectability with the Vivalytic analyzer: Hoechst33342, CFSE, EpCAM-FITC, EPCAM-APC and PI. The dyes, their extinction and emission wavelengths and the results obtained for the stained cells are shown in Table 28. The detection of Hoechst33342 stained cells was not possible as the Vivalytic analyzer had no UV-light excitation source. The most distinct and brightest detection was possible for CFSE despite the short illumination time. Dead cells could be detected successfully by PI staining. EpCAM could be detected using FITC labeled antibodies only with very weak fluorescence. However, staining with and detection of EpCAM-APC was possible.

Table 28: Cells stained with different fluorescent dyes detected using the Vivalytic analyzer and VPhotoStar control software.

Fluorescent dye	Extinction /Emission [nm]	Characteristic detected	Image	Analyzer compatible
-----------------	---------------------------------	----------------------------	-------	------------------------

Hoechst33342	361/497	Nucleus	n.d.*	No UV-light excitation possible
CFSE	494/521	Viable cells		yes
			50 ms	
EpCAM-FITC	490/525	EpCAM-positive		partly
			1950 ms	
Propidium iodide	535/617	Dead cells		yes
			100 ms	
EpCAM-APC	594/633	EpCAM-positive		yes
			1500 ms	

*n.d.: not detectable

The cell dyes CFSE and PI were very well detectable using the Vivalytic system. The cells were visible as distinct light dots. It was not possible to differentiate between single cells and cell clusters, but it was assumed that brighter and larger dots resulted from cell clusters. The cells stained with labeled antibodies were harder to detect and higher illumination time was required

resulting in higher background fluorescence. Finally, cells stained with EpCAM-APC could be detected better than cells stained with EpCAM-FITC.

As a result, the most suitable staining strategy for CTC detection using the Vivalytic analyzer for detection of viable, EpCAM-positive cells and distinction from dead and/or EpCAM-negative cells such as leukocytes was to detect EpCAM positive cells via EpCAM-APC and viable cells by CFSE. For the detection of dead cells, PI can be used. To additionally detect the nucleus after Hoechst33342 staining, an adaptation of the light source will be necessary.

To determine which cells could be detected either as individual cells or cell clusters, optical detection of CFSE stained HCT116 cells captured on the TEM-grid using the fluorescence microscope (Figure 57A and B) and the optical system of the Vivalytic analyzer (Figure 57C) were compared by imaging the exact same TEM-grid.

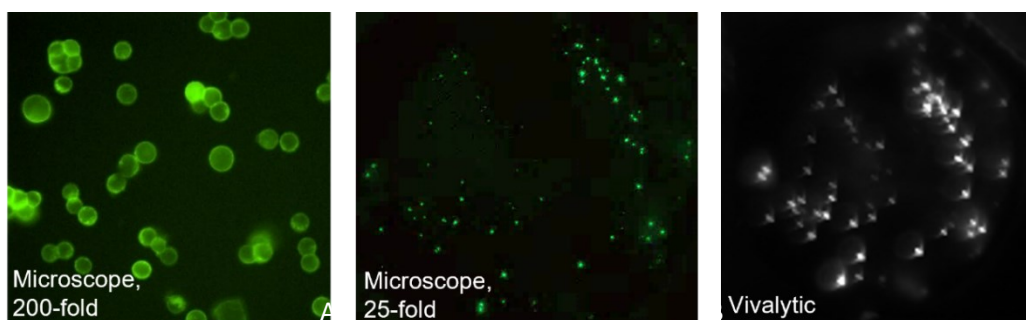


Figure 57: HCT116 cells stained with CFSE and captured on a TEM-grid. As detected by the fluorescence microscope Olympus BX61 (100 ms illumination) at 200-fold and 25-fold magnification and the Vivalytic analyzer (100 ms illumination).

Using the fluorescence microscopical image (Figure 57B), the distances between the cells on the TEM-grid could be measured to determine the minimal distance in which the cells were recognized as single cells in the Vivalytic analyzer. Cells with distances of more than 60 μm (as determined in Figure 57B) could be recognized as single cells and counted. Cell cluster with distances below 60 μm were recognized as one light spot.

3.4. Molecular characterization of the cells captured on the filter

For characterization of the cells captured on the filter element on molecular level, different possibilities to extract nucleic acids were evaluated. All experiments were performed off-chip but were incrementally adapted to on-chip conditions for a proof-of-principle experiment. Cell lysates

prepared in a sample tube were used as a reference and compared to lysates obtained from lysis on the TEM-grid directly as templates in singleplex and multiplex RT-qPCR. Furthermore, the performance of liquid reagents (master mixes, primer-probe-mixes) were used as baseline and compared to the performance of lyophilized master mixes and airdried primer-probe mixes.

RNA extraction from blood and evaluation of the influence of storage on RNA quality

Patient blood was used for RNA extraction for expression analysis. As the samples were transported from the UKT in approximately 2 h at room temperature (RT), the influence of storage at RT in comparison to storage at 4 °C on RNA integrity was evaluated as described in chapter 2.4.1.2.

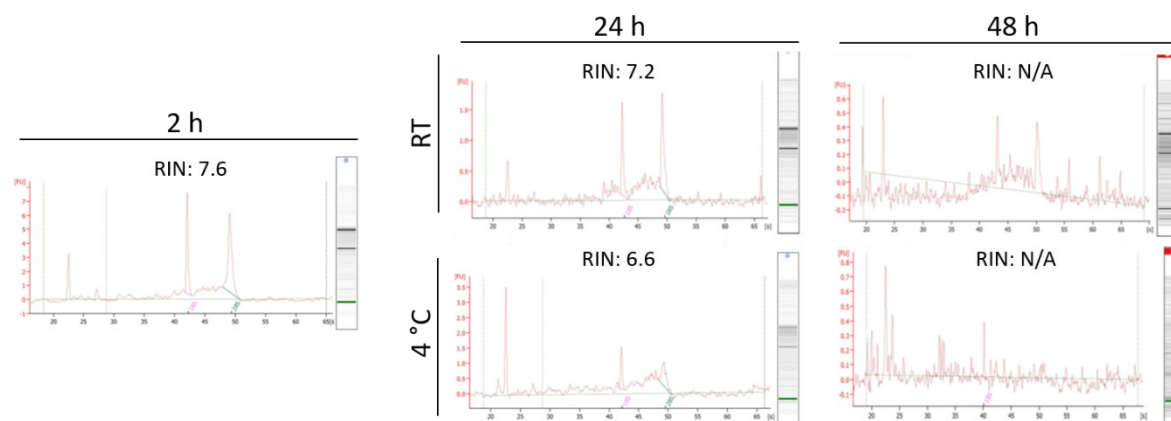


Figure 58: Determination of the RNA integrity after extraction from whole blood.

Using the Bioanalyzer (Agilent Technologies, Santa Clara, USA), RNA integrity was assessed within 2 h after sample taking and transport at RT, and after 24 h and 48 h storage at RT and 4 °C. RIN: relative integrity number. A RIN of > 6 was regarded as sufficient.

As shown in Figure 58, blood sample storage of 2 h at RT resulted in a RIN of 7.6 used as reference value. Storage of 24 h at RT, resulting in a RIN of 7.2, was superior to storage at 4 °C resulting in a RIN of 6.6. After storage for two days, RNA integrity was not maintained. The highest RIN and most distinct 18S and 28S band in the electropherogram were determined on the same day of sampling, after 2 h. Consequently, the patient blood could be used for RNA extraction at the same day or at maximum one day after sample taking and storage at RT.

3.4.1. Correlation of EpCAM staining to EpCAM and mesenchymal marker expression

Epithelial marker EpCAM and mesenchymal markers Snail and Twist were analyzed in patient samples by expression analysis using relative quantification as described in chapter 2.4.3.1. The results of the expression analysis were correlated to the EpCAM cell count determined by the maintrac® method (described in chapter 3.1) and to the disease progression as observed in the clinical examinations. The clinical data was kindly provided by the UKT. Evaluation focused especially on the hypothesis that in case of detection of none or only few EpCAM-positive CTCs, the expression of EpCAM was downregulated and in contrast the expression of Snail and Twist could be upregulated indicating the presence of EMT cells.

As shown Figure 59, the EpCAM cell count of patient BO-645 observed by the maintrac® method showed an increase from 7 CTCs blood to 9 CTCs per 20 μ L from the first to the second sampling time point and afterwards a constant decrease (7 CTCs in the third sample, 5 CTCs in the fourth sample per 20 μ L blood). The EpCAM expression on molecular basis also showed a similar trend. First, EpCAM expression increased 6-fold between the first and second sampling. Then expression decreased to 0.6-fold and 0-fold compared to the baseline expression before therapy. At the same time, Snail expression increased from time point two (0.7-fold) to time point three (5-fold), showing an opposite trend than the EpCAM expression and number of EpCAM positive cells. Twist expression decreased constantly under therapy and was below the baseline expression at all following sampling time points. In contrast to the decreasing number of EpCAM-positive cells, the clinic reported progress after the fourth sample time point. A plausible reason for the contrary course of the EpCAM-cells and the clinical observations could be the EMT of the CTCs and therefore the failed detection by using EpCAM-antibodies.

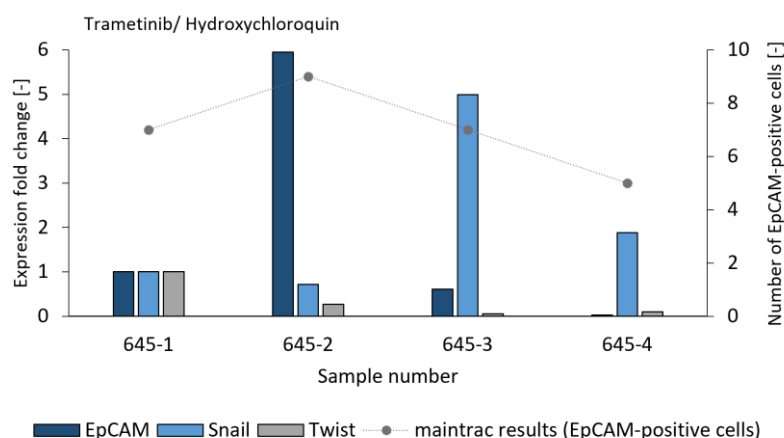


Figure 59: CTC count course and gene expression results of patient BO-645.

The numbers behind the patient pseudonym represent the sampling time point. Sample 1 was taken before therapy, the following samples in intervals of 3-4 weeks. The y-axis on the left side represents the expression fold change and the y-axis on the right side represents the number of EpCAM-positive cells as determined by the maintrac® method using fluorescence microscopy.

The EpCAM cell count of patient BO-408 (Figure 60) determined by the maintrac® method decreased from 7 CTCs to 2 CTCs per 20 µl blood after the first month of therapy and then increased to 25 and 24 CTCs at the third and fourth sampling time point. EpCAM and Snail expression levels were below the baseline expression at time point two and three and increased at time point 4. EpCAM expression level showed a 1.2-fold increase, Snail showed a 2.5-fold increase. Twist expression increased to 12-fold at time point three and 5-fold at the timepoint four compared to the baseline value before therapy. Comparing this to the clinical observations, a correlation of the EpCAM-positive CTC count, increased Twist expression and the disease progression could be observed. Progress was detected by computed tomography at the third sampling time point (marked by the yellow arrow in Figure 60). Consequently, the therapy was changed. No following CTC count course could be determined after change of therapy because no further blood samples were taken. Nevertheless, another progress was observed by computed tomography two months later indicating lack of effect of the adapted medication. On RNA level, EpCAM expression did not correlate to the detection of EpCAM surface antigen by immunofluorescence.

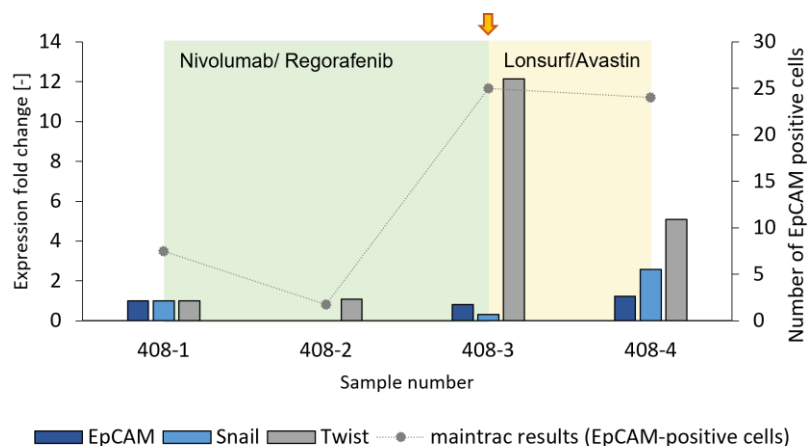


Figure 60: CTC count course and gene expression results of patient BO-408.

The numbers behind the patient pseudonym represent the sampling time point. Sample 1 was taken before therapy, the following samples in intervals of 3-4 weeks. The y-axis on the left side represents the expression fold change and the y-axis on the right side represents the number of EpCAM-positive cells as determined by the maintrac® method using fluorescence microscopy.

In summary, it was observed that the CTC count as determined via the maintrac® method might correlate to disease progression as shown in three individual patients (see Figure 17). Furthermore, the overexpression of the mesenchymal markers Snail and Twist could also indicate a change in therapy success when only few or no EpCAM positive cells could be determined by immunofluorescence as observed for patient BO-645-3. For a definitive conclusion and correlation of observed EpCAM positive cells and RNA markers to therapy success more patient samples need to be analyzed to define changes in CTC count courses or expression patterns that indicate clear clinical relevance.

3.4.2. Evaluation of direct cell lysis and usage of cell lysates as template in RT-qPCR

For analysis of low abundance targets, such as mRNA transcripts in CTCs in a blood sample, a highly efficient RNA extraction method with a low number of steps, was essential to minimize RNA loss. Therefore, a method was established that enables reverse transcription (RT) to be performed directly on the crude cell lysates. Moreover, the filter chamber on the Vivalytic cartridge was used for integration of the TEM-grid for CTC capture (as shown in Figure 52) in the proof-of-principle experiments. Several lysis solutions were evaluated in regard of detection efficiency, RNA stability, reproducibility, and LoC integrability.

Firstly, different cell lysis buffers (as listed in Table 3) were evaluated regarding their ability to lyse 6×10^6 HCT116 cells for release of nucleic acids, especially RNA. Using EpCAM standard curves ranging from 10^6 to 10^2 copies/ μL for absolute quantification, the number of EpCAM copies that were detectable in the cell lysates were determined. The PCR products were evaluated by agarose gel electrophoresis for detection of unspecific bands.

The highest copy number was detected in the lysate generated by LB04 containing Triton-X and BSA and the PCR product was pure without unspecific amplification. Thus, LB04 was used for all further experiments.

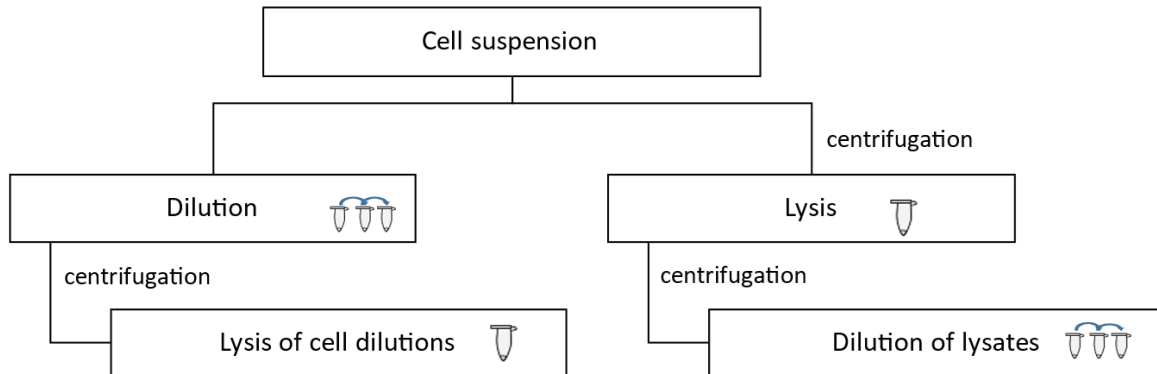
In the next step, two possibilities for off-chip lysate generation for determination of RT-qPCR efficiency using a dilution series were evaluated (see Figure 61A).

First, an approach compatible with on-chip conditions was examined: cell suspensions were first diluted in PBS or cell culture medium, the suspensions were centrifuged, and the obtained pellets were lysed with equal amounts of lysis buffer. The results of the RT-qPCR with the cell lysates generated by this method are shown in Figure 61B. Detection of Twist and Snail was not possible in the lysates of the cell dilutions containing 10^3 and 10^2 cells. EpCAM and GAPDH were detected in the lysates of all cell dilutions. However, PCR efficiencies of EpCAM, Twist, and Snail were only at about 70 %. The PCR efficiency of GAPDH was at 75 %. Thus, the PCR with the lysates from the cell dilutions were not sufficiently efficient. One reason could be that the cell lysates generated from the different cell dilutions all contained lysis buffer and contaminants as well as inhibitors were not diluted before entering the RT-qPCR.

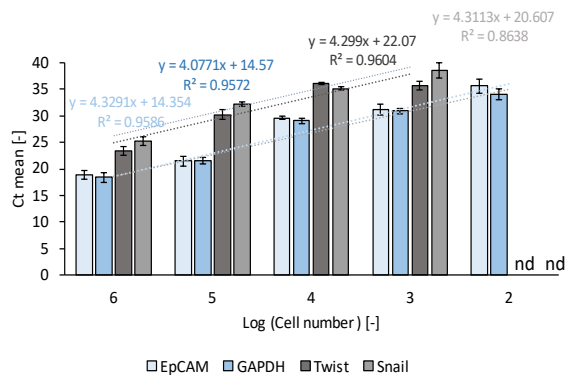
Alternatively, to find out whether cell debris was the reason for the PCR inhibition, the cell suspension of the starting cell concentration of 10^6 cells was lysed with LB04, the obtained lysate was centrifuged to sediment the cell components and the supernatant was serially diluted in LB04 (results in Figure 61C). In this case, all targets were detected in each dilution. Furthermore, the targets were detected at lower Ct values than by the previously described method and PCR efficiencies of EpCAM, GAPDH and Twist were in the desired range between 90 % and 110 % (EpCAM 102 %, GAPDH 103 %, Twist 110 %). Only Snail PCR efficiency was at 89 % and thus only slightly below the desired range of 90 % to 110 %. An explanation for the higher efficiency and lower limit of detection of this method could be the dilution of the cell lysate containing 10^6 cells

initially to generate the following dilutions after centrifugation. Not only the RNA contained in the lysates but also the cell components released, the contaminants and inhibitors were serially diluted. Thus, the PCR inhibiting effect was assumed to result from the cell components rather than from the lysis buffer itself, as the content of lysis buffer was the same for all experiments and cell lysates.

A



B



C

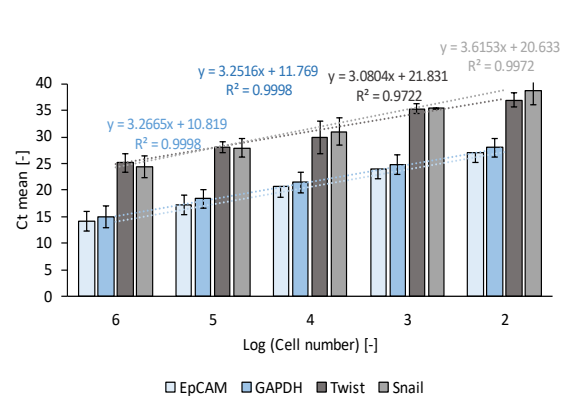


Figure 61: Possibilities for the generation of cell lysates for usage as templates in RT-qPCR.

In (A), the different possibilities to generate cell lysates are depicted. Cell suspensions were either first diluted and the dilutions were lysed by LB04 and directly analyzed by RT-qPCR (B), or the cell suspension was lysed, and the lysate was serially diluted before analysis by RT-qPCR (C).

In conclusion, the cells isolated from blood and lysed after optical detection needed to be diluted for further molecular analysis to maintain high PCR efficiency.

3.4.3. Maximal tolerance of leukocyte background in cell lysates

As the method of choice for CTC isolation using a filtration unit aimed at maximal CTC capture efficiency rather than maximal leukocyte depletion and purity, it was assumed that many leukocytes might be retained on the filter. Therefore, it was determined whether the leukocytes inhibit the RT-qPCR and how much background leukocyte RNA in the lysates is tolerated by the assay. Same numbers of HCT116 cells (10^4) were mixed with leukocytes obtained from 1 mL of blood after erythrocyte lysis. Different leukocyte dilutions from 1:10 to 1:100,000 were used. As shown in Figure 62, the Ct values of EpCAM, Snail, Twist and GAPDH remained about the same for the samples containing leukocytes dilutions 1:1,000; 1:10,000 and 1:100,000 and increased in case of the samples containing the 1:100 and 1:10 dilutions. This led to the assumption that the RT-qPCR was reproducible only after dilution of at least 1:1,000 which corresponds to a blood sample volume of 1 μ L (based on an input blood volume of 1 mL).

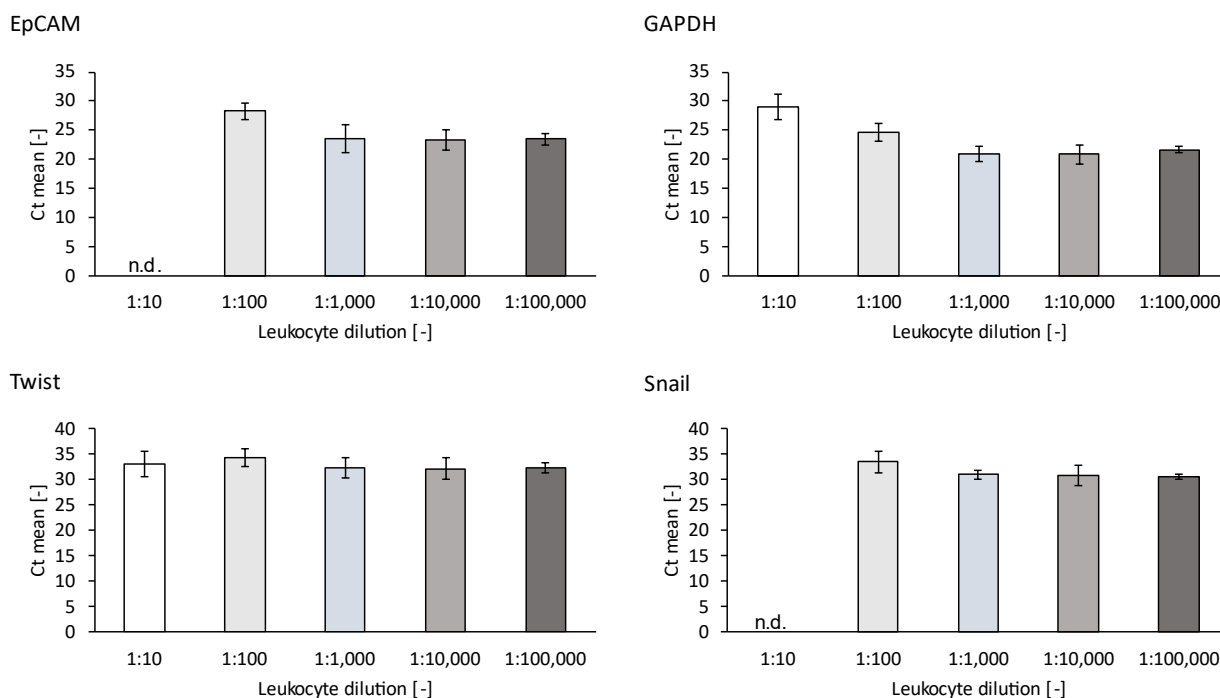


Figure 62: Ct values of the RT-qPCR with lysates of 10^4 HCT116 cells mixed with different leukocyte dilutions obtained from a blood sample of 1 mL after erythrocyte lysis.

Thus, when 100 μ L blood were applied in the filtration for CTC isolation, about 99 % of the leukocytes needed to be depleted for efficient RT-qPCR. As shown in Figure 42 and Figure 43,

> 95 % of the leukocytes could be depleted by filtration with one washing step. For further, sufficient background reduction, the depletion rate could be increased by additional washing steps. However, in this case it must be assured that no target cells are lost.

3.4.4. Cell lysis on the filter

As a LoC compatible possibility, the cell suspension was transported through the filtration functional model as described in chapter 2.3.1.3 and the captured cells were lysed on the filter directly for subsequent RT-qPCR with cell lysates.

Therefore, HCT116 cell suspensions with defined cell numbers of 10^4 , 10^3 , and 10^2 cells were lysed in a sample tube as references. The same cell suspensions were filtrated using the filtration functional model. For lysis of the captured cells on the filter in direct comparison to the lysis in the sample tube, the lysis buffer was filled into the syringe connected to the syringe pump and transferred into the filtration functional model from the outlet site. The lysis buffer was incubated on the filter for 10 min, the lysate was collected in the pipette tip (shown in Figure 30) and transferred to a sample tube for DNase digest and application as template in RT-qPCR. The results of the RT-qPCR are shown in Figure 63A to C. The copy numbers of EpCAM Twist and Snail determined in the direct lysates were regarded as control and were compared to the copy number determined after cell lysis on the filter.

As shown in Figure 63, EpCAM could be detected in all cell dilutions analyzed from both lysates (lysis in the sample tube vs. filter lysates). Twist and Snail could only be detected in all cell dilutions of the sample tube lysate. The detection of Twist and Snail was not possible in the filter lysates of 10^2 cells. Higher copy numbers were detected using the cell lysates generated in the sample tube in all cases. Whereas in the lysates from the sample tube, 1.6×10^7 copies, 1.0×10^6 copies and 1.0×10^5 copies of EpCAM were detected in 10^4 cells, 10^3 cells and 10^2 cells, if 1000 copies can be detected per cell. In the filter lysates only 2.0×10^6 copies, 1.0×10^5 copies and 2.0×10^2 copies of EpCAM were detected in the lysates from filtration of the same initial cell numbers. In the case of Twist, 4.0×10^4 copies, 2.0×10^3 copies and 2.0×10^2 copies were detected in the sample tube lysates of 10^4 , 10^3 and 10^2 cells. In the filter lysates only 8.0×10^3 and 2.0×10^3 copies were detected in the samples of initially 10^4 and 10^3 cells. Detection of Snail and Twist was not possible at all in the filter lysates of initially 10^2 cells (Ct values were higher than 40). This indicates, besides the loss of cells (around 40 % as determined in the experiments described in chapter 3.2.4.2) a

RNA loss could be observed using the cell lysates generated on the filter. A reason for the loss of RNA could be an incomplete lysis of the cells on the filter as observed by optical evaluation of the filter by fluorescence microscopy right after lysis of the cells.

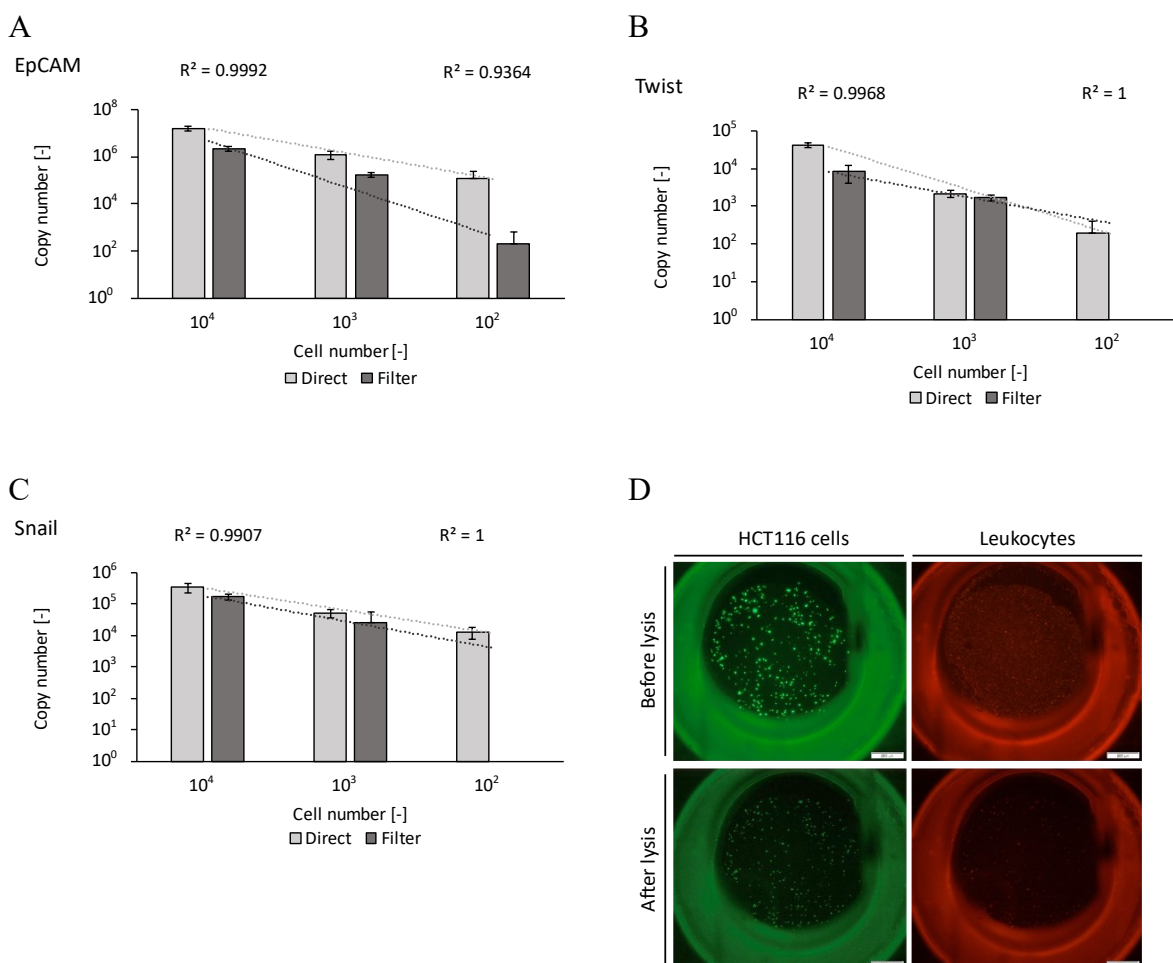


Figure 63: (A) EpCAM, (B) Twist and (C) Snail copy number determined in HCT116 lysates by RT-qPCR. Crude lysates were used as templates and were prepared either by lysis of the cells in a sample tube (= direct) or after capture on the filter (= filter). HCT116 cell numbers of 10^4 , 10^3 and 10^2 were used. D: CFSE stained HCT116 cells and CD45-PE-stained leukocytes captured on the filter shown before lysis and after lysis on the filter.

Regarding the CTC numbers in patient samples (as described in chapter 3.1) this led to the assumption that patient samples containing more than 10^3 , preferably more than 10^4 CTCs per mL blood would be applicable for expression analysis. Then, during filtration of 100 μ L to 200 μ L blood, more than 10^2 cells were expected. As cells needed to be filtrated for optical detection and counting first, and lysis for molecular analysis is performed afterwards one possibility would be to add a higher sample volume to the set-up to capture enough cells for molecular analysis. However,

the filtration capacity of the higher volume needs to be evaluated. Consequently, patient samples containing only 10^2 cells or less cannot be efficiently analyzed on-chip at this moment without significant increase of either sample volume, cell capture rate or assay sensitivity.

3.4.4.1. Increase of sensitivity by nested RT-qPCR

One possibility to increase RT-qPCR sensitivity could be provided by the technique of nested RT-qPCR. Hereby, a second primer pair (outer primer pair, see Table 8) was applied in an additional amplification step before the actual qPCR. The additional primer pair was used for specific preamplification of a larger fragment than the primer pair used for quantification of the targets EpCAM, Snail and Twist. Conventional RT-qPCR as described in chapter 2.4.3 was compared to nested RT-qPCR using cell lysates of 10^4 , 10^3 , 10^2 and 10^1 HCT116 cells. As shown in chapter 3.4.4.1, in the conventional RT-qPCR, EpCAM could not be detected in the cell lysate of 10^1 cells, and Snail as well as Twist could not be detected in the cell lysates of 10^1 and 10^2 HCT116 cells. In the nested RT-qPCR all targets could be detected in the lysates of down to 10^1 HCT116 cells. Sensitivity was significantly increased by the preamplification phase with an outer primer pair. The benefit of the nested RT-qPCR needs to be further evaluated using patient samples. In this context it would require the storage of additional reagents, primers, probes, and master mix components on the cartridge. In addition, two rounds of PCR would need to be performed, increasing the time to result.

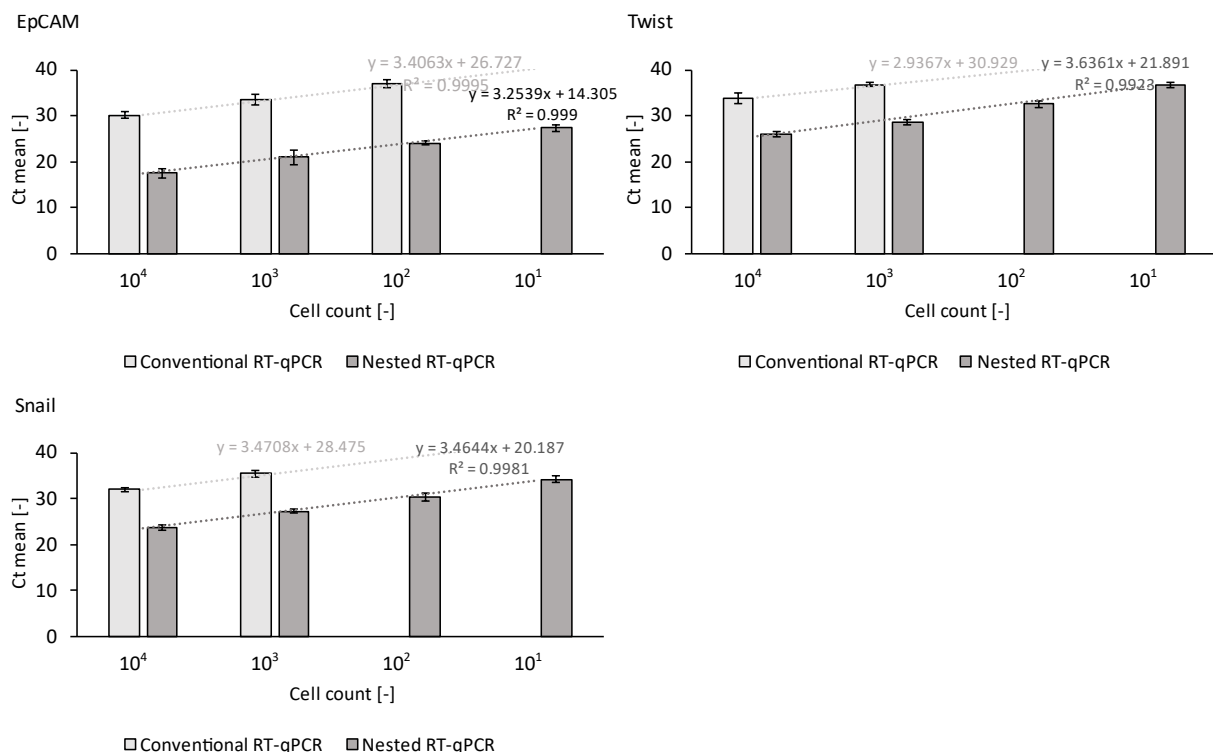


Figure 64: Comparison of conventional and nested RT-qPCR using cell lysates of 10⁴, 10³, 10² and 10¹ HCT116 cells as templates.

3.4.5. Establishment of RT-qPCR protocols for LoC integration

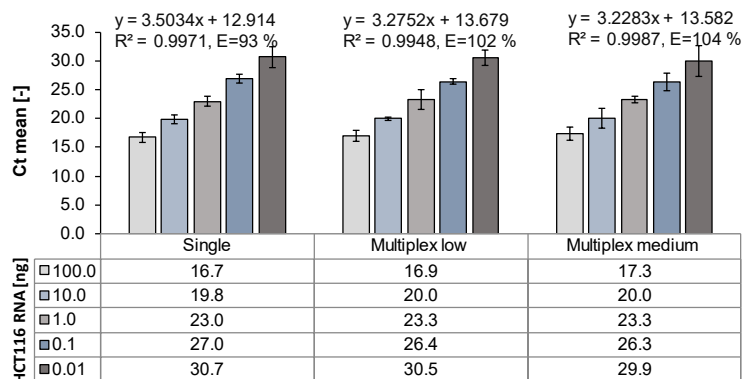
The current cartridge design provided two individual PCR strands. These could be used to detect one target in each PCR strand as singleplex approach. Alternatively, for detection of more than two targets, such as EpCAM, GAPDH, Snail and Twist, the reactions needed to be implemented as multiplex approaches. Furthermore, all components needed to be stable during long-term storage of one year on the cartridge at RT. Therefore, the stability of the PCR components after lyophilization or air-drying was assessed.

3.4.5.1. Establishment of duplex and multiplex RT-qPCR protocols

In a first step, detection of the targets Twist, Snail and EpCAM in duplex reactions in comparison to singleplex reactions were evaluated. Dilutions of HCT116 cell RNA (100 ng to 0.01 ng) were used as templates and singleplex as well as duplex RT-qPCRs were performed. In summary, all the Ct values were 0.3 to 1.6 cycles higher in the multiplex approaches. This results in a higher LOD, and low abundance targets were better detected in singleplex reactions. However, all targets (except Snail in the sample containing 0.01 ng RNA in the multiplex approach) could be

detected both in singleplex and duplex reactions with high efficiency in the acceptable range between 90 % and 110 %.

Consequently, combination of EpCAM, GAPDH and Twist or EpCAM, GAPDH and Snail in triplex reactions was evaluated. For multiplex RT-qPCR, different primer concentration combinations were examined as the targets might differ in abundance. It was assumed that EpCAM and GAPDH were highly abundant in the HCT116 cells, and that Twist abundance was lower. Therefore, the primer concentrations were varied: EpCAM and GAPDH primers were applied in a final concentration of 150 nM and Snail and Twist primers were applied in final concentrations of 300 nM (referred to as medium for medium abundance targets) and 900 nM (referred to as low for low abundance targets). The results are plotted in Figure 65. In Figure 65A, the results of EpCAM detection in either singleplex or triplex approach show maximal Ct differences of 0.8 cycles for the lowest template RNA concentration of 0.01 ng. GAPDH was not detected in the triplex approaches containing 100 ng template RNA. In all other approaches GAPDH could be detected with a maximum difference in Ct values of 0.9 cycles between the singleplex and the triplex approaches. The differences in Ct values of Snail and Twist were higher, ranging between 1.0 and 1.6 cycles for template RNA amounts of 1 ng to 100 ng and between 1.4 and 2.7 cycles difference for template RNA amounts of 0.01 ng and 0.1 ng. The Snail transcripts in the singleplex sample containing 0.01 ng of HCT116 RNA and Snail primer in a final concentration of 900 nM could not be detected at all.



A

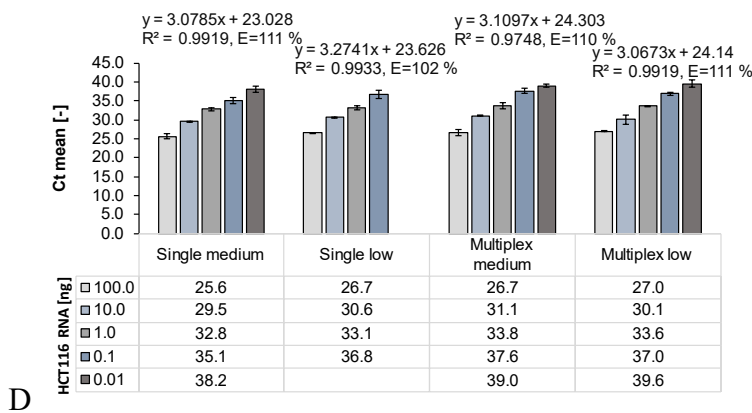
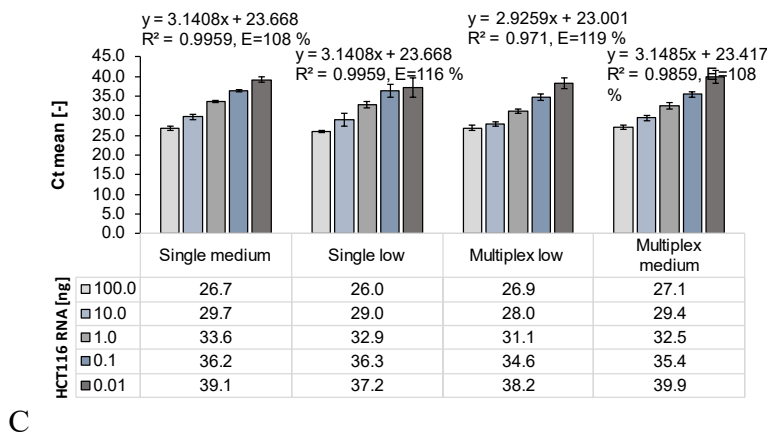
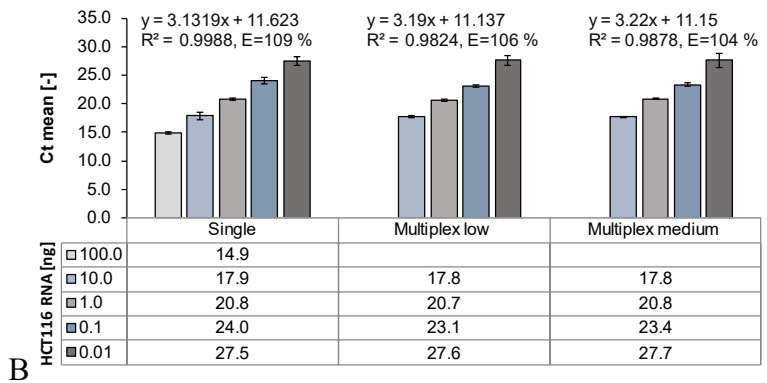


Figure 65: Multiplex RT-qPCR with different primer and target concentration combinations. Different concentration of primers for multiplexing for RT-qPCR with template concentration ranging from 0.01 ng to 100 ng of HCT116 RNA were examined as the targets differed in abundance. A: EpCAM, B: GAPDH, C: Twist, D: Snail were analyzed to determine the PCR efficiencies using the different primer concentrations.

In summary, detecting all desired targets was possible in multiplex approaches, and sensitivity was only decreased compared to singleplex approaches when template concentrations were very low.

However, by varying primer concentration combinations, the efficiency of the multiplex RT-qPCR could be optimized to reach the desired ranges between 90 % and 110 %.

3.4.5.2. Evaluation of long-term stability of RT-qPCR components

Application and long-term storage of liquid mastermixes as used in conventional molecular diagnostic assays is not possible in the LoC system. However, PCR master mixes can be stored on-chip in the PCR chamber as lyophilized beads. Therefore, RT-qPCR using lyophilized master mix beads in comparison to the liquid mix (described in chapter 2.4.3.4) was evaluated. Two different master mix lyophilizates were analyzed and compared to the liquid Luna® Universal Probe One-Step RT-qPCR (New England Biolabs, Ipswich, USA): the CIRRUS Strips RNA (Fluorogenics, Salisbury, UK) and the SCRIPT RT-qPCR ProbesMaster Lyophilisate (Jena Bioscience, Jena, Germany). As shown in the exemplary standard curves in Figure 66, the best result regarding the correlation coefficient of $R^2=0.9985$ was obtained using the liquid mix Luna® Universal Probe One-Step RT-qPCR (New England Biolabs, Ipswich, USA). The PCR efficiency as calculated from the linear regression using Equation 7 to Equation 9 resulted in 91 %. Using the SCRIPT RT-qPCR ProbesMaster Lyophilisate (Jena Bioscience, Jena, Germany), an efficiency of 108 % and a correlation coefficient of $R^2=0.9590$ were achieved and all copy number concentrations could be detected. The RT-qPCR efficiency with the CIRRUS Strips RNA (Fluorogenics, Salisbury, UK) resulted in 172 % with a correlation coefficient of $R^2=0.9639$. This artificially increased efficiency could indicate presence polymerase activators that lead to faster amplification and higher efficiency but are too diluted in the reaction with the lowest copy number of 10^2 copies/ μ L. The latter could not be detected with the CIRRUS Strips mix. It was assumed that the CIRRUS Strip mix was more sensitive to the presence of activators leading to falsified results. As the lowest copy number could not be detected and the efficiency was outside the desired range of 90 % to 110 %, this lyophilizate was not further applied for RT-qPCR experiments. In turn, the SCRIPT RT-qPCR ProbesMaster Lyophilisate (Jena Bioscience, Jena, Germany) was preferred as it was suitable to detect all copy numbers analyzed and the efficiency was within the desired range.

A

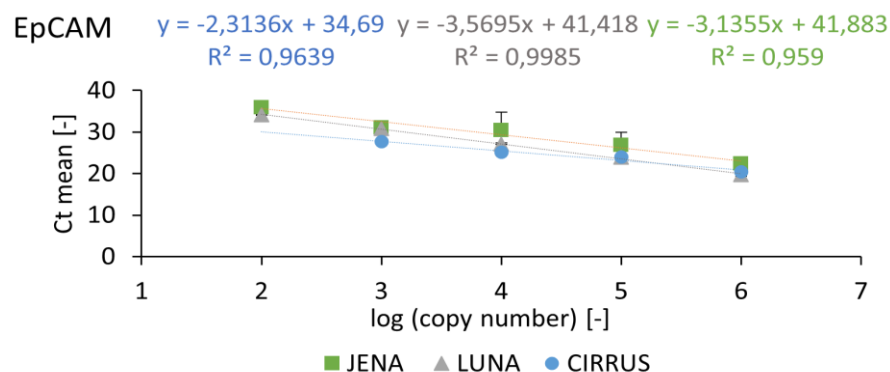


Figure 66: (A): Exemplary EpCAM standard curves.

For comparison of the Luna® Universal Probe One-Step RT-qPCR (New England Biolabs, Ipswich, USA) and the lyophilized RT-qPCR beads CIRRUS Strips RNA (Fluorogenics, Salisbury, UK) and SCRIPT RT-qPCR ProbesMaster Lyophilisate (Jena Bioscience, Jena, Germany).

Due to the higher efficiency and successful detection of all copy number concentrations, SCRIPT RT-qPCR ProbesMaster Lyophilisate (Jena Bioscience, Jena, Germany) was preferred as lyophilized master mix for further experiments. The SCRIPT RT-qPCR ProbesMaster Lyophilisate (Jena Bioscience, Jena, Germany) and the Luna® Universal Probe One-Step RT-qPCR (New England Biolabs, Ipswich, USA) not only resulted in comparable results regarding PCR efficiency and linearity but also required similar PCR temperature and time protocols resulting in 65 min and 77 min duration in total. The temperature protocol of CIRRUS Strips RNA (Fluorogenics, Salisbury, UK) was shorter in time (47 min in total), especially in case of the reverse transcription step (2 min instead of 10 min).

Besides lyophilized master mix beads, also primers and probes needed to be stored in a dry form on the cartridge at RT. Therefore, the possibility to airdry primers and probes and store the components at room temperature for 3 h or 24 h to determine whether the oligonucleotides maintain their function was investigated. In addition, storage for 21 d and 42 d was evaluated (as described in chapter 2.4.3.5) at RT and 55 °C for accelerated storage stability testing. According to Equation 10 to Equation 12, storage at 55 °C for 21 d and 42 d corresponds to an expected storage stability and functionality for 185.3 d and 370,6 d. After the respective time of storage, the dried primers and probes were applied in both singleplex and multiplex RT-qPCR. Air-drying of primers and short-term storage for up to 24 h at RT had no adverse effect on RT-qPCR.

After storage of the oligonucleotides at RT and 55 °C for 21 d and 42 d, multiplex RT-qPCR with the SCRIPT RT-qPCR ProbesMaster Lyophilisate (Jena Bioscience, Jena, Germany) was performed in comparison to a multiplex one-step RT-qPCR with lyophilized master mix and liquid oligonucleotides. As presented in Figure 67, the resulting Ct values obtained from the reactions with the air-dried primer mixes and lyophilized mastermix beads were comparable or even lower for GAPDH, EpCAM and Twist. Solely in the Snail analysis, the Ct values slightly increased in the reactions with the mastermix components dried at RT and 100 ng, 10 ng and 1 ng RNA indicating lower PCR efficiency. However, Snail was still detectable in all approaches and Ct values only differed by one cycle at maximum. The difference in Ct values was even lower using the components that were stored at 55 °C indicating that quicker drying might be favorable for the primer and probe stability during storage.

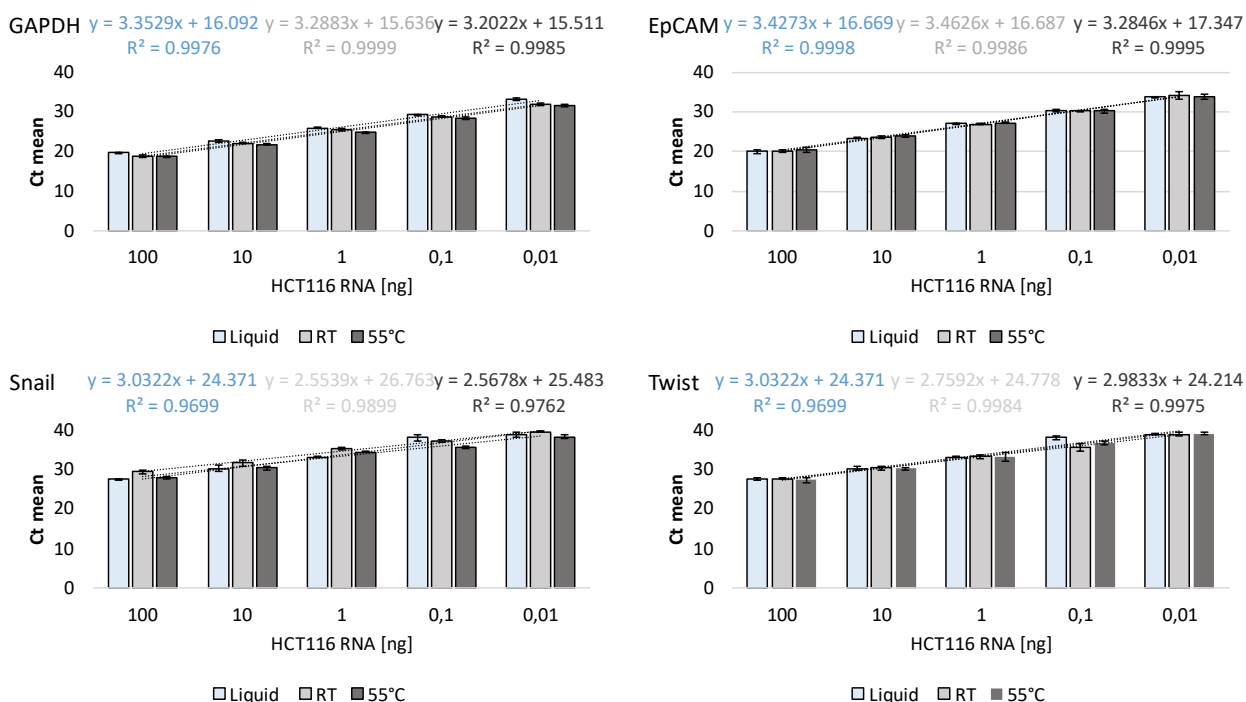


Figure 67: Results of multiplex RT-qPCR with air-dried primers and probes. Primers and probes with 33.3 mM trehalose as additive stored at RT and 55 °C for 21 d for detection of GAPDH, EpCAM, Twist and Snail. Results are given as means \pm SD of biological and technical triplicates.

In conclusion, the results presented, describe the establishment and evaluation of a one-step multiplex TaqMan®RT-qPCR assay for the comparison of EpCAM expression and EMT-related expression of Snail and Twist. The protocols were established and adapted for integration into the

LoC system and were evaluated in a proof-of-principle using LoC compatible off-chip approaches. The targets selected in this assay can be adapted and expanded to further epithelial, mesenchymal, or diagnostically relevant targets.

4. Discussion

Cancer therapy monitoring by liquid biopsy harbors several advantages. Besides being less invasive than tissue biopsy and easier to assess in regular and short time intervals, a more global insight into cancer progression can be acquired as liquid biopsy is not limited to one tumor sight in the body (90).

In this study, an established method for detection of epithelial CTCs was reproduced with model samples, verified in two independent laboratories with the same patient samples in parallel and the results were correlated to the clinical observations. In the next step, the method was adapted with the purpose of automatization by integration into a microfluidic LoC system. The Vivalytic LoC platform is a fully automated microfluidic system enabling molecular diagnostics in a sample-to-answer manner. The previously implemented unit operations, like fluid transport, filter-based nucleic acid extraction, and optical detection were used and adapted for integration of cell detection and analysis. This study's aim was to evaluate the possibility for cell processing on the existing platform. The required unit operations for an implementation of CTC analysis on the LoC system were identified. Thereby, the boundary conditions and parameters of the current Vivalytic LoC system of the Bosch Healthcare Solutions GmbH (Waiblingen, Germany) were considered for the design of the experiments. A microfluidic filtration functional model was fabricated using rapid-prototyping methods and evaluated regarding CTC isolation efficiency and possibility for both quantification and downstream processing of the captured cells. All steps required for isolation and detection of the epithelial CTCs for possible downstream analysis were performed and shown in single unit operations as proof-of-principle. The unit operations that could not be performed on-chip due to the limitations of the system were performed off-chip using prototypes by application of LoC compatible conditions.

The results presented in chapter 3 are critically discussed in the following chapters considering the state-of-the-art methods and current scientific research in the field of liquid biopsy.

4.1. Reproducibility of the maintrac® method and correlation to the disease progression

The maintrac® method was selected as benchmark method for the detection of CTCs from gastrointestinal tumor patient blood samples. The main advantages of the maintrac® method rely

on the simple performance and in the reported high number of positive CTCs detected in blood volumes as little as 20 μL to 100 μL when compared to other methods using several milliliters such as the CellSearch[®] method. One reason might be that the cell loss is minimized because cells are not enriched in an elaborate multi-step process but only differentially stained after erythrocyte depletion and directly detected by fluorescence microscopy. The minimized cell loss was proven in an experiment by comparison of different preparation methods like erythrocyte lysis, density gradient centrifugation and erythrocyte aggregation as shown in chapter 3.2.2. Selective lysis of the erythrocytes had several advantages compared to density gradient centrifugation and erythrocyte aggregation. The method was easy to handle, quick and spike cell recovery was improved compared to the two other methods. $97\% \pm 2\%$ of the spiked BT-474 cells could be recovered after erythrocyte lysis and centrifugation. Lara et al. similarly described a lower recovery of 89 % for MCF-7 cells but still higher than recovery of 73 % with density gradient centrifugation (91). Many CTC isolation methods lose a large fraction of the CTCs during initial sample preparation by using density gradient centrifugation for the depletion of erythrocytes (91) (92). Another reason for CTC loss during sample preparation might be the positive or negative selection by antibody-coated magnetic beads for the recovery of the CTCs. Highly varying recovery rates of 5 % to 95 % were described for immunomagnetic enrichment of CTCs (93) (94) (95) .

The UKT provided samples from gastrointestinal tumor patients for a multicenter proof-of-concept study including sample analysis by the maintrac[®] method at SIMFO and in our laboratory. The aim was to assess the reproducibility and comparability of the method in two laboratories by different operators in parallel. As shown in chapter 4.1, the absolute CTC numbers determined at SIMFO and our laboratory differed significantly, whereas the relative cell count courses were comparable. The raw data obtained by Bosch and SIMFO and the exact procedure of the experiments were compared in a retrospective for an alignment, and differences in sample processing and evaluation were identified:

- Different microscopic equipment was available (including illumination source, optic filter sets, evaluation software)
- the area of the wells scanned were different (correction factor can be calculated from the area of the well)
- the illumination times were different as they were set individually for each sample (EpCAM-sample and isotype control were acquired with the same settings)

- the antibody concentrations were different
- the isotype control concentrations were different and therefore the threshold setting might be different as well as the rate of unspecific binding
- incubation times (of blocking agent) were different
- Bosch evaluation was performed manually, SIMFO evaluation was performed semi-automated
- differences in evaluation of viable and PI-positive cells and cells with EpCAM caps

The differences stated above could have led to the differences in the absolute CTC numbers. Normalization of the CTC counts, and inclusion of an area correction factor might provide comparability of the values.

Regarding the CTC count dynamics of most of the patients analyzed in this study, CTC count changes of 9-fold and less were observed except for the highest increase (25-fold increase) at one instance for patient BO-408. At the same time progression of the disease was detected by CT scanning supporting the observations described in the study of Pachmann et al. of 2008 in which 91 patients in the adjuvant setting were analyzed. CTC counts were determined before treatment, prior to each chemotherapy cycle, and after treatment completion. Here they reported that CTCs were detected in 90% of the patients using the maintrac® method. They described three possibilities in the change of the CTC count course during therapy: a >10-fold decrease, a >10-fold increase or a change of <10-fold in either direction that was regarded as marginal. Comparing this to my own results, a >10-fold change could only be observed for patient BO-408. A 25-fold increase was determined at sampling time point three in comparison to the second sampling time point. At the same time, an increase in LDH and progression of the tumor were reported by the UKT based on clinical examinations. LDH can be used as an indicator for tissue damage as it is caused by tumor growth during initiation, invasion, metastasis, and recurrence (96). Further, elevated levels of serum LDH are also described as prognostic biomarkers for poor survival in multiple cancers and increase especially at terminal phases of cancer disease (97; 98). In the study of Pachmann et al., the development in the CTC count courses showed good correlation with disease outcomes. During a period of 40 months, 22 % of the patients relapsed. Therein included one of 28 patients with a decrease of the CTC count, five of 30 patients with minimal change, and 14 of 33 with an increase of the CTC count (99). Regarding the UKT samples analyzed in this dissertation, a progression was reported for patient BO-749 at sampling time point four at

which the CTC count was doubled compared to the third sampling time point. For patient BO-408 a progression was reported after the 25-fold increase in the CTC count. In contrast, for patient BO-645, a progression was observed despite a continuous decrease in the CTC count. In the latter case, the EMT could be one reason for the decrease in the EpCAM-positive CTC count although tumor progression occurred. This observation is consistent with the RT-qPCR results of the mesenchymal markers described in chapter 4.3. The CTC count of patient BO-572 showed a heterogeneous course over 17 months leading to the assumption that the therapy led to a longer progression free survival.

The proof-of-principle study in this dissertation including correlation of the CTC counts to the clinical finding and disease progression of the patients indicated that the CTC count course and the relative change between two time points are more relevant than the absolute CTC count determined. The determination of the CTC count over the course of a therapy indicated a correlation with the observations by the clinical examinations like tumor markers and CT scans supporting the hypothesis that CTC enumeration could serve as feasible marker for therapy monitoring.

In the underlying comparative study with SIMFO, samples from patients with advanced gastrointestinal tumor cases were analyzed. In these cases, CTCs are described to be detected more numerous and thus more easily than in early stages of the disease (100; 101). For more precise evaluation, early phase trials or the inclusion of samples from other cancer types should also be considered. One use case that could highly profit from therapy and disease monitoring by liquid biopsy is during adjuvant therapy (102) (103). Patients could be monitored to decide whether therapy can be stopped or needs to be continued. Alternatively, patients could be monitored after therapy completion to decide whether another cycle of therapy is necessary. However, if monitoring reveals therapy could be stopped, patients could be spared unnecessary side effects. Another use case might be the detection of CTCs from different pancreatic cancer subtypes, differentiation of epithelial, mesenchymal or hybrid CTCs and identification of their ratios present (104). As shown in (105), the number of epithelial CTCs was a significant independent predictor of overall survival whereas the hybrid types of CTCs were predictors of metastasis.

4.2. Establishment of protocols for LoC integration of CTC detection

The aim of this study was the integration of CTC analysis and enumeration by liquid biopsy into a microfluidic sample processing system comprising several advantages over conventional systems: Microfluidic assays require smaller sample and reagent volumes, which is beneficial in the case of limited patient sample material and expensive reagents such as labelled antibodies for their detection. Furthermore, the hands-on steps could be reduced to transfer of the sample into the LoC system and analysis would run automatically. In this study, time-to-result could be significantly reduced from 2 hours required for manual processing to <30 min required for processing with the microfluidic filtration model or on the Vivalytic cartridge. Thereby reproducibility might be increased by reduction of manual sample preparation steps.

In this study, detection, identification, and discrimination of CTCs from other blood cells was based on the expression of proteins that could be stained using specific antibodies detected by fluorescence microscopy. Given the fact that CTCs mostly originate from an epithelial tumor, most of the CTCs harbor epithelial characteristics and express EpCAM. By using a multitumor tissue microarray (TMA) for determination of the frequency of EpCAM expression among different tumor types, Went et al. found EpCAM expression in 98 of 131 tumor categories, including 81 % of adenocarcinomas of the colon (106). As EpCAM is highly abundant in epithelial tumors, many detection methods depend on identification of epithelial specific markers. According to the staining method used in this study (see chapter 3.2.1), cancer cells were identified based on the presence of EpCAM on their surface. The main advantage in the usage of EpCAM resided in the fact that EpCAM is located on the cell surface and therefore can be stained without prior fixation of the cells. This had the decisive advantage that the cell viability could be assessed in parallel. Cell viability is also an investigated feature of the maintrac® method and a criterion for CTC counting. This was important, because only cells that reside viable in the bloodstream and escape the immune system were considered as potentially metastatic (107). Therefore, FITC-labeled EpCAM antibodies, and dead cell indicator PI were used for immunostaining of spiked cell lines and CTCs present in patient blood samples without fixation and permeabilization. The importance of cell viability assessment was described as cancer-type specific. For example, in the adjuvant setting, viable cells and cells that can divide may provide relevant clinical information. Whereas in metastatic disease, the simple presence of CTCs was described to predict metastatic disease

prognosis, regardless of their viability, in early breast cancer non-viable cells have limited clinical relevance (108) (109). Thus, the assessment of CTC viability is still an important feature for an analysis method and was provided as well by the maintrac® method as by the filtration-based method evaluated in this study.

Another feature required for the self-renewal potential of cells was an intact nucleus. Therefore, nuclei were either visualized by transmitted light microscopy or stained with the dye Hoechst33342 for fluorescence microscopy. The latter option was preferred for integration into a LoC system, as it did not require transmitted light imaging and fluorescence detection is easier in such a system and needed for evaluation of the other described cell properties anyway. Moreover, the Vivalytic LoC platform's optical system already contained one capable of fluorescence detection. Cells that stained positive for EpCAM, Hoechst33342 nucleus dye and negative for PI as dead cell dye were counted as relevant CTC.

Several staining strategies compatible (listed in Table 14) with the Vivalytic system were evaluated and successfully established using cancer cell lines. EpCAM-positive BT-474 cells and HCT116 cells were reproducibly detected after staining with EpCAM antibodies conjugated to either FITC or APC. The APC conjugated antibody showed lower efficiency in staining cells in patient samples. Therefore, the FITC-labeled antibodies were preferred for immunofluorescent analysis of patient samples. Using cancer cell lines, both conjugates were suitable. In the Vivalytic analyzer, the APC conjugated EpCAM antibodies were detected more easily than FITC conjugates EpCAM antibodies. According to the Fluorochrome brightness index (Miltenyi Biotec), APC is rated with the brightness value of 5 based on mean fluorescence intensity, whereas FITC is rated with 2. The highest brightness is rated with a value of 6 and the lowest brightness with a value of 1 (110).

Although overexpression of EpCAM is described for cancer cells of epithelial origin, and the detection of EpCAM-positive cells strongly indicates them as being malignant, the simple presence of EpCAM does not unequivocally identify a cancer cell. Using EpCAM as cancer cell biomarker is critically discussed. EpCAM expression is downregulated during EMT, and CTCs and even normal cells present in blood might show very heterogeneous EpCAM expression leading to misinterpretation (111; 112; 113; 114). As an alternative or additional epithelial cell identifier, cells are often stained for detection of cytokeratines (CK) 8, 18 and 19 to verify the epithelial origin of the detected cells (115). However, for staining with fluorescently labeled CK antibodies, cells need

to be fixed by formaldehyde prior to staining as CKs are intracellular markers (116). Thus, cell viability would have to be determined before CK-staining. Another possibility to enable cytokeratin staining in addition to EpCAM and still assess cell viability would be fixable live/dead staining using amine reactive dyes (117). However, this requires accurate design of experiment regarding fixation and permeabilization time and suitable controls to ensure that permeabilization efficiency is high and no cells are falsely interpreted as live or dead. Besides detection of EpCAM-positive cells (EpCAM⁺) of Cytokeratin-positive cells (CK⁺) alone, in some studies distinction is made between EpCAM⁺/Cytokeratin⁺, EpCAM⁻/Cytokeratin⁺, EpCAM⁻/Cytokeratin⁻ CTCs (111; 112). Wang et al. reported that despite cytokeratin detection in addition to EpCAM based isolation of CTCs in the CellSearch method, there are still potential CTCs that are not determined as such. Some cells that were isolated based on their EpCAM expression stained negative for both cytokeratin as additional epithelial marker and CD-45 as leukocyte marker. This strongly indicates that these cells could have undergone EMT (115). To cover the CTC heterogeneity by immunofluorescence, further cell surface markers need to be evaluated and added to the assays. For example, vimentin is described as mesenchymal marker that is translocated from the cytoplasm to the cell surface in cancer cells during EMT for lung, prostate, breast or colon cancer (118; 119; 120). In normal cells in contrast, vimentin is only detected in the cytoplasm. Thus, a specific cell-surface-vimentin antibody might be an appropriate additional marker (100).

In this study, EpCAM was used as model target antigen to detect and count CTCs in model samples and patient samples and for establishment of the LoC compatible method as the cell lines available for generation of model samples were of epithelial origin and showed uniform EpCAM expression. The aim was to establish an efficient method for counting of these target cells rather than covering a high heterogeneity of cells within the model samples. Detection of known cells enabled real-time detection beneficial for maximization of the quantification efficiency.

In summary, there are no definite criteria to doubtlessly define cells as malignant by immunocytochemistry methods. Ongoing challenges in the use of CTC include improvement in sensitivity and specificity, standardization of techniques, and evidence of reproducibility. Support for identification of cells as tumor cells could be provided by molecular analyses and clinical studies showing their prognostic significance (121).

4.2.1. Evaluation of erythrocyte depletion methods in regard of LoC integration

Erythrocytes are the most abundant cell type in blood (122). The high number of normal blood cells compared to rarity of CTCs made CTC detection and isolation very challenging and was the reason for the high viscosity of the blood sample and pressure difference on the filter. Furthermore, the high amount of hemoglobin hampered optical detection. Therefore, methods that ensure efficient erythrocyte depletion without loss of CTCs were required for sample preparation. Of the three different methods for erythrocyte depletion evaluated in this study, selective erythrocyte lysis with subsequent centrifugation achieved the highest spiked cell recovery.

To establish a method for erythrocyte depletion after selective lysis without centrifugation, a filtration-based method was evaluated using the filtration functional model described in chapter 2.3.1.1. Filtration of samples containing lysed and unlysed erythrocytes was compared revealing that lysis of the erythrocytes was not only favorable in terms of higher recovery rate but also for optical detection of the stained target cells. A reason for this was the release of the hemoglobin contained in the erythrocytes and its dilution by the surrounding medium that resulted in decrease of refractive index and reduced internal scattering of lysed erythrocytes compared to intact erythrocytes. This consequently led to a better transparency of the blood and improved the excitation and detection of the fluorescence signals of the stained cells in the suspension. The thickness of the lipid bilayer membrane of erythrocytes is only $46.0 \pm 0.5 \text{ \AA}$ (123) and intact erythrocytes are highly deformable as they can pass capillaries in the blood system as thin as 8 \mu m (124). The deformability of the erythrocyte was assumed to even increase after selective lysis and can be seen in Figure 26. Furthermore, target cell capture was higher after filtration of samples containing lysed erythrocytes compared to filtration of samples containing intact erythrocytes. Thus, it was supposed that pressure increase was lower because the lysed erythrocytes passed through the filter more easily. However, to better understand the changes in erythrocyte deformability and the effect of selective lysis further methods such as osmotic gradient ektacytometry (125), atomic force spectroscopy (126) or optical tweezers (127) could be used on lysed erythrocytes in comparison to intact erythrocytes.

Viability of cells incubated in the erythrocyte lysis buffer was assessed to ensure that leukocytes and CTCs are not lysed or negatively affected by the buffer. As described in chapter 3.2.2.3, it was found that incubation of CTCs and leukocytes for 15 min was possible without adverse effect.

Viability decreased significantly only after 45 min. However, the erythrocyte lysis process and subsequent filtration for CTC capture using the filtration-based approach should take no longer than 15 to 20 min. Thus, the maintenance of cell viability was complied with. The selectivity of the erythrocyte lysis buffer to lyse erythrocytes but no other cells present in blood resides in its isotonic composition of ammonium chloride, sodium bicarbonate and ethylenediaminetetraacetic acid. As erythrocytes but not the other blood cells possess a $\text{Cl}^-/\text{HCO}_3^-$ exchanger in their membrane, only erythrocytes should be affected by the selective lysis buffer (128). Lara et al. determined 90 % viability of the MCF-7 and 95 % viability of the leukocytes by trypan blue exclusion after erythrocyte lysis with 5 min incubation, 5 min centrifugation and two washing steps (91). In this study, the erythrocyte lysis buffer was incubated with the sample for 10 min to 15 min and centrifuged for 10 min. In case of erythrocytes lysis before sample filtration, the sample was transported through the filter after incubation of 10 min and the filter was washed with 1 x PBS.

4.2.2. CTC isolation evaluated in regard of the integrability to the LoC system

To enable CTC isolation from a blood sample after selective erythrocyte lysis without centrifugation, an alternative separation method was established as the current Vivalytic system did not allow centrifugation. Different CTC isolation methods from literature were compared and rated using the concept decision matrix according to Pugh (129). Taken into consideration all the criteria listed in chapter 3.2.3, mechanical filtration resulted as the method most suitable for Vivalytic integration as it was independent of a constant flow or more specifically compatible with the pulsatile flow of the pressure driven Vivalytic LoC system. The main advantages of a filtration-based approach in regard of the LoC integration are the independence of a constant flow rate as well as the possibility to deplete red blood cells and partly leukocytes without centrifugation. Furthermore, filtration approaches are size-based and biomarker independent enabling the isolation of all types of CTCs and other blood cells matching the pore size of the system. Thus, cells with low EpCAM or cytokeratin expression can be isolated, and all cells captured can be stained for different antigens to obtain a more complete insights into the CTCs variety contained in the blood sample.

In this study, a cell capture rate of 60 % to 90 % depending on the cell type was achieved by filtration of a blood sample using filtration functional models with integrated TEM-grids after selective erythrocyte lysis (88). Although the pores were even smaller than the erythrocyte

diameter, the erythrocytes could be successfully depleted after selective lysis. Coumans et al. (2013) compared capture rates of CTC after sample filtration using TEM-grids to track-etched filters and micro sieves. Thereby, they found that a large area of 83 % of the TEM-grid was covered by red blood cells and therefore described that the track-etched filters and micro sieves were preferred for isolation of CTCs (130). In the study presented here, the erythrocytes were depleted by erythrocyte lysis and passed the filter without comprising the optical detection of the target cells.

During the filtration experiments with the filtration functional model with integrated TEM-grid described in chapter 3.2.4.2, different factors that influenced cell capture and cell recovery rate were identified. These findings were important for integration of the filter element into the LoC cartridge in the subsequent step.

One important influencing factor was passivation of the microfluidic channels with 1 x PBS with 1 % (w/v) BSA to reduce the material hydrophobicity before the filtration experiments was important to successfully prevent cell adsorption to the tubes and channel walls. As shown in Figure 31, 100 % of the cells could be recovered from a passivated filtration functional model without integrated filter, but only $82 \% \pm 4 \%$ without passivation. BSA was described in literature as anti-fouling agent by rendering surfaces like plastic ware used in cell culture hydrophilic (131) (132). Jeyachandran et al. described a blocking efficiency of 90-100% on a hydrophobic and 68-100% on a hydrophilic surface using a solution with a BSA concentration of only 1 mg/mL (compared to 10 mg/ mL used in this study). Passivation of the microfluidic channels on the cartridge might also play a role in preventing the non-specific adsorption of not only the cells but also antibodies and fluorescent dyes used for cell detection as well as primers and probes added for molecular analysis (133).

Another key factor influencing cell capture was the design of the microfluidic model. Experiments with the two different designs of filtration functional models revealed that the even distribution of the cells on the filter achieved with the two-armed design favored both the optical detection and the retention of the cells on the filter. The higher capture rate might result from the reduced pressure difference that was built up when cells were evenly distributed on the filter. In addition, optical detection profited from an even distribution as cells could only be efficiently quantified when captured as monolayer as shown in Figure 32.

Apart from filtration functional model design, cell capture was highly dependent on cell size, deformability, and nucleus to cytoplasm ratio. Consequently, cell capture rates might vary strongly when samples from different tumor types are applied in the filtration-based method. This was observed by comparing capture rates of the spiked epithelial cell lines BT-474 and HCT116. The BT-474 cells have a diameter of $17.4 \mu\text{m} \pm 1.5 \mu\text{m}$ whereas the HCT116 cells possess a diameter of only $12.8 \mu\text{m} \pm 1.6 \mu\text{m}$ which was reflected in the capture rates of $89 \% \pm 6 \%$ and $64 \% \pm 5 \%$. The high capture rate obtained for the BT-474 cells could reside in their higher diameter but also in their lower deformability. Hwang et al. (2016) found that the BT-474 cells were the least deformable among three breast cancer cell lines evaluated by single-beam acoustic trapping (134). This study also showed the effect of deformability by comparing the K562 cells' capture rates to the HCT116 cells. Although the K562 cells have a higher diameter of $15.4 \mu\text{m} \pm 0.8 \mu\text{m}$, a lower capture rate of $54 \% \pm 10 \%$ was observed since K562 originate from the bone marrow and are suspension cells that might be more deformable than the other epithelial cell types examined. Similar observations were made during micro sieve isolation of two different colorectal cancer cell lines (RKO and HCT116 cells) of which the HCT116 cells were smaller but less deformable and capture rate was therefore higher. It was also observed that HCT116 stick together during growth while the RKO cells grow as individual cells that do not attach to the other cells to such great extent (135). These observations emphasize the importance of analyzing both epithelial and mesenchymal cells and their individual capture rate during filtration. This is especially important because it is described that the CTCs that are more deformable show higher invasiveness and aggressiveness (136). Therefore, detection and enumeration of these cells might be more important for evaluating the tumor progression, therapy response and development of resistance to therapy. However, in general CTCs are described to be less deformable than normal, non-malignant cells (137). Furthermore, the nucleus-to-cytoplasm ratio is described to be larger in cancer cells (138). This led to the assumption that the filtration-based method presented here is suitable for CTC detection from a liquid biopsy, especially in combination with the real-time detection method. The proof-of-concept study with the UKT and SIMFO presented in this study was performed with colon cancer cells from either cell line HCT116 or from gastrointestinal cancer patients. These cells were found to range between 11 and 15 μm . For the patient samples, a similar CTC capture rate of $64 \% \pm 5 \%$ was determined which matches the results of the colon cancer cell line HCT116. For a broader understanding of the dependency of cell capture rate from size and deformability or cell

origin, the study could be expanded to analysis of samples from patients suffering from different tumor types as for example breast or cervical cancer. The sizes of these cancer cell types range between 15 μm and 40 μm and therefore capture should be more efficient. Hereby, the usage of real patient samples is particularly important as cell lines cannot cover the heterogeneity of patients' CTCs. Furthermore, in patient samples, varying numbers of CTCs are expected during therapy. In this study, no significant difference was observed regarding the capture rate of different cell spike numbers in a range of realistically expected CTC numbers in patient samples.

Besides high capture efficiency, sample purity and depletion of non-target cells are often evaluated in CTC isolation methods. For evaluation of leukocyte depletion, the leukocytes were stained and counted on the filter and in the waste fraction. This resulted in a depletion rate of 93 % \pm 1.4 %. The second method used for determining leukocyte depletion was comparing the GAPDH expression in control leukocyte lysates and lysates obtained from the leukocytes captured on the filter. A depletion rate of 2.1 to 3.2 log stages was determined (see Figure 43). These results were comparable to the filtration system of Sajay et al. (139) which achieved a leukocyte depletion of 2.3 log stages, but this was achieved by an additional magnetic capture step of leukocytes by CD-45 together with the filtration process. Hereby, they could deplete 97 % of the leukocytes by immunomagnetic capture whereas in this study, more than 93 % of the leukocytes were depleted by filtration alone (see Figure 42). However, additional immunomagnetic capture of the leukocytes using magnetic nanoparticle or immunoaffinity capture on surfaces with immobilized antibodies might be promising methods to increase sample purity further. This might be necessary to increase sensitivity of downstream molecular methods such as expression, mutation analysis or library preparation for sequencing.

It was assumed that the leukocyte type with the largest diameter or the highest granularity was the most probable to be captured on the filter. Considering the cell size and abundance in the human blood, the leukocyte fraction captured on the filter could have been monocytes that have a diameter of 15-20 μm and account for approximately 2 % to 8 % of all blood leukocytes (140). This value correlated with the depletion rates determined. To prove this hypothesis right, monocyte-specific antibodies as for example against CD14 and other leukocyte subtype-specific antibodies could be used to differentiate all leukocytes captured on the filter. This was already shown by Coumans et al., who described that monocytes are enriched by 165 % on track-etched filters whereas

granulocytes and lymphocytes are depleted (130). In total, they state that only 0.1 % of the leukocytes from a 1 mL blood sample are captured on the filter which corresponds to a reduction of 3 log stages and is consistent with the results described in chapter 3.2.4.4 in this study.

4.2.2.1. Cell detection and tracking in real-time increased quantification efficiency

During the cell capture experiments using the filtration functional models, it was observed that cells captured on the filter could pass the filter dependent on the time and cell size. Thus, it was assumed that the filter could serve as deceleration element for all cells. As filtration is prone to cell loss due to heterogeneity in size and deformability, real-time based detection methods were evaluated and established for counting of captured cells during the filtration process instead of after endpoint quantification. The real-time detection method had the advantage that enumeration efficiency was significantly increased. Hereby, cells that could pass the filter after a certain amount of time due to their size or deformability were detected. Although these cells were not captured and available for downstream analysis, their optical detection was ensured. This was achieved by acquisition of an image series or video during filtration of CFSE or EpCAM stained cells. These were then counted either manually, using the microscope software cellSens with the count and measure (without and with manual correction) tool or by a MATLAB based tool. Real-time counting in comparison to endpoint quantification led to an increase of quantification efficiency of up to 20 % based on the evaluation method (see chapter 3.2.4.3). The results obtained by the microscope software without manual correction were significantly lower than with manual correction as cells with lower fluorescence intensity were not detected or cell cluster could not be differentiated. The MATLAB tool was more efficient in terms of separating and recognizing cells cluster and results comparable to the microscope software with manual correction.

For the detection in a video or image series, application of machine learning methods was very useful as manual counting was time consuming and prone to operator dependent errors. Existing cell imaging solutions like the Broad Institute Cell Profiler or the CellSens Dimension tool were evaluated for real-time cell detection. These tools use thresholding-based methods e.g., Otsu's (141) for cell detection and segmentation together with postprocessing algorithms like evaluation of diameter or declumping of cells. Simple frame-by-frame matching between cell detections were used for tracking. Such methods perform well if the signal-to-noise ratio is high and the microscopy parameters can be optimized e.g., to have high contrast and low background

illumination. These conditions could not be met in the filtration-based method developed for CTC detection using the fluorescence microscope or the Vivalytic analyzer. As a result, these standard solutions' performance differed in sample dependence, staining efficiency and microscope settings. Modern computer vision algorithms use convolutional neural networks for the detection and segmentation of target objects. For the detection of cells in serial fluorescence microscopy images, several specialized algorithms are available from literature, e.g., for detecting star-convex polygons (142). These were used for tracking of EpCAM-positive cells captured on the TEM-grid during filtration using the filtration functional model described in chapter 2.3.1.1 and worked well on tracking one cell type in one fluorescent channel. However, challenges that must be considered are varying signal-to-noise ratios, background signal, varying sample and image quality, difficulty in reference input information, heterogeneous sizes, and signal possible leading to errors in tracking results. The limiting factor in differentiating viable from non-viable, nucleus containing EpCAM positive cells resided in the image acquisition using fluorescence microscopy. Switching of the required fluorescence filters was necessary for detection of EpCAM-FITC, Hoechst33342 and PI but was not possible in real-time with the current optical system of the microscope or the Vivalytic. A feasible option might be provided by using multiband filter cubes or fast switching filter wheels enabling faster image acquisition due to quick or simultaneous excitation of the different fluorophores.

4.2.3. Integration of CTC isolation and detection into the Vivalytic LoC platform

The filtration-based CTC capture method could be integrated into the current Vivalytic system for a proof-of-principle. Cell transport in the microfluidic system was successful and parameters for maintenance of cell viability and minimization of cell loss were identified.

Different boundary conditions were given by the current system were considered for the experiments: Centrifugation for erythrocyte depletion was not possible, the analyzer had a specified operating temperature of 40 °C, membrane assisted pump mechanism provided no continuous flow, limited buffer storage, (no toxic components, storage at room temperature), and long-term storability of the reagents.

Of the evaluated erythrocyte depletion and CTC isolation methods (see Pugh matrix in the appendix in figure A1), filtration was the most suitable for integration into the Vivalytic cartridge without major modifications of the current cartridge design. On membrane-based microfluidic systems like

the Vivalytic system, continuous flows cannot be realized as the transport of fluids is driven by filling and emptying pump chambers and valves. The resulting flow profile was pulsatile. One advantage of filtration in regard of the integration into the Vivalytic system is that filtration is not dependent on a continuous flow. As shown in Figure 38, neither the different flow rates nor flow profiles significantly influenced the HCT116 cell capture rate. The TEM-grid used in the filtration functional model (described in chapter 37) had the same diameter (2.5 mm) as the filter chamber designed for the nucleic acid extraction filters. Solely the TPU membrane needed to be enlarged in this area to enable optical detection of the cells on the filter. For fluorescence analysis of the stained cells, the cartridge needed to be removed from the analyzer and observed using the upright fluorescence microscope as the filter chamber is not within the field of view of the analyzer's optical detection system

The highest cell capture rate of $55 \% \pm 7 \%$ was achieved by cell transport through the filter by negative pressure. This was achieved by suction via the pump chamber beneath the filter chamber. By peristaltic pumping, a capture rate of $55 \% \pm 17 \%$ was determined. Thus, suction pumping was regarded as the most beneficial fluidic program for cell capture on the filter. The capture rate was more reproducible when the suction pumping was used, as was determined by the standard deviation of the results. The channel geometry was suitable for fluid distribution onto the filter but impeded the view on the cells captured and led to light scattering during fluorescence detection. However, the current cartridge design with an integrated TEM grid could be used for a successful proof-of-principle of on-chip CTC isolation and detection. Assuming that the cells are evenly distributed on the filter, the area that is covered by the channel can be neglected and the total cell count can be estimated by counting 50 % of the filter and doubling this number. For fully automated CTC detection inside the analyzer, either the optical system needs to be placed above the filter chamber in a future analyzer design, or the filter chamber needs to be placed on the lower part of a future cartridge design (e.g., the array chamber) at the location of the current optical system in the analyzer (see Figure 1 for the current cartridge design).

Besides the high capture rate, viability of the cells should be maintained during the filtration process despite elevated temperature of 40 °C and shear stress inside of the LoC system. In this study, the impact of microfluidic processing on cell viability was assessed by trypan blue and CellTiter Glo assay. Cells were incubated at 40 °C without adverse effect after the required

processing time of 15 min (see Figure 46). The effect of shear stress and microfluidic transport on the viability was strongly dependent on the path and frequency chosen on the cartridge and pump mode. Just as for the capture rate, for the maintenance of cell viability, the fluidic transport of the cells by suction pumping was the most favorable. Viability was reduced by $6\% \pm 7\%$ after transport via peristaltic pumping and only by $5\% \pm 8\%$ via suction pumping. Initially, peristaltic pumping was hypothesized to be the most suitable as flow rates of approximately $2\ \mu\text{L/s}$ (estimated fluid shear stress (FSS) of approximately $1.2\ \text{dyn/cm}^2$) can be achieved whereas using the pump chamber flow rates $> 100\ \mu\text{L/s}$ (FSS of approximately $60\ \text{dyn/cm}^2$) were achieved. However, peristaltic pumping valves are used for fluid transport instead of the pump chamber bearing the risk of cells getting stuck and damaged by the deflection of the TPU membrane. In the case of fluid transport via pump chambers, the risk of cell damage is lower due to the favorable shape of the pump chamber where the contact pressure of the TPU membrane is lower. As observed by Fan et al., shear stress of $60.5\ \text{dyne/cm}^2$ led to decrease of cell viability and cell proliferation of the surviving cells at a circulation time of 1 h (143). However, in the case of the filter-based cell capture method, the time of cell exposure to fluid shear stress can be kept to a minimum of <5 min. During this time, Fan et al. observed no significant reduction in viability (143).

Cells circulating in the blood stream of the human body are also exposed to FSS of $0.5\ \text{dyn/cm}^2$ to $4.0\ \text{dyn/cm}^2$ in the veins and from $4.0\ \text{dyn/cm}^2$ to $30.0\ \text{dyn/cm}^2$ in the arterial system. However, in some regions of blood vessel bifurcation, in the heart or in large vessels, CTCs can even encounter FSS of $> 1000\ \text{dyn/cm}^2$ to up to $3000\ \text{dyn/cm}^2$ (144) (145). This is further described as a reason for the low survival of only 0.1% of all CTCs that exit the tumor mass and enter the blood stream (146). This small proportion of CTC is hypothesized to survive due to resistance to FSS in contrast to non-cancerous cells (147). It was therefore assumed that CTCs isolated from patient samples could be less sensitive to the FSS in the microfluidic system than the cell line cells used in the presented experiments in chapter 3.2.3.

In summary, for cell transport and CTC capture in the current Vivalytic system, processing time and cell contact with valves should be kept to a minimum to maintain cell viability and minimize cell loss. To reduce cell loss, the microfluidic network should be prewetted and coated by BSA as also described beneficial for the filtration functional model (see Figure 31). Furthermore, options to reduce shear stress or cell sensitivity towards shear stress could be evaluated. For example, the addition of agents like Pluronic F-68 ($1\ \text{g/L}$ to $5\ \text{g/L}$) was described to improved robustness of cell

under FSS (148) (149). Besides, another beneficial effect was described for Pluronic F-68: it led to short-term decrease of cell deformability within an incubation time of 3 h (150). This effect can be taken advantage of during cell capture by filtration, possibly leading to a higher cell capture rate.

4.2.3.1. Optical cell detection using Vivalytic

Optical cell analysis using the current optical system of the Vivalytic analyzer and the VPhotoStar software (shown in Figure 10) revealed that the resolution of 60 μm was sufficient for recognition of fluorescence-stained cells as light spots (as shown in Figure 57). The fluorescent signal was dependent on the fluorescent dye and part of the cell that was stained. If cell density were below 10^3 cells/mL and cell distance were above 60 μm , cells could be detected and counted using the Vivalytic optical system. The signal of CFSE stained cells was best detected as CFSE stains the whole cell cytoplasm and results in a larger area that emits fluorescent light. In contrast, cells stained by antibodies against surface antibodies required longer exposure times and resulted in lower brightness as only the outer membrane was stained resulting in a smaller area that emits fluorescent light. Further possibilities for cell detection despite the low resolution and high cell density might be to detect the total fluorescence and estimate the cell number from the mean fluorescence value. However, this might lead to insufficient separation of cell clusters and the assignment of different cell dyes to single cells or single pixels would not be possible. However, this was important for the enumeration of EpCAM-positive, nucleus containing, viable cells whereas dead cells were excluded from the cell count. Thus, for extension of the Vivalytic system by a cell detection function, the optical system would need to be adapted towards increased resolution and magnification to enable detection and comparison of the position of the single cells with the stated properties.

4.3. Complementary information obtained from molecular analysis of captured CTCs

Optical detection, characterization and enumeration of CTCs could give information on the disease progression and therapy success (151). In combination with downstream molecular analysis a more complete insight into disease progression can be obtained as some cell characteristics are not detectable by staining alone or do not allow definition of cell malignancy (152). Moreover, the great potential of CTC analysis and the advantage over cfDNA and ctDNA analysis methods, rely

in the possibility to obtain information on protein expression on the surface and inside the cell to enumerate the cells, as well as expression and mutation analysis after RNA and DNA extraction (153).

In this study, analysis of mesenchymal markers Twist and Snail in comparison to EpCAM was chosen for a proof-of-principle of cell lysis and molecular analysis after capture on the filter. Gene expression of Snail, Twist and EpCAM was correlated to the EpCAM protein expression determined by immunocytochemistry. The aim was to evaluate whether Twist and Snail expression is higher when only few EpCAM positive cells could be determined by immunostaining or whether in turn, Twist and Snail expression was low when many EpCAM positive CTCs could be detected. These experiments were based on the hypothesis that EpCAM expression is downregulated during EMT and therefore, CTCs cannot be detected using antibodies against epithelial surface proteins such as EpCAM. Immunostaining of Twist and Snail in turn was not possible without fixation of the cells and therefore these markers were analyzed on molecular level. By detection of both epithelial and mesenchymal markers, a better insight into disease progression could be obtained.

For this purpose, RNA was extracted from the patient samples as described in chapter 2.4.1.1. The maximum storage time of the blood sample for extraction of RNA of sufficient quality was determined by assessing the RNA integrity number after storage at 4 °C and RT for 24 h and 48 h. After 24 h, the RIN was acceptable for both blood samples stored at 4 °C (RIN=6.6) and RT (RIN=7.2). Similar observations were made by Huang et al. (2017) who described significant quality decline during blood storage of more than 24 h independent of the storage temperature (154). In addition to degradation, Tanner et al. (2002) observed significant changes in gene expression level of anti-inflammatory genes and transcription factors upon storage (155). Thus, RNA from the patient samples obtained from the UKT for gene expression analysis as described in chapter 2.4.3 was extracted at the same day of sample taking or at maximum after 24 h to prevent degradation and changes in expression levels. Only RNA samples from patient blood with a RIN above 5 were used for gene expression analysis by RT-qPCR.

The expression level of EpCAM, Snail and Twist were determined in relation to the housekeeping gene GAPDH and compared to either the baseline value or to a pooled standard RNA sample from leukocytes of healthy anonymous donors.

In the case of patient BO-645, Twist and Snail expression and expression of EpCAM inversely correlated at sampling time point 3. Despite the microscopically observed decrease in the number

of EpCAM-FITC positive cells, a progression of the tumor was observed in the CT-scan in the clinical setting at the same time. The observation led to the assumption that the CTCs present in the sample underwent EMT and the phenotype was mesenchymal and therefore the cells could not be stained by the EpCAM antibody. This corroborates the hypothesis that the mesenchymal markers Snail and Twist can serve as prognostic indicator in case of downregulation of EpCAM during EMT.

As shown in Figure 60, the number of EpCAM positive cells did not correlate to the gene expression level observed by RT-qPCR in the case of patient BO-408. Several research groups have shown that correlation between mRNA and protein abundances in the cell is relatively low (156). Only about 40 % of the variation in protein concentration correlated to mRNA abundances (squared Pearson correlation coefficient of ~ 0.40 , (157; 158)). Gry et al. even found correlation coefficients ranging from only 0.2 to 0.5 when comparing RNA and protein profiles of 23 human cell lines (159). This was also observed during CTC analysis by Nagrath et al. (2018) who found differences in EpCAM protein and RNA expression. They used EpCAM antibodies for capture of the EpCAM-positive cells which indicated protein expression but in contrast determined low expression of EpCAM RNA (160).

Although protein expression and RNA expression only weakly correlate for the same target, valuable information can be obtained from analysis of CTC on protein and RNA level by immunocytochemistry in combination with RT-qPCR as an increase in the transcription factors Twist and Snail analyzed in this study is described to provide insight into the disease progression. Twist overexpression is common in metastatic carcinomas and targeting Twist e.g., by inactivation is described to hold great promise as a cancer therapeutic (161). In summary, the correlation of expression of specific markers with disease progression needs to be proven with a large patient cohort. It would only be beneficial if diagnostic sensitivity were increased by expression analysis. Narrower sample taking would be beneficial to determine which markers give hints on therapy success earlier, CTC count or gene expression level.

4.3.1. Compatibility of the filtration-based CTC capture with downstream analysis

To minimize RNA loss, a method was established that enabled reverse transcription (RT) directly performed using the crude cell lysates. Several lysis buffers were evaluated regarding detection

efficiency, RNA stability, reproducibility, and LoC integrability. LB04 was identified as the most efficient lysis buffer as the highest copy number was detected and agarose gel electrophoresis of PCR product showed solely the desired band. Consequently, the following experiments were performed with LB04. In literature, different lysis buffers were described with varying lysis efficiencies and resulting in different quality of obtained RNA. Non-ionic detergents could be used for generation of crude cell lysates amenable to direct analysis by one-step RT-qPCR without the need of addition of RNase inhibitor (162). According to Svec et al. (163), direct cell lysis with non-ionic detergents or BSA resulted in efficient cell lysis, high RNA stability, and enhanced reverse transcription efficiency and was even described to outperform standard column-based extraction methods in terms of RNA yield (163) (164). The results obtained in this study are consistent with the results described in the literature showing that mRNA loss is likely to occur during column-based extraction, and that therefore direct lysis methods provide an attractive method in which reverse transcription can be performed directly on the cell lysate. Direct lysis methods are also simpler, cheaper, and less time consuming than column-based RNA-extraction methods for subsequent gene expression analysis of CTCs. However, these methods were described more effective for small cell numbers and single CTCs isolated without background cells as for example leukocytes (164). As the focus in this study was set on the analysis of CTCs isolated altogether with leukocytes rather than on the depletion of leukocytes, the tolerance for the maximum number of leukocytes present in the sample was determined (see Figure 62). As described in chapter 85, > 93 % of the leukocytes could be depleted by the filtration-based method. In the experiment in chapter 3.4.3, it was determined that RT-qPCR worked well for all targets starting at a leukocyte dilution of 1:100 which corresponds to a depletion of 99 %. At lower dilutions of 1:10, the RT-qPCR was not linear, due to inhibition effects. This was consistent with the observation that a higher number of leukocytes in the assay resulted in a shift of real-time amplification curves (165). Consequently, for robust RT-qPCR using lysates obtained from the cells captured on the filter, leukocyte depletion needs to be increased by additional washing steps. Alternatively, immunoaffinity isolation of cells via immobilized antibodies could increase sample purity. Several methods have been described in which CTCs are captured on functionalized surfaces (166) (167). Instead of CTC isolation by immunocapture, leukocytes could be depleted by antibody coated surfaces or magnetic beads before filtration. This way, a leukocyte-depleted sample would pass the filter leading to a higher purity of the captured CTC fraction. This was shown in (168), where

stacked layers of chemically functionalized microfluidic channels were used for depletion of millions of white blood cells before CTC capture to up to 90 %. In (169), a depletion of > 2 log-stages by capturing $> 99.5\%$ of white blood cells from 10 mL of blood was achieved with recovery of $> 90\%$ of spiked tumor cells.

After determination of the maximal background tolerance of the RT-qPCR, the possibility to generate cell lysates from target cells in sample tubes or from cell captured on the filter was evaluated. HCT116 cell suspensions with defined cell numbers of 10^4 , 10^3 , and 10^2 cells were filtrated using the filtration functional model as described in chapter 2.3.1.1 and cell suspensions with the same cell numbers were lysed in a sample tube as references. The aim was to determine the minimal cell number required for detection of EpCAM, Twist and Snail copies by RT-qPCR in the cell lysates. Whereas EpCAM could be detected in all cell dilutions analyzed from both lysates from lysis in the sample tube and filter lysates, Twist and Snail could not be detected in the lysates from filtration of 10^2 cells. However, the copy numbers detected in the filter lysates of 10^4 and 10^3 cells were up to 10 times lower than the copy number detected in the sample tube cell lysates. This led to the assumption that besides loss of whole cells through the filter, which was determined to be approximately 40 % (see chapter 3.2.3 for HCT116 capture rates), RNA was lost in the process of cell lysis and recovery of the cell lysate from the filter. In the cell lysate generated from 10^2 cells and recovered from the filter, the RNA yield was probably too low for RT-qPCR detection. Thus, it was suggested that for the combination of blood sample filtration for CTC quantification and subsequent cell lysis for RT-qPCR analysis of at least 10^3 target cells must be captured. Consequently, the blood sample volume might need to be adapted after initial CTC quantification to capture sufficient cells for further analysis. But in summary, it was successfully shown that RT-qPCR analysis was possible with crude cell lysates as templates and did not necessarily need RNA purification in advance. For better standardization of lysate generation in future, a commercially available kit for direct, probe-based RNA detection and quantitation could be used as for example the Luna® Cell Ready One-Step RT-qPCR Kit (New England Biolabs, Frankfurt, Germany), a Cells-to-Ct Kit (Thermo Fisher Scientific, Waltham, USA) or RealTime ready Cell Lysis kit (Roche, Basel, Switzerland). These methods are well described and increase processing speed and throughput and offer possibilities towards automation of RT-qPCR analysis using limited sample material at comparable or improved sensitivity and accuracy compared to conventional methods that require RNA extraction (170).

A method that enables increasing sensitivity independent of increasing the sample purity is the technique of nested PCR. Hereby, the target genes in the samples were successfully pre-amplified to increase sensitivity. As shown in chapter 3.4.4.1, using nested RT-qPCR all targets could be detected in the lysates of down to 10^1 HCT116 cells whereas in the conventional RT-qPCR, EpCAM could not be detected in the cell lysate of 10^1 cells, and Snail and Twist could not be detected in the cell lysates of 10^1 and 10^2 HCT116 cells. This observation is comparable to results reported in the literature for nested and semi-nested RT-qPCR approaches for the detection and enumeration of single tumor cells in a high background of mononuclear blood cells. Thereby, semi-nested PCR enabled the detection of down to 5 target cells per mL blood without the need for RNA extraction (165).

Another important adaptation towards integration into the LoC platform was the possibility of multiplex analysis and long-term storability of RT-qPCR components at RT. Therefore, different primer concentrations and combinations were evaluated in multiplex approaches and primers/probe mixes were air dried and stored for 3 h, 24 h, 21 days and 42 days at RT and 55 °C. Storage at elevated temperatures provided the possibility of accelerated long-term storage stability estimation. As described in chapter 3.4.5.1 and chapter 3.4.5.2, neither multiplexing nor storage of the RT-qPCR components had significant adverse effects on the performance of the RT-qPCR and the proof-of-principle under on-chip conditions was successfully shown (171) (172). The storage experiments revealed only slightly better performance for the RT-qPCR with the components stored with the additive trehalose for stabilization. The same observations were made by Rombach et al. (173), where primers and fluorophore-quencher combinations were stored for one year at room temperature for evaluation of their potential use for in vitro diagnostic (IVD) products comparable to the Vivalytic system. Thus, the expression analysis presented in this study would be suitable for LoC integration.

In summary, in the study presented here, a method for the phenotypic analysis of CTCs isolated from a liquid biopsy was established providing the possibility for cell detection and quantification as well as characterization regarding their epithelial origin. Moreover, a proof-of-principle of expression analysis of the captured cells was shown indicating that additional information on the origin or epithelial or mesenchymal state of the cells could be gained. Cell detection and quantification were shown in the established filtration functional model as a first prototype and in adapted LoC cartridges with slight modifications compared to the current cartridge design. Despite

optical analysis and expression not being technically feasible on the current system, the unit operations have been implemented as proof-of-principle using experimental conditions that were compatible with the LoC system. However, the filtration functional model as such a combination with a syringe pump and a fluorescence microscope can already be used as tool for accompanying CTC analysis in clinical cancer treatment studies to help elucidating whether therapy decisions could be made based on changes in CTC counts.

5. Conclusion and Outlook

The established filtration method presented in this study enables sample processing without manual preprocessing steps, the maintenance of cell viability, real-time detection for the maximization of quantification efficiency in a time to result of less than 20 min. For further applications, it provides the option to stain the cells either before or after capture, to capture the viable cells first and fix them in the second step for staining with further antibodies and the possibility for downstream analysis after quantification of the cells.

CTCs from blood were successfully captured and detected. An even distribution and increased capture of cells on the filter could be achieved by using the two-armed filtration functional model (as described in chapter 3.2.4.2). Furthermore, three different cell lines and patient blood samples were processed with the filtration functional models and imaged by fluorescence microscopy. Large cells ($< 15 \mu\text{m}$) were captured with higher efficiency than smaller cells (capture rates of $54 \% \pm 10 \%$ to $89 \% \pm 6 \%$).

Quantification efficiency for smaller cells was significantly improved by up to 20 % by detecting the captured cells in real-time and first algorithms for automation of cell detection and tracking were established (described in chapter 3.2.4.3). Real-time quantification provided a significant advantage compared to the state-of-the-art endpoint detection and is a promising tool to overcome the disadvantages related to filtration-based approaches for CTC isolation. Future work on the algorithm could include differentiation of different dyes and antibodies, the differentiation of dead and viable target cells and characterization of cell populations.

All sample processing steps presented were compatible with the Vivalytic LoC system, as on-chip cell capture by filtration was successfully shown in the first proof-of-principle experiments. With appropriate fluidic protocols capture rates up to 55 % could be achieved, despite limited optical access (suction pumping, see chapter 3.3.2). Solely, the optical detection needed to be performed off-chip using a fluorescence microscope. Further development towards on-chip optical detection requires an adapted cartridge design without fluidic channels in the optical view field and an improved optical system with higher resolution and faster filter switching.

As a next step, the recovery of captured cells either as intact cells or bulk cell lysate could be evaluated in order to identify the origin of the cells and validate that the captured and counted cells are real tumor cells. In future, multimarker analysis will be necessary including the identification of epithelial and mesenchymal CTCs and the clear distinction from normal blood cells or normal epithelial stem cells. Therefore, additional cell lines will be necessary for mixed spike-in experiments to enable detection of epithelial cells, mesenchymal cells, EMT cells and MET cells. ATCC (Manassas, Virginia, United States) for example, offers cells that have been generated by using CRIPR/Cas9 such as the reporter cell line HCT116 VIM RFP (174).

As filtration-based CTC isolation methods are widely studied, several approaches are described in literature that could be evaluated for further optimization in future. For example, one approach that could increase both cell capture and sample purity might be affinity filtration. Thereby, antibodies immobilized on the filter could be used to capture cells that could pass due to their size but are captured by the antibodies. Alternatively, immunocapture in microfluidic chips with functionalized channels were described for either positive immunocapture of target cells or negative immunocapture of non-target cells for depletion (175) (176). The latter could be used to deplete a higher fraction of leukocytes in a channel before the filter resulting in lower non-target cell background for subsequent molecular analysis. Furthermore, filter pore sizes and filter depths could be varied depending on the target cells that need to be captured because differences in cell size could be expected for different tumor types.

After cell capture for quantification, cells could be recovered from the filter as described in this study using lysis methods from nucleic acid extraction.

Alternatively, a method for recovery of whole intact cells could be established for single cell analysis or cultivation of the isolated cells. CTCs that can be cultivated in-vitro and grow into microspheres were described as a subpopulation of CTCs the cancer stem cells (CSCs). These cells are held responsible for tumor invasion, metastasis, heterogeneity, and resistance to therapy. To evaluate these properties, CTCs can be cultured after isolation and sphere formation can be assessed. One study described that spheres could grow from isolated cells of 79 % of patients and the number of tumor spheres was described to depend on the stage of disease (177). Patients with chemotherapy treatment had lower numbers of tumor spheres compared to patients without chemotherapy. This leads to the assumption that under chemotherapy, the formation of tumor spheres might be an indicator for the lacking response to therapy and the need for therapy

adaptation. Identifying the CTC fraction within a sample that possesses stem cell properties and monitoring the number of these cells during therapy may provide additional clinically relevant prognostic information.

For a first and PCR-based molecular characterization of the CTCs present in blood samples after capture, expression analysis of EMT-markers was established on a few first markers in this study. This could be further extended to the analysis of more genes indicating EMT aiming at more precise prediction of therapy response than achieved by counting epithelial CTCs only. A first proof-of-principle was shown in this study and in case of one patient, the number of EpCAM-positive CTCs inversely correlated with the expression of the mesenchymal markers Snail and Twist. However, a larger cohort of patients should be monitored over a longer period to assess whether the increase of mesenchymal gene expression correlated with therapy response and whether it correlates better or earlier than the CTC count.

Another downstream application of the cells captured on the filter might be DNA extraction for mutation detection. Just as shown for the RNA in this study, DNA could be extracted from the cells captured on the filter after optical detection or even after optical detection of viable cells, fixation and staining of intracellular markers. Subsequently, the DNA could be transferred to an off-chip sample tube for storage and external analysis or analyzed on-chip after establishing further qPCR assays. This should, in the first place, be used to verify whether the captured cells are indeed tumor cells. The captured cell types' composition could be identified by sequencing and implemented either on single cell basis or as a pooled cell fraction. In the first step, cells that can be picked as single cell using a capillary-based picker such as the CellCelector™ (ALS, Jena, Germany) could be subjected to whole genome amplification and low pass sequencing to detect genome-wide copy number variations. This is expected to result in detection of characteristic differences in CTCs cells and confirm their tumor origin. As an alternative, the isolated cells could be subjected to targeted sequencing detecting certain cancer specific mutations.

An additional option to implement mutation detection on the Bosch LoC system could be provided by mutation panels in microarray format such as the BRAS BRAF PIK3CA mutation array (Randox Laboratories Ltd., Crumlin, UK). However, this would require an additional DNA extraction filter or magnetic beads and is therefore subject for an alternative cartridge providing two chambers for filter integration or the possibility to handle magnetic DNA extraction beads.

Overall, the single unit operations for cell capture, (real-time) detection and enumeration with or without deep learning approaches, the recovery of the cells or nucleic acids from the filter element established in this study provided the proof-of-principle of LoC integration of CTC analysis in liquid biopsy samples. It was shown that all steps can be performed in a microfluidic environment and that the steps can be automated and miniaturized for the Vivalytic LoC system. Furthermore, the assays hold the potential for expansion towards analysis of additional antigens or molecular markers.

5.1. Summary

The Bosch Vivalytic system is an automated lab-on-a-chip (LoC) platform for molecular diagnostics at the point of care without the requirement of a fully equipped laboratory or trained staff. The current product portfolio includes tests for detection of different infectious diseases. Future potential applications include assays for cancer diagnostics and therapy monitoring by minimally invasive liquid biopsy using circulating tumor cells (CTCs) as prognostic biomarkers. Circulating tumor cells shed from the primary tumor into the vasculature and are described as the major cause for metastasis. There is evidence that their number correlates with therapy success. Quantification of the cells that reside in the bloodstream despite therapy represents a minimally invasive method for therapy monitoring and personalized treatment optimization. The prognostic significance of CTCs as biomarkers obtained from liquid biopsies is currently under intensive investigation. Since the CTC number in blood is relatively low compared to normal blood cells, their quantification requires highly accurate methods.

In this dissertation, a method for analysis of CTCs from liquid biopsies is presented. **The first step** of this study was to reproduce an existing CTC detection method and adapt it for the automation on the Vivalytic LoC system. The established staining strategy was verified in a clinical study (480/2019BO2, Universitätsklinikum Tübingen) using blood samples from patients with (late stage) gastrointestinal cancer for parallel analysis in two laboratories. Hereby, the absolute cell counts differed, but the cell count dynamics were comparable and correlation to disease progression was observed for three patients. Further patient recruitment is ongoing,

As filtration-based methods are feasible for CTC isolation and compatible with the Vivalytic LoC system, in **the second step** a microfluidic filtration device in microscope slide format was developed and prototyped from a transparent material. This served as a single unit functional model and enabled capture of CTCs on an optically addressable surface and real-time optical observation of the cell capture process. The proof-of-principle was successfully achieved by adding cancer cells from appropriate cell lines into healthy blood for filtration using the prototype, whereby arriving cells were counted to determine the total number of CTCs present in the blood. Providing real-time detection improved quantification efficiency even for small cells that have been retained but pass the filter during the filtration process. While endpoint evaluation resulted in a detection rate of $64 \% \pm 3 \%$ of the spiked cells, manual real-time counting in a video led to $84 \% \pm 4 \%$. For

automated cell detection and one-to-one cell counting, a tracking method has been developed using convolutional neural networks for the detection and segmentation of objects. This resulted in detection of $92 \% \pm 7 \%$ of the cells by real-time tracking compared to $70 \% \pm 20 \%$ of the initially spiked cells when using the last frame for detection.

The **third step of the study** was the transfer and integration of the CTC filtration and detection unit into the Vivalytic cartridge. The unit operations for fluid transport in the microfluidic network of the cartridge required adaptation of fluidic protocols for gentle processing of cell suspensions considering fluid shear stress and loss-free transport maintaining $> 80 \%$ viability.

In **the fourth step**, in addition to enumeration, the isolated CTCs were characterized on the gene expression level using exemplary EMT (epithelial mesenchymal transition) related genes. The gene expression analysis of first patient samples revealed inverse correlation of the EpCAM signal on the cell membrane with the gene expression of Twist and Snail. This may provide crucial information for the association between gene expression profiles and clinical outcome but needs further investigation and validation with additional patient samples. In following studies, CTCs that can be detected by the described method should be isolated as single cells for validation of their tumor origin, for example by single cell sequencing methods.

By reducing the sample preparation steps and providing the possibility for real-time detection, cell loss could be minimized, and the efficiency of CTC quantification could be optimized.

Automation of the presented assay and integration into the Vivalytic system could complement the system by a completely new application for cancer treatment monitoring by counting and characterization of CTCs. This represents a promising tool to enable automated and rapid point-of-care assessment of changes in CTC numbers in patients' blood providing a measure for therapy success.

5.2. Zusammenfassung

Das Bosch Vivalytic System ist eine automatisierte *Lab-on-chip* (LoC) Plattform für die molekulare Diagnostik und Probenanalyse am *Point of Care* ohne den Bedarf eines vollausgestatteten Labors oder geschultem Fachpersonal. Das aktuelle Produktportfolio umfasst Tests für die Analyse von infektiösen Krankheiten. Potenzielle, zukünftige Anwendungen beinhalten Assays für die Krebsdiagnostik und das Therapiemonitoring mittels minimal invasiver Flüssigbiopsie (*Liquid Biopsy*) und den Nachweis von zirkulierenden Tumorzellen (circulating tumor cells; CTCs) als prognostischen Marker. CTCs lösen sich vom Primärtumor, können in die Blutgefäße gelangen. Sie gelten als Hauptauslöser der Metastasierung und es gibt Hinweise darauf, dass ihre Zahl im Blut mit dem Therapieerfolg korreliert. Quantifizierung der Zellen, die trotz Therapie im Blutstrom verbleiben, stellt eine minimal invasive Methode für das Therapiemonitoring und die Optimierung einer personalisierten Behandlung dar. Die prognostische Bedeutung der CTCs als Biomarker aus Flüssigbiopsien wird zurzeit intensiv erforscht. Da deren Zahl im Blut im Vergleich zu gesunden Blutzellen jedoch gering ist, erfordert die Quantifizierung hochpräzise Methoden.

In dieser Dissertation wird eine Methode für die Analyse von CTCs aus Flüssigbiopsien vorgestellt. **Im ersten Schritt** der Arbeit wurde eine existierende CTC-Detektionsmethode reproduziert und für die Automatisierung auf einem LoC System angepasst. Die etablierte Färbestrategie wurde in einer klinischen Studie (480/2019BO2, Universitätsklinikum Tübingen) mit Patientenproben parallel in zwei Laboren überprüft. Hierbei unterschieden sich die ermittelten absoluten CTC-Zahlen, die Zellzahlverläufe waren jedoch vergleichbar und korrelierten bei drei Patienten mit dem Krankheitsverlauf. Da filtrationsbasierte Methoden für die CTC-Isolation leicht umsetzbar und kompatibel mit dem Vivalytic LoC System sind, wurde **im zweiten Schritt** eine mikrofluidische Filtrationseinheit im Objektträgerformat entwickelt und Prototypen aus einem transparenten Material gefertigt. Diese dienten als Einzelfunktionsmuster und ermöglichten den Rückhalt von CTCs auf einer optisch einsehbaren Oberfläche, sowie die optische Detektion des Rückhaltevorgangs in Echtzeit. Der Machbarkeitsnachweis (*proof-of-principle*) erfolgte mit Modellproben durch die Zugabe von geeigneten Tumor-Zelllinien zu gesundem Blut für die Filtration mit Hilfe des Prototyps, währenddessen zurückgehaltene Zellen gezählt wurden, um die CTC-Zahl im Blut zu ermitteln. Die Möglichkeit der Echtzeitdetektion verbesserte die Quantifizierungseffizienz signifikant. Dies galt auch für kleinere Zellen, die initial zurückgehalten wurden, im zeitlichen Verlauf des Vorgangs jedoch durch den Filter hindurchgedrückt wurden.

Während die Endpunkt-Quantifizierung zu einer Detektionsrate von $64 \% \pm 3 \%$ der Zellen führte, konnte die Rate durch manuelle Echtzeit-Zählung auf $84 \% \pm 4 \%$ gesteigert werden. Für die automatisierte Zellerkennung und -zählung wurde eine Tracking-Methode unter Verwendung von neuronalen Netzen für die Detektion und Segmentierung der Objekte entwickelt. Diese erreichte eine Detektionsrate von $92 \% \pm 7 \%$ durch die Echtzeit-Zählung in einem Video im Vergleich zu $70 \% \pm 20 \%$ unter Verwendung des letzten Bildes des Filtrationsvorgangs.

Im dritten Schritt der Arbeit wurde die Filtrations- und Detektionseinheit in die Vivalytic Kartusche integriert. Die Einheitsoperationen für den Flüssigkeitstransport im mikrofluidischen Netzwerk der Kartusche erforderte Anpassung von fluidischen Protokollen für einen schonenden Transport der Zellsuspensionen unter Berücksichtigung von Scherkräften und des verlustfreien Transports unter Erhalt der Viabilität bei $> 80 \%$.

Im vierten Schritt wurden für die isolierten CTCs zusätzlich die Genexpression von exemplarischen EMT (epitheliale mesenchymale Transition) assoziierten Genen untersucht. Die Genexpressionsanalyse des ersten Patienten zeigte eine negative Korrelation des EpCAM-Signals auf der Zellmembran mit der Genexpression von Twist und Snail. Dies könnte einen wichtigen Hinweis auf einen Zusammenhang der Genexpression mit dem klinischen Ausgang darstellen, benötigt jedoch weitere Untersuchung und Validierung mit zusätzlichen Patientenproben.

In zukünftigen Studien sollten die CTCs, die durch die beschriebene Methode detektiert werden, einzeln isoliert und deren Tumorsprung zum Beispiel durch Einzelzell-Sequenzierungsmethoden bestätigt werden. Durch die Reduktion der Probenvorbereitungsschritte und die Möglichkeit der Echtzeit-Detektion, konnte der Zellverlust minimiert und die CTC-Quantifizierungseffizienz optimiert werden.

Die Automatisierung des vorgestellten Assays und die Integration auf die Vivalytic Plattform könnte das System durch eine neue Anwendung für das Krebstherapiemonitoring durch Zählung und Charakterisierung von CTCs erweitern. Dies stellt ein vielversprechendes Werkzeug dar, um die automatisierte und schnelle Point-of-Care-Erfassung von Änderungen der CTC-Anzahl im Blut von Tumorpatienten zu erfassen, die eine Einschätzung des Therapieerfolges ermöglicht.

References

1. **Haney K, Tandon P, Divi R, Ossandon MR, Baker H, Pearlman PC.** The Role of Affordable, Point-of-Care Technologies for Cancer Care in Low- and Middle-Income Countries: A Review and Commentary. *IEEE J Transl Eng Health Med.* 5:2800514 , 2017.
2. **Haber DA, Velculescu VE.** Blood-based analyses of cancer: circulating tumor cells and circulating tumor DNA. *Cancer Discov.* 4(6), 2014, pp. 650-661.
3. **Hayes B, Murphy C, Crawley A, O'Kennedy R.** Developments in Point-of-Care Diagnostic Technology for Cancer Detection. *Diagnostics (Basel).* 8(2), 39, 2018, p. 39.
4. **Arshavsky-Graham S, Segal E.** Lab-on-a-Chip Devices for Point-of-Care Medical Diagnostics. *Adv Biochem Eng Biotechnol.* 179, 2022, pp. 247-265.
5. **Zydron CT, Woodworth A, Storrow AB.** The future of point-of-care testing in emergency departments. *Expert Opin Med Diagn.* 5(3), 2011, pp. 175-81.
6. **Giuliano KK, Grant ME.** Blood analysis at the point of care: issues in application for use in critically ill patients. *AACN Clin Issues.* 13(2), 2002, pp. 204-20.
7. **Syedmoradi L, Norton ML, Omidfar K.** Point-of-care cancer diagnostic devices: From academic research to clinical translation. *Talanta.* 225:122002, 2021.
8. **Mumba JM, Kasonka L, Owiti OB, Andrew J, Lubeya MK, Lukama L, Kasempa C, Msadabwe SC, Kalinda C.** Cervical cancer diagnosis and treatment delays in the developing world: Evidence from a hospital-based study in Zambia. *Gynecol Oncol Rep.* 37:1007, 2021.
9. **Lopez-Barbosa N, Gamarra JD, Osma JF.** The future point-of-care detection of disease and its data capture and handling. *Anal Bioanal Chem.* 408(11), 2016, pp. 2827-37.
10. **GmbH, Bosch Healthcare Solutions.** Bosch Vivalytic. [Online] Bosch Healthcare Solutions GmbH. [Cited: 08 12, 2022.] <https://www.bosch-vivalytic.com/en/tests/>.
11. **Rupp J, Schmidt M, Münch S, Cavalari M, Steller U, Steigert J, Stumber M, Dorrer C, Rothacher P, Zengerle R, Daub M.** Rapid microarray processing using a disposable hybridization chamber with an integrated micropump. *Lab Chip.* 12(7), 2012, pp. 1384-1388.
12. **Organization, World Health.** www.who.int. [Online] [Cited: 10 23, 2022.] https://www.who.int/health-topics/cancer#tab=tab_1.
13. **Institute, National Cancer.** www.cancer.gov. [Online] [Cited: 11 05, 2022.] <https://www.cancer.gov/types/common-cancers>.
14. **Lambert AW, Pattabiraman DR, Weinberg RA.** Emerging Biological Principles of Metastasis. *Cell.* 168(4), 2017, pp. 670-691.

15. **Phan TG, Croucher PI.** The dormant cancer cell life cycle. *Nat Rev Cancer.* 20(7), 2020, pp. 398-411.
16. **Rossari F, Zucchinetti C, Buda G, Orciuolo E.** Tumor dormancy as an alternative step in the development of chemoresistance and metastasis - clinical implications. *Cell Oncol (Dordr).* 43(2), 2020, pp. 155-176.
17. **Toss A, Mu Z, Fernandez S, Cristofanilli M.** CTC enumeration and characterization: moving toward personalized medicine. *Ann Transl Med.* 2, 2014, Vol. 11.
18. **YE, Erdi.** Limits of Tumor Detectability in Nuclear Medicine and PET. *Mol Imaging Radionucl Ther.* 21(1), 2012, pp. 23-8.
19. **Robbins HA, Berg CD, Cheung LC, Chaturvedi AK, Katki HA.** Identification of Candidates for Longer Lung Cancer Screening Intervals Following a Negative Low-Dose Computed Tomography Result. *J Natl Cancer Inst.* 111(9), 2019, pp. 996-999.
20. **J, Fidler I.** The pathogenesis of cancer metastasis: the 'seed and soil' hypothesis revisited. *Nat Rev Cancer.* 3, Juni 2003, Vol. 6, pp. 453-458.
21. **Fuss, I. J., Kanof, M. E., Smith, P. D., & Zola, H.** Isolation of whole mononuclear cells from peripheral blood and cord blood. *Curr Protoc Immunol.* 7(7), 2009.
22. **Roos, D., & Loos, J. A.** Changes in the carbohydrate metabolism of mitogenically stimulated human peripheral lymphocytes. I. Stimulation by phytohaemagglutinin. *Biochim Biophys Acta.* 222(3), 1970, pp. 565–582.
23. **Hemker, M. B., Cheroutre, G., van Zwieten, R., Maaskant-van Wijk, P. A., Roos, D., Loos, J. A., van der Schoot, C. E., & von dem Borne, A. E.** The Rh complex exports ammonium from human red blood cells. *Br J Haematol.* 122(2), 2003, pp. 333–40.
24. **Tanner, M. J., Martin, P. G., & High, S.** The complete amino acid sequence of the human erythrocyte membrane anion-transport protein deduced from the cDNA sequence. *Biochem J.* 256(3), 1988, pp. 703–712.
25. **Pösel, C., Möller, K., Fröhlich, W., Schulz, I., Boltze, J., & Wagner, D. C.** Density gradient centrifugation compromises bone marrow mononuclear cell yield. *PLoS One.* 7(12), 2012.
26. **Emad, A., & Drouin, R.** Evaluation of the impact of density gradient centrifugation on fetal cell loss during enrichment from maternal peripheral blood. *Prenat Diagn.* 34(9), 2014, pp. 878–885.
27. **Nakano, A., Harada, T., Morikawa, S., & Kato, Y.** Expression of leukocyte common antigen (CD45) on various human leukemia/lymphoma cell lines. *Acta Pathol Jpn.* 40(2), 1990, pp. 107–115.
28. **Poppema, S., Lai, R., Visser, L., & Yan, X. J.** CD45 (leucocyte common antigen) expression in T and B lymphocyte subsets. *Leuk Lymphoma.* 20(3-4), 1996, pp. 217–222.

29. **Eslami-S Z, Cortés-Hernández LE, Alix-Panabières C.** Epithelial Cell Adhesion Molecule: An Anchor to Isolate Clinically Relevant Circulating Tumor Cells. *Cells*. 9(8), 2020, p. 1836.
30. **TR., Ashworth.** A case of cancer in which cells similar to those in the tumours were seen in the blood after death. *Australasian Medical Journal*. 14, 1869, pp. 146–147.
31. **Pachmann K, Camara O, Kavallaris A, Krauspe S, Malarski N, Gajda M, Kroll T, Jörke C, Hammer U, Altendorf-Hofmann A, Rabenstein C, Pachmann U, Runnebaum I, Höffken K.** Monitoring the response of circulating epithelial tumor cells to adjuvant chemotherapy in breast cancer allows detection of patients at risk of early relapse. *J Clin Oncol*. 26(8), 2008, pp. 1208-15.
32. **Wallwiener M, Riethdorf S, Hartkopf AD, Modugno C, Nees J, Madhavan D, Sprick MR, Schott S, Domschke C, Baccelli I, Schönfisch B, Burwinkel B, Marmé F, Heil J, Sohn C, Pantel K, Trumpp A, Schneeweiss A.** Serial enumeration of circulating tumor cells predicts treatment response and prognosis in metastatic breast cancer: a prospective study in 393 patients. *BMC Cancer*. 14:512. , 2014.
33. **Yeatman TJ, Nicolson GL.** Molecular basis of tumor progression: mechanisms of organ-specific tumor metastasis. *Semin Surg Oncol*. 9, 1993, Vol. 3, pp. 256-63.
34. **Ruggiero C, Lalli E.** Targeting the cytoskeleton against metastatic dissemination. *Cancer Metastasis Rev*. 40(1), 2021, pp. 89-140.
35. **Aceto N, Bardia A, Miyamoto DT, Donaldson MC, Wittner BS, Spencer JA, Yu M, Pely A, Engstrom A, Zhu H, Brannigan BW, Kapur R, Stott SL, Shioda T, Ramaswamy S, Ting DT, Lin CP, Toner M, Haber DA, Maheswaran S.** Circulating tumor cell clusters are oligoclonal precursors of breast cancer metastasis. *Cell*. 158(5), 2014, pp. 1110-1122.
36. **Frisch SM, Screaton RA.** Anoikis mechanisms. *Curr Opin Cell Biol*. 13, 2001, 5, pp. 555-562.
37. **Wirtz, D., Konstantopoulos, K., & Searson, P. C.** The physics of cancer: the role of physical interactions and mechanical forces in metastasis. *Nat Rev Cancer*. 11(7), 2011, pp. 512–522.
38. **P., Gilmore A.** Anoikis. *Cell Death Differ*. 12 Suppl 2, 2005, pp. 1473–1477.
39. **K., Pachmann.** Longtime recirculating tumor cells in breast cancer patients. *Clin Cancer Res*. 11(15), 2005, pp. 5657–5658.
40. **Camara, O., Rengsberger, M., Egbe, A., Koch, A., Gajda, M., Hammer, U., Jörke, C., Rabenstein, C., Untch, M., Pachmann, K.** The relevance of circulating epithelial tumor cells (CETC) for therapy monitoring during neoadjuvant (primary systemic) chemotherapy in breast cancer. *Ann Oncol*. 18(9), 2007, pp. 1484–1492.

41. **Strilic, B., & Offermanns, S.** Intravascular Survival and Extravasation of Tumor Cells. *Cancer Cell*. 32(3), 2017, pp. 282–293.
42. **Ansieau S, Bastid J, Doreau A, Morel AP, Bouchet BP, Thomas C, Fauvet F, Puisieux I, Doglioni C, Piccinin S, Maestro R, Voeltzel T, Selmi A, Valsesia-Wittmann S, Caron de Fromentel C, Puisieux A.** Induction of EMT by twist proteins as a collateral effect of tumor-promoting inactivation of premature senescence. *Cancer Cell*. 14(1), 2008, pp. 79-89.
43. **Tseng JC, Chen HF, Wu KJ.** A twist tale of cancer metastasis and tumor angiogenesis. *Histol Histopathol*. 30(11), 2015, pp. 1283-94.
44. **Gras B, Jacquaroud L, Wierinckx A, Lamblot C, Fauvet F, Lachuer J, Puisieux A, Ansieau S.** Snail family members unequally trigger EMT and thereby differ in their ability to promote the neoplastic transformation of mammary epithelial cells. *PLoS One*. 9(3), 2014, p. e92254.
45. **Wang Y, Shi J, Chai K, Ying X, Zhou BP.** The Role of Snail in EMT and Tumorigenesis. *Curr Cancer Drug Targets*. 13(9), 2013, pp. 963-972.
46. **Sinha D, Saha P, Samanta A, Bishayee A.** Emerging Concepts of Hybrid Epithelial-to-Mesenchymal Transition in Cancer Progression. *Biomolecules*. 10(11):1561, 2020.
47. **Ilić, M., Szafer-Glusman, E., Hofman, V., Chamorey, E., Lalvée, S., Selva, E., Leroy, S., Marquette, C. H., Kowanetz, M., Hedge, P., Punnoose, E., & Hofman, P.** Detection of PD-L1 in circulating tumor cells and white blood cells from patients with advanced non-small-cell lung cancer. *Ann Oncol*. 29(1), 2018, pp. 193–199. .
48. **Fan T, Kuang G, Long R, Han Y, Wang J.** The overall process of metastasis: From initiation to a new tumor. *Biochim Biophys Acta Rev Cancer*. 1877(4), 2022.
49. **Resel Folkersma L, Olivier Gómez C, San José Manso L, Veganzones de Castro S, Galante Romo I, Vidaurreta Lázaro M, de la Orden GV, Arroyo Fernández M, Díaz Rubio E, Silmi Moyano A, Maestro de Las Casas MA.** Immunomagnetic quantification of circulating tumoral cells in patients with prostate cancer: clinical and pathological correlation. *Arch Esp Urol*. 63, 2010, 1, pp. 23-31.
50. **Pachmann, K.** Longtime recirculating tumor cells in breast cancer patients. *Clin Cancer Res*. 11, 15, pp. 975-979.
51. **Valastyan S, Weinberg RA.** Tumor metastasis: molecular insights and evolving paradigms. *Cell*. 147, 2011, pp. 275-292.
52. **Nagrath S, Sequist LV, Maheswaran S, Bell DW, Irimia D, Ulkus L, Smith MR, Kwak EL, Digumarthy S, Muzikansky A, Ryan P, Balis UJ, Tompkins RG, Haber DA, Toner M.** Isolation of rare circulating tumour cells in cancer patients by microchip technology. *Nature*. 450, 2007, pp. 1235-1239.

53. **Pantel K, Alix-Panabières C.** Circulating tumour cells in cancer patients: challenges and perspectives. *Trends Mol Med.* 16(9), 2010, pp. 398-406.
54. **Lee HL, Chiou JF, Wang PY, Lu LS, Shen CN, Hsu HL, Burnouf T, Ting LL, Chou PC, Chung CL, Lee KL, Shiah HS, Liu YL, Chen YJ.** Ex Vivo Expansion and Drug Sensitivity Profiling of Circulating Tumor Cells from Patients with Small Cell Lung Cancer. *Cancers (Basel).* 12(11):3394, 2020.
55. **Hyun KA, Jung HI.** Advances and critical concerns with the microfluidic enrichments of circulating tumor cells. *Lab Chip.* 14(1), 2014, pp. 45-56.
56. **Dirix L, Buys A, Oeyen S, Peeters D, Liègeois V, Prové A, Rondas D, Vervoort L, Mariën V, Laere SV, Vermeulen P.** Circulating tumor cell detection: A prospective comparison between CellSearch® and RareCyte® platforms in patients with progressive metastatic breast cancer. *Breast Cancer Res Treat.* 193(2), 2022, pp. 437-444. .
57. **Coumans FA, Ligthart ST, Terstappen LW.** Interpretation of changes in circulating tumor cell counts. *Transl Oncol.* 5(6), 2012, pp. 486-91.
58. **Cristofanilli, M., Budd, G. T., Ellis, M. J., Stopeck, A., Matera, J., Miller, M. C., Reuben, J. M., Doyle, G. V., Allard, W. J., Terstappen, L. W., & Hayes, D. F.** Circulating tumor cells, disease progression, and survival in metastatic breast cancer. *The New England journal of medicine.* 351(8), pp. 781–791. .
59. **Theil G, Boehm C, Fischer K, Bialek J, Hoda R, Weber E, Schönburg S, Kawan F, Fornara P.** In vivo isolation of circulating tumor cells in patients with different stages of prostate cancer. *Oncol Lett.* 2021 May and 21(5):357. In vivo isolation of circulating tumor cells in patients with different stages of prostate cancer. *Oncol Lett.* 21(5):357, 2021.
60. **Hekimian, K., Stein, E. L., Pachmann, U., & Pachmann, K.** Demasking of epithelial cell adhesion molecule (EpCAM) on circulating epithelial tumor cells by Tween®20 treatment in breast cancer patients. *Clin Chem Lab Med.* 50(4), 2012, pp. 701–708.
61. **Szczerba, B. M., Castro-Giner, F., Vetter, M., Krol, I., Gkountela, S., Landin, J., Scheidmann, M. C., Donato, C., Scherrer, R., Singer, J., Beisel, C., Kurzeder, C., Heinzelmann-Schwarz, V., Rochlitz, C., Weber, W. P., Beerenwinkel, N., & Aceto, N.** Neutrophils escort circulating tumour cells to enable cell cycle progression. *Nature.* 566(7745), 2019, pp. 553–557.
62. **Egeblad, M., & de Visser, K. E.** Sticking together helps cancer to spread. *Nature.* 566(7745), 2019, pp. 459–460.
63. **Gold, M., Pachmann, K., Kiani, A., & Schobert, R.** . Monitoring of circulating epithelial tumor cells using the Maintrac® method and its potential benefit for the treatment of patients with colorectal cancer. *Mol Clin. Oncol.* 15(4), 201, 2021.

64. **Pizon M, Schott D, Pachmann U, Pachmann K.** The number of tumorspheres cultured from peripheral blood is a predictor for presence of metastasis in patients with breast cancer. *Oncotarget*. 7(30), 2016, pp. 48143-48154.
65. **Harouaka RA, Nisic M, Zheng SY.** Circulating tumor cell enrichment based on physical properties. *J Lab Autom*. 18(6), 2013, pp. 455-68.
66. **Vona G, Sabile A, Louha M, Sitruk V, Romana S, Schütze K, Capron F, Franco D, Pazzagli M, Vekemans M, Lacour B, Bréchet C, Paterlini-Bréchet P.** Isolation by size of epithelial tumor cells : a new method for the immunomorphological and molecular characterization of circulating tumor cells. *Am J Pathol*. 156(1), 2000, pp. 57-63.
67. **Desitter I, Guerrouahen BS, Benali-Furet N, Wechsler J, Jänne PA, Kuang Y, Yanagita M, Wang L, Berkowitz JA, Distel RJ, Cayre YE.** A new device for rapid isolation by size and characterization of rare circulating tumor cells. *Anticancer Res*. 31(2), 2011, pp. 427-41.
68. **Baeuerle PA, Gires O.** EpCAM (CD326) finding its role in cancer. . *Br J Cancer*. 96(9), 2007, p. 1491.
69. **Kinahan, D.J., Glynn, M.T. and Ducrée, J.** Microfluidic Cell Enumeration for Biomedical Diagnostics. *Encyclopedia of Microfluidics and Nanofluidics*. 2015, pp. 1882–1891.
70. **Yu M, Stott S, Toner M, Maheswaran S, Haber DA.** Circulating tumor cells: approaches to isolation and characterization. *J Cell Biol*. 192(3), 2011, pp. 373-82.
71. **Nagrath S, Sequist LV, Maheswaran S, Bell DW, Irimia D, Ulkus L, Smith MR, Kwak EL, Digumarthy S, Muzikansky A, Ryan P, Balis UJ, Tompkins RG, Haber DA, Toner M.** Isolation of rare circulating tumour cells in cancer patients by microchip technology. *Nature*. 450(7173), 2007, pp. 1235-9.
72. **Kirby D, Glynn M, Kijanka G, Ducrée J.** Rapid and cost-efficient enumeration of rare cancer cells from whole blood by low-loss centrifugo-magnetophoretic purification under stopped-flow conditions. *Cytometry A*. 87(1), 2015, pp. 74-80.
73. **Salmanzadeh A, Sano MB, Shafiee H, Stremler MA, Davalos RV.** Isolation of rare cancer cells from blood cells using dielectrophoresis. *Annu Int Conf IEEE Eng Med Biol Soc*. 2012, pp. 590-3.
74. **Xu T, Lu B, Tai YC, Goldkorn A.** **A cancer detection platform which measures telomerase activity from live circulating tumor cells captured on a microfilter.** A cancer detection platform which measures telomerase activity from live circulating tumor cells captured on a microfilter. *Cancer Res*. 70(16), 2010, pp. 6420-6.
75. **Brychta N, Drosch M, Driemel C, Fischer JC, Neves RP, Esposito I, Knoefel W, Möhlendick B, Hille C, Stresemann A, Krahn T, Kassack MU, Stoecklein NH, von Ahsen O.** Isolation of circulating tumor cells from pancreatic cancer by automated filtration. *Oncotarget*. 8(49), 2017, pp. 86143-86156.

76. **Huang C, Liu H, Bander NH, Kirby BJ.** Enrichment of prostate cancer cells from blood cells with a hybrid dielectrophoresis and immunocapture microfluidic system. *Biomed Microdevices*. 15(6), 2013, pp. 941-8.
77. **Ruiz-Rodríguez AJ, Molina-Vallejo MP, Aznar-Peralta I, González Puga C, Cañas García I, González E, Lorente JA, Serrano MJ, Garrido-Navas MC.** Deep Phenotypic Characterisation of CTCs by Combination of Microfluidic Isolation (IsoFlux) and Imaging Flow Cytometry (ImageStream). *Cancers (Basel)*. 13(24):6386, 2021.
78. **Stott SL, Hsu CH, Tsukrov DI, Yu M, Miyamoto DT, Waltman BA, Rothenberg SM, Shah AM, Smas ME, Korir GK, Floyd FP Jr, Gilman AJ, Lord JB, Winokur D, Springer S, Irimia D, Nagrath S, Sequist LV, Lee RJ, Isselbacher KJ, Maheswaran S, Haber DA, Toner M.** Isolation of circulating tumor cells using a microvortex-generating herringbone-chip. *Proc Natl Acad Sci U S A*. 107(43), 2010, pp. 18392-7.
79. **Miller MC, Robinson PS, Wagner C, O'Shannessy DJ.** The Parsortix™ Cell Separation System-A versatile liquid biopsy platform. *Cytometry A*. 93(12), 2018, pp. 1234-1239.
80. **Promega.** https://www.promega.de/en/products/cell-health-assays/cell-viability-and-cytotoxicity-assays/celltiter_glo-luminescent-cell-viability-assay. [Online] [Cited: 11 11, 2021.] https://www.promega.de/en/products/cell-health-assays/cell-viability-and-cytotoxicity-assays/celltiter_glo-luminescent-cell-viability-assay.
81. **Pachmann, K., Pachmann, U.** *Verfahren zur kultivierung einer subpopulation zirkulierender epithelialer tumorzellen aus einer körperflüssigkeit* . EP2880152A1 2012.
82. **Pugh, S.** Concept Selection: A Method that Works. *Proceedings of International Conference on Engineering Design*. 1981, pp. pp. 497-506. .
83. **Podbiel, D, et al.** From CAD to microfluidic chip within one day: rapid prototyping of lab-on-chip cartridges using generic polymer parts. *Journal of Micromechanics and Microengineering*. 2020.
84. **Wang, L., Zhou, S., Zhang, W., Wang, J., Wang, M., Hu, X., Liu, F., Zhang, Y., Jiang, B., & Yuan, H.** Circulating tumor cells as an independent prognostic factor in advanced colorectal cancer: a retrospective study in 121 patients. *Int J Colorectal Dis*. 34(4), 2019, pp. 589–597.
85. **Inc., Thermo Fisher Scientific.** *TaqMan® Multiplex PCR User Guide*. 2014. MAN0010189.
86. **Rombach, M, et al.** Real-time stability testing of air-dried primers and fluorogenic hydrolysis probes stabilized by trehalose and xanthan. *BioTechniques*, 57(3). 2014, pp. 151-155.
87. **QIAGEN.** QIAamp RNA Blood Mini Handbook 02/2021. [Online] 02 2021. [Cited: 03 14, 2022.]

88. **Lux, A., et al.** Real-Time Detection of Tumor Cells during Capture on a Filter Element Significantly Enhancing Detection Rate. *Biosensors* <https://doi.org/10.3390/bios11090312>. 312, November 2021.
89. **Otsu.** A Threshold Selection Method from Gray-Level Histograms. *IEEE Transactions on Systems, Man, and Cybernetics*. 9 (1), 1979, pp. 62-66.
90. **Crowley, E., Di Nicolantonio, F., Loupakis, F., & Bardelli, A.** Liquid biopsy: monitoring cancer-genetics in the blood. *Nat Rev Clin Oncol*. 10(8), 2013, pp. 472–484.
91. **Lara, O., Tong, X., Zborowski, M., & Chalmers, J. J.** Enrichment of rare cancer cells through depletion of normal cells using density and flow-through, immunomagnetic cell separation. *Experimental hematology*, 32(10). 2004, pp. 891–904.
92. **Rosenberg, R., Gertler, R., Friederichs, J., Fuehrer, K., Dahm, M., Phelps, R., Thorban, S., Nekarda, H., & Siewert, J. R.** Comparison of two density gradient centrifugation systems for the enrichment of disseminated tumor cells in blood. *Cytometry*. 49(4), 2002, pp. 150–158.
93. **Sieben, S., Bergemann, C., Lübbe, A., Brockmann, B., & Rescheleit, D.** Comparison of different particles and methods for magnetic isolation of circulating tumor cells. *Journal of Magnetism and Magnetic Materials*. 225(1-2), 2001, pp. 175-179.
94. **Nakamura, M., Decker, K., Chosy, J., Comella, K., Melnik, K., Moore, L., Lasky, L. C., Zborowski, M., & Chalmers, J. J.** Separation of a breast cancer cell line from human blood using a quadrupole magnetic flow sorter. *Biotechnol Prog*. 17(6), 2001, pp. 1145–1155.
95. **Hoshino, K., Huang, Y. Y., Lane, N., Huebschman, M., Uhr, J. W., Frenkel, E. P., & Zhang, X.** Microchip-based immunomagnetic detection of circulating tumor cells. *Lab Chip*. 11(20), 2011, pp. 3449–3457.
96. **Miao, P., Sheng, S., Sun, X., Liu, J., & Huang, G.** Lactate dehydrogenase A in cancer: a promising target for diagnosis and therapy. *IUBMB Life*. 65(11), 2013, pp. 904–910.
97. **Brown, J. E., Cook, R. J., Lipton, A., & Coleman, R. E.** Serum lactate dehydrogenase is prognostic for survival in patients with bone metastases from breast cancer: a retrospective analysis in bisphosphonate-treated patients. *Clin Cancer Res*. 18(22), 2012, pp. 6348–6355.
98. **Suh, S. Y., & Ahn, H. Y.** Lactate dehydrogenase as a prognostic factor for survival time of terminally ill cancer patients: a preliminary study. *Eur J Cancer*. 43(6), 2007, pp. 1051–1059.
99. **Pachmann, K., Camara, O., Kavallaris, A., Krauspe, S., Malarski, N., Gajda, M., Kroll, T., Jörke, C., Hammer, U., Altendorf-Hofmann, A., Rabenstein, C., Pachmann, U., Runnebaum, I., Höffken, K.** Monitoring the response of circulating epithelial tumor cells to adjuvant chemotherapy in breast cancer allows detection of patients at risk of early relapse. *J Clin Oncol*. 26(8), 2008, pp. 1208–1215.

100. Wang, L., Balasubramanian, P., Chen, A. P., Kummar, S., Evrard, Y. A., Kinders, R. J. Promise and limits of the CellSearch platform for evaluating pharmacodynamics in circulating tumor cells. *Seminars in oncology*. 43(4), 2016, pp. 464–475.
101. Sonn, C. H., Cho, J. H., Kim, J. W., Kang, M. S., Lee, J., & Kim, J. . Detection of circulating tumor cells in patients with non-small cell lung cancer using a size-based platform. *Oncology letters*. 13(4), 2017, pp. 2717–2722.
102. A., Shliakhtunou Y. CTCs-oriented adjuvant personalized cytostatic therapy non-metastatic breast cancer patients: continuous non-randomized prospective study and prospective randomized controlled study. *Breast Cancer Res Treat*. 186(2), 2021, pp. 439–451.
103. Matikas, A., Kotsakis, A., Apostolaki, S., Politaki, H., Perraki, M., Kalbakis, K., Nikolaou, M., Economopoulou, P., Hatzidaki, D., & Georgoulas, V. Detection of circulating tumour cells before and following adjuvant chemotherapy and long-term prognosis of early breast cancer. *Br J Cancer*. 2022.
104. Wang, S., Zheng, Y., Yang, F., Zhu, L., Zhu, X. Q., Wang, Z. F., Wu, X. L., Zhou, C. H., Yan, J. Y., Hu, B. Y., Kong, B., Fu, D. L., Bruns, C., Zhao, Y., Qin, L. X., & Dong, Q. Z. The molecular biology of pancreatic adenocarcinoma: translational challenges and clinical perspectives. *Signal Transduct Target Ther*. 6(1), 249, 2021.
105. Sun, Y., Wu, G., Cheng, K. S., Chen, A., Neoh, K. H., Chen, S., Tang, Z., Lee, P. F., Dai, M., & Han, R. CTC phenotyping for a preoperative assessment of tumor metastasis and overall survival of pancreatic ductal adenocarcinoma patients. *EBioMedicine*. 46, 2019, pp. 133-149.
106. Philip T.H Went, Alessandro Lugli, Sandra Meier, Marcel Bundi, Martina Mirlacher, Guido Sauter, Stephan Dirnhofner. Frequent EpCam protein expression in human carcinomas. *Hum Pathol*. 35(1), 2004, pp. 122–128.
107. Payne, R., Wang, F., Su, N. et al. Viable circulating tumour cell detection using multiplex RNA in situ hybridisation predicts progression-free survival in metastatic breast cancer patients. *Br J Cancer*. 106., 2012, pp. 1790–1797.
108. Cristofanilli, M., Budd, G. T., Ellis, M. J., Stopeck, A., Matera, J., Miller, M. C., Reuben, J. M., Doyle, G. V., Allard, W. J., Terstappen, L. W., Hayes, D. F. Circulating tumor cells, disease progression, and survival in metastatic breast cancer. *N Engl J Med*. 351(8), 2004, pp. 781–791.
109. Cristofanilli, M., Hayes, D. F., Budd, G. T., Ellis, M. J., Stopeck, A., Reuben, J. M., Doyle, G. V., Matera, J., Allard, W. J., Miller, M. C., Fritsche, H. A., Hortobagyi, G. N., & Terstappen, L. W. Circulating tumor cells: a novel prognostic factor for newly diagnosed metastatic breast cancer. *J Clin Oncol*. . 23(7), pp. 1420–1430.
110. GmbH, Miltenyi Biotec. Miltenyi Biotec. *Fluorochrome brightness index*. [Online] 2018. [Cited: 01 13, 2022.]

https://www.miltenyibiotec.com/_Resources/Persistent/e4d665f4b7639e2c1b8a3080e70cae321503c425/Fluorochrome%20brightness%20index.pdf.

111. **de Wit, S., van Dalum, G., Lenferink, A. T., Tibbe, A. G., Hiltermann, T. J., Groen, H. J., van Rijn, C. J., & Terstappen, L. W.** The detection of EpCAM(+) and EpCAM(-) circulating tumor cells. *Scientific reports*. 5, 12270, 2015.

112. **Nicolazzo, C., Gradilone, A., Loreni, F., Raimondi, C., & Gazzaniga, P.** EpCAMlow Circulating Tumor Cells: Gold in the Waste. *Disease markers*. 1718920, 2019.

113. **Agnoletto, C., Minotti, L., Brulle-Soumare, L.** Heterogeneous expression of EPCAM in human circulating tumour cells from patient-derived xenografts. *Biomark Res* . 6, 31, 2018.

114. **Imrich, S., Hachmeister, M., Gires, O.** EpCAM and its potential role in tumor-initiating cells. *Cell adhesion and migration*. 6(1), 2012, pp. 30–38.

115. **Mikolajczyk, S. D., Millar, L. S., Tsinberg, P., Coutts, S. M., Zomorodi, M., Pham, T., Bischoff, F. Z., & Pircher, T. J.** Detection of EpCAM-Negative and Cytokeratin-Negative Circulating Tumor Cells in Peripheral Blood. *J Oncol*. 2011: 252361, 2011.

116. **Brajkovic, S., Dupouy, D. G., de Leval, L., & Gijs, M. A.** Microfluidics for rapid cytokeratin immunohistochemical staining in frozen sections. *Lab Invest*. 97(8), 2017, pp. 983–991.

117. **Perfetto, S. P., Chattopadhyay, P. K., Lamoreaux, L., Nguyen, R., Ambrozak, D., Koup, R. A., & Roederer, M.** Amine reactive dyes: an effective tool to discriminate live and dead cells in polychromatic flow cytometry. *J Immunol Methods*. 313(1-2), 2006, pp. 199–208.

118. **Satelli, A., Batth, I., Brownlee, Z., Mitra, A., Zhou, S., Noh, H., Rojas, C. R., Li, H., Meng, Q. H., & Li, S.** EMT circulating tumor cells detected by cell-surface vimentin are associated with prostate cancer progression. *Oncotarget*. 8(30), 49329, 2017.

119. **Xie, X., Wang, L., Wang, X., Fan, W. H., Qin, Y., Lin, X., Xie, Z., Liu, M., Ouyang, M., Li, S., & Zhou, C.** Evaluation of Cell Surface Vimentin Positive Circulating Tumor Cells as a Diagnostic Biomarker for Lung Cancer. *Front Oncol*. 11, 672687, 2021.

120. **Satelli, A., Mitra, A., Brownlee, Z., Xia, X., Bellister, S., Overman, M. J., Kopetz, S., Ellis, L. M., Meng, Q. H., & Li, S.** Epithelial-mesenchymal transitioned circulating tumor cells capture for detecting tumor progression. *Clin Cancer Res*. 21(4), 2015, pp. 899–906.

121. **Oakman C, Pestrin M, Bessi S, Galardi F, Di Leo A.** Significance of micrometastases: circulating tumor cells and disseminated tumor cells in early breast cancer. *Cancers (Basel)*. 2(2), 2010, pp. 1221-35.

122. **L, Dean.** Blood Groups and Red Cell Antigens; Table 1, Complete blood count. . *National Center for Biotechnology*. [Online] 2005. [Cited: Jan 07, 2022.] <https://www.ncbi.nlm.nih.gov/books/NBK2263/table/ch1.T1/>.

123. **Himbert, S., Alsop, R. J., Rose, M., Hertz, L., Dhaliwal, A., Moran-Mirabal, J. M., Verschoor, C. P., Bowdish, D. M., Kaestner, L., Wagner, C., & Rheinstädter, M. C.** The Molecular Structure of Human Red Blood Cell Membranes from Highly Oriented, Solid Supported Multi-Lamellar Membranes. *Sci Rep.* 7, 39661, 2017.
124. **Müller, B., Lang, S., Dominiotto, M., Rudin, M., Schulz, G., Deyhle, H., Germann, M., Pfeiffer, F., David, C., Weitkamp, T.** High-resolution tomographic imaging of microvessels. *Proc. SPIE.* 7078, 2088, pp. 89-98.
125. **Llaudet-Planas, E., Vives-Corróns, J. L., Rizzuto, V., Gómez-Ramírez, P., Sevilla Navarro, J., Coll Sibina, M. T., García-Bernal, M., Ruiz Llobet, A., Badell, I., Velasco-Puyó, P., Dapena, J. L., & Mañú-Pereira, M. M.** A valuable screening test for hereditary spherocytosis and other red blood cell membrane disorders. *Int J Lab Hematol.* 40(1), 2018, pp. 94–102.
126. **Chen, X., Feng, L., Jin, H., Feng, S., & Yu, Y.** . Quantification of the erythrocyte deformability using atomic force microscopy: correlation study of the erythrocyte deformability with atomic force microscopy and hemorheology. *Clin Hemorheol Microcirc.* 43(3), 2009, pp. 243–251.
127. **Zhu, R., Avsievich, T., Popov, A., & Meglinski, I.** Optical Tweezers in Studies of Red Blood Cells. *Cells.* 9(3), 545, 2020.
128. **Chernyshev, A. V., Tarasov, P. A., Semianov, K. A., Nekrasov, V. M., Hoekstra, A. G., & Maltsev, V. P.** Erythrocyte lysis in isotonic solution of ammonium chloride: theoretical modeling and experimental verification. *J Theor Biol.* 251(1), 2008, pp. 93–107.
129. **Pugh, S.** Concept selection: a method that works. *Proceedings international conference on engineering design.* Mar 1981, pp. 497 – 506.
130. **Coumans, F. A., van Dalum, G., Beck, M., & Terstappen, L. W.** Filter characteristics influencing circulating tumor cell enrichment from whole blood. *PloS one.* 8(4), 2013, e61770.
131. **Jeyachandran, Y. L., et al.** Efficiency of blocking of non-specific interaction of different proteins by BSA adsorbed on hydrophobic and hydrophilic surfaces. *Journal of colloid and interface science,* 341(1). 2010, pp. 136-142. .
132. **Koblinski, J. E., Wu, M., Demeler, B., Jacob, K., & Kleinman, H. K.** Matrix cell adhesion activation by non-adhesion proteins. *Journal of cell science.* 118, 13 , 2005, pp. 2965–2974.
133. **Man, Y., Lv, X., Iqbal, J.** Adsorptive BSA Coating Method for CE to Separate Basic Proteins. *Chromatographia.* 76, 2013, pp. 59–65.
134. **Hwang, J. Y., Kim, J., Park, J. M., Lee, C., Jung, H., Lee, J., & Shung, K. K.** Cell Deformation by Single-beam Acoustic Trapping: A Promising Tool for Measurements of Cell Mechanics. *Scientific reports.* 6, 27238, 2016.

135. **Li, F., Cima, I., Vo, J. H., Tan, M. H., & Ohl, C. D.** Single Cell Hydrodynamic Stretching and Microsieve Filtration Reveal Genetic, Phenotypic and Treatment-Related Links to Cellular Deformability. *Micromachines*. 11(5), 486, 2020.
136. **Swaminathan, V., Mythreye, K., O'Brien, E. T., Berchuck, A., Blobe, G. C., & Superfine, R.** Mechanical stiffness grades metastatic potential in patient tumor cells and in cancer cell lines. *Cancer res.* 71(15), 2011, pp. 5075–5080.
137. **Li, P., Liu, X., Kojima, M., Huang, Q., & Arai, T.** Automated Cell Mechanical Characterization by On-Chip Sequential Squeezing: From Static to Dynamic. *Langmuir*. 37(27), 2021, pp. 8083–8094.
138. **Yamauchi, K., Yang, M., Jiang, P., Yamamoto, N., Xu, M., Amoh, Y., Tsuji, K., Bouvet, M., Tsuchiya, H., Tomita, K., Moossa, A. R., Hoffman, R. M.** Real-time in vivo dual-color imaging of intracapillary cancer cell and nucleus deformation and migration. *Cancer Res.* 65(10), 2005, pp. 4246–4252.
139. **Sajay, B. N., Chang, C. P., Ahmad, H., Khuntontong, P., Wong, C. C., Wang, Z., Puiu, P. D., Soo, R., & Rahman, A. R.** Microfluidic platform for negative enrichment of circulating tumor cells. *Biomedical microdevices*, 16(4). 2014, pp. 537–548.
140. **Loos, H., Blok-Schut, B., Kipp, B., van Doorn, R., & Meerhof, L.** Size distribution, electronic recognition, and counting of human blood monocytes. *Blood*. 48(5), 1976, pp. 743–753.
141. **Otsu, N.** A Threshold Selection Method from Gray-Level Histograms. *IEEE Transactions on Systems, Man, and Cybernetics*,. 9 (1), 1979, pp. 62-66.
142. **Schmidt, U., Weigert, M., Broaddus, C., Myers, G.** Cell Detection with Star-Convex Polygons. *Springer Cham*. 11071, 2018.
143. **Fan, R., Emery, T., Zhang, Y., Xia, Y., Sun, J., & Wan, J.** Circulatory shear flow alters the viability and proliferation of circulating colon cancer cells. *Sci Rep.* 6, 27073, 2016.
144. **Mitchell, M. J., Denais, C., Chan, M. F., Wang, Z., Lammerding, J., & King, M. R.** Lamin A/C deficiency reduces circulating tumor cell resistance to fluid shear stress. [ed.] 736-746. *Am J Physiol Cell Physiol*. 309(11), 2015.
145. **Reneman, R. S., & Hoeks, A. P.** Wall shear stress as measured in vivo: consequences for the design of the arterial system. *Med Biol Eng Comput.* 46(5), 2008, pp. 499–507.
146. **Meng, S., Tripathy, D., Frenkel, E. P., Shete, S., Naftalis, E. Z., Huth, J. F., Beitsch, P. D., Leitch, M., Hoover, S., Euhus, D., Haley, B., Morrison, L., Fleming, T. P., Herlyn, D., Terstappen, L. W., Fehm, T., Tucker, T. F., Lane, N., Wang, J., & Uhr,.** Circulating tumor cells in patients with breast cancer dormancy. *Clin Cancer Res.* 10(24), 2004, pp. 8152–8162.
147. **Barnes, J. M., Nauseef, J. T., & Henry, M. D.** Resistance to fluid shear stress is a conserved biophysical property of malignant cells. *PloS one.* 7(12), e50973, 2012.

148. **Tharmalingam, T., Ghebeh, H., Wuerz, T., & Butler, M.** Pluronic enhances the robustness and reduces the cell attachment of mammalian cells. *Mol Biotechnol.* 39(2), 2008, pp. 167–177.
149. **Chang, D., Fox, R., Hicks, E., Ferguson, R., Chang, K., Osborne, D., Hu, W., & Velev, O. D.** Investigation of interfacial properties of pure and mixed poloxamers for surfactant-mediated shear protection of mammalian cells. 156, 2017, pp. 358–365.
150. **Guzniczak, E., Jimenez, M., Irwin, M., Otto, O., Willoughby, N., & Bridle, H.** Impact of poloxamer 188 (Pluronic F-68) additive on cell mechanical properties, quantification by real-time deformability cytometry. *Biomicrofluidics.* 12(4), 2018.
151. **Yamada, T., Matsuda, A., Koizumi, M., Shinji, S., Takahashi, G., Iwai, T., Takeda, K., Ueda, K., Yokoyama, Y., Hara, K., Hotta, M., Matsumoto, S., & Yoshida, H.** Liquid Biopsy for the Management of Patients with Colorectal Cancer. *Digestion.* 99(1), 2019, pp. 39–45.
152. **Sharma, S., Zhuang, R., Long, M., Pavlovic, M., Kang, Y., Ilyas, A., & Asghar, W.** Circulating tumor cell isolation, culture, and downstream molecular analysis. *Biotechnology advances.* *Biotechnol Adv.* 36(4), 2018, pp. 1063–1078.
153. **Agashe R, Kurzrock R.** Circulating Tumor Cells: From the Laboratory to the Cancer Clinic. *Cancers (Basel).* 12(9), 2020.
154. **Huang, L. H., Lin, P. H., Tsai, K. W., Wang, L. J., Huang, Y. H., Kuo, H. C., & Li, S. C.** The effects of storage temperature and duration of blood samples on DNA and RNA qualities. *PloS one.* 12(9), 2017.
155. **Tanner, M. A., Berk, L. S., Felten, D. L., Blidy, A. D., Bit, S. L., & Ruff, D. W.** Substantial changes in gene expression level due to the storage temperature and storage duration of human whole blood. *Clin Lab Haematol.* 24(6), 2002, pp. 337–341.
156. **Kosti, I., Jain, N., Aran, D., Butte, A. J., & Sirota, M.** Cross-tissue Analysis of Gene and Protein Expression in Normal and Cancer Tissues. *Sci Rep.* 6, 24799, 2016.
157. **de Sousa Abreu, R., Penalva, L. O., Marcotte, E. M., & Vogel, C.** Global signatures of protein and mRNA expression levels. *Mol Biosyst.* 5(12), 2009, pp. 1512–1526.
158. **Maier, T., Güell, M., & Serrano, L.** Correlation of mRNA and protein in complex biological samples. *FEBS Lett.* 583(24), 2009, pp. 3966–3973.
159. **Gry, M., Rimini, R., Strömberg, S., Asplund, A., Pontén, F., Uhlén, M., & Nilsson, P.** Correlations between RNA and protein expression profiles in 23 human cell lines. *BMC Genomics.* 10, 365, 2009.
160. **Kozminsky, M., Fouladdel, S., Chung, J. S., Wang, Y., Smith, D. C., Alva, A., Azizi, E., Morgan, T., & Nagrath, S.** Detection of CTC Clusters and a Dedifferentiated RNA-Expression Survival Signature in Prostate Cancer. *Adv Sci (Weinh).* 6(2), 2018.

161. **Khan, M. A., Chen, H. C., Zhang, D., & Fu, J.** Twist: a molecular target in cancer therapeutics. *Tumour Biol.* 34(5), 2013, pp. 2497–2506.
162. **Shatzkes, K., Teferedegne, B. & Murata, H.** A simple, inexpensive method for preparing cell lysates suitable for downstream reverse transcription quantitative PCR. *Sci Rep.* 4, 4659, 2014.
163. **Svec, D., Andersson, D., Pekny, M., Sjöback, R., Kubista, M., & Ståhlberg, A.** Direct cell lysis for single-cell gene expression profiling. *Front Oncol.* 3, 274, 2013.
164. **Viet-Phuong Le, A., Huang, D., Blick, T. et al.** An optimised direct lysis method for gene expression studies on low cell numbers. *Sci Rep.* 5, 12859, 2015.
165. **Pfützner, C., Schröder, I., Scheungraber, C., Dogan, A., Runnebaum, I. B., Dürst, M., & Häfner, N.** Digital-Direct-RT-PCR: a sensitive and specific method for quantification of CTC in patients with cervical carcinoma. *Sci Rep.* 4, 3970, 2014.
166. **Ahmed, M. G., Abate, M. F., Song, Y., Zhu, Z., Yan, F., Xu, Y., Wang, X., Li, Q., & Yang, C.** Isolation, Detection, and Antigen-Based Profiling of Circulating Tumor Cells Using a Size-Dictated Immunocapture Chip. *Angew Chem Int Ed Engl.* 56(36), 2017, pp. 10681-10685.
167. **Varillas, J. I., Zhang, J., Chen, K., Barnes, I. I., Liu, C., George, T. J., & Fan, Z. H.** Microfluidic Isolation of Circulating Tumor Cells and Cancer Stem-Like Cells from Patients with Pancreatic Ductal Adenocarcinoma. *Theranostics.* 9(5), 2019, pp. 1417–1425.
168. **Chu, C. H., Liu, R., Ozkaya-Ahmadov, T., Boya, M., Swain, B. E., Owens, J. M., Burentugs, E., Bilen, M. A., McDonald, J. F., & Sarioglu, A. F.** Hybrid negative enrichment of circulating tumor cells from whole blood in a 3D-printed monolithic device. *Lab Chip.* 19(20), 2019, pp. 3427–3437.
169. **Chu, C. H., Liu, R., Ozkaya-Ahmadov, T., Swain, B. E., Boya, M., El-Rayes, B., Akce, M., Bilen, M. A., Kucuk, O., & Sarioglu, A. F.** Negative enrichment of circulating tumor cells from unmanipulated whole blood with a 3D printed device. *Sci Rep.* 11(1), 2021.
170. **Van Peer, G., Mestdagh, P., & Vandesompele, J.** Accurate RT-qPCR gene expression analysis on cell culture lysates. *Sci rep.* 2, 222, 2012.
171. **Biosystems, Applied.** *TaqMan® multiplex PCR optimization for optimization of multiplex PCR using 7500/7500 Fast, ViiA™ 7, and QuantStudio™ real time PCR systems.* s.l. : Thermo Fisher Scientific, 2014. Publication part number MAN0010189..
172. **Mubarak, SMH, Al-Koofee, DAF, Radhi OA, Ismael JM, Al-Zubaidi ZF.** An optimization and common troubleshooting solving in polymerase chain reaction technique. *Syst Rev Pharm.* 11 (2), 2020, pp. 427-436.
173. **Rombach, M., Kosse, D., Faltin, B., Wadle, S., Roth, G., Zengerle, R., & von Stetten, F./.** Real-time stability testing of air-dried primers and fluorogenic hydrolysis probes stabilized by trehalose and xanthan. *Biotechniques.* 57(3), 2014, pp. 151–155.

174. **Shu, W., Douglas, D.L., Kumari, S., Romero, L.E., Rodriguez, L.G., Zou, C., & Newman, R.** Abstract 1884: Development of a novel VIM-RFP reporter line for colorectal cancer EMT study and drug discovery. *Cancer Res.* 79, 2019, Vol. (13_Supplement): 1884.
175. **Varillas, J. I., Zhang, J., Chen, K., Barnes, I. I., Liu, C., George, T. J., & Fan, Z. H.** Microfluidic Isolation of Circulating Tumor Cells and Cancer Stem-Like Cells from Patients with Pancreatic Ductal Adenocarcinoma. *Theranostics.* 9(5), 2019, pp. 1417–1425.
176. **Chen, J., Liu, C. Y., Wang, X., Sweet, E., Liu, N., Gong, X., & Lin, L.** 3D printed microfluidic devices for circulating tumor cells (CTCs) isolation. *Biosens Bioelectron.* 150, 111900, 2020.
177. **Pizon M, Schott D, Pachmann U, Pachmann K.** The number of tumorspheres cultured from peripheral blood is a predictor for presence of metastasis in patients with breast cancer. *Oncotarget.* 26;7(30), 2016, pp. 48143-48154.
178. **Hou, H., Warkiani, M., Khoo, B. et al Hou H, Warkiani M, Khoo B, Li Z, Soo R, Tan D, Lim W, Han J, Bhagat A, Lim C.** Isolation and retrieval of circulating tumor cells using centrifugal forces. *Sci Rep.* 2013; 3(1259).
179. **Wang G, Benasutti H, Jones JF, Shi G, Benchimol M, Pingle S, Kesari S, Yeh Y, Hsieh LE, Liu YT, Elias A, Simberg D.** Isolation of Breast cancer CTCs with multitargeted buoyant immunobubbles. *Colloids Surf B Biointerfaces.* Jan 2018, Vol. 161, 200-209.
180. **Liu P, Jonkheijm P, Terstappen LWMM, Stevens M.** Magnetic Particles for CTC Enrichment. *Cancers (Basel).* Nov 2020, Vol. 12(12), p. 3535.
181. **Rombach, M, et al.** Real-time stability testing of air-dried primers and fluorogenic hydrolysis probes stabilized by trehalose and xanthan. *BioTechniques,* 57(3). 2014, pp. 151–155.
182. **Wirtz D, Konstantopoulos K, Searson PC.** The physics of cancer: the role of physical interactions and mechanical forces in metastasis. *Nat Rev Cancer.* 11(7), 2011, pp. 512-22.
183. **Craig, N., Fletcher, S. L., Daniels, A., Newman, C., O'Shea, M., Tan, W. S., Warr, A., & Tait-Burkard, C.** Direct Lysis RT-qPCR of SARS-CoV-2 in Cell Culture Supernatant Allows for Fast and Accurate Quantification. *Viruses.* 14(3), 508, 2022.
184. **Toss A, Mu Z, Fernandez S, Cristofanilli M.** CTC enumeration and characterization: moving toward personalized medicine. *Ann Transl Med.* 2(11):108, 2014.

Appendix

Table A1: List of devices

Device	Supplier
2100 Bioanalyzer Instrument	Agilent Technologies, St. Clara, USA
7500 Real-Time PCR System	ThermoFisher Scientific, Waltham, USA
–80 °C Freezers MDF-Q500VX-PE	Panasonic
Cell counter model R1	Olympus, Shinjuku, Japan
Centrifuge Heraeus 17	ThermoFisher Scientific, Waltham, USA
Centrifuge 5810R	Eppendorf, Hamburg, Germany
Environmental scanning electron microscope	Thermo Fisher Scientific
Fusion Solo S	Vilber Lourmat, Eberhardzell, Germany
Ice machine	Zigna, Isernhagen, Germany
Incubators	Binder, Tuttlingen, Germany
Kryotank BR2200	Cryo diffusion, Léry, France
Microscope BX61	Olympus, Shinjuku, Japan
Microscope IX83	Olympus, Shinjuku, Japan
pH-meter Five Easy	Mettler Toledo, Columbus, USA
Pipet boy	Integra Biosciences
Pipettes, 10 µL, 200 µL, 1000 µL	Eppendorf
Plate centrifuge	Benchmark Scientific, Sayreville, USA
Plate thermos-shaker	Biosan
Refrigerator	Bosch
Safety cabinets	Berner, Elmahorn, Germany
Scales	Mettler Toledo
Environmental scanning electron microscope	Thermo Fisher Scientific, Waltham, USA
Spectramax	Molecular Devices, San Jose, USA
Syringe pump neMESYS	Cetoni, GmbH, Korbußen, Germany
ThermoMixer C	Eppendorf
GL.compact Laser system	GFH GmbH, Deggendorf, Germany
UV flow benches	Kisker
Vortexer IKA Ms3	Sigma-Aldrich, Steinheim, Germany
Water bath	Memmert
NanaoDrop2000	Thermo Fisher Scientific, Waltham, USA
Qubit	Thermo Fisher Scientific, Waltham, USA

Table A2: List of disposables

Disposables	Supplier
--------------------	-----------------

Blood sample tubes, 3.4 mL, 7.5 mL	Sarstedt
Cell counting slides	Olympus
Cell culture flasks	Greiner Bio-One, Kremsmünster, Austria
Cell culture plates, 12-well, 24-well	Greiner Bio-One, Kremsmünster, Austria
Luminescence assay plates, Pierce™	ThermoFisher Scientific, Waltham, USA
96-Well Polystyrene Plates, White Opaque	
Maintrac® assay plates, 96 Well Black/Clear Bottom Plate	ThermoFisher Scientific, Waltham, USA
96-well microtiter plates	Greiner Bio-One, Kremsmünster, Austria
PCR plates	ThermoFisher Scientific, Waltham, USA
PCR sealing foil	Life Technologies
Pipette tips, 10 µL, 200 µL, 1000 µL	Sigma Aldrich
Polycarbonate microscopic slides	Robert Bosch GmbH
Sample tubes, 15 mL, 50 mL	
Sample tubes, cell culture, 1.5 mL	Eppendorf
Sample tubes, PCR-clean, 1.5 mL	Eppendorf
Serological pipettes	
Silicon tubes	
TEM-grids	Plano GmbH,
Transportation boxes maintrac® samples	SIMFO, Bayreuth, Germany
Vivalytic cartridges	Robert Bosch GmbH

EBERHARD KARLS
UNIVERSITÄT
TÜBINGEN



**Universitätsklinikum
Tübingen**

Medizinische Fakultät

Ethik-Kommission

Prof. Dr. med. Karl Jaschonek
Vorsitzender

Telefon: +49 7071 29-77661

Telefax: +49 7071 29-5965

E-Mail:

ethik.kommission@med.uni-tuebingen.de

Ethik-Kommission an der Medizinischen Fakultät der Eberhard-Karls-Universität
und am Universitätsklinikum Tübingen, Gartenstraße 47, 72074 Tübingen

Herrn
Prof. Dr. med. Michael Bitzer
Medizinische Klinik
Abteilung Innere Medizin I
Otfried-Müller-Str. 10
72076 Tübingen

nachrichtlich:
Herrn Prof. Dr. med. Nisar Peter Malek
480/2019B02
unsere Projekt-Nummer

05.11.2019
eingegangen am

02.01.2020
Datum

**Therapy monitoring by circulating tumor cells (CTC) for patients with advanced
gastrointestinal tumors (GI-CTC monitoring).**

Hier:

**Schreiben vom 29.10.2019, Beantwortung der Fragen der Ethik-Kommission aus dem
Schreiben vom 20.08.2019, Studienprotokoll Version 1.1 vom 29.10.2019 mit sichtbaren
Änderungen, Information für Studienteilnehmer Version Oktober 2019 mit sichtbaren Än-
derungen, Information und Einwilligungserklärung zum Datenschutz Version 1.1 vom
29.10.2019 mit sichtbaren Änderungen**

Sehr geehrter Herr Kollege,

die Unterlagen zur oben genannten Studie hatten der Ethik-Kommission an der Medizinischen
Fakultät und am Universitätsklinikum Tübingen bereits zur Beratung vorgelegen. Mit Schreiben
vom 20.08.2019 hatte die Kommission um weitere Informationen zum Prüfplan und um Ände-
rungen/Ergänzungen des Informationstextes gebeten. Die geänderten und ergänzten Unterla-
gen haben nunmehr der Ethik-Kommission erneut zur Beratung vorgelegen.

Danach bestehen gegen die geplante Studie seitens der Kommission keine Bedenken.

Für die Durchführung Ihres Studienvorhabens wünschen wir viel Erfolg.
Mit freundlichen Grüßen

Prof. Dr. med. Dieter Luft
Stellvertretender Vorsitzender der Ethik-Kommission

Seite 2: Allgemeine Hinweise zum Schreiben der Ethik-Kommission

Universitätsklinikum Tübingen
Anstalt des öffentlichen Rechts
Sitz Tübingen
Geissweg 3 • 72076 Tübingen
Tel. 07071/29-0
www.medizin.uni-tuebingen.de
Steuer-Nr. 86156/09402
USt-ID. DE 146 889 674

Aufsichtsrat
Ulrich Steinbach (Vorsitzender)
Vorstand
Prof. Dr. Michael Bamberg (Vorsitzender)
Gabriele Sonntag (Stellv. Vorsitzende)
Prof. Dr. Karl Ulrich Bartz-Schmidt
Prof. Dr. Ingo B. Autenrieth
Klaus Tischler

Baden-Württembergische Bank Stuttgart
BLZ 600 501 01 Konto-Nr. 7477 5037 93
IBAN: DE 41 6005 0101 7477 5037 93
BIC (SWIFT-Code): SOLADEST600
Kreissparkasse Tübingen
BLZ 641 900 20 Konto-Nr. 14 144
IBAN: DE 79 6415 0020 0000 0141 44
BIC (SWIFT-Code): SOLADES1TUB

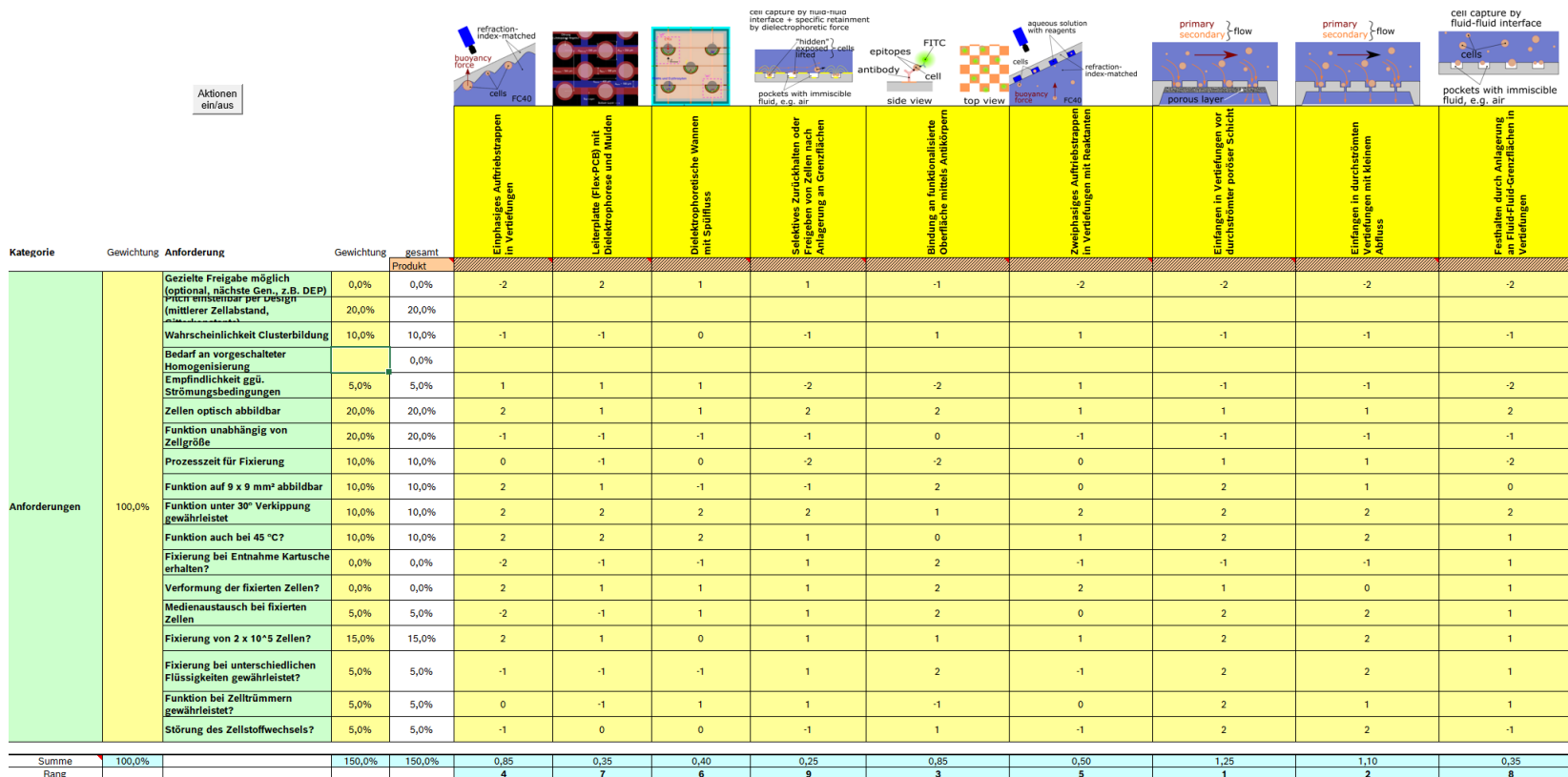


Figure A1: Concept decision matrix according to Pugh

Real-time counting of cells during capture on the filter – MATLAB Code

```

%VideoSize = [432 528];
VideoSize = [800 1200];

%Create a System object to read video from avi file.
filename = 'Film1.avi';
hvfr = VideoReader(filename);

% Create a BlobAnalysis System object to find the centroid of the segmented cells in the
video.
hblob = vision.BlobAnalysis( ...
    'AreaOutputPort', false, ...
    'BoundingBoxOutputPort', false, ...
    'OutputDataType', 'single', ...
    'MinimumBlobArea', 4, ...
    'MaximumBlobArea', 300, ...
    'MaximumCount', 1500);

% Acknowledgement
ackText = ['Data set courtesy of Jonathan Young and Michael Elowitz, ' ...
    'California Institute of Technology'];

%Create a System object to display the video.
hVideo = vision.VideoPlayer;
hVideo.Name = 'Results';
%hVideo.Position(1) = round(hVideo.Position(1));
%hVideo.Position(2) = round(hVideo.Position(2));
hVideo.Position(1) = 20;
hVideo.Position(2) = 20;
hVideo.Position([4 3]) = 50+VideoSize;

%scale video to window frame
set(0,'showHiddenHandles','on')
fig_handle =(gcf);
fig_handle.findobj % to view all the linked objects with the vision.VideoPlayer
ftw = fig_handle.findobj ('TooltipString', 'Maintain fit to window'); % this will search the
object in the figure which has the respective 'TooltipString' parameter.
ftw.ClickedCallback() % execute the callback linked with this object

%Stream Processing Loop
%Create a processing loop to count the number of cells in the input video.
% This loop uses the System objects you instantiated above.
frameCount = int16(1);

%set up array handle to store Centroid positions for every frame
numberOfFrames = hvfr.Duration*hvfr.FrameRate;
Centroid_handle = cell(numberOfFrames,1);
image_handle = cell(numberOfFrames,1);
image_handle_marker = cell(numberOfFrames,1);

```

```

while hasFrame(hvfr)
    % Read input video frame
    % crop circle
    image = im2single(readFrame(hvfr));
    imageSize = size(image);

    ci = [880, 1300, 750]; % center and radius of circle ([c_row, c_col, r])
    [xx,yy] = ndgrid((1:imageSize(1))-ci(1),(1:imageSize(2))-ci(2));
    mask = (xx.^2 + yy.^2)<ci(3)^2;
    croppedImage = zeros(size(image));
    croppedImage(:, :, 1) = image(:, :, 1).*mask;
    croppedImage(:, :, 2) = image(:, :, 2).*mask;
    croppedImage(:, :, 3) = image(:, :, 3).*mask;

    % image = rgb2gray(im2single(readFrame(hvfr)));
    image = rgb2gray(croppedImage);

    % Apply a combination of morphological dilation and image arithmetic
    % operations to remove uneven illumination and to emphasize the
    % boundaries between the cells.
    y1 = 4*image - imdilate(image, strel('square',7));
    y1(y1<0) = 0;
    y1(y1>1) = 1;
    y2 = imdilate(y1, strel('square',7)) - y1;

    th = multithresh(y2); % Determine threshold using Otsu's method
    y3 = (y2 <= th*0.9); % Binarize the image.

    Centroid = step(hblob, y3); % Calculate the centroid
    Centroid_handle{frameCount} = Centroid; %store Centroid positions for current frame in
array handle
    numBlobs = size(Centroid,1); % and number of cells.
    image_handle{frameCount}=image; %store image of current frame in array handle

    % Display the number of frames and cells.
    frameBlobTxt = sprintf('Frame %d, Count %d', frameCount, numBlobs);
    image = insertText(image, [1 1], frameBlobTxt, ...
        'FontSize', 35, 'BoxOpacity', 0, 'TextColor', 'white');
    image = insertText(image, [1 size(image,1)], ackText, ...
        'FontSize', 10, 'AnchorPoint', 'LeftBottom', ...
        'BoxOpacity', 0, 'TextColor', 'white');

    % Display video
    image_out = insertMarker(image, Centroid, '*', 'Color', 'green', 'size', 15);
    step(hVideo, image_out);
    image_handle_marker{frameCount}=image_out; %store image mit Centroid positions
positions for current frame in array handle

    frameCount = frameCount + 1;

```

```
end
```

```
close all
```

```
% anderer Ansatz: wir schauen einfach nur, wie viele Cells pro Frame dazu
% kommen und integrieren einfach nur diese Differenz auf. Dann haben wir
% nicht die Positionen der Cells, aber zumindest die Gesamt-Anzahl
```

```
numberOfCells_AllFrames = 0;
differenceCells = zeros(numberOfFrames,1);
differenceCells(1) = size(Centroid_handle{1},1);
for i = 2:numberOfFrames
    numberOfCellsA = size(Centroid_handle{i-1},1);
    numberOfCellsB = size(Centroid_handle{i},1);
    differenceCells(i) = numberOfCellsB-numberOfCellsA;
    if numberOfCellsB > numberOfCellsA
        numberOfCells_AllFrames = numberOfCells_AllFrames + (numberOfCellsB-
numberOfCellsA);
    end
end
cells = msgbox(['The counter counted ', num2str(numberOfCells_AllFrames), ' cells!']);
```

List of publications, inventions, and conference contributions

Journal publication

Parts of this dissertation were published in:

Lux, A., Bott, H., Malek, N. P., Zengerle, R., Maucher, T., & Hoffmann, J. (2021). Real-Time Detection of Tumor Cells during Capture on a Filter Element Significantly Enhancing Detection Rate. *Biosensors*, 11(9), 312. <https://doi.org/10.3390/bios11090312>

Patent applications

Reduktion von Scherstress auf Zellen bei der nicht-lyserenden Akkumulation über ein Rückhalteelement in einem Lab-on-Chip-System

Anmeldenummer: 102021208831.7, angemeldet am 12.08.2021

Maucher Tanja (CR/ATC4), Grumaz Christian (CR/ATC4), Bott Hannah (CR/ATM3), Lux Astrid (CR/ATC4)

Verfahren zur Fixierung und Stabilisierung eines Zustandes von Flüssigkeiten in einer Kartusche eines Lab-on-Chip und zugehörige Kartusche

Anmeldenummer: 102020202269.0, angemeldet am 21.02.2020

Maucher Tanja (CR/ATC4), Lux Astrid (CR/ATC4), Bott Hannah (CR/ATM3)

DE102020215567A1

Rückhaltevorrichtung und Verfahren zur Separierung von Zellen

Anmeldenummer: 102020215567.4, angemeldet am 09.12.2020

Hoffmann Jochen (CR/ATM3), Lux Astrid (CR/ATC4), Maucher Tanja (CR/ATC4), Bott Hannah (CR/ATM3)

Contributions to scientific conferences:

Astrid Lux, Lars Rosenbaum, Hannah Bott, Nisar Malek, Tanja Maucher, Jochen Hoffmann (2022) Integration of a cell quantification function into a Lab on Chip system – Isolation and real time counting of circulating tumor cells. *SelectBio Lab-on-a-Chip and Microfluidics Europe, Rotterdam*. Poster

Astrid Lux (2021) Enrichment and molecular analysis of circulating tumor cells. *10th Robert Bosch PhD Conference, Renningen*. Presentation

Supervision of master theses

P. Häubi. (2020) Development of a New Microfluidic Unit Operation for Rare Cell Separation on a Lab-on-a-Chip System. *ETH Zürich, Laboratory of Thermodynamics in Emerging Technologies*

T. Hein (2021) Charakterisierung einer Zellisolationsmethode in einem mikrofluidischen System und Evaluierung des Einflusses auf die Zellen. *Fachhochschule Münster, Fachbereich Physikalische Technik, Master Biomedizinische Technik*

K. Hoffmann (2021) Analysis of epithelial-mesenchymal transition-related gene expression of circulating tumor cells and integration into a Lab-on-a-chip platform. *Technische Universität Darmstadt, Center for Synthetic Biology*

Erklärung zum Eigenanteil der Dissertationsschrift

Die Arbeit wurde im Zentrum für Forschung und Vorausbildung der Robert Bosch GmbH in Zusammenarbeit mit der Inneren Medizin I der Universitätsklinikums Tübingen unter Betreuung von Prof. Dr. Nisar Peter Malek durchgeführt.

Die Konzeption der Studie durch Prof. Dr. Michael Bitzer in Zusammenarbeit mit Prof. Dr. Nisar Peter Malek (Doktorvater) und die Versuchsplanung erfolgte in Zusammenarbeit mit Tanja Maucher (Robert Bosch interne Betreuerin).

Sämtliche Versuche wurden (nach Einarbeitung durch Labormitglieder der Robert Bosch GmbH) von mir durchgeführt.

Die Vergleichsversuche für die CTC-Detektion und Zählung nach der maintrac® Methode wurden von SIMFO in Bayreuth durchgeführt. Die jeweiligen Ergebnisse wurden zum Ende der Therapie des jeweiligen Patienten ausgetauscht.

Die im Anhang der Dissertation aufgeführten Simulationen wurden durch Hannah Bott (Robert Bosch GmbH) durchgeführt und sind in der unten angegebenen, gemeinsamen Publikation enthalten.

Der Code für die MATLAB-basierte Zelldetektion im Ergebnisteil 3.2.4.3 wurde im Rahmen der Masterarbeit von Tabea Hein erstellt. Die Auswert-Algorithmen für die Python-basierte Echtzeit-Zelldetektion im Ergebnisteil 3.2.4.3 wurden von Lars Rosenbaum (Robert Bosch GmbH) erstellt.

Die statistische Auswertung erfolgte eigenständig durch mich.

Ich versichere, das Manuskript selbständig verfasst zu haben und keine weiteren als die von mir angegebenen Quellen verwendet zu haben.

Ergebnisse der Dissertationsschrift wurden im September 2021 im Journal „Biosensors“ des MDPI-Verlags mit dem Titel „Real-Time Detection of Tumor Cells during Capture on a Filter Element Significantly Enhancing Detection Rate“ (doi: 10.3390/bios11090312) veröffentlicht. Die Publikation ist als vollständiger Text online einzusehen. Alle Koautoren waren mit der Veröffentlichung und der Nutzung der Ergebnisse für die Dissertation einverstanden. Alle in der Doktorarbeit verwendeten Abbildungen und Texte aus dieser Publikation sind entsprechend in der Beschreibung oder als Zitat kenntlich gemacht.

Weitere Präsentationen der Ergebnisse der Doktorarbeit fanden bei den folgenden Kongressen statt:

- Vortrag auf der Robert Bosch PhD Konferenz am 18.09.2020 in Renningen unter dem Titel „Enrichment and molecular analysis of circulating tumor cells“
- Posterpräsentation auf der “SELECTBIO - Lab-on-a-Chip and Microfluidics Europe 2022” vom 21.06. bis 22.06.2023 in Rotterdam unter dem Titel “Integration of a cell quantification function into a Lab-on-Chip system – Isolation and real-time counting of circulating tumor cells“

Renningen, den 02.06.2023

Astrid Lux

Danksagung

An erster Stelle möchte ich mich bei meinem Doktorvater Prof. Dr. Nisar Malek für die Offenheit gegenüber der Betreuung einer Industriepromotion und die Unterstützung des Forschungsthemas bedanken. Bei Ihnen und Prof. Dr. Michael Bitzer möchte ich mich herzlich bedanken für das Interesse am Thema und die regelmäßigen Besprechungen zu Zwischenergebnissen, sowie den fachlichen Input vonseiten der Klinik und der Universität bedanken.

Bei Prof. Dr. Michael Bitzer, Verena May, Lisa Jödicke, Ursula Koppenhöfer, Corinna Walker möchte ich mich herzlich bedanken für die Organisation der Studie und die Probennahme. Zudem danke ich allen Mitarbeitern der Firma SIMFO, insbesondere Frau Prof. Dr. Pachmann, Frau Pizon und Frau Schott für die Zusammenarbeit in der Analyse der Patientenproben. Die Diskussionen und Austauschrunden waren ein wertvoller Beitrag zu dieser Arbeit.

Die vorliegende Arbeit wurde unter Anleitung von Tanja Maucher, Karin Lemuth und Anke Timm der Robert Bosch GmbH in Renningen angefertigt. Für die großartige Betreuung meiner Doktorarbeit möchte ich mich herzlich bei Euch bedanken. Durch die regelmäßigen Rücksprachen und Euren fachlichen Input konnte die Arbeit vorangetrieben und stetig verbessert werden.

Für die Ermöglichung der Dissertation in der CR/ATC4 und im Healthcare Team und das stete Interesse an meiner Arbeit möchte ich Bernd Reinsch, Jürgen Rapp, Jochen Feichtinger, Franz Lärmer und Jochen Hoffmann ein großes Dankeschön zukommen lassen.

Ein großes Dankeschön geht an meine Doktoranden-Kollegen Anne Hoffmann, Manuel Loskyll, Janik Kärcher und insbesondere an das Team-CTC Samir Kadic, Michael Knapp, Hannah Bott. Ich danke Euch für all den fachlichen Austausch, Input und die wissenschaftlichen und nicht-wissenschaftlichen Diskussion rund um das Promotionsthema und was uns Doktoranden sonst noch beschäftigt hat, sowie für die vielen unterhaltsamen Kaffeerunden.

Meinen Studenten Patrick Häubi, Katharina Hoffmann, Tabea Hein, Julia Schon, die mich tatkräftig bei meinem Projekt unterstützt haben, möchte ich ebenfalls danken. Ein besonderer Dank geht an Katha und Tabea für die lustigen Stunden im Labor und im OneNote Laborbuch, das auch jetzt noch sehr unterhaltsam zu lesen ist.

Ein riesiges Dankeschön geht an alle Mitarbeiter und Mitarbeiterinnen des HCS-Teams für das tolle Arbeitsklima, die wissenschaftlichen Diskussionen in Regelmeetings und im Labor, das Interesse an meinem Promotionsthema und die interessanten und lustigen After-Lunch-Coffee-Kuchen-Runden. Ich bin froh auch nach meiner Promotionszeit weiterhin Teil diesen großartigen Teams zu sein und freue mich auf alle weiteren Themen und Aktivitäten innerhalb und außerhalb der Arbeitszeit mit Euch.

An die Kollegen aus den anderen Bosch Abteilungen Christian Hoffmann, Freya Kiesewetter, Lars Rosenbaum richtet sich ein großes Dankeschön für die Unterstützung im Rahmen von weiterführenden Analysen und Methodiken im Rahmen der Dissertation. Ebenfalls bedanken möchte ich mich bei Christoph Essig für die Betreuung meiner ersten Stelle bei Bosch im Rahmen eines Praktikums.

Der größte Dank gilt meiner Familie, die mir diese Ausbildung ermöglicht hat. Danke, dass Ihr mich auf diesem Weg stets unterstützt und bestärkt habt und somit einen wesentlichen Anteil am Erfolg dieser Arbeit geleistet habt. Ganz besonders möchte ich auch meinem Mann Peter Lux danken. Danke, dass Du mich in allen Phasen der Dissertation unterstützt und mir Kraft gegeben hast und immer die nötigen motivierenden oder auch kritischen Worte gefunden hast, die mir sehr geholfen haben, die Dissertation fertigzustellen. Ich liebe Euch!